Constraining the physics of relativistic jets with radio through (sub-)millimetre properties of X-ray binaries

by

Alexandra Jean Tetarenko

A thesis submitted in partial fulfillment of the requirements for the degree of

Doctor of Philosophy

Department of Physics
University of Alberta

Abstract

Astrophysical jets are ubiquitous phenomena in our universe, linked to a wide range of objects, from young stars to black holes. These powerful, highly collimated outflows deposit significant amounts of energy and matter into the surrounding medium, affecting star formation, galaxy evolution, and even the distribution of matter in the universe. However, despite decades of research, our current knowledge of the physics that gives rise to and governs the behaviour of these jets is still extremely limited. Of all the systems that launch jets, X-ray binaries are particularly excellent testbeds, as they evolve through bright outburst phases on rapid timescales of days to months, providing a real-time view of how these jets evolve and interact with their environment.

In this thesis, I develop a new suite of data reduction, analysis, and modelling techniques to extract unknown jet properties from observational data of X-ray binary jets. In particular, I explore how the jet emission changes with frequency (through the broad-band spectrum), time (through the temporal variability properties and high resolution imaging), and in response to changes in the X-ray emission from the accretion flow (through disc-jet coupling correlations). I also analyze the conditions in regions where these jets are interacting with their local environment. Further, through this work I demonstrate that

the relatively untested mm/sub-mm frequency bands provide a unique viewpoint on these jets, and allow us to open up new ways to study jet phenomena across the X-ray binary population.

Preface

This thesis is original work by Alexandra Jean Tetarenko, conducted under supervision by Gregory Sivakoff.

Chapter 2 of this thesis has been published in Tetarenko, A.J. et al. 2016, "Disc-jet coupling in the Terzan 5 neutron star X-ray binary EXO 1745–248", *MNRAS*, 460, 345–355.

Chapter 3 of this thesis has been published in Tetarenko, A.J. et al. 2018, "A Radio Frequency Study of the Accreting Millisecond X-ray Pulsar, IGR J16597–3704, in the Globular Cluster NGC 6256", *ApJ*, 854, 125, 1–8.

For the work presented in Chapters 2 and 3, I performed the VLA radio data reduction and analyses, and wrote the papers. V. Tudor performed the ATCA data reduction, and A. Bahramian performed the X-ray data reduction. G. Sivakoff led the planning of the observations and writing of the VLA/*Swift* telescope proposals to obtain the data, with assistance from all authors. All authors contributed to the manuscripts.

Chapter 4 of this thesis consists of a manuscript in preparation, to be submitted to the *Monthly Notices of the Royal Astronomical Society (MNRAS)* journal as Tetarenko, A.J. et al. 2018, "Radio timing analysis of the compact jet in the black hole X-ray binary Cygnus X-1". I performed the VLA data reduction and all analyses, and wrote the paper. B. Tetarenko reduced the *NuStar* data. P. Casella, J. Miller-Jones, and G. Sivakoff assisted with the data analysis and interpretation. G. Sivakoff and J. Miller-Jones led the planning of the observations and writing of the VLA and *NuStar* telescope proposals to obtain the data, with assistance from all authors. All authors contributed to the manuscript.

Chapter 5 of this thesis has been published in Tetarenko, A.J. et al. 2017, "Extreme jet ejections from the black hole X-ray binary V404 Cygni", *MNRAS*, 469, 3141–3162.

Chapter 6 of this thesis has been has been submitted to the *Monthly Notices of the Royal Astronomical Society (MNRAS)* journal as Tetarenko, A.J. et al. 2018, "Tracking the variable jets of V404 Cygni during its 2015 outburst".

For the work presented in Chapters 5 and 6, I performed the VLA, SMA, and JCMT data reduction, all data analysis, and wrote the papers. M. Bremer performed the NOEMA data reduction, K. Mooley performed the AMI data reduction, and A. Bahramian performed the *Swift* data reduction. I wrote the telescope proposals and planned the observations for the SMA, JCMT, and NOEMA telescopes, and G. Sivakoff and J. Miller-Jones led the writing of the telescope proposals and planning of the observations for the VLA telescope, with assistance from all authors. All authors contributed to the manuscripts.

Chapter 7 of this thesis consists of excerpts from a manuscript in-preparation, to be submitted to the *Nature* journal as Miller-Jones, J.C.A., Tetarenko, A.J. et al. 2018, "Rapidly-precessing relativistic jets from the stellar-mass black hole V404 Cygni". I wrote the text in Chapter 7 based on an in preparation paper led by J. Miller-Jones, for which I will be second author. For the work presented in Chapter 7, I was responsible for performing the Monte-Carlo modelling, I participated in writing the telescope proposals used to obtain the data, contributed to manuscript edits, and was strongly involved in analyzing the data. J. Miller-Jones also led the writing of the telescope proposal BM421, and designed, processed, and analyzed the VLBA observations. G. Sivakoff led the writing of the telescope proposal BS249. M. Middleton led the interpretation of the data, as well as performed the Lense-Thirring precession calculations.

Chapter 8 of this thesis has been published in Tetarenko, A.J. et al. 2018, "Mapping jet-ISM interactions in X-ray binaries with ALMA: a GRS 1915+105

case study", *MNRAS*, 475, 448–468. I wrote the ALMA telescope proposal to obtain the data, planned the observations, performed the data reduction and analyses, and wrote the paper. E. Rosolowsky assisted with designing and planning the observations, data analysis, and interpretation. All authors contributed to the telescope proposal and manuscript.

A significant part of results presented in this thesis are based on new observations obtained from the following observatories: Karl G. Jansky Very Large Array (VLA; Chapters 2, 3, 4, 5, and 6), Australian Telescope Compact Array (ATCA; Chapter 2), Very Long Baseline Array (VLBA; Chapter 7), Arc-minute Microkelvin Imager Large Array (AMI-LA; Chapter 6), Sub-millimeter Array (SMA; Chapter 5 and 6), James Clerk Maxwell Telescope (JCMT; Chapter 5 and 6), Northern Extended Millimetre Array (NOEMA[1]; Chapter 6), Atacama Large Millimeter/Sub-millimeter Array (ALMA; Chapter 8), Nuclear Spectroscopic Telescope Array (NuSTAR; Chapter 4), *Chandra* Observatory (Chapters 2 and 3), and Neil Gehrels *Swift* Observatory (Chapter 2, 3, and 6). Archival observations from the Hubble Space Telescope (HST; Chapter 3), *Herschel* Space Observatory (Chapter 8), Wide-field Infrared Survey Explorer (WISE; Chapter 8), United Kingdom Infrared Telescope (UKIRT; Chapter 8), Caltech Sub-millimeter Observatory (CSO; Chapter 8), and Spitzer Space Telescope (Chapter 8) are also utilized in this thesis.

---

[1]Formerly known as the Plateau de Bure Interferometer (PdBI).

Dedication

For my Mom & Dad, who instilled in me the belief that I could do anything I put my mind to, and that no one should ever have the ability to convince me otherwise.

Acknowledgements

No one ever accomplishes anything alone, and this thesis is certainly no exception. Here I want to recognize everyone who helped me along the way, not only making this thesis what it is today, but also influencing who I have become as a researcher and a person. As such, in true Canadian fashion, the next few pages will likely contain enough thank you's to fill a whole other thesis, but I assure you I mean every single one of them.

First and foremost I need to thank my supervisor, Greg Sivakoff, for putting up with me for the last 6 years. I still remember the first day I walked into your office, you showed me a talk on the JACPOT project, and sufficed to say I was hooked from the get go. I mean studying jets launched from black holes, how cool is that! While I may have a lot more knowledge on the subject today, that sentiment still stands. Beyond introducing me to this amazing field of study and schooling me in the dark arts of interferometry, you have given me abundant opportunities to learn and grow as a researcher; you allowed me to take lead on multiple projects, trusted me with more responsibility then you probably should have, introduced me to many awesome people who I now call collaborators, and allowed me to travel all over the world to share my work. Ultimately, you took me in as an inexperienced student and turned me into a real astrophysicist, and for that I am forever grateful.

Next, I wish to offer a special thanks to James Miller-Jones for a great many things; for sharing his seemingly infinite knowledge on everything from interferometry to jet physics (I swear I learn something new every time I talk to you!), for the many emails and Skype chats, for always providing helpful feedback and advice on everything from proposals, to papers, to talks, to deciding

the newest weird thing CASA is doing to our data. You guys were always there to listen to me rant, and more often then not, talked me off the ledge. Quite honestly, you guys kept me sane most of the time. Thank you to Aarran and Kenny for being more than worthy hockey adversaries. Our Oilers/Flames rivalry was a lot of fun to participate in, and I will treasure that video of you guys decked out in Flames gear forever! Thank you also to all my office mates over the years for not being fazed by my craziness (or at least pretending to not be).

Thank you to my closest collaborators, that I am incredibly fortunate to have had the opportunity to work with and learn from; Sebastian, Sera, Dipankar, Dave, Poshak, Diego, Matt, Laura, Jay, Rich, Nathalie, Rudy, and Tom.

Thank you to my observing contacts for teaching me the ins and outs of sub-mm observing, often going above and beyond to support me and my team through many observing campaigns over the years; Glen, Ryan, Mark G., Iain, Jan, Mark R., Brenda, Gerald, Michael, Melanie, and Jan Martin. Thank you also to my observing partners on Maunakea, for answering my many questions and showing me how everything worked; Tony, Andrew, and Will.

A significant amount of work presented in this thesis is based on observational data obtained from telescopes located on Maunakea. As such, I also wish to recognize and acknowledge the very significant cultural role and reverence that the summit of Maunakea has always had within the indigenous Hawaiian community. I am incredibly fortunate to have had the opportunity to conduct observations from this mountain.

Thank you to my parents for encouraging me to pursue every one of my dreams, and supporting me through all of it. Mom, thanks especially for the numerous care packages filled with your cooking and baking, they helped more than you could ever know. Dad, the super human levels of strength and resilience I have seen you display absolutely amaze me, and I strive to find those

same qualities in myself.

Thank you to my twin sister, who is simultaneously my arch nemesis and my greatest ally, you push me to be better every day like no one else can.

Thank you to Ben (who takes on many roles; my canine brother, my shrink, my extra hairy best buddy, my running partner) for never leaving my side, and always succeeding in cheering me up, even on the worst of days.

Lastly, I am thankful for all the dreadful Edmonton winters of minus crazy below I have suffered through, which clearly convinced the universe that I deserved to move to Hawaii for my first postdoc.

Contents

8 Mapping jet-ISM interactions in X-ray binaries with ALMA: a GRS 1915+105 case study   271

List of Tables

List of Figures

List of Abbreviations

AGN	Active Galactic Nuclei
ALMA	Atacama Large Millimeter/Sub-millimeter Array
AIPS	Astronomical Image Processing System
AMI-LA	Arc-Minute MicroKelvin Imager Large Array
AMXP	Accreting Milli-Second X-ray Pulsar
ASIC	Application Specific Integrated Circuit
ATCA	Australian Telescope Compact Array
AU	Astronomical Unit
	(1 AU=1.4×10^{13} cm or 500 light-seconds)
BAT	Burst Alert Telescope
BH	Black Hole
BHXB	Black Hole X-ray Binary
CASA	Common Astronomy Software Application
CCF	Cross-Correlation Function
CSO	Caltech Sub-millimeter Observatory
CV	Cataclysmic Variable
FFT	Fast Fourier Transform
GHz	GigaHertz (1 GHz = 10^9 Hz)
GLIMPSE	Galactic Legacy Infrared Mid-Plane
	Survey Extraordinare
GTI	Good Time Interval
HST	Hubble Space Telescope
INTEGRAL	International Gamma-ray
	Astrophysics Laboratory
IR	Infrared
IRAS	Infrared Astronomical Satellite

IRAM	Institute de Radioastronomie Millimetrique
IGM	InterGalactic Medium
ISM	InterStellar Medium
JCMT	James Clerk Maxwell Telescope
Jy	Jansky (1 Jy=10^{-23} erg s^{-1} cm^{-2} Hz^{-1})
kpc	kiloparsec (1 kpc=3.086×10^{15} cm)
$L_{\rm Edd}$	Eddington Luminosity
	($L_{\rm Edd} = 1.3 \times 10^{38} \frac{M}{M_\odot}$ erg s^{-1})
QPO	Quasi-Periodic Oscillation
mas	milli-arcseconds (1 mas = 10^{-3} arcsec)
MAXI	Monitor of All-sky X-ray Image
MCMC	Markov Chain Monte-Carlo
MHD	Magneto-HydroDynamics
mid-IR	mid-Infrared
MIRIAD	Multichannel Image Reconstruction,
	Image Analysis and Display
mJy	milli-Janksy (1 mJy = 10^{-3} Jy)
mm/sub-mm	Millimeter/Sub-millimeter
NIR	Near-Infrared
NOEMA	NOrthern Extended Millimetre Array
NRAO	National Radio Astronomy Observatory
NS	Neutron Star
NSXB	Neutron Star X-ray Binary
NuSTAR	Nuclear Spectroscopic Telescope Array
Opt.	Optical
PA	Position Angle
PACS	Photoconductor Array Camera and Spectrometer
PC	Photon Counting
pc	parsec (1 pc=3.086×10^{18} cm)

PdBI	Plateau de Bure Interferometer
PWV	Precipitable Water Vapor
PV	Position-Velocity
PSD	Power Spectral Density
R_g	Gravitational Radius ($R_g = \frac{GM}{c^2} = 1.47 \times 10^5 \frac{M}{M_\odot}$ cm)
RFI	Radio Frequency Interference
SCUBA-2	Submillimetre Common User Bolometer Array 2
SMA	Sub-Millimeter Array
SWARM	SMA Wideband Astronomical ROACH2 Machine
SPIRE	Spectroscopic and Photometric Imaging Reciever
tMSP	Transitional Milli-Second Pulsar
UCXB	Ultra-Compact X-ray Binary
μJy	micro-Janksy ($1\,\mu$Jy $= 10^{-6}$ Jy)
UKIRT	United Kingdom Infrared Telescope
UKIDSS	United Kingdom Infrared Telescope Deep Sky Survey
ULX	UltraLuminous X-ray Source
μm	micro-meters (1μm $= 10^{-6}$ m)
UV	Ultra-Violet
VLA	(Karl G. Jansky) Very Large Array
VLBA	Very Long Baseline Array
VLBI	Very Long Baseline Interferometry
WISE	Wide-Field Infrared Survey Explorer
WT	Window Timing
XB	X-ray Binary
XRT	X-ray Telescope
XSPEC	X-ray Spectral Fitting Package

Chapter 1

Introduction to Studying Jets in Astrophysics

Astrophysical jets are powerful outflows of energy and matter that have been identified in a wide range of objects (e.g., young stars, supernovae, gamma-ray bursts, and black holes; Mirabel & Rodríguez 1999; Fender 2010). These jets are thought to play key roles in many different astrophysical processes, from star formation to galaxy evolution (Silk & Rees, 1998; Fabian, 2012; Mirabel et al., 2011). Of all the systems that launch jets, X-ray binaries (XBs) are ideal laboratories for studying jet phenomena, due to their close proximity (located at kiloparsec distances) and the rapid timescales of XB jet activity (days–months), which provide a real-time view of how these jets evolve and interact with their environment.

1.1 X-ray Binaries (XBs)

XBs are binary systems containing a stellar mass black hole or neutron star (BH or NS; i.e., the compact remnant of a massive star), that is accreting matter from a companion star (see Figure 1.1). In these binary systems, the matter transferred away from the companion star possesses a significant amount
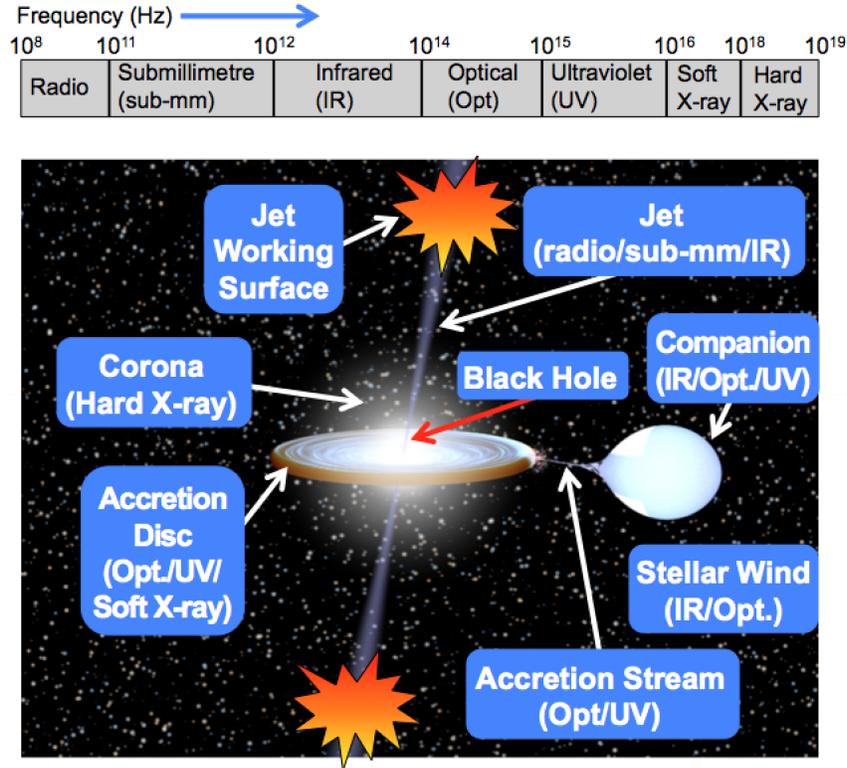
Figure 1.1: Schematic of an XB system and its surrounding environment, where, in this case, the compact object is a black hole. The components of the system (and the frequencies at which their emission dominates), as well as the zones where the jets collide with the surrounding medium (jet working surfaces), are labelled. A map of the frequency bands from the electromagnetic spectrum that can be sampled by different telescopes and are considered in this thesis, is shown at the top of the panel (background image credit: R. Hynes).

of angular momentum, preventing the accreted material from directly falling toward the compact object. Alternatively, a differentially rotating accretion disc is formed (Frank et al., 2002). As the matter in this accretion disc orbits around the compact object, angular momentum is transferred outwards (due to processes that convert kinetic energy into internal energy that can be radiated away; Balbus & Hawley 1991), resulting in the matter falling farther toward the compact object. At some point, a portion of the accreted material can also be transported back outwards in the form of a bi-polar relativistic jet.

From an observational perspective, these binary systems produce emission

across the electromagnetic spectrum, where jet emission dominates in the lower frequency bands (radio, sub-mm, infrared) and emission from the accretion flow dominates in the higher frequency bands (optical, X-ray). The jet emission originates from synchrotron radiation (characterized by a non-thermal spectrum, high brightness temperature[1], and at times a high degree of linear polarization), due to the presence of highly relativistic electrons and magnetic fields in these systems (Mirabel & Rodríguez, 1999; Fender, 2006).

1.1.1 Types of Jets

Two types of jets have been observed in XBs, depending on the rate at which mass is accreted onto the compact object; a compact jet at lower accretion rates, and ballistically moving jet ejecta, with apparent proper motions that can exceed the speed of light, at higher accretion rates.

Compact jets are collimated outflows of relativistic plasma. Observationally, these compact jets are characterized by a flat to slightly inverted optically thick broad-band spectrum ($\alpha > 0$, where $f_\nu \propto \nu^\alpha$; Fender 2001), extending from radio through sub-mm frequencies and above (Corbel & Fender, 2002; Casella et al., 2010; Tetarenko et al., 2015d). This spectrum becomes optically thin ($\alpha \sim -0.7$; Russell et al. 2013b) often around infrared frequencies, resulting in a spectral break ($\nu_{\text{break}} \sim 10^{11-14}$ Hz; e.g. Russell et al. 2013b,c; Díaz Trigo et al. 2018). While compact jets are traditionally thought of as steady, persistently emitting phenomena, compact jet emission in XBs has been observed to vary over a range of timescales (< 1 day to months; e.g., Pooley & Fender 1997; Corbel et al. 2000; Fender et al. 2004a; Miller-Jones et al. 2009; Fender et al. 2009; Curran et al. 2014; Tetarenko et al. 2015d). Further, compact jets have only been directly imaged (resolved) with Very Long Baseline Interferometry

---

[1] The brightness temperature is defined as the temperature of a black-body having the same brightness as the target source at that particular frequency. This term is often used in radio astronomy, where the Rayleigh-Jeans regime is applicable (Taylor et al., 1998).
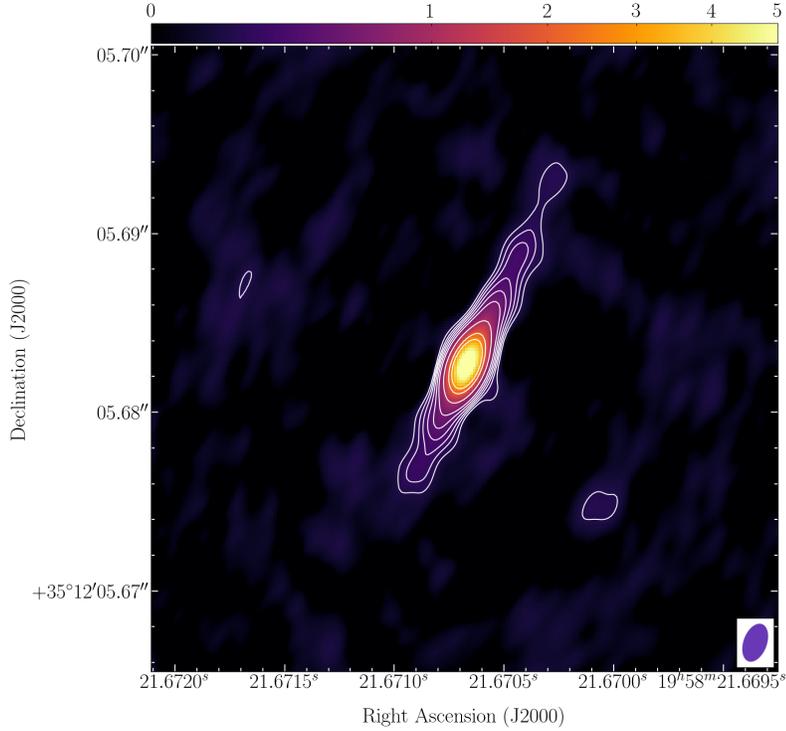
Figure 1.2: An example of radio emission observed from a XB compact jet. This high resolution image of the compact jet in Cygnus X-1 is created from a data set taken with the Very Long Baseline Array (VLBA) in the 15.4 GHz band (image credit: J. Miller-Jones, private communication). The color scale (units of mJy) and contours (2^n times the base level of $0.016\,\mathrm{mJy\,bm^{-1}}$, where $n = 2.3, 3, 3.5, 4, 4.5, 5, 6, 7, 7.5$) represent the intensity of the radio emission. The purple ellipse indicates the synthesized beam size. The compact jet in Cygnus X-1 is resolved along the jet axis out to ~ 15 mas (at a distance of 1.86 kpc this corresponds to ~ 18 AU). An asymmetric, one-sided jet is observed in this system due to the Doppler boosting effect (see §1.1.3 for details).

(VLBI) in a limited number of cases (e.g., GRS 1915+105 and Cygnus X-1; Stirling et al. 2001; Dhawan et al. 2000). These VLBI studies suggest that compact jet size scales along the axial direction are on the order of a few astronomical units (AU; $1\,\mathrm{AU} = 1.5 \times 10^{13}\,\mathrm{cm}$ or ~ 500 light seconds), and place upper limits on compact jet widths on the order of sub-AU scales (see Figure 1.2).

The spectral, temporal, and morphological characteristics of compact jets are all consistent with their being produced as a result of partially self-absorbed

synchrotron emission, where each frequency below the spectral break probes emission from the optical depth $\tau = 1$ surface, coming from a narrow range of distances downstream in the jet (Blandford & Königl, 1979; Falcke & Biermann, 1995). In this model, emission from the higher frequencies (i.e., sub-mm/infrared) originates from regions along the jet axis that are closer to where the jet is launched, while lower frequency (i.e., radio) emission originates from regions farther down the jet axis. The location of the spectral break marks the most compact region of the jet, where particles are first accelerated to high energies (Markoff et al., 2001, 2005). The exact spectral shape (i.e., optically thick and thin spectral indices) is believed to depend on jet properties such as geometry, magnetic field structure, and particle density profiles (Heinz & Sunyaev, 2003; Markoff et al., 2005; Casella & Pe'er, 2009; Russell et al., 2013c; van der Horst et al., 2013; Russell et al., 2014), as well as the plasma conditions in the region where the jet is first accelerated (Polko et al., 2010, 2013, 2014; Koljonen et al., 2015).

Jet ejecta are discrete clouds of plasma travelling at bulk relativistic speeds (see Figure 1.3). Observationally, these ejecta are characterized by an optically thin spectrum at frequencies above the self-absorption turnover in the spectrum ($\alpha < 0$), can be routinely resolved with VLBI (e.g., Hjellming & Rupen 1995; Tingay et al. 1995; Miller-Jones et al. 2004), and are often accompanied by bright, multi-frequency flaring activity. Based on the above observational characteristics, jet ejection events are believed to be the result of the injection of energy and particles to create an adiabatically expanding synchrotron emitting plasma, threaded by a magnetic field (e.g., van der Laan synchrotron bubble model; van der Laan 1966; Hjellming & Johnson 1988; Hjellming & Han 1995). These ejection events have been linked to both X-ray spectral and timing signatures (e.g., Fender et al. 2009; Miller-Jones et al. 2012; Russell et al. 2014; Kalemci et al. 2016), although a definitive sequence of events leading to jet ejection has not yet been identified.
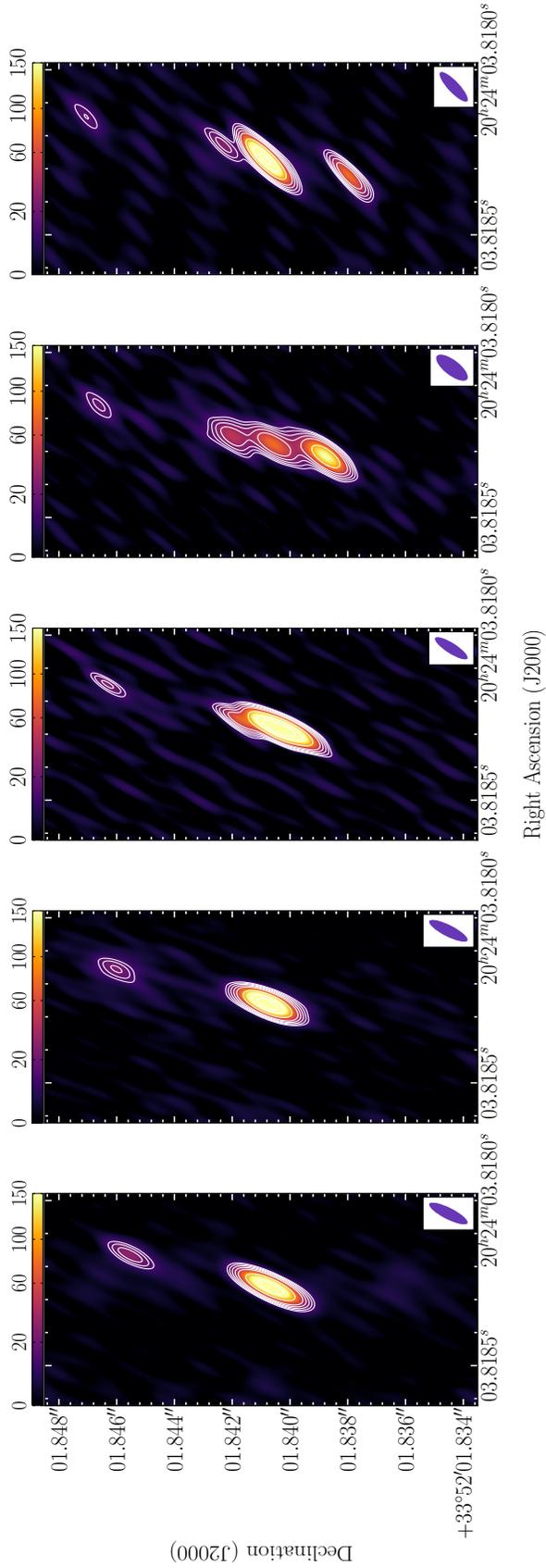
Figure 1.3: An example of radio emission observed from XB jet ejecta. This sequence of high resolution images of the jet ejecta launched from V404 Cygni (spaced by 30 minutes) is created from a data set taken with the Very Long Baseline Array (VLBA) in the 15.4 GHz band (image credit: J. Miller-Jones, private communication; note that these data are also presented in Chapter 7 of this thesis). The color scale (units of mJy) and contours (2^n times the base level of $1.5 \, \mathrm{mJy} \, \mathrm{bm}^{-1}$, where $n = 3, 3.5, 4, 4.5, 5, 6, 7, 7.5$) represent the intensity of the radio emission. The purple ellipses indicate the synthesized beam size. Multiple discrete blobs of emission, whose bulk motion can be tracked, are clearly resolved in these images. The rapid (hourly) timescale of the ejections shown here represents an extrema of jet ejecta behaviour in XBs, where ejecta observed from other systems tend to evolve on much longer (day–month) timescales.

6
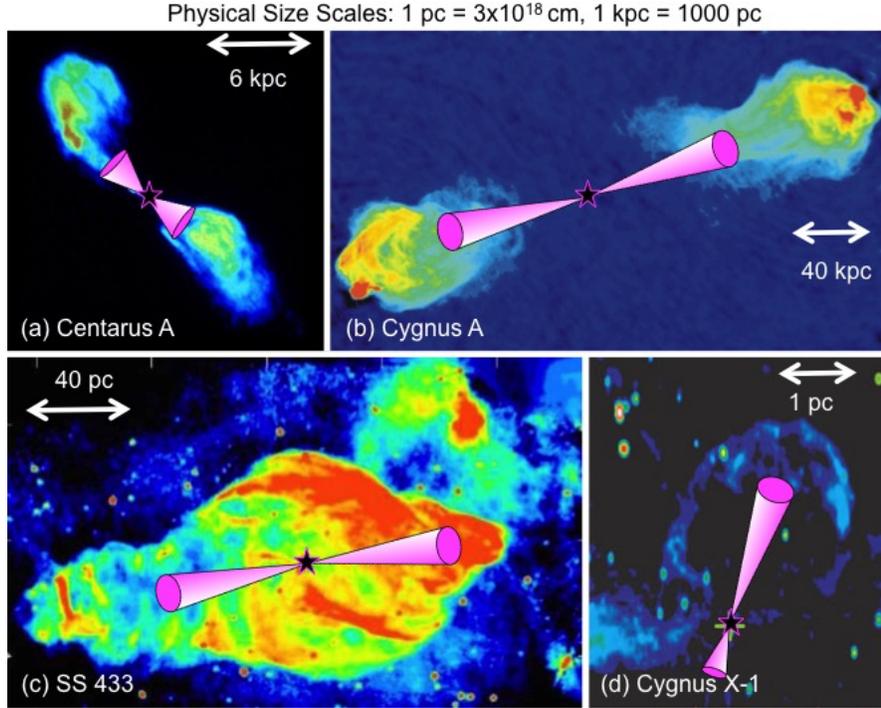
Figure 1.4: Examples of jet interaction sites identified near known black hole jet sources. Panels (a) and (b) display radio frequency images of active galactic nuclei (AGN; the more massive analoges to XBs, where a super-massive black hole can accrete at the center of a galaxy, image credits: NRAO), where large scale radio lobe structures are observed. Panels (c) and (d) display jet interaction sites near XB sources in our Galaxy (Dubner et al., 1998; Gallo et al., 2005b). The location of the black hole (black star), and the direction in which the jets propagate (purple cones) are indicated, where the background color map represents the intensity of the radio emission (blue is faint, red is bright).

Given that XBs can release a large portion of liberated accretion power into their relativistic jets (Heinz & Grimm, 2005; Russell et al., 2010), both types of jets are predicted to significantly influence their surrounding environment. For example, Fender et al. 2005 estimate that XB jets can inject $\sim 1\%$ of the time-averaged luminosity of supernovae into the surrounding ISM. XB energy injection can work to heat the ISM, generates interstellar turbulence, produces high-energy cosmic rays, seed the ISM with magnetic fields, and possibly stimulate star formation (Heinz et al., 2008; Mirabel et al., 2015). However, the way in which these jet-ISM interactions manifest themselves (e.g., flux, morphology,

7

chemistry) near XBs has not been well characterized. To date, there are only two XBs (SS 433; Dubner et al. 1998, and Cygnus X-1; Gallo et al. 2005b; see Figure 1.4) where confirmed jet-ISM interaction sites have been detected (i.e., a jet-blown bubble/cavity and shock excited gas are observed). Although, a number of other potential candidate interaction sites have been suggested in the vicinity of different XBs (e.g., 1E1740–2942; Mirabel et al. 1992, GRS 1758-258; Martí et al. 2002, GRS 1915+105; Kaiser et al. 2004; Rodríguez & Mirabel 1998; Chaty et al. 2001; also see Chapter 8 of this thesis).

Despite being studied for decades and across multiple XB systems, there are still many fundamental unknowns when it comes to both types of XB jets. The most notable unknowns include jet composition, jet speeds, the occurrence of jet precession, and jet launching mechanisms. For example, while it is clear the jet plasma contains electrons, it is unclear whether they are paired with positrons or protons (where evidence for baryonic jet content, in the form of relativistically Doppler shifted emission lines, has been observed in only two XB sources, SS 433 and 4U 1630–47[2]; Margon et al. 1979; Kotani et al. 1994; Díaz Trigo et al. 2013). While jet ejecta speeds have been directly measured in multiple XBs ($\Gamma \sim 1 - 2$; Hjellming & Johnson 1981; Hjellming et al. 2000b; Hjellming & Rupen 1995), compact jet speed has never been directly measured.

Further, the mechanisms by which these jets are launched and accelerated remains as another open question in the field today. While several mechanisms of jet production and collimation have been suggested, the magnetically driven theories are currently favoured, as magnetic acceleration mechanisms can simultaneously produce the required relativistic velocities and collimation properties

---

[2]We note that while Díaz Trigo et al. (2013) interpret the discovery of Doppler shifted X-ray emission lines in 4U 1630-47 as evidence for baryonic matter in the jets of this system, alternate explanations have also been presented. For example, Wang & Méndez (2016) reanalyze the data presented in Díaz Trigo et al. (2013), finding that a different X-ray spectral model (utilizing different S and Fe abundances in the ISM material along the line of sight) can also fit the data. Additionally, Neilsen et al. (2014) find no evidence of Doppler shifted emission lines in an earlier observation of this source.

of these jets (Mirabel & Rodríguez, 1999; Meier et al., 2001). This magneto-hydrodynamical (MHD) mechanism has been applied to accretion discs and rotating black holes in the form of two main models, the Blandford-Payne mechanism (Blandford & Payne 1982) and the Blandford-Znajek mechanism (Blandford & Znajek 1977). The Blandford-Payne mechanism operates by extracting rotational energy and angular momentum from the accretion disc through magnetic fields anchored to the disc, while the Blandford-Znajek mechanism operates by extracting the spin energy of the black hole through magnetic field lines threading the event horizon[3]. Although, it is important to note that it is entirely possible for more than one launching mechanism to be operating in accreting XB systems, under different conditions or at different scales.

1.1.2 Phenomenology and Evolution

Many XB systems are transient in nature, evolving from periods of inactivity into a bright out-bursting state on timescales of days to months. In these transients, outburst periods are characterized by rapid increases in the X-ray luminosity (an observational proxy for mass accretion rate), which can approach levels as high as the Eddington limit[4], as well as the increase in intensity of the jet emission. As XBs evolve from quiescence into outburst and back again, they pass through different accretion states (defined through various X-ray spectral and temporal properties; see Done et al. 2007 and references within for details). Multi-wavelength observational studies of many XBs throughout their outbursts have revealed that changes in the accretion flow (probed by

---

[3]Punsly & Coroniti 1990 imagined another jet production mechanism similar to the Blandford-Znajek mechanism. In this mechanism, the magnetic field lines do not thread the event horizon, but instead are anchored in the accreting plasma, and in turn are subject to frame dragging effects near the black hole.

[4]The Eddington limit is the luminosity, assuming pure hydrogen accretion and spherical symmetry, where the outwards radiation force (on the electrons) balances the inwards gravitational force (on the protons). The Eddington luminosity scales linearly with mass, $L_{\text{Edd}} = \frac{4\pi G M m_p c}{\sigma_T} \cong 1.3 \times 10^{38} \frac{M}{M_\odot} \, \text{erg s}^{-1}$ (Frank et al., 2002).

the X-ray emission) are closely linked to morphological, spectral, and temporal changes in the jet (probed by radio emission, e.g., Migliari & Fender 2006; Tudose et al. 2009; Miller-Jones et al. 2012; Corbel et al. 2013).

In black hole X-ray binary (BHXB) systems, a phenomenological model has been put forward to explain this disc-jet connection, where changes in mass accretion rate are the catalyst driving changes in jet behaviour (Tananbaum et al., 1972; Blandford & Königl, 1979; Vadawale et al., 2003; Fender et al., 2004a, 2009). In quiescence and the hard X-ray accretion state a compact jet is present. As the system evolves through the rising hard state, where the X-ray luminosity (and, in turn the mass accretion rate) increases, the jet velocity and power are also thought to increase. At the same time, the compact jet spectrum has been observed to evolve, where the location of the spectral break appears to shift to lower frequencies (toward the radio regime), as the source begins to transition into a softer accretion state (van der Horst et al., 2013; Russell et al., 2014). This spectral evolution cannot be driven solely by optical depth effects, which predict an opposite scaling for the spectral break frequency ($\nu_{\mathrm{break}} \propto \dot{M}^{2/3}$). Alternatively, recent work (Koljonen et al., 2015), which shows a correlation between the location of the spectral break and the photon index of the X-ray spectrum, suggests that the flux density and location of the spectral break (tracing the particle acceleration properties within jets) may instead be connected to the properties of the plasma close to the black hole. When the source makes the transition from hard to soft accretion states at higher luminosities, the system launches discrete jet ejecta (Mirabel & Rodríguez, 1994; Hjellming & Rupen, 1995; Kuulkers et al., 1999; Corbel et al., 2002; Miller-Jones et al., 2012; Brocksopp et al., 2013), possibly as a result of internal shocks in the jet flow produced by the changes in jet velocity. Once the source reaches the soft state, jet emission is believed to be quenched altogether (or faint enough to be below the detection thresholds of current instruments; Fender et al. 1999b; Corbel et al. 2001; Russell et al.

2011; Coriat et al. 2011b; Rushton et al. 2016), with any residual radio emission usually attributed to an interaction between the jet ejecta and the surrounding medium (e.g., Corbel et al. 2004). The compact jet is then re-established as the source moves back into the hard state (where the jet is re-established well before quiescence; Kalemci et al. 2013).

Similar to BHXBs, neutron star X-ray binary (NSXB) jet behaviour is also thought to be governed by mass accretion rate (e.g., Homan et al. 2010). In terms of the disc-jet connection, NSXB and BHXB systems display both similarities and differences (Migliari & Fender, 2006). A compact jet is observed in NSXBs at lower X-ray luminosities ($< 0.1 L_{\mathrm{edd}}$) in hard accretion states (Migliari et al. 2010), and discrete jet ejections have been found at higher X-ray luminosities (e.g., Fender et al. 2004b, Fomalont et al. 2001a; Spencer et al. 2013), as seen in BHXBs. However, BHXBs tend to be much more radio loud than NSXBs at the same X-ray luminosity (Fender & Kuulkers 2001; Migliari & Fender 2006), and NSXB jets do not all appear to be fully quenched in softer accretion states (Migliari et al., 2004).

A key observational tracer of the disc-jet connection in different classes of XBs is the radio/X-ray correlation (see Figure 1.5), relating radio and X-ray luminosities ($L_{\mathrm{R}} \propto L_{\mathrm{X}}^{\beta}$, where β represents the disc-jet coupling index; Gallo et al. 2003; Corbel et al. 2013). This empirical relationship couples a compact, partially self-absorbed synchrotron jet (probed by radio emission) to the properties of the accretion flow (probed by X-ray emission), where we assume that the total jet power is a fixed fraction of the accretion power and that X-ray luminosity depends on mass accretion rate (Falcke & Biermann 1995; Heinz & Sunyaev 2003; Markoff et al. 2003). Further, through the addition of a mass parameter, this correlation has been extended across the BH mass scale to include AGN, the supermassive analogues of BHXBs (Merloni et al., 2003; Falcke et al., 2004; Plotkin et al., 2012). While BHXBs have been well studied in this plane (where different systems, sampled over several orders of
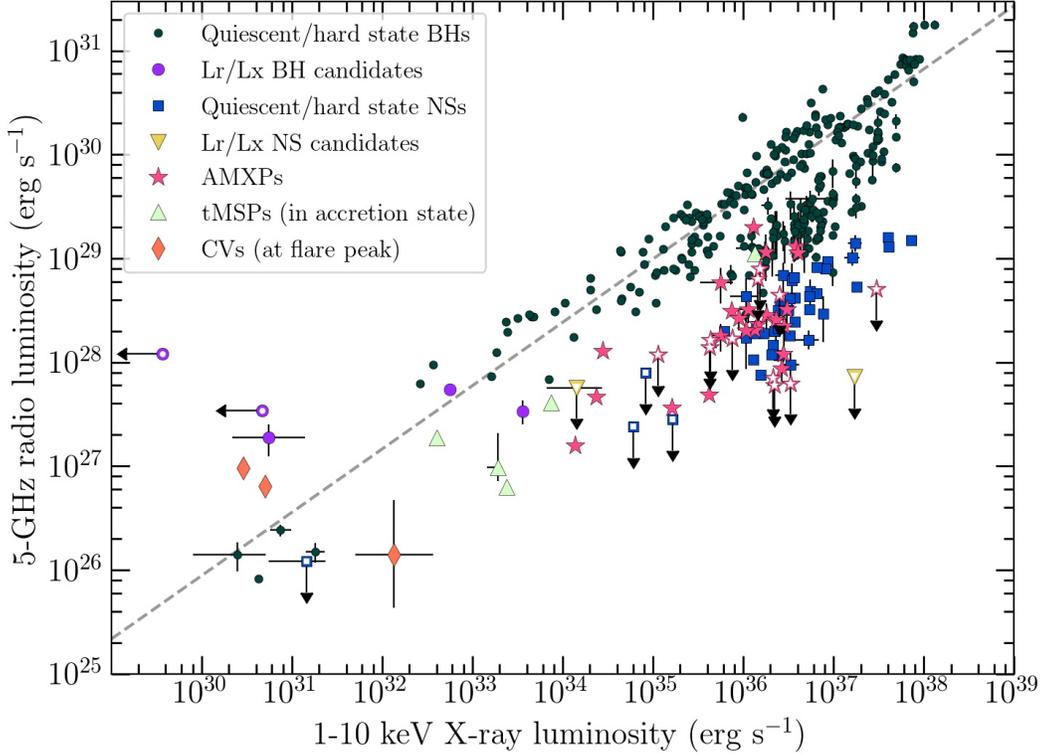
Figure 1.5: Disc-jet coupling correlation for XBs, relating radio luminosity (at 5 GHz) to X-ray luminosity (in the 1-10 keV band). Different types of accreting stellar-mass compact objects are shown; black holes (BHs; binaries harboring black holes), neutron stars (NS; binaries harboring non-pulsating neutron stars), accreting milli-second X-ray pulsars (AMXPs; accreting neutron star binaries where X-ray pulsations at the spin period of the neutron star are observed), transitional milli-second pulsars (tMSPs; accreting neutron star binaries that switch between a rotation-powered pulsar state and an accretion-powered state), and out-bursting cataclysmic variables (CVs; binaries harboring white dwarfs). The best-fit relation for black holes ($\beta = 0.61$, grey dashed; Gallo et al. 2014) is also shown. This plot is produced using the repository of Bahramian et al. 2018.

magnitude in X-ray luminosity, are known to display correlations that range from $\beta \sim 0.6 - 1.8$; Coriat et al. 2011b; Gallo et al. 2014; Russell et al. 2015; Gallo et al. 2018), the different classes of NSXBs are not as well sampled, and have shown more complex behaviour when compared to the BHXBs (Migliari & Fender, 2006; Miller-Jones et al., 2010; Deller et al., 2015; Papitto et al., 2013; Tudor et al., 2017). An active area of research today involves building a larger sample of XB systems with measurements in this plane, to understand

what factors drive the differences between black hole and neutron star systems.

1.1.3 Relativistic Effects

As XB jets are moving at relativistic speeds and the jet axis is often inclined to our line of sight, both relativistic and projection effects will influence the emission we observe. In particular, there are several important effects that take place.

Relativistic Beaming: Relativistic beaming is an effect in which radiation from a relativistically moving source (where $\beta = \frac{v}{c}$ represents the velocity as a fraction of the speed of light) appears concentrated in the direction of its motion, according to a stationary observer. This effect is a direct consequence of light aberration, or the apparent shift in the direction of radiation emitted by a moving source, and is described as follows (Bradt, 2008),

$$\cos \theta = \frac{\cos \theta' + \beta}{1 + \beta \cos \theta'} \, , \tag{1.1}$$

where $'$ denotes variables in the rest frame of the source, and θ represents the angle between the jet axis and the line of sight. The broad-band spectrum we observe from relativistic jets is a direct consequence of this effect. As the electrons in the jet spiral around the magnetic fields lines, a beam of synchrotron radiation emitted from these jets sweeps past the observers line of sight. The observer sees a narrow pulse of radiation, whose Fourier transform produces the observed spectrum from these jets.

Doppler Boosting: Doppler boosting is an effect that enhances/diminishes (boosts/de-boosts) the intensity of the received radiation from a relativistically moving source. This effect originates from a combination of the relativistic Doppler effect ($\nu = \delta \nu'$; where the Doppler factor $\delta = \frac{\sqrt{1-\beta^2}}{1 \mp \beta \cos \theta}$) and relativistic beaming. Considering a source of relativistically moving electrons from a

jet emitting synchrotron emission (which follows a power-law spectrum, with spectral index α), the intensity of the observed jet synchrotron emission is related to the intensity seen in the rest frame (at the same frequency)[5] through $I_\nu(\nu) = \delta^{3-\alpha} I'_\nu(\nu)$. In the context of relativistic jets, Figure 1.2 displays a direct consequence of Doppler boosting, where we only observe a one-sided jet from the XB Cygnus X-1.

Superluminal Motion: Superluminal motion is apparent motion that appears to be faster than the speed of light. For a discrete blob of relativistic plasma ejected at a speed βc, and at an angle θ with respect to the line of sight, the transverse motion travelled across the sky in some interval of time, Δt, can be represented as (Mirabel & Rodríguez, 1999),

$$\beta_{\text{trans}} c = \frac{d_{\text{trans}}}{\Delta t} = \beta\, c\, \sin\theta \tag{1.2}$$

However, due to the classical Doppler effect the interval between the reception of two photons by the observer is smaller than the interval between their emission. Therefore, we must replace Δt above by $\Delta t_{\text{obs}} = \Delta t - \frac{v \cos\theta \Delta t}{c} = \Delta t(1 - \beta\cos\theta)$, yielding the following apparent motion of the blob across the sky as seen by the observer,

$$\beta_{\text{app}}\, c = \frac{\beta\, c \sin\theta \Delta t}{\Delta t_{\text{obs}}} = \frac{\beta\, c \sin\theta}{(1 - \beta\cos\theta)} \tag{1.3}$$

At highly relativistic velocities (like those present in a jet), angles of $\theta \sim 5°-10°$ will produce apparent velocities across the sky that exceed the speed of light. The detection of superluminal motion from XB jet sources (first observed in GRS 1915+105 and GRO J1655-40; Mirabel & Rodríguez 1994, 1999; Tingay et al. 1995), represented the first evidence that these jet sources were travelling

---

[5]This doppler factor dependence is only true for discrete emission. For a continuous jet the flux is reduced by one doppler factor, as the observed emitting length of the jet is compressed by Lorentz contraction.

at significantly relativistic velocities (with Lorentz factors $\Gamma \geq 2$, where $\Gamma = (1 - \beta^2)^{-1/2}$).

1.2 Observational Techniques

To observe XB jets in the lower frequency (radio and mm/sub-mm) bands, we must utilize either single dish telescopes or interferometers (an array of multiple single dish telescopes operating together to synthesize a large aperature telescope with increased sensitivity and angular resolution). In this section, I outline how both types of telescopes measure astronomical signals, the calibration procedures needed to extract scientific measurements from the data, and special considerations that need to be taken into account when observing at higher mm/sub-mm frequencies.

1.2.1 Interferometric Arrays and Single Dish Telescopes

An interferometer measures the spatial coherence function of the electric field of a astronomical signal (referred to as the complex visibility, V_ν). This spatial coherence function is related to the sky brightness distribution (modified by atmospheric and instrumental effects) through the Fourier transform (Taylor et al., 1998).

In the case of a simple two-element interferometer, the complex visibility can be expressed as,

$$V_\nu(\mathbf{b}) = \int \int I_\nu(\mathbf{s}) e^{-2\pi i \nu \frac{\mathbf{b} \cdot \mathbf{s}}{c}} d\Omega \qquad (1.4)$$

where the baseline vector ($\mathbf{b}$) defines the separation between the two antennas, $\mathbf{s}$ represents the vector direction of the astronomical source, and $I(\mathbf{s})$ indicates the observed intensity, at a frequency ν, from solid angle $d\Omega$.

In multi-element interferometers (containing N antennas and N(N-1)/2 base-

lines between antennas), a specific geometric coordinate system referred to as the uv-plane is utilized. In this system, the baseline vectors have components, u, v and w (measured in wavelengths), while positions on the sky are defined with components l, m and $n = \sqrt{1 - l^2 - m^2}$, which represent direction cosines measured with respect to the u, v, and w axes, respectively. In this coordinate frame (and ignoring the w terms), the complex visibility can be expressed as,

$$V(u,v) = \int\int \mathcal{A}_\nu(l,m)I_\nu(l,m)e^{-2\pi i[ul+vm]}dldm\,, \qquad (1.5)$$

where $A_\nu(l,m)$ represents the primary beam, describing the sensitivity of the interferometer to the direction of the arrival of the radiation. The interferometer will make several measurements of this complex visibility (each measurement contains an amplitude and phase) at different points in the uv-plane.

The observed visibilities sampled by the interferometer differ from the true visibilities due to instrumental (hardware and software, electronics, and digital correlation) and environmental (atmospheric conditions, weather, and RFI) properties. Therefore, a calibration process must be used to recover the true visibilities. Denoting the observed visibilities as $\widetilde{V}_{i,j}(t,\nu)$ and the true visibilities as $V_{i,j}(t,\nu)$, the basic calibration formula is as follows,

$$\widetilde{V}_{i,j}(t,\nu) = \mathcal{G}_{i,j}(t,\nu)V_{i,j}(t,\nu)\,, \qquad (1.6)$$

where $\mathcal{G}_ij(t,\nu)$ represents factorable antenna based complex gains, dependent on frequency and time. These complex gains can be separated into antenna-based amplitude and phase corrections.

To utilize the calibration equation, calibrator sources (whose true visibilities are known) are observed in the sky intermittently with the target source. This sequence allows one to solve for the complex gains, and apply these corrections to the target source data. However, calibration using these external calibrators is imperfect and sometimes cannot completely correct errors in the target source

visibilities (e.g., most calibrators can not be observed simultaneously with the target and all calibrators are not in the exact same position in the sky as the target). Therefore, in some cases, self-calibration, an iterative process in which a target is essentially used to calibrate itself by producing a model (through *clean*, see below) of the sky intensity distribution, can be used.

To estimate the sky brightness distribution, the Fourier transform of the calibrated visibilities is taken,

$$T^D(l, m) = \int \int V(u, v) e^{2\pi i[ul+vm]} dl dm \qquad (1.7)$$

where $T^D(l, m)$ represents the modified sky brightness (or dirty image). Mathematically, the dirty image is represented as, $T^D(l, m) = \mathcal{A}(l, m) I(l, m) \star s(l, m)$; containing contributions from the true sky brightness, multiplied by the primary beam, and convolved with the point spread function ($s(l, m)$; or dirty beam). The dirty beam represents the Fourier transform of the sampling pattern in the *uv*-plane, and thus takes into account the fact that we are sampling the Fourier domain at discrete points. To recover an image of the true sky brightness distribution from the dirty image, we must use the deconvolution process. This process utilizes non-linear iterative techniques to interpolate our measured visibility samples into un-sampled regions of the *uv*-plane, and Fourier transforms them to produce an image. The *clean* algorithm (Hogbom, 1974; Clark, 1980) is the predominant deconvolution algorithm used today in radio astronomy, and on the majority of data in this thesis. Although, we note that in cases where the *uv*-plane is sparsely sampled, building a source model directly in *uv* space (instead of through the *clean* process) can be beneficial (see Chapter 7 of this thesis).

A single dish telescope operates on the same basic principles as an interferometer. In particular, a single dish telescope can be visualized as a zero-spacing interferometer (baseline $\mathbf{b} = 0$), which measures the total power received (Sta-

nimirovic et al., 2002),

$$P_{\text{tot}} \propto \int \int I_\nu(\mathbf{s}) P_n(\mathbf{s}) d\Omega \,. \tag{1.8}$$

Here $P_n(\mathbf{s})$ represents the sensitivity of the antenna as a function of the direction of received radiation. A single dish can detect a target source signal by discerning small changes in this received power, and separating the real astronomical signal from the noise. The signals received by a single dish telescope are defined in terms of the antenna temperature,

$$T_A = \frac{1}{\Omega_A} \int \int T(\mathbf{s}) P_n(\mathbf{s}) d\Omega \,, \tag{1.9}$$

where $\Omega_A = \frac{\lambda^2}{A_e}$ represents the antenna beam solid angle (dependent on wavelength λ, and the effective collecting area of the antenna A_e), and $T(\mathbf{s})$ represents the brightness temperature (or equivalent temperature of a black-body for the given source brightness). To separate the target source signal from the noise component, a single dish auto-correlates the signal received, in contrast to an interferometer, which cross-correlates signals from many antennas.

Single dish telescopes operating at short mm/sub-mm wavelengths (as used in this thesis) often use incoherent detectors, known as bolometers, to probe continuum emission (measuring only intensity, and not preserving the phase information of the incoming radiation). A bolometer is simply a very sensitive thermometer or total power detector, which identifies changes in heat input from its surroundings and converts this to a measurable quantity such as voltage/current (Stanimirovic et al., 2002).

Similar to interferometry, to calibrate single dish data the contributions from the sky, atmosphere, ground, and electronics must be removed to extract the astronomical source signal, and the signal measured by the telescope must be converted to physical units. As the specific calibration techniques used for single dish telescopes are typically dependent on the instrument and atmo-

spheric conditions of the observing site, I will focus only on the procedures of the James Clerk Maxwell Telescope (JCMT) telescope used in this thesis. This telescope operates in a scan observing mode, where the telescope continuously moves in a well defined pattern about the target source position, designed to best distinguish the fixed source signal from a slowly varying noise signal (e.g., from the atmosphere). In turn, an iterative calibration process is implemented, whereby individual contributions of the total time-dependent bolometer signal are modelled, and then subtracted in order of decreasing magnitude to ultimately isolate the target source signal. An image is produced by resampling the remaining time series bolometric data onto a predefined map grid, where this map is deconvolved to estimate a target source brightness model. The output data from this process is converted to flux units using a similar process to an interferometer, whereby calibrator sources with known flux properties are observed to solve for a conversion scale factor between instrumental and physical units.

The fundamental difference between single dish antennas and interferometric arrays is the range of spatial frequencies to which the instrument is sensitive (e.g., a single dish probes emission on larger scales that will be resolved out by an interferometer). Thus, most observations of XBs (which are often point source type objects, not extended objects), can be accomplished with both single dish and interferometric arrays.

1.2.2   Observing in the (Sub)-millimetre Bands

The mm/sub-mm frequency bands offer an important view of XB jets, as they uniquely allow us to isolate radiation produced by the jet from radiation produced in the accretion flow in regions near the black hole, where the jet is launched and accelerated. However, observing at sub-mm frequencies is technically more difficult than lower radio frequencies, due to both the adverse effects of the atmosphere on the observed signal and the availability of bright

calibrator sources.

In the tropospheric layer of the atmosphere, water vapor can significantly increase the opacity at mm/sub-mm frequencies. This increased opacity will alter both the observed amplitudes (high opacity can attenuate the source signal and add thermal noise to the signal) and phases (variable water vapor leads to path length variations of the signal, and in turn phase fluctuations) of the astronomical signal observed. Phase fluctuations can be particularly detrimental, as they can lead to de-correlation (the source flux is effectively spread throughout the image, reducing the observed amplitudes of the target souce from the true value), poor seeing (poor phase stability can limit spatial resolution), and anomalous refraction (phase gradients across an antenna can change the apparent position of the source).

To account for these atmospheric effects, two additional calibration steps need to be taken at mm/sub-mm frequencies: a system temperature calibration to correct for the amplitude effects, and a water vapor correction to correct for the phase effects. The system temperature correction typically involves comparing measurements of the sky and an ambient load, to estimate the background sky and receiver temperatures. The water vapor correction involves the monitoring of an atmospheric water line. These real-time water vapor measurements are then combined with an atmospheric model to estimate path delays and phase corrections. Both of these corrections can be applied on-the-fly during observations or as apriori offline calibration steps.

Another consideration facing mm/sub-mm observations is the limited availability of absolute flux calibrators. At lower radio frequencies, non-variable point sources, such as quasars, are used as flux calibrators. However, these quasars are typically faint at mm/sub-mm frequencies (due to their optically thin spectrum), and often cannot be used at mm/sub-mm frequencies. In turn, solar system objects, which can be approximated as black-bodies of known size and temperature, are commonly used. However, as many of these solar system

20

bodies are resolved (i.e., they are not point sources) with mm/sub-mm inter-ferometers, and can exhibit bright lines in their spectra at sub-mm frequencies (e.g., CO lines in Titan), care must be taken when establishing an accurate model of the calibrator source for use in calibration procedures.

1.3 Statistical and Computational Techniques

Bayesian statistics are used throughout this thesis for data analysis. Therefore, in this section I will outline the Bayesian statistical theory, discuss how to set up astronomical problems in the Bayesian formalism, and introduce the computational methods I used to perform Bayesian data analysis.

1.3.1 Bayesian Statistics

Bayesian statistics is a probability theory used to interpret observed data. This theory can be derived from two main rules (Sharma, 2017),

$$p(H|I) + p(\widetilde{H}|I) = 1 \qquad \text{sum rule}\,,$$

$$p(H,G|I) = p(H|G,I)p(G|I) = p(G|H,I)p(H|I) \quad \text{product rule}\,,$$

where H represents a certain hypothesis being true, G represents an alternative hypothesis, $\widetilde{H}$ represents the suggestion that the hypothesis H is false, and I represents background information on the probabilities. The sum rule simply states that the sum of the probabilities for a hypothesis being true and false is equivalent to unity, while the product rule describes conditional probabilities.

The product rule also directly leads to the Bayes Theorem,

$$P(H|D,I) = \frac{p(D|H,I)p(H|I)}{p(D|I)}\,, \tag{1.10}$$

where D represents the observed data, I represents prior knowledge (or background information) on the problem, and H represents the hypothesis. The term on the left hand side is referred to as the posterior probability distribution, and represents the belief about the truth of the hypothesis given the observed data. The right hand side terms are as follows: $p(D|H, I)$ (*likelihood*), which describes the probability of observing the data if the hypothesis is true, $p(H|I)$ (*prior*), which describes our prior knowledge of the hypothesis being true, and $p(D|I)$ (*evidence*), which acts as a constant normalization factor.

To implement Bayesian inference to solve an astronomical problem, we need to establish a likelihood function, define our prior distributions, and compute the posterior distribution using Bayes theorem.

With many astronomical problems, we have a model ($f(\theta)$; where θ represents the model parameters) that can describe our data, consisting of a set of measurements, $\{x_i, y_i\}$, with σ_i measurement errors. The probability of observing a certain data point, y, given our model (with y_m representing a data point generated by the model) and the measurement uncertainties, can be expressed as (Sharma, 2017; Foreman-Mackey et al., 2013),

$$p(y|\theta, \sigma) = \int f(y_m|\theta)p(y|y_m, \sigma_y)dy_m \,. \tag{1.11}$$

For example, in the simple case of a linear model ($y = mx + b$), this conditional probability becomes,

$$p(y_i|x_i, \sigma_i, m, b) = \frac{1}{\sqrt{2\pi\sigma_i^2}} \exp\left(\frac{-[y_i - mx_i - b]^2}{2\sigma_i^2}\right) \tag{1.12}$$

The likelihood (or total probability) for a set of N measured data points ($Y = y_1, ..., y_N$), is equivalent to the product of the conditional probabilities,

$$\mathcal{L} = p(Y|\theta, \sigma) = \prod_{i=1}^{N} p(y_i|\theta, \sigma_i) \,. \tag{1.13}$$

Prior distributions are defined to express our state of knowledge about the parameters in our model. These priors can restrict allowed values of the posterior distribution to smaller regions of the parameter space, when compared to the region allowed from the likelihood function. Priors come in one of two forms: informative (some prior knowledge on allowable parameter values is known, e.g., normal distribution) or uninformative (no prior knowledge of a parameter is known, e.g., uniform distribution).

In most cases, substituting the likelihood and priors into Bayes theorem does not lead to an analytical solution for the posterior distribution. Therefore, we often must use other Monte Carlo based methods, which sample from the posterior distribution, to solve the problem.

1.3.2   Markov Chain Monte-Carlo (MCMC) Methods

Markov Chain Monte-Carlo (MCMC) is one of the most commonly implemented methods used to sample the posterior distribution. This method uses random numbers to drive a Markov Chain (a sequence of random variables, where each point in the sequence depends only on the position at the previous step). When used in Bayesian inference, MCMC generates a random walk in the parameter space, that over time will draw representative samples from the posterior distribution. This process is analogous to common Monte-Carlo integration methods, with the main difference being that in MCMC random samples are not statistically independent (i.e., they are correlated; Sharma 2017).

While there are many different MCMC algoirthms that can be utilized, the most general MCMC algorithm is the Metropolis-Hastings algorithm (Metropolis et al., 1953; Hastings, 1970). This iterative algorithm operates by placing a "walker" within the parameter space at initial position X_0. The next proposed position (X_1) is sampled from a proposal distribution (an easy to sample distribution, such as a multivariate Gaussian centered on the current position X_0),

where the proposed step is either accepted or declined based on an acceptance ratio comparing the probabilities, $p(X_1|D)$ and $p(X_0|D)$ (D represents the observed data). This process is then repeated until convergence is reached. There exist several diagnostics to define convergence, e.g., using the auto-correlation length to estimate the number of independent samples in a chain, and comparing the chains of multiple walkers to check that the intra-chain variance across samples is consistent with the inter-chain variance at a given sample.

In this thesis, I utilize the EMCEE package to implement the MCMC process (Foreman-Mackey et al., 2013). This package is a pure-python implementation of Goodman & Weares Affine Invariant MCMC Ensemble Sampler (Goodman & Weare, 2010), running a modified version of the above Metropolis-Hastings algorithm. The modified algorithm is much more efficient then the standard Metropolis-Hastings algorithm, as it utilizes the "stretch move", whereby it simultaneously evolves an ensemble of walkers through the parameter space, and the next proposed position for each walker is based on the current position of all the other walkers in the ensemble.

1.3.3   Hierarchical Bayesian Models

The simplest case of Bayes theorem (outlined in §1.3.1) describes a situation where observed data, Y, are generated by a model having a specific set of parameters, θ, inferred by $p(\theta|Y) \propto p(Y|\theta)p(\theta)$. However, real-world problems are often more complex, where for instance, the primary model parameters depend on another set of parameters through $p(\theta|\phi)p(\phi)$ or the observed data depend upon another set of hidden variables, X, which in turn depend on the primary model parameters. In these situations, we can develop a hierarchy of Bayesian models. In the former case, θ and ϕ can be inferred using $p(\theta, \phi, Y) \propto p(Y|\theta)p(\theta|\phi)p(\phi)$, while in the latter case, θ and X can be inferred using $p(\theta, X|Y) \propto p(Y|X)p(X|\theta)p(\theta)$ (Sharma, 2017). A hierarchical Bayesian model is utilized in Chapters 2 and 3 of this thesis to fit the radio/X-ray cor-

relation.

1.4 Overview and Goals of Thesis

To study XB jets and understand their properties, we must be able to characterize jet emission in different domains. Jet emission can be studied directly, by observing how the emission changes with frequency (through the broad-band spectrum), time (through the temporal variability properties and high resolution imaging), or in response to changes in the X-ray emission from the accretion flow (through disc-jet coupling correlations), as well as indirectly, through analyzing regions where these jets are interacting with their local environment. Each of these jet observables will be explored in this thesis, with the main goal of developing a new suite of data reduction, analyses, and modelling techniques to extract unknown jet properties from observational data. Further, a secondary (but equally important) goal of this thesis is to build programs that allow us to accurately sample XB jets in the relatively untested mm/sub-mm frequency bands for the first time, exploring how the unique mm/sub-mm viewpoint can add to our understanding of XB jets.

Chapters 2 and 3 describe a collection of works exploring the empirical disc-jet coupling relationship, relating radio and X-ray luminosity, in the XB population. In particular, these works aim to analyze the mechanisms that govern radio luminosity in neutron star systems, where this coupling relationship had not previously been well studied. I use the results of these studies to quantify the similarities and differences between this disc-jet coupling relationship in different accreting systems, to understand the key factors that may govern jet production and evolution (e.g., mass, spin, magnetic fields).

Chapter 4 describes the development and implementation of observational techniques and computational tools designed to overcome the challenges of performing a radio frequency time domain analysis, ultimately allowing us to

connect jet variability properties to internal jet physics.

Chapters 5, 6, and 7 describe a case study of the BHXB V404 Cygni, analyzing the spectral, temporal, and morphological properties of jet emission observed during its 2015 outburst. These works focus on utilizing different observational techniques to constrain the geometry, speed, energetics and dynamics of the different types of jets launched in V404 Cygni, as well as exploring how the dynamics of the accretion flow can impact jet production.

Chapter 8 describes the development and implementation of a technique where astrochemistry is used to identify and probe the regions where BHXB jets are colliding with the surrounding ISM.

Chapter 9 contains a summary of the main results presented in this thesis, as well as an overview of future work.

Chapter 2

Disc-jet coupling in the Terzan 5 neutron star X-ray binary EXO 1745-248

This chapter details the work published in Tetarenko, A.J. et al. 2016, "Disc-jet coupling in the Terzan 5 neutron star X-ray binary EXO 1745-248", *MNRAS*, 460, 345-355, exploring the disc-jet coupling relationship in the neutron star X-ray binaries EXO 1745-248, Aql X-1, and 4U 1728−34.

Abstract

We present the results of VLA, ATCA, and *Swift/XRT* observations of the 2015 outburst of the transient neutron star X-ray binary (NSXB), EXO 1745−248, located in the globular cluster Terzan 5. Combining (near-) simultaneous radio and X-ray measurements we measure a correlation between the radio and X-ray luminosities of $L_R \propto L_X^\beta$ with $\beta = 1.68^{+0.10}_{-0.09}$, linking the accretion flow (probed by X-ray luminosity) and the compact jet (probed by radio luminosity). While such a relationship has been studied in multiple black hole X-ray binaries (BHXBs), this work marks only the third NSXB with such a measurement. Constraints on this relationship in NSXBs are strongly needed, as

comparing this correlation between different classes of XB systems is key in understanding the properties that affect the jet production process in accreting objects. Our best fit disc-jet coupling index for EXO 1745−248 is consistent with the measured correlation in NSXB 4U 1728−34 ($\beta = 1.5 \pm 0.2$) but inconsistent with the correlation we fit using the most recent measurements from the literature of NSXB Aql X-1 ($\beta = 0.76^{+0.14}_{-0.15}$). While a similar disc-jet coupling index appears to hold across multiple BHXBs in the hard accretion state, this does not appear to be the case with the three NSXBs measured so far. Additionally, the normalization of the EXO 1745−248 correlation is lower than the other two NSXBs, making it one of the most radio faint XBs ever detected in the hard state. We also report the detection of a type-I X-ray burst during this outburst, where the decay timescale is consistent with hydrogen burning.

2.1   Introduction

The accretion process onto compact objects and the production of relativistic jets are fundamentally connected. Low mass X-ray binaries (XBs), which contain a stellar-mass compact object, such as a black hole (BH) or neutron star (NS), accreting from a companion star, are ideal candidates to study this relationship, as the rapid (day–week) outburst timescales of these systems allow us to track accretion and jet behaviour in real-time.

Multi-wavelength studies of XBs have linked changes in the accretion flow (probed by spectral and variability properties of the X-ray emission) to those in the jet (probed by radio emission, e.g., Migliari & Fender 2006; Tudose et al. 2009; Miller-Jones et al. 2012; Corbel et al. 2013). In BHXB systems, a phenomenological model has been put forward to explain this connection, where changes in mass accretion rate are the catalyst driving changes in jet behaviour (Tananbaum et al., 1972; Blandford & Königl, 1979; Vadawale et al., 2003; Fender et al., 2004a, 2009). In the hard X-ray accretion state an optically-thick,

steady, compact jet is present. As the mass accretion rate increases during the rise of the outburst, the jet velocity and power are also thought to increase (although this has not yet been directly proven from observational data, as measurements of jet velocity in the hard state are difficult to make). When the source makes the transition from hard to soft accretion states at higher luminosities , the system launches discrete, optically-thin, relativistically-moving ejecta, possibly as a result of internal shocks in the jet flow produced by the changes in jet velocity. The compact jet is quenched as the source moves into the softer accretion state, and then re-established as the source moves back into the hard state (where the jet is re-established well before quiescence; Kalemci et al. 2013).

Similar to BHXBs, NSXB outburst behaviour is also thought to be governed by mass accretion rate (e.g., Homan et al. 2010). In terms of the connection between inflow and outflow, NSXB and BHXB systems display both similarities and differences (Migliari & Fender, 2006). A steady, compact jet is observed in NSXBs at lower X-ray luminosities ($< 0.1\,L_{\mathrm{edd}}$) in hard accretion states (i.e., island accretion states; Migliari et al. 2010), and discrete jet ejections have been found at higher X-ray luminosities (typically seen in Z sources persistently accreting at high fractions of Eddington; e.g., Fender et al. 2004b, Fomalont et al. 2001a; Spencer et al. 2013), as seen in BHXBs. However, BHXBs tend to be much more radio loud than NSXBs at the same X-ray luminosity (Fender & Kuulkers 2001; Migliari & Fender 2006). While this could imply NS jets are less powerful, Körding et al. (2006) suggest that jet power is comparable in NS/BH systems, and properties such as the mass of the compact object or radiative efficiency are responsible for the different radio luminosity levels. Additionally, NSXB jets do not all appear to be fully quenched in softer accretion states as they are in BHXBs (Migliari et al., 2004). While commonalities could indicate that the physical mechanism (possibly related to the mass accretion rate) powering the jets in both classes of system is similar, differences suggest

the nature of the compact object still may play an important role. Analyzing and quantifying the similarities and differences between these systems is key to understanding the properties that affect the jet production process (e.g., mass, spin, existence of a surface or event horizon) across all scales.

A key observational tracer of the accretion-jet connection in XBs is the correlation found between radio and X-ray luminosities in the hard state ($L_R \propto L_X^{\beta}$, where β represents the disc-jet coupling index, e.g., $\beta_{\mathrm{BH}} \sim 0.6$; Corbel et al. 2003; Gallo et al. 2003; Corbel et al. 2013)[1]. This non-linear correlation is consistent with scale-invariant jet models, where a self-absorbed synchrotron jet is coupled to an accretion flow, total jet power is a fixed fraction of the accretion power, and X-ray luminosity depends on mass accretion rate (Falcke & Biermann 1995; Heinz & Sunyaev 2003; Markoff et al. 2003). Further, through the addition of a mass parameter, this correlation has been extended across the mass scale to include AGN, the supermassive analogues of BHXBs (Merloni et al., 2003); $\log(L_X) = \xi_R \log(\nu L_R) - \xi_M \log M_{BH} + B$, with the coefficients, $\xi_R = 1.45 \pm 0.04$, $\xi_M = 0.88 \pm 0.06$, and $B = -6.07 \pm 1.10$ (Falcke et al. 2004; Plotkin et al. 2012).

The $L_R \propto L_X^{\beta}$ correlation has been shown to hold in multiple BHXBs from quiescent luminosities as low as $10^{-9} L_{\mathrm{edd}}$ to outburst luminosities as high as $10^{-2} L_{\mathrm{edd}}$, above which the compact jet is quenched (we note that while the correlation holds tightly in individual systems, there is more scatter when the whole sample of BHXBs is considered together; Gallo et al. 2014; Plotkin et al. 2016). However, our knowledge of this correlation in individual NS systems is limited. Two NSXBs (4U 1728−34 and Aql X−1), have measured correlations, including data spanning only one order of magnitude in X-ray luminosity (Migliari & Fender, 2006). While 4U 1728−34 shows a correlation

---

[1]We note that Coriat et al. 2011b present evidence for two different tracks in this correlation for BH systems, a radio-loud and radio-quiet track, although, recent work by Gallo et al. 2014 found that a two track description is only statistically preferred when luminosity errors are < 0.3 dex.

of $L_R \propto L_X^{1.5}$ (Migliari et al., 2003), consistent with what we would expect from radiatively efficient accretion due to the NS's surface, there have been conflicting results for this correlation in Aql X-1. Tudose et al. (2009) measured $L_R \propto L_X^{0.4}$ for Aql X-1, which is more consistent with radiatively inefficient accretion flows (like those seen in BHXBs). However, Tudose et al. (2009) took Aql X-1 data from a mixture of accretion states; Migliari & Fender (2006) show the correlation is consistent with $L_R \propto L_X^{1.4}$ when including only data taken in the hard accretion states for both Aql X-1 and 4U 1728−34 (we note that the Migliari & Fender (2006) correlation only included 2 data points from Aql X-1, while the data from the full hard state coverage of the outburst, presented in Miller-Jones et al. (2010), is more consistent with a flatter correlation). Including data from softer accretion states could account for the differing disc-jet coupling indices between Aql X−1 and 4U 1728−34, although we direct the reader to the discussion section of this paper for an updated correlation for Aql X-1 and discussion of this discrepancy. Further, three transitional milli-second pulsars (tMSPs; binary NS systems that have been found to switch from a rotation powered pulsar state to an accreting XB state), have recently been shown to all lie on a shallower correlation, $L_R \propto L_X^{0.7}$, distinct from hard state NSXBs and much more consistent with BHXBs (Deller et al., 2015). . In addition to the disc-jet coupling index, the intrinsic normalization of this correlation clearly varies between BHXBs, NSXBs and tMSPs as groups, and between individual BHXB systems (Gallo et al., 2014). More well measured correlations, including normalization and disc-jet coupling indices are needed to determine which NSXB behaviour is the norm, and determine the mechanisms driving the difference between the correlations of hard state NSXBs and tMSPs. Here we report on the third individual NSXB radio/X-ray correlation measured to date, from data taken during the 2015 outburst of the NSXB EXO 1745-248, located in the globular cluster Terzan 5.

2.1.1 Terzan 5: EXO 1745-248

Terzan 5 is a massive ($\sim 10^6 M_\odot$; Lanzoni et al. 2010) globular cluster located in the Galactic centre region (distance of 5.9±0.5 kpc; Valenti et al. 2007), with a high stellar density, leading to a very high stellar encounter rate (the highest measured so far; Bahramian et al. 2013). This cluster contains three transient X-ray sources confirmed to be accreting NSs, EXO 1745−248 (Terzan 5 X-1), IGR J17480−2446 (Terzan 5 X-2), and Swift J174805.3−244637 (Terzan 5 X-3; Wijnands et al. 2005; Bordas et al. 2010; Strohmayer & Markwardt 2010; Degenaar & Wijnands 2012; Bahramian et al. 2014), as well as several other detected quiescent X-ray sources (Heinke et al., 2006). Historically, X-ray activity was first detected from Terzan 5 in 1980, in the form of multiple X-ray bursts, indicating the presence of an outbursting NSXB (Makishima et al., 1981; Inoue et al., 1984). Subsequent X-ray activity was observed in 1984, 1990, 1991, 2000, 2002, 2010, 2011, and 2012, where activity in 2000 and 2011[2] was attributed to EXO 1745−248[3] (Heinke et al. 2003; Altamirano et al. 2012; Serino et al. 2012; see Table 1 in Degenaar & Wijnands 2012 and references therein for a review of past X-ray activity in Terzan 5).

On 2015 March 13, renewed X-ray activity from Terzan 5 was detected (Altamirano et al., 2015) by the *Swift* Burst Alert Telescope (BAT; Krimm et al. 2013) transient monitor. While the X-ray position from follow up *Swift* X-ray Telescope (XRT) observations (Bahramian et al., 2015b) was consistent with EXO 1745−248, IGR J17480−2446, and several other quiescent X-ray sources (Heinke et al., 2006), the spectrum showed a higher than typical hydrogen column density, $N_H = 4 \pm 0.8 \times 10^{22}$, for sources in Terzan 5 (Bahramian et al. 2014), consistent with previous observations of EXO 1745−248 (Kuulkers et al., 2003). Linares et al. (2015) measured a refined *Swift/XRT* source

---

[2]The 2011 outburst showed superburst activity (Altamirano et al., 2012).

[3]We note that it is not known whether the Terzan 5 outbursts in the early 80s and 90s are associated with EXO 1745−248.

position centered on the known X-ray position of EXO 1745−248 (2.2 arcsec error circle) further suggesting that the outbursting source in Terzan 5 was in fact EXO 1745−248. Tremou et al. (2015) detected a radio counterpart with observations by the Karl G. Jansky Very Large Array (VLA). These radio observations, which localized the source within 0.4 arcsec of the published *Chandra* coordinates (source CX3 in Heinke et al. 2006), and later optical observations that identified the optical counterpart during this outburst (Ferraro et al., 2015), confirmed the identification by Linares et al. (2015).

We obtained multiple epochs of (near-) simultaneous VLA, Australia Telescope Compact Array (ATCA), and *Swift/XRT* observations during the 2015 outburst of EXO 1745−248. In §2.2 we describe the data collection and reduction processes. In §2.3 we present a refined radio position of EXO 1745−248, measurements of the jet spectral index, and the radio/X-ray correlation in this source. §2.4 contains an interpretation of this correlation, comparison to other NS and BH XB sources, and an analysis of an X-ray burst detected in one of the *Swift/XRT* observations. A summary of the results is presented in §2.5.

2.2 Observations and Data Analysis

2.2.1 X-ray Observations

We monitored the outburst of EXO 1745−248 multiple times per week with *Swift/XRT* following its detection in 2015. This paper considers only those observations that are most relevant to analyzing the radio/X-ray correlation and accretion state transition. We summarize these observations in Table 2.1 and Figure 2.1; these consist of two observations in photon counting (PC) mode, which produces 2D images, and 19 observations in windowed timing (WT) mode, which collapses data to 1-dimension for fast readout.

We used HEASOFT v16.6 and FTOOLS[4] (Blackburn, 1995) for all data reduction and analysis. All *Swift/XRT* observations were reprocessed via `xrtpipeline` and `xselect` was used to manually extract source and background spectra. We used `xrtmkarf` to produce ancillary response files. Finally, we performed spectral analysis using XSPEC v12.8.2 (Arnaud, 1996) in the 0.3–10 keV band for PC mode data and the 0.6–10 keV band for WT mode data.

Our PC mode observations in this campaign were heavily piled-up due to the high count rate of the source. Thus we followed the UK *Swift* Science Data Centre pile-up thread[5] and extracted source spectra from an annulus (13–70 arcsec for the first PC mode observation and 20–100 arcsec for the second PC observation), excluding the piled-up region in these observations. The PC mode observations only showed evidence for one bright source.

For heavily absorbed sources, WT data show low energy spectral residuals, which can cause spectral uncertainties in the $\lesssim 1.0$ keV region[6]. These residuals mostly affect grade 1 events and above, and events below ~ 0.6 keV. Thus for our WT mode data, we extracted spectra only from grade 0 events and excluded events below 0.6 keV.

We extracted a spectrum from each observation separately and performed spectral fitting. Our main model for spectral analysis is an absorbed power-law (TBABS*PEGPWRLW in XSPEC), where we assume the cross sections from Verner et al. (1996) and abundances from Wilms et al. (2000). We use a comparison of *Swift/XRT* and MAXI light curves (Figure 2.1) to aid in defining which observations are in the hard/soft accretion state. This comparison reveals a large drop in the hard flux simultaneous with a rise in the soft flux, indicative of a hard-to-soft state transition on MJD 57131. Thus for spectra from *Swift/XRT* observations after this point, we tried both absorbed power-law and absorbed disc blackbody (TBABS*DISKBB in XSPEC) models, and

---

[4]`http://heasarc.gsfc.nasa.gov/ftools/`
[5]`http://www.swift.ac.uk/analysis/xrt/pileup.php`
[6]`http://www.swift.ac.uk/analysis/xrt/digest_cal.php#abs`

chose the fit with lower χ^2 for this study. Although a two-component model (e.g., DISKBB+PEGPWRLW) is often used to fit NSXB soft states, we are only interested in identifying the dominant component (as opposed to performing a detailed characterization of the spectrum) and obtaining a flux estimate. Thus we only fit simple one component models for the purpose of this work.

We note that the MAXI and *Swift/BAT* data do not clearly show the soft-to-hard state transition, probably because it occurred at a lower luminosity where the S/N of these instruments is low. However, all observed XB out-bursts return to the hard state at luminosities above $10^{35}\,\mathrm{erg\,s^{-1}}$ (Maccarone, 2003; Tetarenko et al., 2016c), so we conclude it is extremely likely that the last two *Swift* data points, and the ATCA measurement between them, oc-curred during the hard state. The power law index measured for the June 21 observation, which was more consistent with the hard state observations than the soft state observations, support this conclusion. *Swift/XRT* observations and results of our spectral analysis are reported in Table 2.1. We note that there is some evidence for a varying N_H between *Swift/XRT* observations in Table 2.1. However, given that historical observations of EXO 1745-248 show little evidence for N_H variation (Degenaar & Wijnands, 2012), and that in-strumental issues (e.g., pile up in PC mode, low-level calibration issues in WT mode) can cause uncertainties in spectral fit parameters to be underestimated, any variations in N_H we observe can likely be attributed to systematic effects and not a real intrinsic effect in the source. We also detected an X-ray burst during the March 25 observation, which is discussed in detail in §2.4.2.

Table 2.1: Summary of *Swift XRT* Observations of EXO 1745−248

Obs ID	Exp. Time (s)	Mode	Date (2015)	MJD^a	Count Rate (cnt s^{-1})	N_H (10^{22} cm^{-2})	Γ^b	kT^c (keV)	$F_{1-10}^{d,e}$ (10^{-10} erg s^{-1} cm^{-2})	χ^2_ν	dof
Hard State											
32148017^f	1965.36	PC	Mar 17	57098.7491	$0.73^{+0.03}_{-0.02}$	$4.41^{+0.85}_{-0.74}$	$1.12^{+0.22}_{-0.21}$	$\dots$	$3.77^{+0.26}_{-0.23}$	1.01	44
32148021	1188.47	WT	Mar 21	57102.8797	$9.11^{+0.19}_{-0.22}$	$3.36^{+0.20}_{-0.19}$	$1.24^{+0.08}_{-0.07}$	$\dots$	$14.19^{+0.32}_{-0.32}$	1.09	117
32148023	771.57	WT	Mar 23	57104.0629	$7.33^{+0.26}_{-0.29}$	$3.01^{+0.29}_{-0.27}$	$1.31^{+0.11}_{-0.10}$	$\dots$	$10.61^{+0.36}_{-0.34}$	1.07	62
32148024^g	898.50	WT	Mar 25	57106.2081	$9.12^{+0.20}_{-0.22}$	$3.11^{+0.22}_{-0.21}$	$1.22^{+0.08}_{-0.08}$	$\dots$	$13.73^{+0.36}_{-0.35}$	1.09	90
32148024	323.36	WT	Mar 25	57106.2564	$8.66^{+0.25}_{-0.27}$	$2.65^{+0.37}_{-0.33}$	$1.13^{+0.15}_{-0.14}$	$\dots$	$12.49^{+0.56}_{-0.55}$	0.87	30
32148025	513.67	WT	Mar 26	57107.8624	$7.84^{+0.24}_{-0.26}$	$3.17^{+0.38}_{-0.35}$	$1.20^{+0.14}_{-0.14}$	$\dots$	$11.84^{+0.45}_{-0.44}$	1.00	44
32148025	534.59	WT	Mar 26	57107.9322	$7.21^{+0.24}_{-0.27}$	$2.85^{+0.33}_{-0.31}$	$1.16^{+0.13}_{-0.13}$	$\dots$	$11.48^{+0.43}_{-0.43}$	1.01	42
32148026	302.78	WT	Mar 28	57109.5274	$7.86^{+0.25}_{-0.26}$	$2.44^{+0.41}_{-0.37}$	$0.94^{+0.16}_{-0.15}$	$\dots$	$11.79^{+0.56}_{-0.55}$	1.29	42
32148027	344.07	WT	Apr 02	57114.4467	$7.76^{+0.29}_{-0.33}$	$2.43^{+0.38}_{-0.34}$	$1.00^{+0.15}_{-0.15}$	$\dots$	$11.15^{+0.52}_{-0.51}$	0.95	46
32148029	764.11	WT	Apr 06	57118.1135	$9.47^{+0.25}_{-0.27}$	$2.09^{+0.20}_{-0.18}$	$0.87^{+0.08}_{-0.08}$	$\dots$	$13.74^{+0.37}_{-0.38}$	1.21	80
32148030	443.32	WT	Apr 12	57124.3745	$25.84^{+0.57}_{-0.63}$	$2.13^{+0.15}_{-0.14}$	$0.86^{+0.07}_{-0.07}$	$\dots$	$38.96^{+0.87}_{-0.86}$	1.08	99
32148031	704.54	WT	Apr 13	57125.8931	$12.18^{+0.60}_{-0.66}$	$2.20^{+0.18}_{-0.18}$	$0.90^{+0.08}_{-0.08}$	$\dots$	$29.05^{+0.74}_{-0.73}$	1.04	98
32148032^f	849.08	PC	Apr 14	57126.4853	$6.34^{+0.10}_{-0.09}$	$2.07^{+0.21}_{-0.20}$	$0.84^{+0.09}_{-0.09}$	$\dots$	$43.41^{+1.33}_{-1.31}$	1.11	48
Soft State^h											
32148033	615.82	WT	Apr 20	57132.2902	$95.13^{+1.63}_{-1.74}$	$2.47^{+0.05}_{-0.05}$	$\dots$	$2.62^{+0.07}_{-0.06}$	$121.39^{+1.19}_{-1.19}$	1.26	100
32148033	579.58	WT	Apr 20	57132.6898	$110.15^{+1.01}_{-1.01}$	$3.37^{+0.09}_{-0.09}$	$1.53^{+0.04}_{-0.04}$	$\dots$	$158.37^{+1.96}_{-1.91}$	1.38	107
32148034	385.78	WT	Apr 22	57134.1423	$106.36^{+1.15}_{-1.20}$	$2.44^{+0.06}_{-0.06}$	$\dots$	$3.76^{+0.18}_{-0.16}$	$140.70^{+1.76}_{-1.75}$	1.35	45
32148034	290.99	WT	Apr 22	57134.2161	$113.53^{+1.26}_{-1.39}$	$2.95^{+0.15}_{-0.14}$	$0.93^{+0.06}_{-0.06}$	$\dots$	$184.63^{+3.01}_{-2.96}$	0.93	36
32148035	376.85	WT	Apr 24	57136.4053	$80.21^{+1.10}_{-1.17}$	$3.37^{+0.17}_{-0.16}$	$1.53^{+0.07}_{-0.07}$	$\dots$	$112.37^{+2.27}_{-2.18}$	1.32	31
32148036	988.60	WT	Apr 26	57138.1412	$66.57^{+1.12}_{-1.20}$	$2.52^{+0.05}_{-0.05}$	$\dots$	$3.13^{+0.09}_{-0.09}$	$81.7^{+0.08}_{-0.08}$	1.41	71
Hard State											
32148053	1106.30	WT	Jun 21	57194.6817	$0.14^{+0.03}_{-0.04}$	$1.66^{+1.17}_{-0.84}$	$1.44^{+0.74}_{-0.62}$	$\dots$	$0.32^{+0.06}_{-0.05}$	1.19	9
32148054^i	79.91	WT	Jun 24	57197.8643	$0.09^{+0.06}_{-0.03}$	$\dots$	$\dots$	$\dots$	$0.09^{+0.11}_{-0.06}$	$\dots$	$\dots$

^{a} All MJD values quoted represent the mid point of the observations.
^{b} Γ represents the power-law photon index.
^{c} T represents the DISKBB temperature.
^{d} Uncertainties are quoted at the 1σ level.
^{e} 1–10 keV flux; see footnote 11 for discussion of why this X-ray band is chosen.
^{f} Note that this observation was piled-up; please see §2.2.1 for details.
^{g} This observation contained an X-ray burst; see §2.2.1 & 2.4.2 for details. We excluded the burst interval when performing our spectral analysis of this observation.
^{h} Soft state measurements are not included in our analysis. We show them here for comparison purposes and to clearly show the transition between the hard and soft state.
^{i} Due to the limited exposure time of this observation, the flux for this observation is determined by using the model fits from the previous observation.
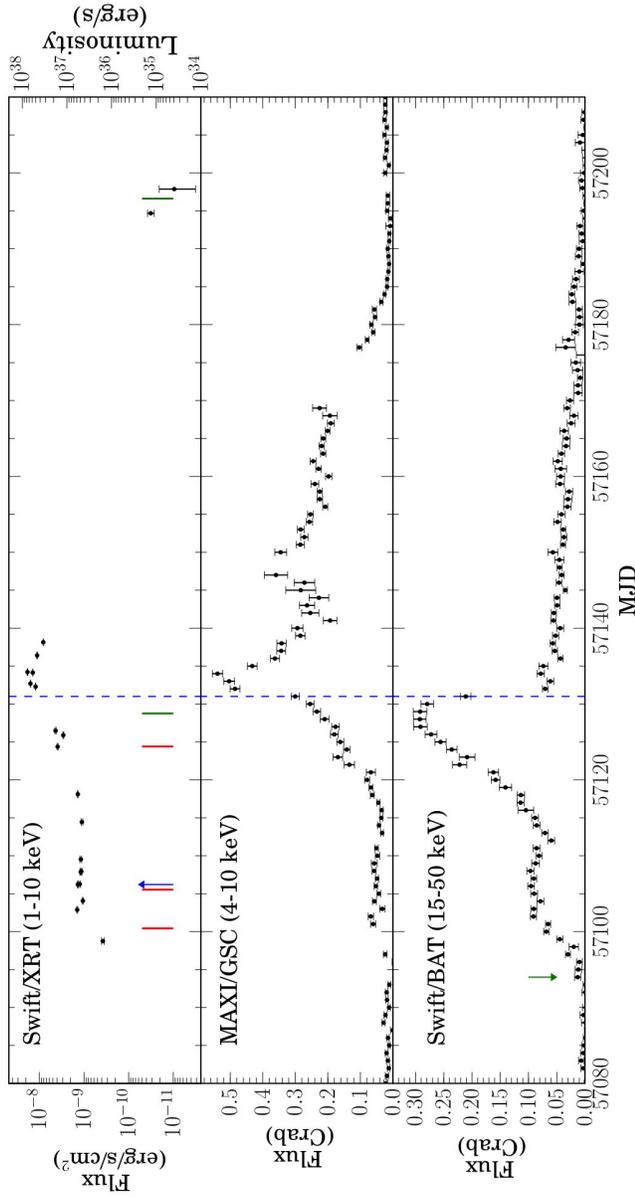
Figure 2.1: X-ray light curves of the 2015 outburst from EXO 1745−248 as seen by *Swift/XRT* (top), MAXI/GSC (middle; http://maxi.riken.jp) and *Swift/BAT* (bottom; Krimm et al. 2013). *Swift/XRT* fluxes are derived from spectral fitting (see §2.2.1 in text). To calculate luminosity in the top panel, we assumed a distance of 5.9 kpc. The blue dashed line shows the apparent hard to soft state-transition at MJD 57131. Vertical bars in the top panel indicate the time of radio observations by the ATCA (green) and VLA (red). The blue arrow in the top panel indicates the time of the detected X-ray burst, and the green arrow in the bottom panel indicates the time of the first detection of the outburst in *Swift/BAT*. Note that while we only use the hard state measurements in our radio/X-ray correlation analysis, we show some of the soft state measurements near the times of our radio observations to clearly show the hard-soft transition and the luminosity at that transition.

2.2.2 Radio Observations

2.2.2.1 VLA

Terzan 5 was observed with the VLA (Project Code: 14B-216) in three epochs, 2015 March 19, March 24, and April 12. The array was in the B configuration, with a resolution of 0.6 arcsec, and we had 25.9 min on source for each epoch. All observations were made with the 3-bit samplers in X band $(8-12\,\mathrm{GHz})$, comprised of 2 base-bands, each with 16 spectral windows of 64 2-MHz channels each, giving a total bandwidth of 2.048 GHz per base-band. Flagging, calibration and imaging of the data were carried out within the Common Astronomy Software Application package (CASA[7]; McMullin et al. 2007) using standard procedures. When imaging we used a natural weighting scheme to maximize sensitivity, two Taylor terms (nterms=2) to account for the large fractional bandwidth, and did not perform any self-calibration. We used 3C286 (J1331+305) as a flux calibrator and J1751−2524 as a phase calibrator. Flux densities of the source were measured by fitting a point source in the image plane (Stokes I with the `imfit` task), and, as is standard for VLA X band data, systematic errors of 1% were added. All flux density measurements are reported in Table 2.2.

2.2.2.2 ATCA

During the 2015 outburst of EXO 1745−248, Terzan 5 was observed with the ATCA (Project Code: C2877) in two epochs, 2015 April 16 and June 23. The array was in the 6A configuration (resolution of 1.89/1.16 arcsec at 5.5/9 GHz) in the first epoch, and the 6D configuration (resolution of 1.91/1.16 arcsec at 5.5/9 GHz) in the second epoch. We had 8.0 hrs on source for both epochs. All observations were carried out at 5.5 and 9 GHz simultaneously, where each frequency band is comprised of 2048 1-MHz channels, giving a

---

[7]`http://casa.nrao.edu`

Table 2.2: Summary of Radio Frequency Observations and Flux Densities of EXO 1745−248

Telescope	Date (2015)	MJD[a]	Freq. (GHz)	Flux[b,c] (μJy bm^{-1})	Spectral Index[d]
VLA	Mar 19	57100.43155	9.0	28.7±6.0	. . .
VLA	Mar 19	57100.43155	11.0	22.8±8.0	-1.20±1.97
VLA	Mar 24	57105.53915	9.0	47.8±6.0	. . .
VLA	Mar 24	57105.53915	11.0	30.3±8.0	-2.20±1.4
VLA	Apr 12	57124.40413	9.0	238.1±8.3	. . .
VLA	Apr 12	57124.40413	11.0	247.6±9.3	0.15±0.26
ATCA	Apr 16	57128.75694	5.5	372.0±7.0	. . .
ATCA	Apr 16	57128.75694	9.0	340.0±7.8	-0.18±0.06
ATCA	Jun 23	57196.60938[e]	5.5	< 17	. . .
ATCA	Jun 23	57196.60938[e]	9.0	< 19	. . .

[a] All MJD values quoted represent the mid point of the observations.
[b] Uncertainties are quoted at the 1σ level.
[c] Radio flux density, where uncertainties quoted include the 1% systematic errors appropriate to both VLA X-band observations and the ATCA 3/6 cm observations.
[d] All spectral indices given use the formalism, $f_\nu \propto \nu^\alpha$; where α is the spectral index.
[e] The source was not detected in these observations, fluxes presented here are 3σ upper limits.

total bandwidth of 2.048 GHz per frequency band. Flagging and calibration were carried out with the Multichannel Image Reconstruction, Image Analysis and Display (MIRIAD) software (Sault et al., 1995), using standard procedures. We used 1934-638 as a flux calibrator and 1748-253 as a phase calibrator. Imaging of the data was carried out within CASA using a Briggs weighting scheme (robust=1) and two Taylor terms (nterms=2). We did not perform any self-calibration. Flux densities of the source were measured by fitting a point source in the image plane (Stokes I with the `imfit` task), and, as is standard for ATCA data, systematic errors of 1% were added. All flux density measurements are reported in Table 2.2.

2.3 Results

2.3.1 Radio Source Position

Through stacking all three epochs of our VLA data in the *uv*-plane, we measure a refined radio position of EXO 1745−248 to be the following (J2000),

$$\mathrm{RA}: \quad 17^\mathrm{h}48^\mathrm{m}05^\mathrm{s}.22467 \pm 0.00084 \pm 0.01$$

$$\mathrm{DEC}: \quad -24°46'47''.666 \pm 0.033 \pm 0.06$$

where the quoted error bars represent the statistical error from fitting in the image plane and the nominal systematic uncertainties of 10% of the beam size, respectively.

This source position is within 0.33 arcsec of the published X-ray location of EXO 1745-248 (CX 3 in Heinke et al. 2006; RA/DEC errors 0.002s/0.02 arcsec), and within 0.10 arcsec of the optical location of EXO 1745-248 (Ferraro et al. 2015; RA/DEC errors 0.01s/0.2 arcsec). The radio source is clearly unassociated with the two other previously identified NSXBs in Terzan 5; it is 2.4 arcsec away from IGR J17480−2446 (CX 24 in Heinke et al. 2006; RA/DEC errors 0.005s/0.09 arcsec) and 10.3 arcsec away from Swift J174805.3−244637 (Bahramian et al. 2014; RA/DEC errors 0.02s/0.2 arcsec).

2.3.2 Jet Spectral Indices

To obtain the jet spectral indices we fit (linearly in log space) a power-law to the derived radio flux densities (between the two-base-bands in the VLA data and between 5.5 and 9 GHz in the ATCA data) against frequency at each epoch ($f_\nu \propto \nu^\alpha$; where α is the spectral index). All spectral index measurements are reported in Table 2.2. In the March 19 and April 12 VLA epochs, the spectral index measurements are consistent with a flat ($\alpha = 0$) or slightly inverted ($\alpha > 0$) spectrum, although, in the March 24 VLA epoch and the ATCA epoch

on Apr 16, the spectral index appears to be more consistent with a slightly steeper index ($\alpha < 0$). However, both the March 19 and March 24 VLA epochs have large uncertainties (due to the low signal-to-noise ratio and small lever arm in frequency) that make it impossible to conclusively distinguish between steep, flat, or an inverted spectra. A flat or slightly inverted spectrum, commonly seen from compact jets during hard accretion states in BHXBs (Fender et al., 2001) and some NSXBs (e.g., Migliari & Fender 2006; Migliari et al. 2010), is believed to be produced as the result of the superposition of many different synchrotron components originating from different regions along the jet (e.g., Blandford & Königl 1979).

2.3.3 Radio X-Ray Correlation in EXO 1745−248

To fit the radio/X-ray correlation in EXO 1745−248, we use radio and X-ray luminosities (spanning ~ 1 dex in X-ray luminosity[8]) at 10 GHz (combined base-band measurements) and 1–10 keV, respectively[9], and a Markov Chain Monte Carlo (MCMC[10]) fitting algorithm. To properly account for uncertainties in both distance (5.9 ± 0.5 kpc; Valenti et al. 2007) and flux, we build a hierarchical model within our MCMC, where we include distance as an additional parameter. This in turn allows us to calculate luminosities using our measured fluxes/uncertainties and samples drawn from the distance distribution (i.e., a Gaussian with mean of 5.9 and standard deviation of 0.5), and then perform a linear fit in log space on these luminosities. Although many previous studies only compare the X-ray measurements closest in time to the radio mea-

---

[8]While our radio observations span ~ 3 dex in X-ray luminosity, our lowest luminosity point only has an upper limit on radio luminosity and thus is not very constraining.

[9]In previous studies that compute the radio/X-ray correlation, the X-ray energy band used can vary from author to author, but in this work we choose the 1–10 keV band, as we have found that this band is most commonly used in recent literature; e.g., Gallo et al. 2014; Corbel et al. 2013; Deller et al. 2015.

[10]In this work, all of our codes use the EMCEE python package to implement the MCMC algorithms (Hogg et al., 2010; Foreman-Mackey et al., 2013).
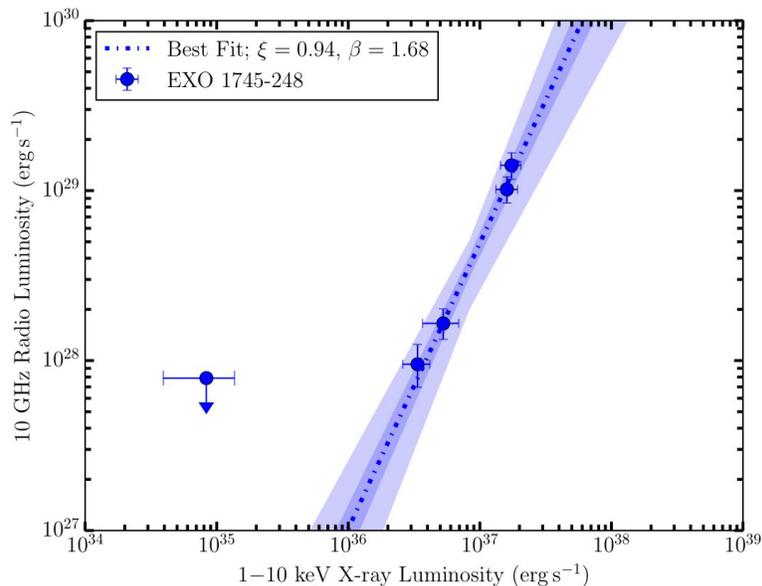
Figure 2.2: Radio/X-ray correlation during the hard accretion state of the 2015 outburst of EXO 1745−248. The dash-dotted line indicates the best fit using our MCMC techniques (see text for best fit parameters and uncertainties). The shaded regions represent the 1σ (dark blue) and 3σ (light blue) confidence intervals of the regression. Note that we do include the upper limit data point in our fit. The luminosities displayed here are calculated assuming a distance of 5.9 kpc.

surements, our method takes a more conservative approach to data that is not strictly simultaneous. In particular, as our *Swift/XRT* X-ray observations were not strictly simultaneous with the VLA radio observations, we use a MCMC linear interpolation method to estimate X-ray fluxes at the times of the radio observations. However, as the X-ray flux of outbursting NSXBs can vary on timescales of less than a day (the maximum separation between our radio and X-ray observations), our linear interpolation method may underestimate the uncertainties on the interpolated X-ray fluxes. Therefore, we conservatively scale the uncertainties on the interpolated X-ray fluxes to cover the full flux range of the neighbouring X-ray data (see Table 2.3 for radio and interpolated X-ray fluxes used in our MCMC fitting).

We follow Gallo et al. (2014) when performing our MCMC fit with the

Table 2.3: Radio and interpolated X-ray fluxes of EXO 1745−248 used in the radio/X-ray correlation analysis

MJD	$\mathbf{F_{10GHz}}^{a,b}$ $(\boldsymbol{\mu}\mathbf{Jy\,bm^{-1}})$	$\mathbf{F_{1-10keV}}^{a,c}$ $(\mathbf{10^{-10}erg\,s^{-1}cm^{-2}})$
57100.43155	23.2±5.0	$8.02^{+0.41}_{-0.40}$
57105.53915	40.0±4.0	$12.78^{+0.67}_{-0.69}$
57124.40413	245.3±5.6	$38.78^{+0.82}_{-0.89}$
57128.75694	340.0±7.8	$41.89^{+1.39}_{-1.47}$
57196.60938^{d}	< 19	$0.20^{+0.13}_{-0.11}$

[a] Uncertainties are quoted at the 1σ level.
[b] 10 GHz radio flux from combining the 2 base-bands.
[c] Interpolated X-ray fluxes in the 1–10 keV band.
[d] The source was not detected in this observation, the flux presented here is 3σ upper limit.

following functional form,

$$(\log L_R - \log L_{R,c}) = \log \xi + \beta(\log L_X - \log L_{X,c}) \qquad (2.1)$$

where, L_R and L_X are radio (10 GHz) and X-ray (1–10 keV) luminosity, respectively, centering values $L_{R,c} = 3.89 \times 10^{28}\,\mathrm{erg\,s^{-1}}$ and $L_{X,c} = 8.38 \times 10^{36}\,\mathrm{erg\,s^{-1}}$ are the geometric means of the simultaneous radio and X-ray luminosity measurements (not including the upper limit data point), ξ represents the normalization constant and β represents the disc-jet coupling index. To include the upper limit data point in our fit, and better constrain the normalization and disc-jet coupling index, we add a condition in our log probability that does not allow solutions where, at the X-ray luminosity of the upper limit data point, the corresponding radio luminosity would exceed the upper limit value. Our best fit parameters are, normalization $\xi = 0.94^{+0.14}_{-0.13}$ and disc-jet coupling index $\beta = 1.68^{+0.10}_{-0.09}$, where uncertainties are quoted at the 15th and 85th percentiles (as done in Gallo et al. 2014; also see Figure 2.2).
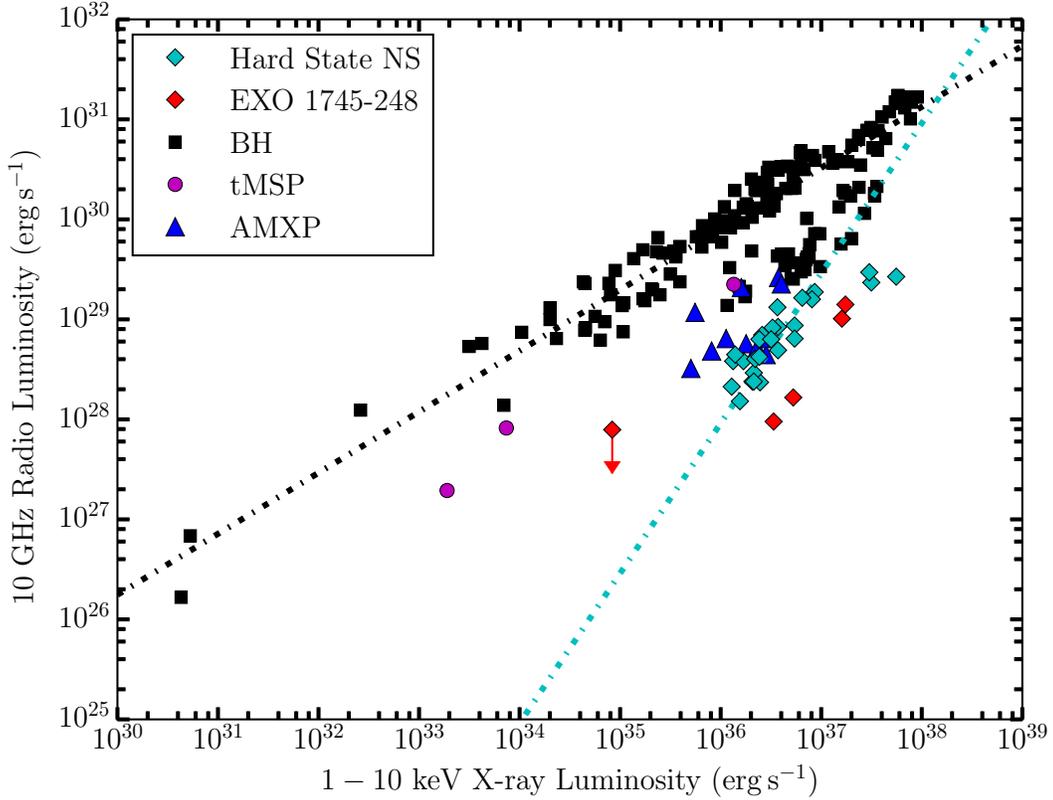
Figure 2.3: Radio/X-ray correlation for different types of accreting stellar mass compact objects. Data points from the literature include, BHs (Miller-Jones et al. 2011; Gallo et al. 2012; Ratti et al. 2012; Corbel et al. 2013; Gallo et al. 2014), hard state NSs (Migliari & Fender, 2006; Miller-Jones et al., 2010), transitional binary millisecond pulsars (tMSPs) and accreting milli-second X-ray pulsars (AMXPs; Hill et al. 2011; Papitto et al. 2013; Deller et al. 2015). Note that to convert between different radio bands we assume a flat radio spectral index. The dot-dashed lines show the best fit relations for BHs ($\beta = 0.61$, black; Gallo et al. 2014) and hard state NSs systems ($\beta = 1.40$, cyan; Migliari & Fender 2006). The new measurements of EXO $1745-248$ reported in this paper (highlighted in red; luminosities assume a distance of 5.9 kpc) are more radio quiet and/or X-ray loud when compared with the other hard state NS measurments. Note that error bars are not included in this plot for clarity.

2.4 Discussion

In the framework of scale-invariant jet models coupled to an accretion flow, X-ray luminosity scales with mass accretion rate $(L_X \propto \dot{M}^q)$[11], total jet power is a fraction of the accretion power $(Q_{\mathrm{jet}} = f\dot{M}c^2)$, and the jet luminosity scales with jet power, according to (Falcke & Biermann 1995; Heinz & Sunyaev 2003; Markoff et al. 2003) ,

$$L_\nu \propto Q_{\mathrm{jet}}^\eta \tag{2.2}$$

Here, $\eta = \frac{2p-(p+6)\alpha+13}{2(p+4)}$ depends on the power-law index of the electron energy distribution (p), and the jet spectral index (α). When the jet is observed in the radio regime this in turn implies,

$$L_R \propto L_X^{\eta/q} \tag{2.3}$$

where radiatively efficient flows display $q = 1$, and radiatively inefficient flows display $q = 2 - 3$.

In the previous section we reported a disc-jet coupling index of $1.68^{+0.10}_{-0.09}$ for EXO 1745−248, which is consistent with a radiatively efficient accretion flow (possibly due to the neutron star surface; see Migliari & Fender 2006 and references therein for discussion) coupled to a steady, compact jet (i.e., values of $q = 1$, $2 \lesssim p \lesssim 3$, $-0.7 \lesssim \alpha \lesssim 0.1$ will produce values of $1.4 < \eta < 2.0$ within the confidence interval we derived for EXO 1745−248).

---

[11]Although this is a standard assumption in many papers, we point out two caveats for NSXBs. First, this assumes that the bolometric correction (in the hard state) remains constant so that the X-ray luminosity measured over limited energies is representative of the bolometric luminosity. Second, there may be multiple mass accretion rates (e.g., that in the disc versus that in a radial inflow) contributing to the X-ray luminosity of a NSXB, and it is unclear which of these would impact jet production.

2.4.1 Comparison to other Neutron Star and Black Hole Systems

While several BHXBs have measured disc-jet coupling indices (e.g., Gallo et al. 2014 combine data from 24 different BHXB systems to yield a best-fit disc-jet coupling index of 0.61 ± 0.03), to date there are only two individual NSXBs with previously measured disc-jet coupling indices, Aql X-1 and 4U 1728−34. Migliari et al. (2003) report a disc-jet coupling index of 1.5 ± 0.2 in 4U 1728−34, while different works report conflicting correlations for Aql X-1. The Aql X-1 data used to fit the correlation in Tudose et al. (2009) originates from mixed accretion states. While Migliari & Fender (2006) find that 4U 1728−34 and Aql X-1 are well fit together with a disc-jet coupling index of 1.40 ± 0.23, this fit only includes two data points from Aql X-1. More recently Migliari et al. (2011) reported that Aql X-1 is fit by a disc-jet coupling index of ~ 0.6 (with no errors reported).

Therefore, we combined the most recent hard state Aql X-1 data from the literature, including the two measurements from Migliari & Fender (2006), as well as measurements from Miller-Jones et al. (2010), but excluding data with radio upper limits or hard X-ray colour[12] < 0.75. We find a disc-jet coupling index of $0.76^{+0.14}_{-0.15}$. This new Aql X-1 result is not consistent with the 4U 1728−34 result, and suggests that the use of mixed accretion state measurements in Tudose et al. (2009) is not the sole cause of the flatter disc-jet coupling index. Instead the disc-jet coupling index of Aql X-1 is more consistent with those of BHXBs. However, this correlation in Aql X-1 is only measured over ~ 0.8 dex, and we note that Corbel et al. (2013) observed temporary excursions from the typical radio/X-ray correlation in BHXB GX 339-4 when measured over < 2 dex in X-ray luminosity.

---

[12]Hard X-ray colour is defined in Miller-Jones et al. (2010) as the count rate ratio between the 9.0-16.0 keV and 6.0-9.7 kev bands.

Our measurement for EXO 1745−248 is much more consistent with 4U 1728−34, rather than Aql X-1 or the BHXBs (see Figure 2.3), where the EXO 1745−248 and 4U 1728−34 indices are what is expected from the model presented above for a radiatively efficient accretion flow coupled to a compact jet. Interestingly, Aql X-1 has (only once) shown evidence of X-ray pulsations (Casella et al., 2008), suggesting that it may be more similar to the AMXPs or tMSPs.

Deller et al. (2015), recently combined radio and X-ray measurements for three tMSPs to fit a correlation of $L_R \propto L_X^{0.7}$ over ~ 3 dex in X-ray luminosity, which occupies a region of the radio/X-ray plane distinct from all the hard state NSXBs, like EXO 1745−248 (see Figure 2.3). Given that there is only one data point for this correlation in each individual tMSP, we are forced to only consider the correlation of this entire sample; although, given the correlation in BHXBs, we might expect the sample correlation to have a larger scatter than one might find in an individual source. The disc-jet coupling indices of tMSPs as a group are much more consistent with Aql X-1 than with EXO 1745−248 or 4U 1728−34. Deller et al. (2015) suggest that tMSPs are undergoing a propeller accretion mode, where the pressure of in-falling material is balanced by the magnetic field of the NS, and the NS's rotation accelerates the inner disc, in turn causing the majority of the material to be ejected in outflows as opposed to falling inward. This theory can explain the radiatively inefficient jet dominated states seen at lower accretion rates in tMSPs (i.e. the tMSP correlation, $L_R \propto L_X^{0.7}$), which display a similar disc-jet coupling index as those of BHXBs, just at fainter radio luminosities (the offset between BHXBs and tMSPs could be due to differing jet power, radiative efficiency, compact object mass, or jet launching mechanisms). However, it is unknown whether this jet dominated state occurs in all NSXBs or if entrance into this state is solely dependent on intrinsic NS characteristics such as magnetic field strength or spin period. In the current published NSXB sample (excluding tMSPs), only one correlation

measurement (i.e., our lowest luminosity point in EXO 1745−248) probes X-ray luminosities $\lesssim 10^{35}\,\mathrm{erg\,s^{-1}}$. However, this measurement only has an upper limit on radio luminosity. While this data point appears not to be consistent with the tMSP correlation, we are unable to definitely determine whether this point lies on the extrapolation of our hard state NSXB best fit correlation at lower X-ray luminosities or perhaps, is part of an intermediate regime where the disc-jet coupling index flattens out during the transition between a steeper and flatter index (as seen in the multiple BHXBs, H1743−322; Coriat et al. 2011b, XTE J1752−223; Ratti et al. 2012, and MAXI J1659−152; Jonker et al. 2012).

From Figure 2.3 it is also clear that EXO 1745−248 has a lower normalization compared to the other hard state NSs, Aql X-1 and 4U 1728−34, by about a factor of 5 in radio luminosity at the same X-ray luminosity. Among transient XBs measured in the hard state at $L_X > 10^{36}\,\mathrm{erg\,s^{-1}}$, EXO 1745−248 is the most radio faint source reported to date. This differing normalization may be analagous to what is seen in BH sources, where different individual sources appear to have different normalizations (Gallo et al., 2014). We note that while this difference could arise from having a well-known distance for EXO 1745−248 compared to more uncertain distances to Aql X-1 and 4U 1728−34, the distances to Aql X-1 and 4U 1728−34 would have to increase by a factor of three if this was a distance effect alone, which seems unlikely. On the other hand, a factor of 5 lower in radio luminosity at a given X-ray luminosity requires masses lower by a factor of about 10 if the sources follow the fundamental plane of BH accretion. Since NSs do not have such a large range of masses, mass alone can not explain the lower luminosity of EXO 1745−248, unless NSs and BHs follow very different fundamental planes of accretion. Further, Migliari et al. (2011) found a possible relation between spin frequency and jet power, with faster spinning neutron stars being more radio luminous. Based on its X-ray burst properties (§2.4.2), we expect EXO 1745−248 to have a typical

spin (200–600 Hz). However, Migliari et al. (2011) did not include the recent results from tMSPs. At $L_X \sim 10^{36}\,\mathrm{erg\,s^{-1}}$, the tMSP M28I (254 Hz; Papitto et al. 2013) has a significantly higher radio luminosity than Aql X-1 (550 Hz; Watts et al. 2008). While this compares a tMSP to a NS, we take this as evidence that spin alone also cannot explain how radio loud a NSXB will be. Thus it seems likely that a combination of factors (e.g., mass, spin, inclination, magnetic field, radiative efficiency) may be required to produce a given radio luminosity.

This highlights the need for more radio/X-ray measurements of NSXBs, especially at the lower end of the luminosity spectrum, to answer these open questions. However, we note that obtaining such observations is very difficult, given that these NSXB sources decay very quickly (timescales on the order of a few days) through this desired luminosity range of $10^{34} - 10^{36}\,\mathrm{erg\,s^{-1}}$, necessitating intensive monitoring of these sources.

2.4.2 X-ray Burst Analysis

During our analysis we observed the presence of an X-ray burst, which we use here to further constrain the properties of this NSXB. *Swift/XRT* detected an X-ray burst from Terzan 5 on 2015 March 25, with a net peak count rate at 04:56:42 UT of about $120\,\mathrm{cnts\,s^{-1}}$ (0.5-10 keV), on top of the persistent emission ($\sim 10\,\mathrm{cnts\,s^{-1}}$). From the 0.5 s time-resolution light curve we estimate a rise time of 1.8 s (defined as the time to go from 25% to 90% of the net peak count rate). The burst lasted for about 25 s and then reached a "plateau" for another $\sim$25 s, at a level higher than the pre-burst count rate. About 50 s after the burst onset the observation was interrupted (see Figure 2.4).

To study the spectral evolution of the X-ray burst, we extracted a series of 3 s-long spectra from *Swift/XRT* WT data, using a 100 s interval before the burst to subtract the persistent (source plus background) emission. We used a 20-pixel radius region to extract the spectra, and verified that excluding

49

the innermost 2 pixels (to correct for potential pile up) leads to consistent results. We created an exposure map and ancilliary response file and used the latest response matrix from the calibration database. We grouped the resulting spectra to a minimum of 5 counts per channel, and fitted those spectra with more than 50 net counts in total with an absorbed blackbody model (TBABS*BBODYRAD in XSPEC), with the column density frozen at the value derived from the persistent emission ($3 \times 10^{22}\,\mathrm{cm}^{-2}$).

We find a slow decay in temperature along the burst decay ("cooling tail"), from ~2.9 keV to ~1.4 keV, identifying this unequivocally as a thermonuclear event. The burst bolometric peak luminosity was $(10 \pm 4) \times 10^{37}\,\mathrm{erg\,s}^{-1}$, the apparent emitting radius between 3 and 5 km (without color or redshift corrections), and the total radiated energy about 1.0×10^{39} erg (see Figure 2.4). The persistent (0.5-10 keV) luminosity during the observation where the burst occurred was $(5.6 \pm 0.1) \times 10^{36}\,\mathrm{erg\,s}^{-1}$ (about 5% of the Eddington limit for a bolometric correction factor of 2 and $L_{\mathrm{Edd}} = 2.5 \times 10^{38}\,\mathrm{erg\,s}^{-1}$).

The peak of the 2015 outburst occurred on April 22, at about ten times higher L_X, i.e., not far from 50% L_{Edd} (for a $1.4 M_\odot$ NS). Despite good *Swift/XRT* coverage (~ 5 ksec) of the following two weeks, when L_X dropped by about a factor 2, no other bursts were detected. This burst behaviour resembles that of most thermonuclear bursters, where bursts virtually disappear at mass accretion rates above 10% Eddington.

A second burster in Terzan 5, IGR 17480-2446, displays drastically different behaviour, namely a copious number of thermonuclear bursts at mass accretion rates between 10% and 50% Eddington (Linares et al., 2012). The atypical behaviour in IGR J17480-2446 has been attributed to its slow (11 Hz) spin (Cavecchi et al., 2011; Linares et al., 2012). Under this interpretation, the typical bursting behaviour of EXO 1745-248 would imply that it contains a rapidly rotating neutron star ($\sim 200 - 600$ Hz), like most low-mass NSXBs.

Galloway et al. (2008) define a burst timescale as $\tau = E_{\mathrm{Burst}}/F_{\mathrm{Peak}}$, where
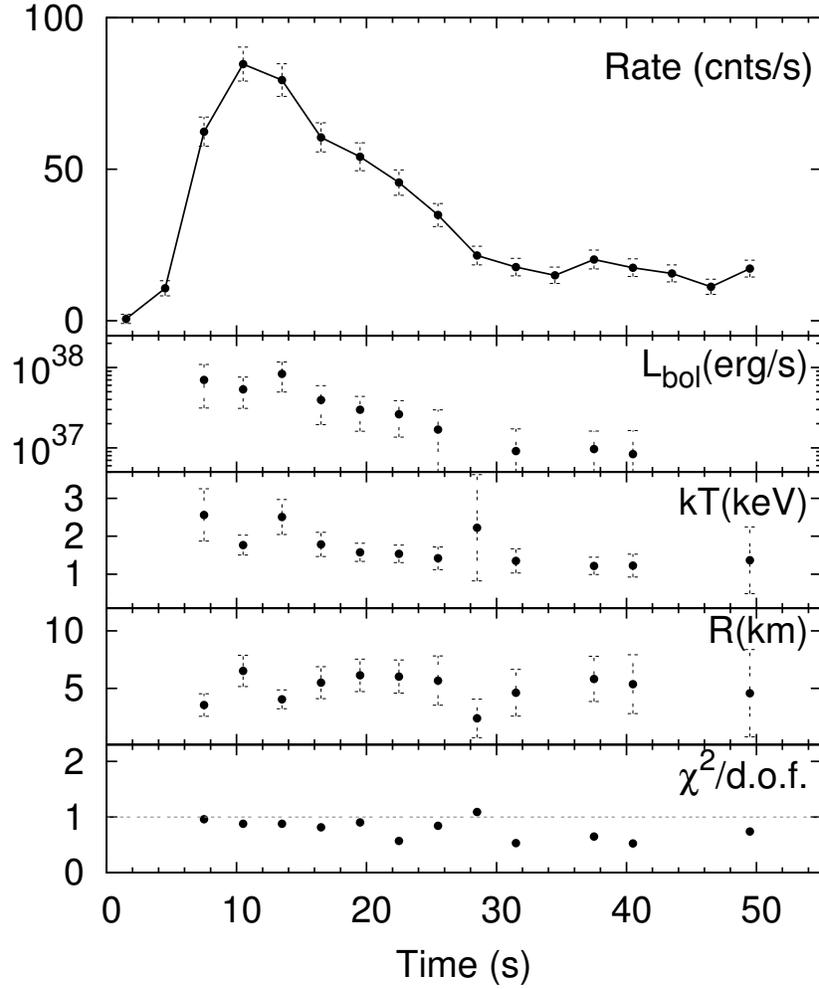
Figure 2.4: Time-resolved spectroscopy of the detected type-I X-ray burst. An absorbed blackbody model was used to fit the data. We found evidence indicating slow cooling during the burst decay, however we found no evidence of photospheric radius expansion. Panels from *top* to *bottom*: *Swift/XRT* count rate, bolometric luminosity, temperature, apparent radius, reduced χ^2 of the spectral fit.

E_{Burst} is the total fluence during the burst and F_{Peak} is the peak flux of the burst. Following their definition, we find a burst timescale of ~ 22 s for EXO 1745$-$248. The 21 bursts seen by RXTE early in the 2000 outburst of EXO 1745$-$248 showed long burst durations ($\tau \sim 25$ s) and other characteristics of H burning. However, two bursts seen later in the outburst were shorter ($\tau \sim 10$ s), suggesting pure He (the explanation of this change in behaviour is not clear; Galloway et al. 2008). Therefore, we conclude that the measured timescale of this burst indicates the donor is likely hydrogen-rich.

2.5 Conclusions

In this paper, we present the results of our observations of the Terzan 5 NSXB EXO 1745$-$248 during its 2015 outburst at radio and X-ray frequencies, with the VLA, ATCA, and *Swift/XRT*. Our (near-) simultaneous radio and X-ray measurements, all taken during the hard accretion state, allow us to construct and fit the radio/X-ray correlation for this source ($L_R \propto L_X^{\beta}$; β represents the disc-jet coupling index), which links the accretion flow to the relativistic jet in XBs. In contrast to the multiple BHXBs with a measured correlation, only two NSXBs have a measured radio/X-ray correlation, Aql X-1 ($L_R \propto L_X^{0.76}$) and 4U 1728$-$34 ($L_R \propto L_X^{1.5}$). Additionally, an ensemble of tMSPs has been shown to follow a correlation, $L_R \propto L_X^{0.7}$, much more consistent with BHXBs. As such, more measurements from NSXBs are needed to disentangle the different correlations. This work marks the third NSXB where the radio/X-ray correlation is measured in a single source, and the first where the distance is well known.

To fit the radio/X-ray correlation in EXO 1745$-$248 we developed a new MCMC based technique. We find a best fit normalization and disc-jet coupling index for the radio/X-ray correlation in EXO 1745$-$248 of $\xi = 0.94^{+0.14}_{-0.13}$ and $\beta = 1.68^{+0.10}_{-0.09}$, respectively, where $(\log L_R - \log L_{R,c}) = \log \xi + \beta(\log L_X - $

$\log L_{X,c}$), with centering values $L_{R,c} = 3.89 \times 10^{28} \, \text{erg s}^{-1}$ and $L_{X,c} = 8.38 \times 10^{36} \, \text{erg s}^{-1}$.

This disc-jet coupling index is consistent with what we would expect for a compact jet coupled to a radiatively efficient accretion flow (presumably due to the NSs surface), rather than a radiatively inefficient flow (as thought to exist in most BHXBs and possibly tMSPs). Empirically this index is consistent with the index for NSXB 4U 1728−34, but inconsistent with our measured index for NSXB Aql X-1. Therefore, a similar radio/X-ray correlation in the hard accretion state does not appear to hold across all three NSXBs measured so far, as it does in the BHXB population. However, all three NSXB correlations are measured over a smaller lever arm in X-ray luminosity (~ 1 dex) when compared to BHXBs.

Notably, we find that EXO 1745−248 is much more radio faint when compared to 4U 1728−34 and Aql X-1, where neither distance, mass, or spin considerations alone appear to be able to account for the discrepancy.

Finally, we detected an X-ray burst during this outburst. Through performing time-resolved spectral analysis, we find evidence of cooling during the decay of this burst and that the burst timescale is consistent with hydrogen burning, suggesting that this was a hydrogen Type-I X-ray burst.

Chapter 3

A Radio Frequency Study of the Accreting Millisecond X-ray Pulsar, IGR J16597-3704, in the Globular Cluster NGC 6256

This chapter details the work published in Tetarenko, A.J. et al. 2018, "A Radio Frequency Study of the Accreting Millisecond X-ray Pulsar, IGR J16597-3704, in the Globular Cluster NGC 6256", *ApJ*, 854, 125 (8 pages), exploring the disc-jet coupling relationship in the accreting millisecond X-ray pulsar IGR J16597-3704, as well as other pulsating and non-pulsating neutron star X-ray binary systems.

Abstract

We present Karl G. Jansky Very Large Array radio frequency observations of the new accreting millisecond X-ray pulsar (AMXP), IGR J16597$-$3704, located in the globular cluster NGC 6256. With these data, we detect a radio counterpart to IGR J16597$-$3704, and determine an improved source position.

Pairing our radio observations with quasi-simultaneous *Swift/XRT* X-ray observations, we place IGR J16597−3704 on the radio – X-ray luminosity plane, where we find that IGR J16597−3704 is one of the more radio-quiet neutron star low-mass X-ray binaries known to date. We discuss the mechanisms that may govern radio luminosity (and in turn jet production and evolution) in AMXPs. Further, we use our derived radio position to search for a counterpart in archival *Hubble Space Telescope* and *Chandra X-ray Observatory* data, and estimate an upper limit on the X-ray luminosity of IGR J16597−3704 during quiescence.

3.1 Introduction

Relativistic jets are launched from many different types of accreting stellar-mass compact objects (black holes, neutron stars, and possibly white dwarfs; Fender 2006; Migliari & Fender 2006; Körding et al. 2008; Coppejans et al. 2015; Russell et al. 2016); however our current knowledge of the physics that gives rise to and governs jet behaviour is still somewhat limited. A crucial step towards understanding the mechanisms that drive jet behaviour is characterizing jet properties (and how these properties are coupled to the conditions in the accretion flow) in different accreting systems across the mass scale.

A key observational diagnostic for comparing jet properties between different systems is the radio – X-ray correlation, relating radio and X-ray luminosities ($L_{\rm R} \propto L_{\rm X}^{\beta}$, where β represents the disc-jet coupling index; Gallo et al. 2003; Corbel et al. 2013). This empirical relationship, which couples a compact, partially self-absorbed synchrotron jet (probed by radio emission) to the properties of the accretion flow (probed by X-ray emission), has been well studied in black hole X-ray binary systems (BHXBs; binary systems harbouring a black hole accreting matter from a companion star). In particular, different BHXB systems, sampled over several orders of magnitude in X-ray luminosity, are known

to display correlations that range from $\beta \sim 0.6 - 1.8$ (potentially following one of two tracks in the radio X-ray plane at $L_X > 10^{36}\,\mathrm{erg\,s^{-1}}$; Coriat et al. 2011b; Gallo et al. 2014; Russell et al. 2015). However, the different classes of neutron star X-ray binary systems (NSXBs; binary systems harbouring a neutron star accreting matter from a companion star) are not as well sampled (in particular due to the limited range of X-ray luminosities that have been sampled to date), and have shown more complex behaviour in the radio – X-ray plane, as compared to the BHXBs.

While NSXBs are generally more radio quiet than BHXBs, different neutron star X-ray binary classes have shown varying correlation indices[1] and normalizations in the radio-X-ray plane (Migliari et al., 2003; Migliari & Fender, 2006; Tudose et al., 2009; Miller-Jones et al., 2010; Tetarenko et al., 2016b; Tudor et al., 2017). For example, some non-pulsating neutron stars display $\beta \sim 1.4$ (Migliari & Fender, 2006; Miller-Jones et al., 2010), while some accreting millisecond X-ray pulsars (AMXPs; accreting neutron star binaries where X-ray pulsations at the spin period of the neutron star are observed) and three transitional millisecond X-ray pulsars (tMSPs; accreting neutron star binaries that switch between a rotation-powered pulsar state and an accretion-powered state; Archibald et al. 2009; Papitto et al. 2013; Bassa et al. 2014; Patruno et al. 2014) have been suggested to follow a shallower correlation of $\beta \sim 0.7$ (Deller et al., 2015). Further, differences are also observed between individual systems of the same class. For example, recent work has shown that not all AMXPs and non-pulsating NSXBs follow the above mentioned "standard" tracks in the radio – X-ray plane (where some systems may display lower/higher radio luminosities; Tetarenko et al. 2016b; Tudor et al. 2017). Many different factors could play a role in causing these observed differences, such as variations in jet power, compact object mass, spin, magnetic field, and jet launching mechanism. To

---

[1]We note that these correlation indices are measured over a limited range of X-ray luminosity, and Corbel et al. (2013) found that an X-ray luminosity lever arm extending across at least 2 dex is needed to accurately measure a correlation in the radio – X-ray plane.

disentangle these factors, understand the reason(s) for a lack of clear correlation(s) and the wide range of radio luminosities observed in neutron star systems, constraints from a larger population of neutron star systems (especially at $L_X < 10^{36}\,\mathrm{erg\,s^{-1}}$), are strongly needed. However, sampling neutron star systems at X-ray luminosities between $10^{34} < L_X < 10^{36}\,\mathrm{erg\,s^{-1}}$ is observationally challenging, as neutron stars tend to evolve quickly in this luminosity range and are faint at radio frequencies. Rapid, coordinated radio and X-ray observations of new X-ray transients discovered in our Galaxy can in principle provide these much needed constraints.

IGR J16597−3704 is a new X-ray transient discovered with the INTErnational Gamma-Ray Astrophysics Laboratory (*INTEGRAL*) on 2017 October 21 (Bozzo et al., 2017a). Followup *Swift* X-Ray Telescope (XRT; Burrows et al. 2005) observations (Bozzo et al., 2017b) on 2017 October 22 confirmed the presence of a new bright X-ray source within the *INTEGRAL* error circle, and placed this new transient in the globular cluster NGC 6256 ($D = 9.1$ kpc; Valenti et al. 2007). To determine the nature of IGR J16597−3704 and localize its position, we performed Karl G. Jansky Very Large Array (VLA) radio frequency observations of IGR J16597–3704 on 2017 October 23 and 27 (Tetarenko et al., 2017a). These radio observations were taken within 3 days of *Swift/XRT* observations of the source, allowing us to also place this new source in the radio – X-ray correlation plane. The preliminary position of IGR J16597−3704 on the radio – X-ray plane strongly suggested that this new transient is a neutron star system. This classification was confirmed by Sanna et al. (2018), who report the discovery of X-ray pulsations, find that IGR J16597−3704 is an ultra-compact binary (~ 46 minute orbital period), with a short spin period (9.5 ms), and suggest a high magnetic field ($9.2 \times 10^8 < B < 5.2 \times 10^{10}$ G). IGR J16597−3704 was also observed with *Chandra* on 2017 October 25 (Chakrabarty et al., 2017). In this paper, we report on our VLA radio and *Swift/XRT* X-ray observations, as well as our search for the optical and quies-

cent X-ray counterparts to IGR J16597−3704.

3.2 Observations and Data Analysis

3.2.1 VLA radio observations of IGR J16597-3704

IGR J16597−3704 was observed with the VLA (project code VLA/17B-257) over two epochs, 2017 October 23 and 27 (see Table 3.2 for observation times), with 88.6 min on source at each epoch. The array was in its B configuration, with a beam size of 2.2 × 0.8 arcsec. All observations were taken using the 3-bit samplers at X-band (8–12 GHz), and were comprised of two base-bands, each with 16 spectral windows of sixty-four 2-MHz channels, providing a total bandwidth of 2.048 GHz per base-band. We carried out flagging, calibration, and imaging within the Common Astronomy Software Application package (CASA, v5.1.1; McMullin et al. 2007), using standard procedures outlined in the CASA Guides[2] for VLA data reduction (i.e., a priori flagging, re-quantizer gain corrections, setting the flux density scale, initial phase calibration, solving for antenna-based delays, bandpass calibration, gain calibration, scaling the amplitude gains, and final target flagging). When imaging we used a natural weighting scheme to maximize sensitivity and two Taylor terms (nterms=2) to account for the large fractional bandwidth. We used 3C 286 (J1331+305) as a flux calibrator and J1717-3948 as a phase calibrator (with a cycle time of 9 minutes on source, and 1 minute on the calibrator).

We significantly detect a radio source at a position consistent with the *Swift* X-ray position reported in Bozzo et al. (2017b) (see Figure 3.1). In the combined 4 GHz of bandwidth centered on 10 GHz, we measure flux densities of $17.7 \pm 4.4\,\mu$Jy and $24.4 \pm 4.3\,\mu$Jy on October 23 and 27, respectively. To measure these flux densities we fit a point source in the image plane (with the

---

[2]https://casaguides.nrao.edu
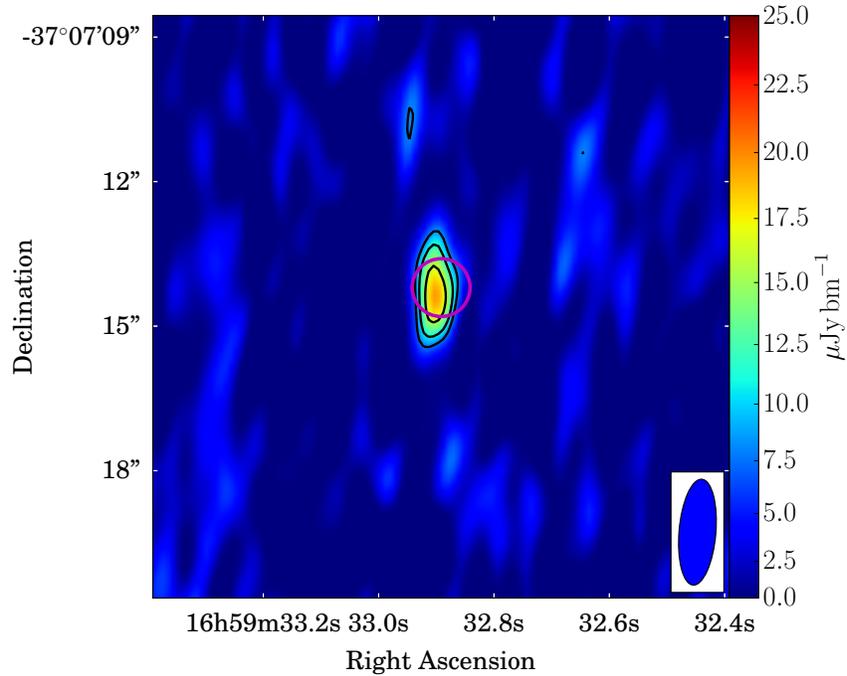
Figure 3.1: VLA radio image of IGR J16597−3704 taken at 10 GHz. We produced this image by stacking the data of both VLA epochs in the *uv*-plane. The source is clearly detected in the image, where contour levels are $2^{n/2} \times$ the RMS noise of $2.8\mu\mathrm{Jy\,bm}^{-1}$, with $n = 3, 4, 5$. The color bar represents the flux density in units of $\mu\mathrm{Jy\,bm}^{-1}$, and the blue ellipse is the VLA beam (the elongated beam shape is due to the low declination of IGR J16597−3704). The *Chandra* (pink circle) X-ray error region is also shown, indicating that the VLA and *Chandra* localizations of the source are consistent.

`imfit` task). The fluxes were too low to obtain a meaningful constraint on the radio spectral index using images of the two individual basebands. The corresponding radio luminosities are shown in Table 3.2.

Additionally, we searched for intra-observation variability within both epochs of VLA data, on timescales as short as 30 min, which is the shortest timescale we can probe given the low source brightness. In both observations, the variance in the data points is consistent with the measurement uncertainties; we thus find no statistically significant evidence for flux variability on intra-observation timescales.

3.2.2 Swift X-ray observations of IGR J16597-3704

IGR J16597$-$3704 was observed with *Swift/XRT* twice following its detection with *INTEGRAL*. These observations occurred on 2017 October 22 in photon counting mode (PC; which produces 2-dimensional images), and 2017 October 25 in windowed timing mode (WT; which collapses data to 1-dimension for fast readout). Observation times are displayed in Table 3.2.

We used HEASOFT v6.22 and FTOOLS[3] (Blackburn, 1995) for all data reduction and analysis. All *Swift/XRT* observations were reprocessed via `xrtpipeline`, and `xselect` was used to manually extract source and background spectra. We used `xrtmkarf` to produce ancillary response files. Finally, we performed spectral analysis using XSPEC v12.9.1n (Arnaud, 1996).

The PC mode observation was piled up. Therefore, we followed the recommended procedure for handling pile up[4], and extracted a source spectrum from an annulus, excluding the piled up region (estimated to be ~ 10 arcsec), out to 80 arcsec. Following the recommended procedure for *Swift/XRT* data analysis, we used events from grades 0-12, and performed spectral analysis in the 0.3–10 keV band.

---

[3]http://heasarc.gsfc.nasa.gov/ftools/
[4]http://www.swift.ac.uk/analysis/xrt/pileup.php

Table 3.1: Best-fit X-ray spectral fitting parameters for IGR J16597$-$3704

Epoch	N_H [a] $(\times 10^{22}\,\mathrm{cm^{-2}})$	Photon Index	$F_{1-10\mathrm{keV}}$ [b] $(\times 10^{-10}\,\mathrm{erg\,s^{-1}\,cm^{-2}})$
1	1.5 ± 0.2	1.5 ± 0.1	2.73 ± 0.11
2	1.1 ± 0.1	1.3 ± 0.1	2.80 ± 0.08

[a] Absorption column density.
[b] Unabsorbed 1–10 keV flux.

For the WT mode observation we used circular regions with a radius of ~ 47 arcsec (20 pixels) for both source and background. To minimize the effects of WT spectral residuals[5], we only extracted a spectrum from grade 0 events and performed spectral analysis in the 0.5-10 keV band, as these residuals become prominent around and below 0.5 keV.

We extracted the X-ray spectrum from each *Swift/XRT* observation separately to perform spectral fitting. Both of the *Swift/XRT* spectra are well fit with an absorbed power-law (TBABS*PEGPWRLW in XSPEC), where we assume photo-electric cross sections from Verner et al. (1996) and abundances from Wilms et al. (2000). We chose to use the TBABS ISM absorption model, as this model implements more recent estimates for the elemental abundance of the ISM, when compared with older models (e.g., PHABS or WABS; Bahramian et al. 2015a; Foight et al. 2016). The best fit spectral fitting parameters for both epochs are shown in Table 3.1, and the corresponding X-ray luminosities are shown in Table 3.2. We report 1σ confidence intervals on all fitted parameters. To calculate these 1σ confidence intervals, we first binned each spectrum to a minimum of 50 counts per bin using the `grppha` task, and utilized χ^2 statistics for spectral analysis. Following this analysis, the parameter uncertainties were estimated using the `error` task in XSPEC [6].

[5]For more details on these effects see the *Swift/XRT* calibration digest; `http://www.swift.ac.uk/analysis/xrt/digest_cal.php#abs`

[6]For details on how this task works see `https://heasarc.gsfc.nasa.gov/xanadu/xspec/manual/node80.html`

Table 3.2: Radio & X-ray observation details for IGR J16597−3704

Epoch	Radio Observation (mm/dd/yy, UTC)	X-ray Observation (mm/dd/yy, UTC)	$L_{\rm 5GHz}$ [a,b] ($\times 10^{28}$ erg s^{-1})	$L_{\rm 1-10\,keV}$ [a] ($\times 10^{36}$ erg s^{-1})
1	10/23/2017, 21:01−22:42	10/22/2017, 20:29−20:47	0.87 ± 0.22	2.69 ± 0.11
2	10/27/2017, 20:44−22:25	10/25/2017, 07:30−07:51	1.20 ± 0.21	2.76 ± 0.08

[a] To calculate the luminosities, we use a distance to NGC 6256 of $D = 9.1$ kpc (Valenti et al., 2007). Uncertainties include measurement errors only, and are quoted at the 1σ level.
[b] We calculate 5 GHz radio luminosities ($L_R = \nu L_\nu$) by combining the two VLA base-bands in each observation and assuming a flat spectral index to extrapolate to 5 GHz.

3.2.3 Archival Optical and X-ray observations

We obtained archival X-ray and optical data of the field surrounding IGR J16597-3704 (see Figure 3.2), taken with the *Chandra* X-ray Observatory and the *Hubble Space Telescope* (*HST*). *Chandra* data were taken on 2008 January 26 (13:09:51 UTC start time, 9.4 ks exposure time, Obs ID: 8951) with the ACIS-S instrument. We reprocessed the data using CIAO v4.9 (Fruscione et al., 2006). *HST* images were obtained from the Hubble Legacy Archive (`http://hla.stsci.edu/`) in the F555W and F814W filters. These *HST* observations were taken with the WFC3/UVIS1 detector on 2009 August 02 (19:47:12/20:43:35 UTC start time, 1.1/0.3 ks exposure time, in the F555W/F814W filters). The absolute astrometry of the *HST* images was corrected by matching sources in the field to the *Gaia* catalog (Gaia Collaboration et al., 2016). We estimate that after matching to the *Gaia* catalog, the uncertainty in the absolute position registration of the *HST* images is < 0.02 arcsec.
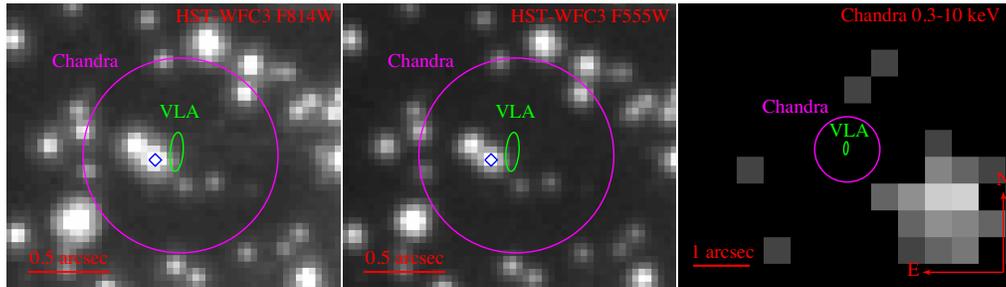
Figure 3.2: Archival *HST* and *Chandra* images of the field surrounding IGR J16597−3704. The left panel displays the *HST* F814W image, the middle panel displays the *HST* F555W image, and the right panel displays the *Chandra* (0.3–10 keV band) image. The *Chandra* (magenta circles), and VLA (green ellipses) error regions are indicated in all panels, and the blue diamonds indicate the possible counterpart discussed in §3.3.2. Note the different scales in the optical (*left* and *middle*) and X-ray (*right*) images. We do not detect an optical or quiescent X-ray counterpart to IGR J16597−3704 in these archival data.

3.2.4 Additional neutron star sources

We supplement[7] these new radio/X-ray data on IGR J16597−3704 with our team's recent radio/X-ray measurements of a number of other neutron star sources for further comparison, MAXI J0911–635 (Tudor et al., 2016), SAX J1748.9–2021 (Miller-Jones et al., 2010; Tetarenko et al., 2017b), Swift J175233.9–290952 (Tetarenko et al., 2017c), and 4U 1543–624 (Ludlam et al., 2017). Additionally, we also include older detections of MAXI J0556–332 (Coriat et al., 2011a) and MXB 1730–335 (Rutledge et al., 1998) in this work. Table 3.3 displays a summary of the radio and X-ray luminosity measurements for these sources.

---

[7]The additional neutron star data reported in this section have only been reported in Astronomer's Telegrams, and not previously published in refereed journals.

Table 3.3: Radio and X-ray luminosities of additional neutron star sources

Source	$\mathbf{L_{5GHz}}$ [a,b] $(\,\mathrm{erg\,s^{-1}})$	$\mathbf{L_{1-10\,keV}}$ [a] $(\,\mathrm{erg\,s^{-1}})$	$\mathbf{D}$ [c] (kpc)	$\mathbf{Ref.}$ [d]
MAXI J0911$-$635	$< 4.5 \times 10^{28}$	2.5×10^{36}	10.4	[1]
SAX J1748.9$-$2021	$< 4.5 \times 10^{27}$	2.1×10^{36}	8.5	[2]
	$< 5.1 \times 10^{28}$	3.0×10^{37}		[3]
Swift J175233.9$-$290952	$< 5.7 \times 10^{27}$	1.4×10^{34}	8.0	[4]
4U 1543$-$624	$< 7.2 \times 10^{27}$	1.7×10^{37}	6.7	[5]
MAXI J0556$-$332	5.3×10^{28}	1.8×10^{37}	8.0	[6]
MXB 1730$-$335[e]	2.0×10^{28}	6.1×10^{35}	8.6	[7]
	1.6×10^{29}	4.0×10^{37}		
	1.3×10^{29}	4.1×10^{37}		
	1.5×10^{29}	7.2×10^{37}		
	1.8×10^{28}	3.3×10^{36}		

[a] Upper limits are quoted at the 3σ level.
[b] We calculate 5 GHz radio luminosities ($L_R = \nu L_\nu$) by assuming a flat spectral index to extrapolate to 5 GHz.
[c] Distance value used to calculate luminosity.
[d] **References:** [1] Tudor et al. (2016); [2] Tetarenko et al. (2017b); [3] Miller-Jones et al. (2010); [4] Tetarenko et al. (2017c); [5] Ludlam et al. (2017); [6] Coriat et al. (2011a); [7] Rutledge et al. (1998).
[e] Note that we use a model with $N_{\mathrm{H}} = 1.7 \times 10^{22}\,\mathrm{cm^{-2}}$ (Marshall et al., 2001), and a photon index of 1.5, to convert from RXTE count rates to flux for this source.

3.3 Results

3.3.1 Radio source position

Stacking both epochs of our VLA data in the *uv*-plane (see Figure 3.1) refines the radio position of IGR J16597−3704 to be the following (J2000),

$$\text{RA}: \quad 16^h 59^m 32^s.90230 \pm 0.00092 \pm 0.005$$

$$\text{DEC}: \quad -37°07'14''.278 \pm 0.088 \pm 0.22,$$

where the quoted errors represent the statistical error from fitting in the image plane and the nominal systematic uncertainties of 10 percent of the beam size, respectively. The elongated beam shape arises from the low declination of the source. This radio source position is consistent (within 0.04 arcsec) with the best X-ray position of the source during outburst from *Chandra* (Chakrabarty et al., 2017).

3.3.2 Search for the quiescent X-ray and optical counterparts

We examined archival *Chandra* and *HST* observations in search of the quiescent X-ray and optical counterparts to IGR J16597−3704.

In the archival *Chandra* data, there is an X-ray source ∼ 2.2 arcsec to the south-west of the VLA radio position (see Figure 3.2 *right panel*). However, this *Chandra* source is unlikely to be the quiescent counterpart of IGR J16597-3704 given the typical *Chandra* absolute astrometric accuracy of 0.5 arcsec. To further confirm the *Chandra* absolute astrometry is accurate (i.e., as good as 0.5 arcsec or better), we compare the positions of known X-ray sources in the cluster to their radio and optical counterparts. In particular, there is a radio continuum source ∼ 2.5 arcmin from the center of the cluster that has a *Chandra* X-ray counterpart, and the positions of these match to within 0.5

arcsec. Additionally, there are three X-ray sources in the outer regions of the cluster, where the optical source density is lower, that all clearly match bright stars present in the *Gaia* catalog. The individual offsets between the *Gaia* and *Chandra* positions vary from 0.6–1.0 arcsec, well within the uncertainties of the individual X-ray positions, and there is no evidence of a significant net astrometric shift. Together these arguments strongly suggest that the bright X-ray source in question is not associated with IGR J16597−3704, and that the quiescent counterpart of this transient is undetected in existing X-ray data.

We assert a non-detection in this *Chandra* observation and estimate a 95% upper limit on the count rate of $2.9 \times 10^{-4} \, \text{cts} \, \text{s}^{-1}$. Assuming a distance of $D = 9.1$ kpc (Valenti et al., 2007), hydrogen column density of $\sim 1.1 \times 10^{22} \, \text{cm}^{-2}$, and power law spectrum (with a canonical photon index of 1.5), this translates to upper limits of $4.9 \times 10^{-15} \, \text{erg} \, \text{s}^{-1} \, \text{cm}^{-2}$ on the absorbed X-ray flux in the 0.5-10 keV band, and $L_X < 6.4 \times 10^{31} \, \text{erg} \, \text{s}^{-1}$ for the luminosity, of the quiescent counterpart. Alternatively, assuming an neutron star atmosphere model (NSATMOS in XSPEC) with canonical values of $1.4 M_\odot$ and a radius of 10 km, this translates to upper limits of $1.1 \times 10^{-15} \, \text{erg} \, \text{s}^{-1} \, \text{cm}^{-2}$ on the absorbed X-ray flux in the 0.5-10 keV band, and $L_X < 9.9 \times 10^{30} \, \text{erg} \, \text{s}^{-1}$ for the luminosity. In this model, the upper limit on the absorbed flux corresponds to a neutron star temperature of $< 75 \, \text{eV}$. Neutron star temperatures have been measured in other systems to extend across a range of values, from $< 50 \, \text{eV}$ for the coolest neutron stars (e.g., EXO 1745−248, SAX J1808.4−3658, 1H 1905+000; Jonker et al. 2007; Heinke et al. 2009; Degenaar & Wijnands 2012), up to $\sim 150 \, \text{eV}$ for the hottest neutron stars (e.g., XTE J1701-462; Wijnands et al. 2017). Our new temperature measurement indicates that the neutron star in IGR J16597−3704 is not an overly hot neutron star, but rather is consistent with an average or lower temperature neutron star, when compared with the current measured population.

In the *HST* data, there is no clear optical source within the VLA error circle

(see Figure 3.2 *left* & *middle*). However, we identify a bright optical source 0.13 arcsec to the SE of our VLA radio position, which lies outside the 1σ VLA confidence interval. Optical photometry indicates this *HST* source was at $m_{F555W/F814W} \sim 22.4/20.3$ (AB magnitudes) on 2009 August 02, consistent with a typical giant star within the NGC 6256 cluster. Given that IGR J16597$-$3704 has been recently identified (Sanna et al., 2018) to be an ultra-compact system (which typically have compact white dwarf companions), this *HST* source is unlikely to be the optical counterpart. Therefore, the optical counterpart is probably too faint to be detected in the existing *HST* data. We estimate 3σ upper limits from the archival *HST* images of $m_{F555W/F814W} < 26.0/23.4$.

3.3.3   Radio – X-ray correlation

To explore the nature of IGR J16597$-$3704, we place our observations on the radio – X-ray plane, using the 5 GHz radio luminosity and the 1.0$-$10 keV X-ray luminosity (where that frequency and band are chosen to match measurements from the literature; see Figure 3.3 & Table 3.2).

The location of IGR J16597$-$3704 on the radio – X-ray plane lies at least an order of magnitude below most BHXBs, and instead is more consistent with neutron star systems (both non-pulsating NSXBs and AMXPs/tMSPs; see Figure 3.3). The recent detection of X-ray pulsations from this source with *NuSTAR* (Sanna et al., 2018), confirms that IGR J16597-3704 is a new AMXP source. All of the neutron star sources presented in this work display a significant range in radio luminosity. In particular, IGR J16597$-$3704, along with SAX J1748.9-2021, Swift J175233.9-290952, and 4U 1543-624, display radio luminosities that are at the low end of the sampled NSXB population, while MAXI J0911-635, MAXI J0556-332, MXB 1730-335 display radio luminosities at the mid to high end of the sampled NSXB population.
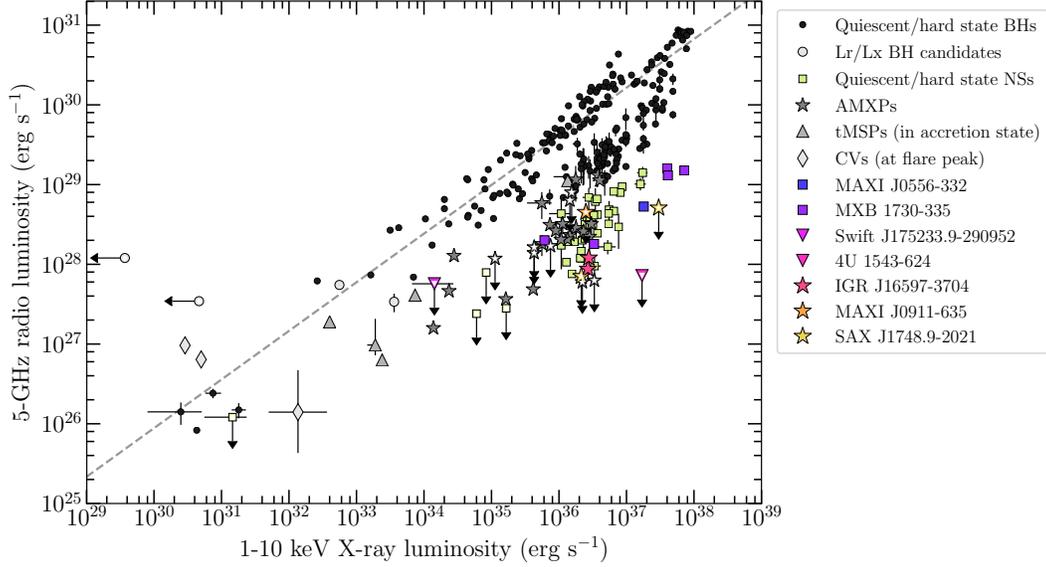
Figure 3.3: The radio – X-ray correlation for different types of accreting stellar-mass compact objects: black holes, different classes of neutron stars (non-pulsating NSXBs, AMXPs, and tMSPs), and out-bursting cataclysmic variables. This plot is adapted from Bahramian et al. (2017), with additional measurements from more recent publications, as well as those displayed in Table 3.3; Rutledge et al. 1998; Gallo et al. 2006; Miller-Jones et al. 2010; Coriat et al. 2011a; Russell et al. 2015; Marsh et al. 2016; Tetarenko et al. 2016b; Rushton et al. 2016; Tudor et al. 2016; Ribó et al. 2017; Plotkin et al. 2017; Tudor et al. 2017; Tetarenko et al. 2017b; Gusinskaia et al. 2017; Tetarenko et al. 2017c; Ludlam et al. 2017; Bogdanov et al. 2018; Dincer et al. 2018. The best-fit relation for black holes ($\beta = 0.61$, grey dashed; Gallo et al. 2014) is also shown. Our measurements of IGR J16597−3704 and the measurements of other NSXBs reported in Table 3.3 are displayed with colored symbols (where non-pulsating NSXBs, AMXPs, and unclassified sources are indicated by the square, star, and inverted triangle shapes, respectively). IGR J16597−3704 (pink star shapes) is one of the more radio quiet systems in the NSXB population.

3.4   Discussion

In this paper, we have reported on the discovery of the radio counterpart to the new AMXP, IGR J16597−3704, located in the NGC 6256 globular cluster. We do not conclusively identify an optical or quiescent X-ray counterpart to IGR J16597−3704 in archival *HST* and *Chandra* data; our 3σ upper limits are $m_{\text{F555W/F814W}} < 26.0/23.4$ and $L_X < 6.1 \times 10^{31}$ erg s^{-1}.

Our recent radio observations indicate that IGR J16597−370 is one of the more radio faint systems in the NSXB population. For example, IGR J16597−3704 displays a similar radio luminosity to IGR J17511−3057 (AMXP; Tudor et al. 2017), SAX J1748.9−2021 (AMXP; Tetarenko et al. 2017b), and EXO 1745−248 (non-pulsating NSXB; Tetarenko et al. 2016b). Examining our updated radio – X-ray plane figure (Figure 3.3), it is clear that both non-pulsating NSXBs and AMXPs can display a range of radio luminosities at a similar X-ray luminosity (where it is unclear whether the radio-brighter or radio-fainter systems form the dominant population). Here we postulate on the mechanisms driving the radio luminosity in IGR J16597−3704 (and potentially other AMXPs), by exploring the relationships between radio luminosity and spectral state, spin, magnetic field, orbital period, accretion regime, and evolutionary state.

The jets from some NSXBs (like BHXBs) have been observed to be quenched by over an order of magnitude (or faded below current detection limits; e.g., Migliari et al. 2003; Gusinskaia et al. 2017) during softer accretion states. As such, we may naively expect radio jets to be fainter in these states when compared to their harder accretion states. Since, the X-ray spectral properties reported in §3.2.2 suggest that IGR J16597−3704 was in a canonical hard state during our observations, it is unlikely that jet quenching in the soft accretion state explains the low radio luminosity of IGR J16597−3704. By extension, many other radio quieter systems in the sampled population, such as

EXO 1745−248 (Tetarenko et al., 2016b), have also been observed firmly in the hard accretion state.

Sanna et al. (2018) have shown that IGR J16597−3704 displays a longer spin period (9.5 ms), when compared to the average values for AMXPs (Patruno & Watts, 2012; Mukherjee et al., 2015; Patruno et al., 2017, 2018). The spin of a neutron star has long been suggested to potentially affect the radio luminosity of NSXBs (Migliari et al., 2011). Depending on how the magnetic field (anchored to the NS magnetic poles) interacts with the accretion disc, AMXP jets could be directly powered by the extraction of energy from the spin of the neutron star, or the jet may be driven by the rotation power of the accretion disc (Migliari et al., 2011; Migliari et al., 2012). In both cases, we expect the neutron star spin period to correlate with jet power. For example, a longer spin period could be linked to a lower radio luminosity in AMXPs, analogous to the spin dependence of jet power for black holes ($L_{\mathrm{jet}} \propto a^2$, where a is the black hole spin parameter) predicted by Blandford & Znajek (1977). Past studies (Migliari et al., 2011) have found hints of a possible positive correlation[8] between spin frequency of the neutron star and jet power in AMXPs, and our measurements of IGR J16597−3704 are compatible with this scaling. Therefore, it seems plausible that spin period may play a role in governing the radio luminosity levels in IGR J16597−3704 (and potentially other radio-quiet AMXPs).

Similar to the spin period, IGR J16597−3704 may also display a higher magnetic field ($9.2 \times 10^8 < B < 5.2 \times 10^{10}$ G) when compared to the average values for AMXPs. The role of a high magnetic field in jet production is still an open question. Past works have suggested that high magnetic fields ($\gtrsim 10^{11}$ G; Fender & Hendry 2000; Migliari et al. 2012) may inhibit jet formation, but

---

[8]Although, we note that the jet power was not measured directly in this work, with the normalization of the sources on the radio X-ray plane (assuming a disc-jet coupling index of 1.4) being used as a proxy for jet power. Thus this correlation may break down for different disc-jet coupling indices.

the recent work by van den Eijnden et al. 2018a,b (described below) provides a counterpoint, thus we explore both possibilities here. Using the condition that the gas pressure must dominate over the magnetic pressure, Massi & Kaufman Bernadó (2008) derive a condition for jet formation based on the magnetic field strength (B_*) and accretion rate ($\dot{M}$), such that,

$$\frac{R_A}{R_*} = 0.87 \left(\frac{B_*}{10^8\,\mathrm{G}}\right)^{4/7} \left(\frac{\dot{M}}{10^{-8}\,M_\odot\mathrm{yr}^{-1}}\right)^{-2/7} \tag{3.1}$$

where R_A is the Alfvén radius, and $\frac{R_A}{R_*} \approx 1$ indicates the portion of the parameter space where jet formation is likely to not be suppressed by the neutron star magnetic field. Substituting in estimates of $9.2 \times 10^8 < B_* < 5.2 \times 10^{10}$ G (Sanna et al., 2018) and $\dot{M} = 5 \times 10^{-12}\,M_\odot\mathrm{yr}^{-1}$ (estimated from the $\dot{M}/P_\mathrm{orb}$ relationship reported in van Haaften et al. 2012[9]) for IGR J16597$-$3704, indicates that IGR J16597$-$3704 may be in a regime ($\frac{R_A}{R_*} > 1$) where the magnetic field could potentially be inhibiting jet formation (and in turn lead to the lower radio luminosity observed).

Contrary to this hypothesis, radio emission (consistent with a synchrotron jet) has been recently detected in the high magnetic field neutron star systems GX 1+4 (van den Eijnden et al., 2018a) and Her X-1 (van den Eijnden et al., 2018b). Moreover, another AMXP, IGR J17511$-$43057, displays a magnetic field strength similar to the average AMXP population, but lower than average radio luminosity (Tudor et al., 2017). Furthermore, if high magnetic fields are linked to lower radio luminosities in neutron stars, we may expect that the AMXP population in general would display lower radio luminosities compared to the population of non-pulsating NSXBs (which presumably display lower magnetic fields than pulsating systems). This is clearly not the case, as for example, the non-pulsating NSXB, EXO 1745$-$248, displays a radio luminosity

---

[9]While Sanna et al. (2018) report an $\dot{M} = 5.5 \times 10^{-10}\,M_\odot\,\mathrm{yr}^{-1}$, this estimate only represents the peak $\dot{M}$ in the outburst.

similar to IGR J16597−3704 (also see Figure 3.3). Therefore, there does not appear to be a clear relationship between magnetic field strength of the neutron star and radio luminosity in the current sampled population, suggesting that the high magnetic field in IGR J16597−3704 does not strongly influence the radio luminosities we observe.

Although, if different jet production mechanisms are at work in different classes of neutron star systems, we may expect a much more complicated (beyond a simple scaling) relationship between the magnetic field strength of the neutron star and the radio luminosity. For instance, the jet production mechanism in neutron star systems could be highly dependent on how dynamically important the magnetic field of the neutron star is in each system (i.e, how significant a role the stellar magnetic fields play in the accretion process). In this case, jets launched from non-pulsating NSXBs, with dynamically unimportant magnetic fields, may be powered by the accretion disc, similar to BHXBs, while the dynamically important magnetic fields in tMSPs/AMXPs could disrupt this physical connection between the jet and the disc. Therefore, in some systems we may not be observing an accretion powered jet, but rather another mechanism, such as the propeller effect[10] (Romanova et al., 2009; Parfrey et al., 2017), which may be powering the jet (e.g., the propeller effect is thought to be the origin of the anti-correlation between radio and X-ray luminosity observed in PSR J1023+0038; Bogdanov et al. 2018).

As IGR J16597−3704 is an ultra-compact binary (with an orbital period < 80 min), we opt to briefly investigate a possible link between radio luminosity and orbital period, by compiling a list of all the ultra-compact neutron star binaries with radio frequency measurements (see Table 3.4 and Figure 3.4). We find that in these ultra-compact binaries, the orbital period does not appear to be correlated with the position of the system in the radio – X-ray plane.

---

[10]In the case of the propeller effect, the radio emission may originate in a broader outflow, as opposed to a well-collimated jet.

Table 3.4: Properties of ultra-compact neutron star binaries

Source	$L_{5\,GHz}$ [a,b] ($erg\,s^{-1}$)	$L_{1-10\,keV}$ [a] ($erg\,s^{-1}$)	D [c,d] (kpc)	P_{orb} [d] (min)	Ref. [e]
4U 1728-34	6.83×10^{28}	5.2×10^{36}	5.2	10.8?[‡]	[1]
4U 1820-303	8.78×10^{28}	9.7×10^{36}	7.9	11	[1]
4U 0513-40	$< 5.50 \times 10^{28}$	2.9×10^{36} *	12.1	17	[2]
2S 0918-549	$< 5.21 \times 10^{28}$	9.5×10^{35} *	5.4	17.4	[3]
4U 1543-624	$< 7.20 \times 10^{27}$	1.7×10^{37}	6.7	18.2	[4]
4U 1850-087	4.60×10^{28}	1.2×10^{36} *	6.9	20.6	[5]
M15 X-2	3.67×10^{28}	2.3×10^{37}	10.4	22.6	[6]
4U 1916-053	$< 1.80 \times 10^{29}$	2.7×10^{36} *	9.3	50	[7]
4U 0614+091	1.72×10^{28}	3.2×10^{36}	3.2	51?[‡]	[8]
XTE J1751-305	$< 1.14 \times 10^{28}$	$< 2.3 \times 10^{32}$ [†]	8.0	42	[9]
XTE J0929-314	1.37×10^{29}	4.7×10^{36}	8.0	43.6	[10]

[a] Upper limits are quoted at the 3σ level.
[b] We calculate 5 GHz radio luminosities ($L_R = \nu L_\nu$) by assuming a flat spectral index to extrapolate to 5 GHz.
[c] Distance value used to calculate luminosity.
[d] All distance and orbital period measurements are taken from Cartwright et al. (2013).
[e] **References:** [1] Díaz Trigo et al. 2017; [2] Machin et al. 1990; [3] Zwarthoed et al. 1993; [4] Ludlam et al. 2017; [5] Lehto et al. 1990; [6] Sivakoff et al. 2011; [7] Grindlay & Seaquist 1986; [8] Migliari et al. 2010; [9] Iacolina et al. 2010; [10] Rupen et al. 2002
* These systems did not have X-ray measurements reported with their radio measurements; we place limits on the X-ray luminosity by using the luminosity functions reported in Cartwright et al. (2013).
[†] XTE J1751$-$305 did not have an X-ray measurement reported with its radio measurement; we use the upper limit on the quiescent X-ray luminosity reported in Wijnands et al. (2005).
[‡] Cartwright et al. (2013) classify these estimates of orbital period as more uncertain, as they are supported by only weak evidence.
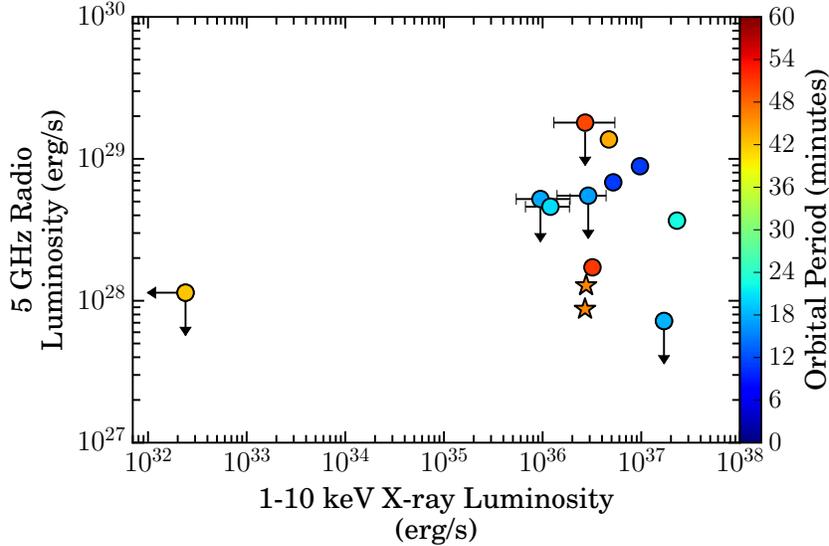
Figure 3.4: Radio – X-ray correlation for ultra-compact neutron star binaries. The data points are color coded by orbital period. Our IGR J16597−3704 measurements are indicated by the star symbols. The data points with horizontal error bars represent those systems for which the X-ray luminosity measurement were estimated from luminosity functions or quiescent X-ray limits (see Table 3.4 for details). We observe no clear correlation between the position of these sources on the radio – X-ray plane and orbital period.

Further, we also find no evidence of a direct correlation between orbital period and radio luminosity (Spearman rank correlation coefficient of −0.22, and p-value of 0.46). This suggests that orbital period may not play a key role in governing the radio luminosity in IGR J16597−3704 or other systems.

Lastly, the radio luminosity in AMXPs may be closely tied to the evolutionary state or the accretion regime (i.e., X-ray spectral state and mass accretion rate, as suggested by Migliari et al. 2011) of the system. In IGR J16597−3704, Sanna et al. (2018) estimate that very little mass has been accreted so far in the system, and suggest that this indicates it is in an early stage of its evolution (i.e., it is a partially-recycled pulsar). However, the likelihood of catching this system in such a short-lived early evolutionary state is quite low. Since IGR J16597−3704 is an ultra-compact binary (with a low donor star mass; Sanna et al. 2018), it is much more consistent with a system in the later stages

of its evolution. This uncertainty makes it difficult to postulate whether the evolutionary state of IGR J16597−3704 (and other AMXPs) influences their observed radio luminosities, without further study.

A larger sample of radio luminosity constraints from AMXPs is needed to definitively determine whether the spectral state, spin period, magnetic field strength, orbital period, or accretion regime/evolutionary state are linked to jet behaviour.

Overall, these results highlight the need for more radio and X-ray measurements of all classes of NSXBs to place improved constraints on the mechanisms that govern radio luminosity, jet production and jet evolution in NSXBs. The low X-ray luminosity regime ($L_X < 10^{36}\,\mathrm{erg\,s^{-1}}$) is particularly vital, as this regime remains under-sampled for the different classes of NSXBs. Finally, despite the lack of a clear correlation for neutron star systems, IGR J16597−3704 is a clear example that the radio – X-ray plane can still be a reliable diagnostic to identify the nature of the accretor in these binary systems.

Chapter 4

Radio timing analysis of the compact jet in the black hole X-ray binary Cygnus X-1

This chapter is based on a manuscript in preparation, to be submitted to the *Monthly Notices of the Royal Astronomical Society (MNRAS)* journal as Tetarenko, A.J. et al. 2018, "Radio timing analysis of the compact jet in the black hole X-ray binary Cygnus X-1", describing a detailed study of rapid (second to hour timescale) compact jet variability at radio frequencies in a black hole X-ray binary.

Abstract

We present simultaneous multi-band radio and X-ray observations of the black hole X-ray binary Cygnus X-1, taken with the Karl G. Jansky Very Large Array (VLA) and the Nuclear Spectroscopic Telescope Array (NuSTAR). With these data we extract high time resolution light curves, in which we detect clear flux variability in the form of small amplitude flaring events. The radio variability is of lower amplitude and more smoothed out at lower frequencies, consistent with emission from a variable compact jet. To characterize the radio

variability we observe and probe how the variability signal propagates down the jet flow, we perform detailed timing analyses of our data, including cross-correlation analyses and a Fourier domain analyses. We find that the radio jet emission shows no significant power at Fourier frequencies $f \gtrsim 0.03$ Hz (below ~ 30 sec timescales), and that the higher frequency radio bands (9/11 GHz) are strongly correlated over a range of time scales, displaying a roughly constant time lag with Fourier frequency of a few tens of seconds. However, in the lower frequency radio bands we find a significant loss of coherence over the same range of timescales. We discuss different mechanisms that could be causing this effect. Further, we detect a correlation between the X-ray and radio emission, measuring time lags between the X-ray and radio bands on the order of tens of minutes. We use these X-ray/radio lags to solve for the compact jet speed, finding that the Cyg X-1 jet is more relativistic than usually assumed for compact jets, where $\beta = 0.92^{+0.03}_{-0.06}$, ($\Gamma = 2.59^{+0.79}_{-0.61}$). Lastly, we constrain how the jet size scale changes with frequency, finding a shallower relation ($\propto \nu^{-0.4}$) than predicted by simple jet models ($\propto \nu^{-1}$), and we estimate the jet opening angle to be $\phi \sim 0.4 - 1.8$ degrees. With this study we have developed observational techniques designed to overcome the challenges of radio timing analyses and created the tools needed to connect rapid radio jet variability properties to internal jet physics.

4.1   Introduction

Black holes drive the most powerful outflows in the Universe, from the kiloparsec-scale jets launched by the most massive black holes in Active Galactic Nuclei (AGN), to the smaller-scale jets launched by their stellar mass analogues, black hole X-ray binaries (BHXBs). BHXBs are often the targets of jet studies, as these accreting binary systems rapidly evolve through bright outburst phases (typically lasting days to months), providing a real-time view of jet behaviour.

78

At the beginning of an outburst, the BHXB is typically in a hard accretion state, where there exists a compact, relativistic jet, an inner radiatively inefficient accretion flow (which may be synonymous with the base of the jet; Narayan & Yi 1995; Markoff et al. 2005), and a slightly truncated accretion disc (McClintock & Remillard, 2006; Fender et al., 2004a). The compact jets primarily emit at radio, sub-mm and infrared frequencies (Fender, 2001; Corbel & Fender, 2002; Chaty et al., 2011; Russell et al., 2006; Tetarenko et al., 2015d) as a result of partially self-absorbed synchrotron emission (Blandford & Königl, 1979), where higher frequencies probe regions closer to the black hole (although in some cases optically thin synchrotron emission above the self-absorption turnover in the spectrum may contribute significantly at frequencies up to the X-ray band, e.g., Russell et al. 2010). On the other hand, the accretion flow (in the hard state) primarily emits in the X-rays, and is dominated by thermal comptonization of photons from the accretion disc in the inner accretion flow/jet base region (although the outer accretion disc can also emit at infrared, optical, and UV frequencies; Done et al. 2007). This X-ray emission is known to be strongly variable (fractional rms 10–50%), on as short as sub-second timescales (power at Fourier frequencies as high as hundreds of Hz; van der Klis 2006).

While broad-band spectral measurements and high resolution radio imaging studies with Very Long Baseline Interferometry (VLBI; e.g. Stirling et al. 2001) are traditionally used to constrain jet properties (e.g., speed and geometry), and probe the connection between the jet and accretion flows (e.g., van der Horst et al. 2013; Russell et al. 2014), time domain observations offer a promising new way to address the key open questions in jet research (Uttley & Casella, 2014). Detecting and characterizing rapid flux variability in jet emission from multiple BHXBs can allow us to probe detailed jet properties that are difficult, if not impossible, to measure by other means. For instance, measuring the shortest timescale over which the compact jet flux is significantly changing provides a

direct measure of the jet size scale at different observing frequencies. At its best, high resolution VLBI can only image the jets from BHXBs (which are located at kiloparsec distances) down to AU size scales. In fact, in the few published cases where a compact jet was resolved in the axial direction (GRS 1915+105 and Cygnus X-1; Stirling et al. 2001; Dhawan et al. 2000), VLBI has failed to resolve structure perpendicular to the jet axis, suggesting jet widths on the order of sub-AU scales. Therefore, while determining the cross-section and opening angle of BHXB jets is beyond current imaging capabilities, detecting jet variability on second timescales, probing scales as small as mAU (for emitting regions travelling at light speed), could be used to recover new information on jet geometry.

Additionally, as the jet flow propagates downstream from the black hole, optical depth effects cause lower frequency emission to appear as a delayed version of high frequency emission (Blandford & Königl, 1979; Hjellming et al., 1988; Falcke & Biermann, 1995). Through measuring the time delay between small emission features (i.e., small flaring events) at different frequencies, we can estimate the compact jet speed, for which there are currently no direct measurements (Uttley & Casella, 2014). Further, detecting correlated variability across a wide range of frequencies, probing both the jet and accretion flow emission, can effectively allow us to track accreting matter from inflow to outflow, revealing how variations in the accretion flow manifest themselves further downstream in the jet. Recent work has shown evidence of correlations between optical/infrared and X-ray variability on sub-second timescales (Malzac et al., 2003; Casella et al., 2010; Kalamkar et al., 2016; Gandhi et al., 2017; Vincentelli et al., 2018), suggesting variations in the accretion flow could subsequently drive variability in the jet emission. Directly linking changes in the accretion flow with changes in jet emission at different scales (where different frequencies probe different distances along the jet axis) provides unparalleled insight into the sequence of events leading to jet launching and acceleration.

Broad-band variability measurements also allow for detailed tests of both standard and new jet theory models. In particular, Blandford & Königl (1979) predict that the jet size scale is inversely proportional to frequency ($z \propto \nu^{-1}$, where z represents the distance down-axis from where the jet is launched). Additionally, recent models predict that jet variability is driven by the injection of discrete shells of plasma at the base of the jet with variable speeds (Turler et al., 2004; Jamil et al., 2010; Malzac, 2014; Drappeau et al., 2015, 2017). In these works, the behaviour of these shells (traced by the jet variability properties) is directly linked to the X-ray power density spectrum (quantifying the amplitude of X-ray variability at different timescales). As the timescale of the jet variability depends on the shock speed and shell thickness in this model, detecting correlated variability over a wide frequency range could disentangle these parameters.

To date, compact jet emission in BHXBs at radio frequencies has been observed to vary over a range of timescales (minutes to months). While the longer timescale variations have been tracked and well characterized in many systems, this is not the case for the short (< 1 hour) timescale variations, for which there are only a handful of detections (e.g., variations detected on minute to hour timescales; Pooley & Fender 1997; Fender & Pooley 2000; Corbel et al. 2000; Miller-Jones et al. 2009; Tetarenko et al. 2015d; Curran et al. 2014). Further, little effort has been made to analyze this short timescale radio variability (e.g., Nipoti et al. 2005 present the only radio frequency Fourier domain study, where the shortest timescales probed were days), search for variability at higher sub-mm frequencies (probing the base of the jet close to the black hole), or connect radio variability properties (e.g., amplitudes, timescales) with internal jet physics.

While time-resolved observations are a staple for BHXB studies at higher frequencies (optical, X-ray), there are many challenges that accompany such studies at low frequencies (radio, sub-mm). In particular, it can be difficult to

81

disentangle intrinsic source variations from atmospheric or telescope gain variations (the radio sky at > 10 GHz is sparse enough that in-beam comparison sources will be rare), observations often involve routinely cycling between observing a target source and a calibrator, and in most cases only one frequency band can be sampled at a time. These obstacles prevent continuous observations of the jet and introduce artificial periodic signals in the data, both of which complicate time-domain analyses. Further, until recently, most telescopes were not sensitive enough, nor capable of taking the rapid data to probe second timescales. However, with today's more sensitive interferometric arrays, which also offer observing modes that allow for the use of sub-arrays, sub-second time resolution, and custom non-periodic target+calibrator scan design, we can lift the limitations presented above and accurately sample BHXB jets at radio frequencies in the time domain. Here we present new simultaneous, high time resolution, multi-band radio and X-ray observations of the compact jet in the BHXB Cygnus X-1, and perform a detailed study of rapid (probing second to hour timescales) compact jet variability at radio frequencies.

4.1.1   Cygnus X-1

Cygnus X-1 (hereafter Cyg X-1) is a high-mass X-ray binary (containing an O-type super-giant companion; Gies & Bolton 1986) discovered in the X-rays by the UHURU satellite in 1971 (Tananbaum et al., 1972). It is located at a distance of 1.86 ± 0.12 kpc[1] (Reid et al., 2011), with an orbital period of 5.6 d (Holt et al., 1979) and an inclination angle of 27.1 ± 0.8 degrees to our line of sight (Orosz et al., 2011). Cyg X-1 spends the majority of its time in a canonical hard accretion state (e.g., Ling et al. 1983; Miyamoto et al. 1992; Wilms et al. 2006; Zdziarski et al. 2002; Grinberg et al. 2013), where the radio through sub-mm spectrum is very flat ($f_\nu \propto \nu^\alpha$, where $\alpha \simeq 0$), displaying an average

---

[1]Note that there is a discrepancy between this radio parallax distance and the *Gaia* DR2 distance of 2.37 ± 0.18 kpc (Gaia Collaboration et al., 2018; Gandhi et al., 2018).

flux density of ~ 15 mJy (Fender et al., 2000). Although, Cyg X-1 has shown small-scale radio frequency variability, with amplitudes up to 20–30% of the average flux density, on timescales of hours to months. The shorter timescale variability (hours–days) is thought to be linked to changes in the mass accretion rate, while the longer timescale variability (months) has been attributed to jet precession, and orbital modulation originating from variable absorption by the stellar wind of the companion star (Pooley et al., 1999; Brocksopp et al., 2002; Gleissner et al., 2004; Nipoti et al., 2005; Pandey et al., 2006; Wilms et al., 2007). The hard state radio jet in Cyg X-1 has been resolved along the jet axis out to scales of $\sim$15 mas at 8.4 GHz (Stirling et al., 2001), but has not been resolved in the direction perpendicular to the jet flow, constraining the jet opening angle to be < 2 degrees.

Cyg X-1 is also known to be strongly variable in the X-rays during the hard state (fractional rms 40–50%), showing power on a large range of Fourier frequencies from mHz to over 100 Hz (Pottschmidt et al., 2003). Despite the extended time Cyg X-1 spends in the hard state, the source has been known to make occasional transitions to a softer accretion state, where it was in such a soft state (with no compact jet) from 2010 until late 2015 (Grinberg et al., 2011, 2014, 2015).

In 2016 February, while Cyg X-1 was in a well-established hard accretion state, we obtained simultaneous, high time resolution, multi-band radio and X-ray observations with NSF's Karl G. Jansky Very Large Array (VLA) and NASA's Nuclear Spectroscopic Telescope Array (*NuSTAR*). In §4.2 we describe the data collection and reduction processes. In §4.3 we present high time resolution light curves, cross-correlation functions, and Fourier domain analyses of the radio and X-ray emission we detect from Cyg X-1. In §4.4 we discuss the time domain properties of the jet emission from Cyg X-1 and place constraints on jet speed, geometry, and size scales. A summary of the results is presented in §4.5.

4.2 Observations and data analysis

4.2.1 VLA radio observations

Cyg X-1 was observed with the VLA (Project Code: 16A-241) on 2016 February 11, for a total on-source observation time of 2.7 hours. The array was in the C configuration at the time of our observations, where we split the full array into 2 sub-arrays of 13 and 14 antennas. Observations in each sub-array were made with the 8-bit samplers in S $(2 - 4\,\mathrm{GHz})$ and X $(8 - 12\,\mathrm{GHz})$ band. Each band was comprised of 2 base-bands, with 8 spectral windows of 64 2-MHz channels each, giving a total bandwidth of 1.024 GHz per base-band. We chose to use the $2 - 4\,\mathrm{GHz}$ and $8 - 12\,\mathrm{GHz}$ bands, as they provide pairs of widely separated base-bands, allow us to avoid the difficulties of observing at higher frequencies, and act as a compromise between high frequencies that probe closer to the black hole, and lower frequencies that are more sensitive with the VLA. The sub-array setup allows us to push to smaller correlator dump times than would be possible if we were utilizing the full array. In these observations, we set a 0.25-second correlator dump time, providing the highest time resolution possible, while staying within the standard $25\,\mathrm{MB\,s^{-1}}$ data rate limit. Further, we implemented a custom non-periodic target+calibrator cycle for each sub-array. This custom cycle began with 30 minutes for the dummy setup scan and standard calibration in two bands. Following this standard calibration, each sub-array alternated observing Cyg X-1 and calibrators, such that we obtained uninterrupted data of Cyg X-1 in the $8 - 12\,\mathrm{GHz}$ band for the first 75 minutes of the observations, and uninterrupted data of Cyg X-1 in the $2 - 4\,\mathrm{GHz}$ band for the second 75 minutes of the observations (with sparser coverage of the second band across each 75-min period). We hand-set target+calibrator scans to between 9 and 15 minutes (with approximately logarithmic separation). Flagging, calibration and imaging of the data were carried out within the Common Astronomy Software Application package (CASA

v5.1.2; McMullin et al. 2007) using standard procedures outlined in the CASA Guides[2] for VLA data reduction (i.e., a priori flagging, setting the flux density scale, initial phase calibration, solving for antenna-based delays, bandpass calibration, gain calibration, scaling the amplitude gains, and final target flagging). We used 3C48 (J0137+331) as a flux/bandpass calibrator and J2015+3710 as a phase calibrator. To obtain high time resolution flux density measurements, we utilized our custom CASA variability measurement scripts[3], where flux densities of the source in each time bin were measured by fitting a point source in the image plane (with the `imfit` task). When imaging each time bin we used a natural weighting scheme to maximize sensitivity and did not perform any self-calibration. Note that we only analyze radio light curves on timescales as short as 1 sec in this work (despite the 0.25 sec time resolution), as we found no significant power on sub-second timescales (see §4.3.3.1). Additionally, to check that any variability observed in these Cyg X-1 radio frequency light curves is dominated by intrinsic variations in the source, and not due to atmospheric or instrumental effects, we also ran our calibrator sources through these scripts (see Appendix 4.6.1 for details).

4.2.2 NuSTAR X-ray observations

Cyg X-1 was observed with *NuSTAR* (Harrison et al., 2013) on 2016 Febuary 11, for a total exposure time of 13.5 ks (ObsID 90101020002). The *NuSTAR* telescope consists of two co-aligned focal plane modules; FPMA and FPMB. The data were reduced using the *NuSTAR* data analysis software (NUSTAR-DAS v1.8.0) within the HEASOFT software package (v6.22[4]) following standard procedures[5]. We first used the `nupipeline` task to filter the observations for

---

[2]https://casaguides.nrao.edu

[3]These scripts are publicably available on github; https://github.com/Astroua/AstroCompute_Scripts

[4]http://heasarc.nasa.gov/lheasoft/

[5]*NuSTAR* data analysis procedures are detailed at https://heasarc.gsfc.nasa.gov/docs/nustar/analysis/

passages through the South Atlantic Anomaly and produce cleaned event files. Then we extracted light curves from both FPMA and FPMB using a circular region with a 60 arcsec radius centred on the source. Similarly, background light curves were extracted from an 100 arcsec radius circular region centred on a source-free region on each detector. Lastly, the HEASOFT task `lcmath` was used to create final background subtracted light curves. Note that we extracted light curves in the 3–10 keV, 10–30 keV, 30–79 keV, and full 3–79 keV energy bands, on time scales as short as 1 sec (matching our radio observations; see §4.2.1), for the analysis presented in this paper.

4.3 Results

4.3.1 Light curves

Simultaneous radio and X-ray frequency light curves of Cyg X-1 taken with the VLA and *NuSTAR* are shown in Figure 4.1 (also see Figure 4.8). In the radio light curves, the flux density ranges from 12–19 mJy, with the average flux density at all frequencies ~ 15 mJy (as expected from historical observations of the source; Pooley et al. 1999; Fender et al. 2000; Brocksopp et al. 2002). However, we also observe structured variability in the radio light curves, in the form of small amplitude flaring events, on top of smoother, longer-timescale variations. For example, the largest flare detected at 11 GHz (~ 20:06 UT) rises from ~ 14 mJy to a peak flux of ~ 19 mJy ($\sim 30\%$ of the average flux density) over a timescale of ~ 12 min. This large flare is asymmetric in shape, showing a secondary peak ~ 30 min after the main peak. Similarly, in the X-ray light curves we also observe a couple of small flares (e.g., at ~ 17:55 UT, ~ 19:25 UT), all of which precede the radio flaring activity.

Through comparing the emission we observe in the different radio bands, the lower frequency emission appears to lag the higher frequency emission (with the lag increasing as the frequency decreases). Additionally, the variability in

86

the 2/3 GHz light curves appears to be of lower amplitude and much more smoothed out when compared to the 9/11 GHz light curves. This emission pattern is consistent with what we expect from a compact jet, where the higher frequency emission originates in a region with a smaller cross-section closer to the black hole, while the lower frequencies probe emission from larger regions farther downstream in the jet flow.
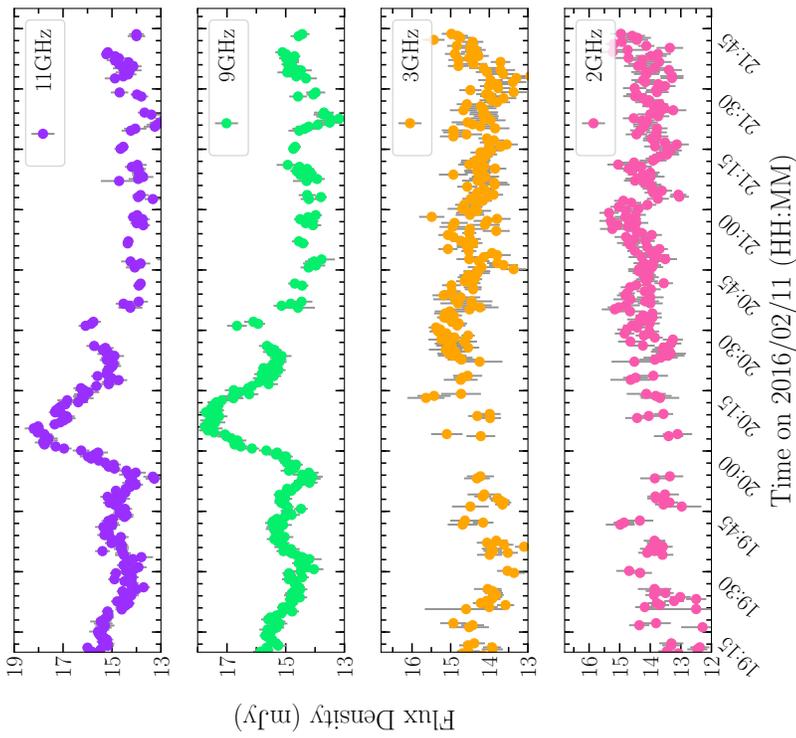
Figure 4.1: Multi-frequency light curves of the BHXB Cyg X-1 (with 30 sec time-bins). The *left* panels display *NuSTAR* X-ray light curves in three different energy bands, while the *right* panels display VLA radio light curves in four different frequency bands. The gray shading in the *left panel* represents the period of overlap between the VLA and *NuSTAR* observations, where simultaneous X-ray and radio data was obtained. The *NuSTAR* light curves displayed here are a zoomed in version of the full light curves, shown in Figure 4.8 in Appendix 4.6.2. We observe flux variability in both the radio and X-ray light curves, in the form of small-scale flaring activity. The radio variability appears to be of lower amplitude and more smoothed out in the lower frequency bands.

4.3.2 Cross-Correlation Functions

The morphology of our Cyg X-1 light curves hints at a potential correlation between the emission within the radio bands, and between the radio and X-ray bands. To characterize any correlations and place estimates on time-lags between the bands, we computed cross-correlation functions (CCFs) of our light curves using the z-transformed discrete correlation function (ZDCF; Alexander 1997, 2013). The ZDCF algorithm is designed for analysis of unevenly sampled light curves[6], improving upon the classic discrete correlation function (DCF; Edelson & Krolik 1988) or the interpolation method (Gaskell & Peterson, 1987). The calculated CCFs are displayed in Figure 4.2.

The location of the CCF peak will indicate the strongest positive correlation, and thus the best estimate of any time-lag between the light curves from different frequency bands. To estimate the CCF peak with corresponding uncertainties, we implement the maximum likelihood method of Alexander (2013). We note that this method estimates a fiducial interval rather than the traditional confidence interval. The approach taken here is similar to Bayesian statistics, where the normalized likelihood function (i.e., fiducial distribution) is interpreted as expressing the degree of belief in the estimated parameter, and the 68% interval around the likelihood function's maximum represents the fiducial interval. Additionally, to estimate the significance level of any peak in the CCF, we perform a set of simulations allowing us to quantify the probability of false detections in our CCFs, by accounting for stochastic fluctuations and intrinsic, uncorrelated variability within each light curve. For these simulations, we randomize each light curve 1000 times (i.e., Fourier transform the light curves, randomize the phases, then inverse Fourier transform back, to create simulated light curves that share the same power spectra as the real light

---

[6]Note that we utilize the full radio light curves, not just the continuous data chunks (as is done for the Fourier analysis in §4.3.3), to create the CCFs, as the ZDCF algorithm can handle unevenly sampled data.

curves) and calculate the CCF for each randomized case. We then determine the 95% and 99% significance levels based on the fraction of simulated CCF data points (at any lag) above a certain level.

Our calculated CCFs (Figure 4.2) suggest the presence of a correlation between both the X-ray and radio emission from Cyg X-1, as well as between the emission in the individual radio bands. In particular, we measure a time lag between the 3–79 keV X-ray and the 11 GHz radio bands of $33.5^{+1.9}_{-1.7}$ min, and time lags between the 11 GHz and 9, 3, 2 GHz radio bands of $1.0^{+0.9}_{-0.3}$ min, $24.1^{+1.6}_{-1.3}$ min, and $27.6^{+3.0}_{-0.7}$ min, respectively (although see below for caveats on the 11/3 GHz and 11/2 GHz lag measurements). With these lags, we observe a trend with frequency, where the lower frequency bands always lag the higher frequency bands (and the lag increases as the frequency decreases in the comparison band). This trend is consistent with what we expect from emission originating in a compact jet, where the lags presumably trace the propagation of material downstream along the jet flow (from higher frequencies to lower frequencies; Malzac et al. 2003; Gandhi et al. 2008; Casella et al. 2010; Gandhi et al. 2017). We also split the 8-12 GHz radio data into four sub-bands (centered on 8.75, 9.25, 10.75 and 11.25 GHz) and re-ran our CCF analysis. However, the measured lags we obtain are all consistent with each other within uncertainties. Thus we do not gain any new information through splitting our radio data into finer frequency bands and do not report on that data hereafter.

We note that when comparing the 3–79 keV/11 GHz and 11 GHz/9 GHz bands, the CCFs show relatively symmetric peaks at the measured time lag, both of which reach or exceed the 99% significance level. Therefore, we consider these detected time lags statistically significant, and are confident they are tracking a real correlation between the light curves. On the other hand, when comparing the 11 GHz/3 GHz and 11 GHz/2 GHz bands, the CCFs display much more complicated structure, including secondary peaks and anti-correlation dips at negative lags. While the measured time lag peaks represent

significant correlations (i.e., reach or exceed the 99% significance level), the secondary peaks can at times reach a lower, but still significant level (e.g., peak at ~ 10 min when comparing 11 GHz/3 GHz, or peak at ~ 50 min when comparing 11 GHz/2 GHz), and the anti-correlation dips can reach levels more significant than our positive lag peaks. Even though the measured 11 GHz/3 GHz and 11 GHz/2 GHz radio lags are physically plausible in terms of what we may expect from compact jet emission, the statistics and data structure do not conclusively back up these lag measurements. Therefore, for the remainder of this paper we opt to take a Bayesian approach, whereby we consider the negative lags as unphysical, and take our measured lags to be the best estimate of the true lags between these radio bands. Although, the reader should keep these caveats in mind when considering the 11/2 GHz and 11/3 GHz lag interpretations moving forward. Lastly, an important technical caveat to note in all our CCF calculations is that we are calculating the CCFs up to delays that are comparable to the duration of the data set (i.e., outside the stationarity limit). As the CCF is formally defined only on the assumption of stationarity, we are pushing the CCF method to its limits. We thus choose to remain conservative in our claims of time lag detections in this paper given these statistical limitations of our methods.

In the literature, there exist a few studies reporting on X-ray/radio correlations on short (minute) timescales in Cyg X-1. In particular, Gleissner et al. 2004 found no statistical evidence for correlations between X-ray and radio emission in Cyg X-1 on timescales < 5 hours, suggesting that any possible correlations they observed were consistent with artifacts of white noise statistics. The significance level simulations we performed in this paper rule out our correlations being statistical artifacts. Further, the radio frequency data used in the Gleissner et al. 2004 study was obtained with the Ryle Telescope, which was much less sensitive than the current VLA (the VLA has more antennas with larger dishes). Therefore, our study is able to measure lower level signals,

giving us better statistics in our CCFs when compared to the Gleissner et al. 2004 study. Additionally, Wilms et al. 2007 report the detection of an X-ray/15 GHz lag of ~ 7 min, which is significantly lower than the measured ~ 33 min X-ray/11 GHz lag reported in this work. However, we note that the Wilms et al. 2007 data sampled Cyg X-1 during a transition from the soft to the hard accretion state, and displayed different flare morphology (e.g., a higher amplitude of ~ 4 times the average flux level and a much more symmetric radio flare shape) when compared to our data. The jet emission in BHXBs during these accretion state transitions is often dominated by emission from discrete jet ejections (typically characterized by higher amplitude, more symmetric radio flares; e.g., Tetarenko et al. 2017), rather than a compact jet (as seen in the hard state). Therefore, the difference between these measured time lags could be due to both studies sampling a different form of jet emission with different properties (e.g., bulk speeds, opening angles, energetics). Alternatively, in either study it is possible that the pairs of correlated X-ray/radio flares were misidentified, and are in turn not actually correlated (e.g., it is possible that additional X-ray flares occur within the orbital gaps in the data, and see for example Capellupo et al. 2017 who show it can be difficult at times to know whether X-ray/radio flares are truly connected).
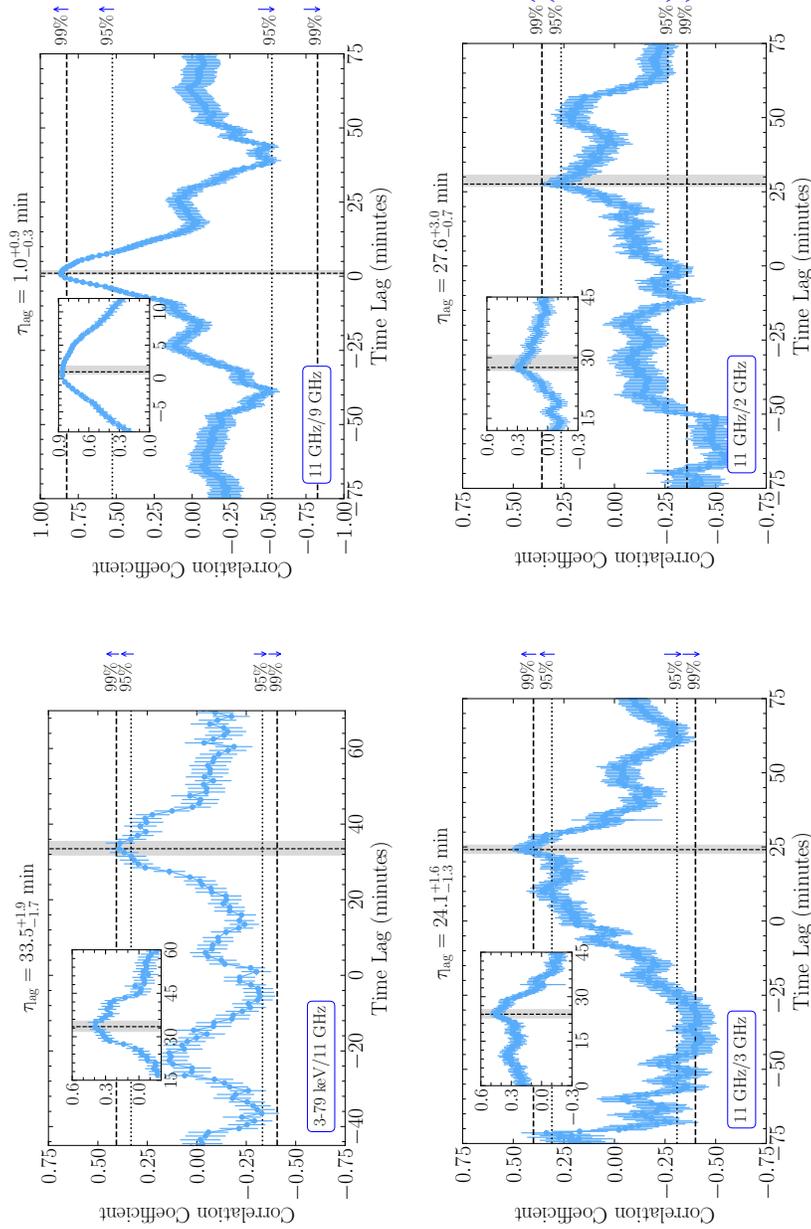
Figure 4.2: Cross-correlation functions (CCFs) between X-ray and radio emission from Cyg X-1; between 3–79 keV/11GHz (*top left*), 11GHz/9GHz (*top right*), 11GHz/3GHz (*bottom left*), and 11GHz/2GHz (*bottom right*). All CCFs displayed here are created with 30 sec time-bin data. The peak of each CCF (indicating the strongest positive correlation at τ_{lag}) is shown by the black dotted line, with the 68% fiducial confidence interval indicated by the shaded grey region, and 99/95% significance levels indicated by the black dashed/dotted lines (see §4.3.2 for details). The insets in each panel display a zoomed view of the region surrounding the peak of each CCF. A positive time lag indicates that the lower frequency band lags behind the higher frequency band. Through taking a Bayesian approach (whereby negative lags are considered unphysical; see §4.3.2), we measure time lags between the X-ray and radio bands, as well as between the individual radio bands, ranging from minutes to tens of minutes.

93

4.3.3   Fourier Analyses

To better characterize the variability properties of our radio frequency light curves of Cyg X-1, we opted to also perform Fourier domain analyses. As part of these analyses, we calculate the power spectral density (PSD), as well as perform cross-spectral analyses, allowing us to characterize lag and correlation behaviour across many distinct timescales of variability (Vaughan & Nowak, 1997; Uttley & Casella, 2014). While Fourier domain analysis is common practice at higher frequencies (infrared, optical, X-ray; Gandhi et al. 2008; Casella et al. 2010; Vincentelli et al. 2018), previous studies of this nature in the radio bands are limited (e.g., see Nipoti et al. 2005, probing timescales as short as days only). Here we present the first Fourier domain study of an BHXB (including a cross-spectral analysis) undertaken at radio frequencies on timescales as short as seconds. We utilize the STINGRAY software package[7] (Huppenkothen et al., 2016) for all of our Fourier domain analysis below.

4.3.3.1   Power Spectra

To create our radio PSDs, we consider only the continuous chunks of data in each radio light curve (i.e., first ∼75 min at 9/11 GHz and second ∼75 min at 2/3 GHz), and divide the light curves into 15 min segments, averaging them to obtain the final PSD. The segment size was chosen to reduce the noise in the PSDs. Further, a geometric re-binning in frequency was applied (factor of $f = 0.3$, where each bin-size is $1 + f$ times larger than the previous bin size) to reduce the scatter at higher Fourier frequencies. All our PSDs are normalized using the fractional rms-squared formalism (Belloni & Hasinger, 1990) and white noise has been subtracted (white noise levels were estimated by fitting a constant to Fourier frequencies above 0.05 Hz & 0.01 Hz for the 9/11 GHz & 2/3 GHz bands, respectively; see Appendix 4.6.3). Note that PSDs in the

---

[7]`https://stingray.readthedocs.io/en/latest/`

9/11 GHz bands are created from data imaged with 1 sec time-bins, while the 2/3 GHz PSDs are created from data imaged with 5 sec time-bins[8]. We utilize a different imaging timescale between radio bands to roughly match the rms noise in each time-bin's image across the bands, while still leaving enough of a Fourier frequency lever arm to accurately measure the white noise level. To create our X-ray PSDs, we follow the same averaging and binning procedure as the radio PSDs (additionally making use of the good time interval feature[9] of the STINGRAY package to take into account the orbital gaps in the data) and use frequencies above 0.4 Hz to estimate the white noise level. Figure 4.3 displays the radio PSDs, while Figure 4.4 displays the X-ray PSDs.

The radio PSDs all appear to display a power-law type shape, where the highest power occurs at the lowest Fourier frequencies (corresponding to the longest timescales sampled) and no significant power is observed at Fourier frequencies above ~ 0.03 Hz (~ 30 sec timescales). Additionally, we observe a trend where the PSDs from the higher frequency radio bands display larger power when compared to the lower frequency radio bands on the longer timescales (where the larger uncertainties make it difficult to compare the power between the radio bands on smaller timescales/higher Fourier frequencies). These observed PSD features fit with our compact jet picture, where we expect higher radio frequencies to display larger variability amplitudes and the highest Fourier frequency variations to be more suppressed, due to the increasing size scale of the emitting region at radio frequencies (when compared to the X-ray) smearing the variability signal. In fact, VLBI imaging of Cyg X-1 (Stirling et al., 2001) suggests jet cross-sections at 8.4 GHz of $< 3.1 \times 10^{13}$

---

[8]The maximum frequency for Fourier analysis is equivalent to half the resolution of our light curves, or the Nyquist frequency of $\nu_{\mathrm{N}} = \frac{1}{2} t_{\mathrm{res}}^{-1} = 0.5/0.1$ Hz for the 9/11GHz and 2/3GHz PSDs, respectively.

[9]This good time interval (GTI) feature computes the start/stop times of equal time intervals, taking into account both the segment size (timescale over which the individual PSDs are averaged together) and the GTIs. This "time mask" (array of time stamps) is then used to start each FFT from the start of a GTI, and stop before the next gap in the data (end of GTI).

cm, which is consistent with the light crossing times of the shortest timescales for which we detect significant power (in ~ 30 sec a signal propagating at the speed of light travels 1×10^{12} cm)[10].

The X-ray PSDs also appear to display a power-law type shape at lower Fourier frequencies (< 0.01 Hz), then flatten out at higher Fourier frequencies, with a turnover occuring at ~ 0.3 Hz. No quasi-periodic oscillations are observed, although we do observe a bump around ~ 0.008 Hz (this X-ray PSD shape is consistent with previous studies; e.g., Nowak et al. 1999). Interestingly, when comparing the X-ray and radio PSDs, we find that the X-ray PSDs show similar power at the lowest Fourier frequencies (longest timescales) as the highest frequency radio band PSDs. This feature was also seen at Fourier frequencies as low as $\sim 10^{-6} - 10^{-7}$ Hz by Nipoti et al. (2005) in their earlier, longer timescale study (and notably was a unique feature to Cyg X-1, not observed in the long timescale radio PSDs of other XB sources; GRS 1915+105, Cyg X-3, and Sco X-1). However, the X-ray emission is significantly more variable overall, displaying an integrated fractional rms (across the 0.001 to 0.5 Hz range) of $\sim 20\%$, while all the radio bands show $\sim 2 - 7\%$.

---

[10]For a conical jet, the jet cross-section at distance z_0 from where the jet is launched is represented by $z_{\mathrm{cross}} = z_0 \tan \phi$, where ϕ is the jet opening angle. VLBI imaging of Cyg X-1 (where the jet is observed out to ~ 15 mas scales, along a jet axis inclined to our line of sight by ~ 27 degrees; Stirling et al. 2001) suggests $z_0 \sim 8.9 \times 10^{14}$ cm at 8.4 GHz and opening angles of < 2 degrees, corresponding to a cross-section at 8.4 GHz of $< 3.1 \times 10^{13}$ cm).
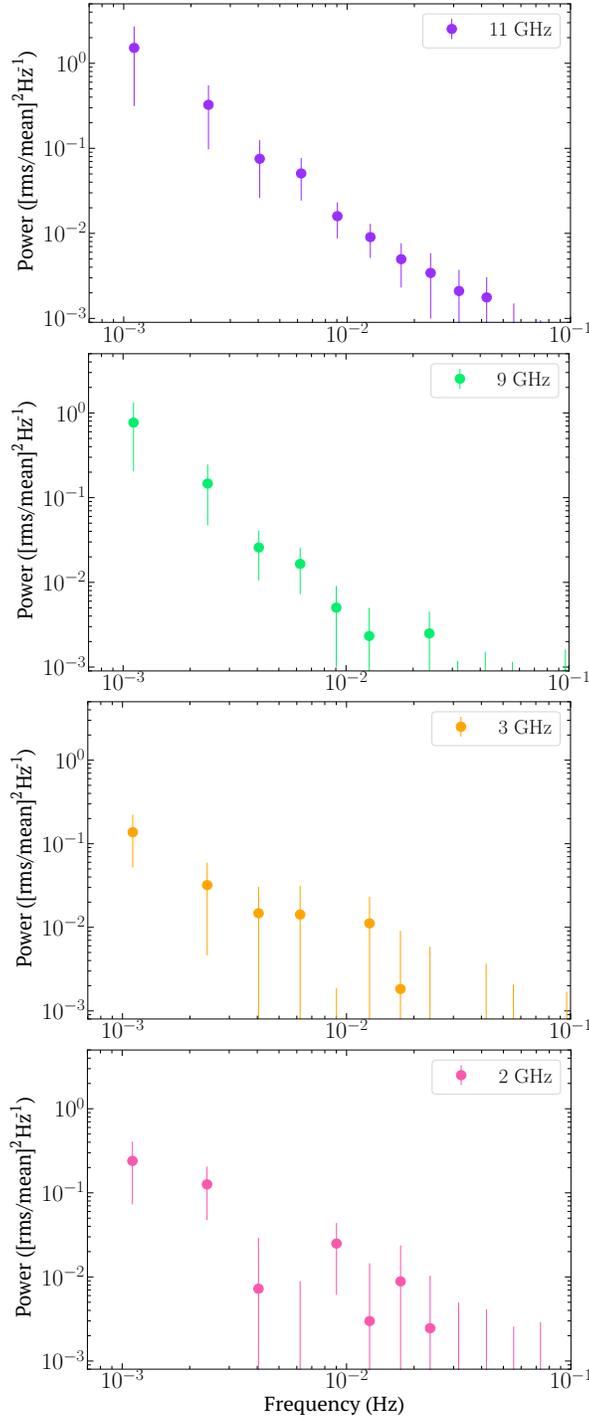
Figure 4.3: White noise subtracted radio PSDs of Cyg X-1. Top to bottom, the panels display the power spectra from the 11, 9, 3, and 2 GHz bands. The PSDs in the 9/11 GHz bands are created from data imaged with 1 sec time-bins, while the 2/3 GHz PSDs are created from data imaged with 5 sec time-bins. While all the radio bands display a similar PSD shape (decreasing power at higher Fourier frequencies), when considering the longest timescales, we observe higher power in the higher frequency radio band PSDs. Note that the pre-white noise subtracted PSDs are shown in Figure 4.9.

97
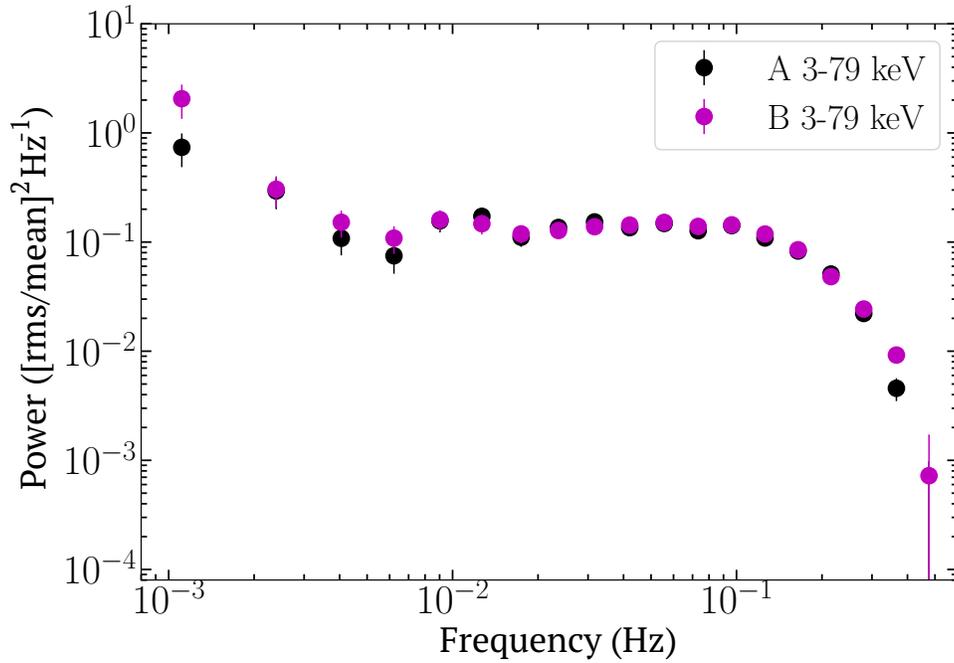
Figure 4.4: White noise subtracted X-ray PSDs of Cyg X-1 in the 3–79 keV band. These power spectra are created from data with 1 sec time-bins (matching our radio frequency light curves). PSDs for the two *NuSTAR* modules are shown separately (FPMA represented by the black markers, FPMB represented by the magenta markers). The X-ray PSDs show a clear turnover at higher frequencies (~ 0.3 Hz), and no quasi-periodic oscillations are observed.

4.3.3.2   Cross Spectra

Through a cross-spectral analyses we can examine the causal link between two time series signals. For this analysis we only consider the segments of the respective radio light curves for which we have continuous data with no scan gaps (as was done in creating our PSDs) and use the same averaging/binning procedure as described for the PSDs. Further, we only compare the signals we observe between the two-basebands in each VLA frequency band (i.e., between 9 and 11 GHz, and between 2 and 3 GHz), as our observational setup only allowed for the simultaneous, continuous observations needed for such an analysis between these radio frequencies.

Figure 4.5 displays the results of our cross spectral analyses, where we show three different metrics used to quantify the causal relationship between the two time series signals: phase lags, time lags, and coherence. The lags describe the phase/time differences between intensity fluctuations for each Fourier frequency component, while the coherence is a measure of the fraction of the rms amplitude of one signal (at a given Fourier frequency) that can be predicted from the second signal through a linear transform (i.e., the degree of linear correlation between the two signals as a function of Fourier frequency).

When considering the higher frequency radio bands (9/11 GHz), we observe a high level of coherence on longer timescales ($f < 0.005$ Hz), which drops to ~ 0.25 at ~ 0.005 Hz, then to a point where no significant correlation is detected above ~ 0.05 Hz. Additionally, we observe a relatively constant trend in the phase lags, corresponding to a mostly constant time lag of a few tens of seconds, across Fourier frequencies up to ~ 0.01 Hz (although we do note that there is some scatter in the time-lags at ~ 0.005 Hz). These time lags are consistent with the lower end of the confidence interval estimated from our CCF measured lag of $1.0^{+0.9}_{-0.3}$ min, within the uncertainty limits. However, when considering the lower frequency radio bands (2/3 GHz), we observe very little coherence, even on the longer timescales (~ 0.25 at 0.001 Hz, but coherence consistent

with zero within the large uncertainties). Further, there is no clear trend in the phase lags, and the time lags are mostly consistent with zero. However, despite the large uncertainty, the time lag in the lowest Fourier frequency bin is consistent with what we might expect from our CCF measured lags of ~ 3 min.
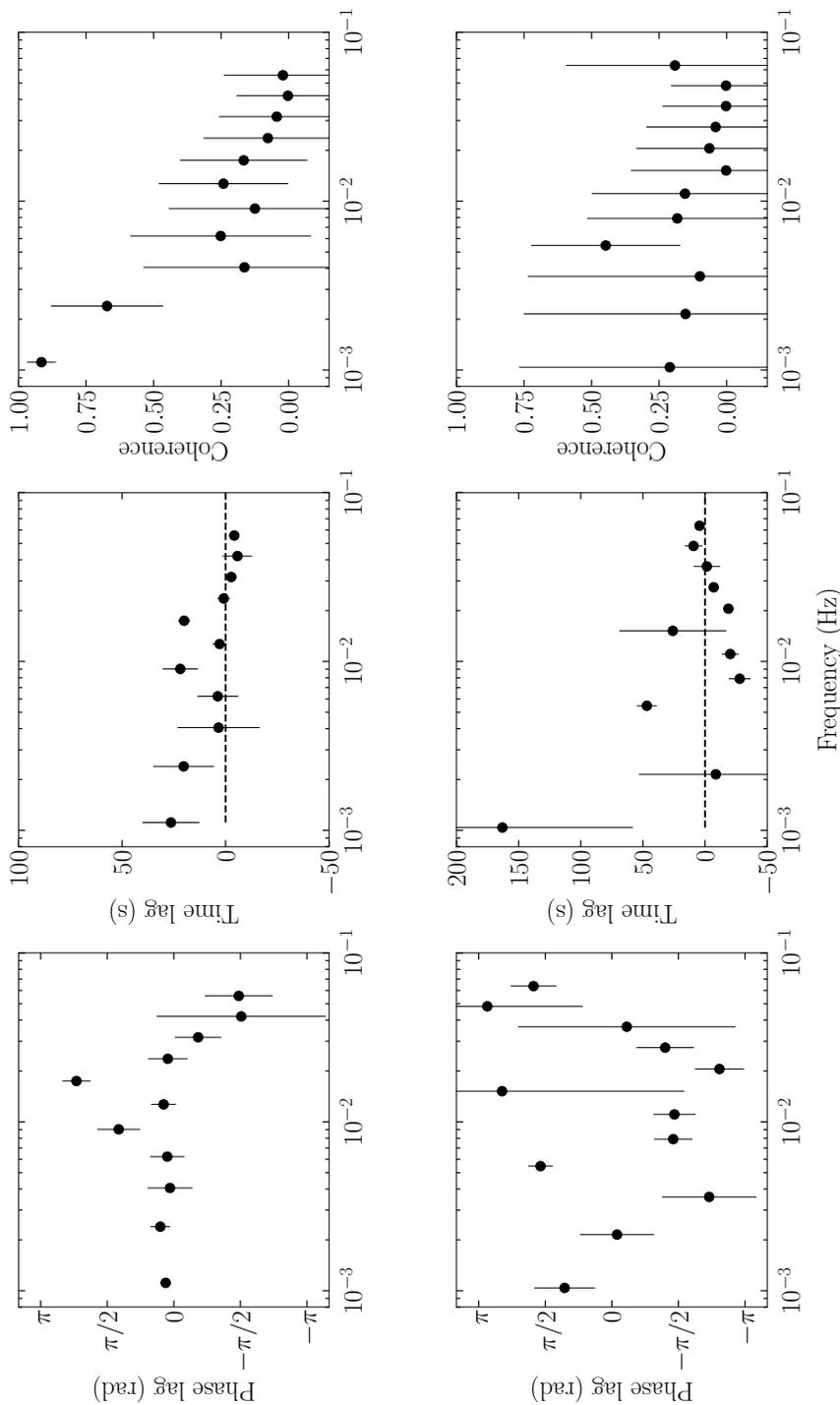
Figure 4.5: Cross-spectral analysis of radio emission from Cyg X-1. The *top* three panels display a cross-spectral analysis between the 9/11 GHz bands (using 1 sec time-bin data), while the *bottom* three panels display a cross-spectral analysis between 2/3 GHz bands (using 10 sec time-bin data, to further increase the signal to noise when compared to the 5 sec time-bin data used in the PSD procedure for these bands). Left to right, the panels display phase lags, time lags, and coherence. Positive lags indicate that the lower frequency band lags the higher frequency band, and a time lag of zero is indicated by the black dashed line in the *middle* panels. The higher frequency radio bands (*top*) show high levels of coherence and near constant time-lags on the longer timescales (Fourier frequencies < 0.01 Hz), while the lower frequency radio bands (*bottom*) comparatively show very little coherence across all time scales.

4.4 Discussion

To characterize the variability properties of the compact jet emission in the BHXB Cyg X-1, we have performed a time domain analysis on multi-band VLA radio and *NuSTAR* X-ray observations of this system. We implement several different metrics in our analysis; cross-correlation functions, PSDs, and cross-spectral analysis. In the following sections, we discuss what each of these metrics reveals about the jet variability properties and how these variability signals propagate down the jet. Additionally, we derive constraints on jet speed, geometry, and size scales.

4.4.1 Interpreting PSDs, lags, and coherence

The X-ray and radio PSDs presented in Figures 4.3 and 4.4 show remarkably similar power on the longest timescales, but display very different shapes. In particular, the radio bands display a monotonically decreasing trend with frequency (where there is no significant power at Fourier frequencies above ~ 0.03 Hz), while the X-ray band displays a double power-law type shape that turns over at ~ 0.3 Hz. In previous BHXB jet variability studies performed at higher frequencies (Gandhi et al., 2008; Casella et al., 2010; Vincentelli et al., 2018), infrared and optical PSDs of compact jet emission displayed a similar shape to our X-ray PSDs, where a break is observed at higher Fourier frequencies ($\sim 3/1$ Hz at optical/infrared bands in GX 339-4). This damping of the power at higher Fourier frequencies is thought to reflect the physical size scale of the emitting region. Therefore, we might expect any break in the radio PSDs to occur at lower Fourier frequencies than we can probe with our data set (e.g., a VLBI transverse size scale estimate of $< 3.1 \times 10^{13}$ cm at 8.4 GHz gives a light crossing time of ~ 1100 sec or $< 9 \times 10^{-4}$ Hz; and see Figure 6 in Malzac 2014 where theoretical jet models also predict this PSD shape). In the Fourier analysis of Nipoti et al. 2005, who probed much longer timescales than

our study (days-months), the radio PSD shows a higher power (at all sampled Fourier frequencies) when compared to our PSDs, that is nearly constant at Fourier frequencies between $10^{-6} - 10^{-5}$ Hz. Therefore, this is suggestive of a break in the radio PSDs occurring in the un-sampled Fourier frequency range ($10^{-5} - 10^{-3}$ Hz). If this is the case, the radio PSDs we present here could be sampling the drop off in power after a lower Fourier frequency turnover. A set of longer radio observations (sampling the $10^{-5} - 10^{-3}$ Hz Fourier frequency range) and/or observations at higher radio/sub-mm frequencies are needed to confirm this theory, and test whether there is a frequency dependent trend in the location of this turnover across different radio bands (as suggested between the infrared/optical PSD turnovers observed in GX 339-4). Measuring such a trend could (in principle) be used to map out the jet size scale in different regions of the jet flow.

In our cross-spectral analysis, we observed that the higher frequency radio bands (9/11 GHz) were highly correlated on longer timescales (> 200 s; $f < 0.005$ Hz), and display a constant lag with Fourier frequency consistent with our CCF measured lag. However, in the lower frequency radio bands (2/3 GHz) we observed very little correlation across all timescales, and a lag consistent with our CCF analysis only in the lowest Fourier frequency bin. In the situation where one signal is related to the other through a delay, due to propagation of variability down the jet flow, we would expect both the coherence and time lags to be constant with frequency. While we observe constant time lags below a certain Fourier frequency in our analysis, the coherence either drops at higher Fourier frequencies (9/11 GHz) or is very low across all Fourier frequencies (2/3 GHz). Therefore, if the radio signals are related by a propagation type model, some other process must be damping the correlation at higher Fourier frequencies. In our radio signals, the coherence and radio variability amplitude (traced through the PSDs) appear to be damped over the same range of Fourier frequencies. Therefore, it seems plausible that the

drop in coherence traces the process whereby a higher frequency radio signal is both delayed and smoothed out (due to the larger cross-sectional area and the fact that emission at a given radio frequency band is coming from a range of distances in the jet) as it propagates down the jet to lower frequencies (we expect a smoothed signal to contain very little variability on shorter timescales and thus low levels of coherence). Additionally, on time scales shorter than the propagation time between the regions emitting our radio signals, mechanisms such as turbulence in the jet flow could also distort the variability signals (Gleissner et al., 2004). In BHXB jet variability studies performed at higher infrared frequencies (Vincentelli et al., 2018), a similar trend (constant time lags with Fourier frequency but a decreasing trend in coherence) was seen in the cross-spectral analysis. However, in the infrared bands there appears to be a different mechanism at work (when compared to our radio signals) that damps the correlation between signals, but does not affect the infrared variability amplitude (i.e., the PSD breaks at 1 Hz but the coherence begins to drop at lower Fourier frequencies).

Other factors could also be contributing to the loss of coherence between the radio signals. In particular, a strong noise component in the radio light curves may lead to a loss of coherence (as random noise signals are not correlated). To further investigate this possibility, we opted to compute the intrinsic coherence (using Equation 8 in Vaughan & Nowak 1997), which takes into account noisy signals by applying a correction term to the measured coherence. Through this computation, we find that the intrinsic coherence is nearly identical to the measured coherence at the Fourier frequencies for which the Vaughan & Nowak 1997 expression is valid (< 0.01 Hz). This suggests that the noise component in the radio light curves is not a significant cause of any loss of coherence we observe. However, we note that both the measured/intrinsic coherence measurements between the 2/3 GHz radio signals display large uncertainties. Therefore, the noise component appears to limit our ability to accurately calculate and com-

pare the intrinsic/measured coherence between the lower frequency (2/3 GHz) radio signals.

Alternatively, a loss of coherence could also occur if more than one source of emission contributes to the signals in these bands (even if individual sources produce coherent variability; Vaughan & Nowak 1997) or if the signals are acted on by a nonlinear process (e.g., internal shocks in the jet flow). For instance, the strong stellar wind from the companion star in Cyg X-1 has been shown to partially absorb the radio emission by up to about 10 % (Pooley et al. 1999; Brocksopp et al. 2002), and thus could potentially be distorting the radio signals we observe. While Brocksopp et al. (2002) showed that 2.25 GHz radio emission does not vary much around the orbit, implying that this lower frequency emission could originate outside the wind photosphere (see Figure 1 in Brocksopp et al. 2002), our observations were taken at an orbital phase where the black hole was behind a significant amount of the wind (orbital phase 0.88, where superior conjunction is at orbital phase 0). Therefore, we would expect the wind to have close to a maximal effect on the radio emission we observe during our observations. Further, Brocksopp et al. (2002) estimate the size of the wind photosphere to be $4.6 \times 10^{14}/1.8 \times 10^{14}$ cm at 2.25/8.3 GHz, which are both larger than the size scales to the radio emitting regions estimated from our CCF X-ray to radio lag estimates, suggesting that the stellar wind could reasonably be affecting our radio signals. The emission from the counter-jet (i.e., the portion of the bi-polar jet travelling away from the observer) could also be contaminating our radio signals. The ratio of the flux densities between the approaching and receding jets in Cyg X-1 can be estimated using $\frac{F_{\mathrm{app}}}{F_{\mathrm{rec}}} = \left(\frac{1+\beta\,\cos\theta}{1-\beta\,\cos\theta}\right)^{2-\alpha}$ (where β, θ, and α represent the jet speed, inclination angle of the jet axis to the line of sight, and the radio spectral index, respectively). However, given values of $\beta = 0.92$, $\theta = 27$ degrees, and $\alpha = 0$ (see §4.4.2), we find $\frac{F_{\mathrm{app}}}{F_{\mathrm{rec}}} \sim 102$, suggesting that any contributions from the counter-jet will likely be negligible in our radio signals. Further, the

emission in the radio frequency bands could have contributions from a region where the jet is colliding with the surrounding ISM. These regions can display a working surface shock at the impact point (e.g., Corbel et al. 2005; Miller-Jones et al. 2011; Yang et al. 2011; Rushton et al. 2017) and typically show brighter fluxes at lower radio frequencies, potentially contributing more to the overall observed emission in lower radio frequency bands (where we see increased loss of coherence). In the case of Cyg X-1, the jet is thought to have carved out a parsec scale cavity in the intervening medium ($\sim 2 \times 10^5$ AU; Gallo et al. 2005b; Russell et al. 2007; Sell et al. 2015, see also Chapter 8 §8.5.5 for more details), which may make further jet impact sites closer (less than the VLA beam of 7 arcsec or 10^4 AU at 1.86kpc) to the central source unlikely. However, we note that Cyg X-1 was in a soft accretion state (with presumably no jet) from 2010 to a few months prior to our observations in early 2016. Therefore, the strong stellar wind from the companion star could have had time during this soft state to refill at least a portion of this cavity, and the jets we observe could be interacting with this newly deposited material.

4.4.2 Constraints on jet properties

If the X-ray emission we observe originates[11] in a region close to the black hole (inner accretion flow or at the base of the jet) and information from X-ray emission regions propagates down the axis of the jet to the radio emission regions, then the distance between the radio emission regions and the black hole, z_{radio}, can be represented as,

$$z_{\mathrm{radio}} = \beta \, c \, \tau_{\mathrm{lag}} \, (1 - \beta \cos \theta)^{-1} \,. \tag{4.1}$$

Here, β represents the bulk jet speed (in units of v/c, where c indicates the speed of light), τ_{lag} represents the X-ray to radio time lag, and θ represents the inclination angle of the jet axis to our line of sight. Note that the term in parentheses indicates a correction factor due to the transverse Doppler effect (where the interval between the reception of two photons by the observer is smaller than the interval between their emission).

As we measured time lags between the X-ray and multiple radio bands, we can use Equation 4.1 to solve for the jet speed. Through rearranging Equation 4.1, and substituting in a metric to relate jet size scale to the radio frequency band[12] ($z \propto 1/\nu^{\epsilon}$), we obtain,

$$\tau_{\mathrm{lag}} = \frac{z_{\mathrm{norm}} \left(\frac{1}{\nu_{\mathrm{radio}}^{\epsilon}} - \frac{1}{\nu_{\mathrm{xray}}^{\epsilon}} \right) (1 - \beta \cos \theta)}{\beta \, c} \,. \tag{4.2}$$

Here ν_{radio} and ν_{xray} (set to 9.91×10^{9} GHz, indicating the middle of the X-ray

---

[11] If the X-ray emission originates from an accretion flow that is not co-spatial with the jet base, we may expect some additional time delay in getting the accreted material into the jet base, and subsequently accelerating this material. While these timescales are not known for BHXBs, if for example the jet is launched at 1000 gravitational radii from the black hole (Gandhi et al., 2017), this timescale could correspond to a light travel time delay of tens of milli-seconds. In this case, milli-second timescales are minuscule when compared to the tens of minutes delays we are discussing here. Further, if the X-ray variations originate in the accretion disc, we may expect an additional delay on the order of the viscous timescale for these variations to propagate inwards.

[12] While simple jet models predict $z \propto 1/\nu$ (Blandford & König, 1979), we allow for a more general case in our analysis.

band at 41 keV) represent the frequencies between which the time lags were measured. To normalize the jet size scale to radio frequency band relation, we can express z_{norm} in terms of the distance between the X-ray emitting region and the $\tau = 1$ surface (l_{norm} in angular units of mas projected on the sky) at a specific radio frequency (ν_{norm}), yielding,

$$z_{\mathrm{norm}} = (1.49 \times 10^{13}\,\mathrm{cm})\, \frac{l_{\mathrm{norm}}\, D_{\mathrm{kpc}}}{\sin\theta}\, (\nu_{\mathrm{norm}})^{\epsilon} \qquad (4.3)$$

Based on the VLBI images of Cyg X-1 presented in Stirling et al. 2001 at $\nu_{\mathrm{norm}} = 8.4$ GHz, we set a wide uniform prior on l_{norm} ranging from 0.01 mas to 15 mas (max distance to which jet emission was resolved in the VLBI images).

We fit Equation 4.2 to our measured X-ray/radio time lags using a Markov Chain Monte-Carlo (MCMC) algorithm (Foreman-Mackey et al., 2013). However, instead of fitting directly for β, we choose to fit for the bulk Lorentz factor, $\Gamma = (1 - \beta^2)^{-1/2}$, instead. This is because the MCMC algorithm performs better when there are not hard limits on model parameters (i.e., β can only have values between 0 and 1). In our MCMC runs, we allow Γ, ϵ, and l_{norm} to be free parameters, and sample from the known distance (1.86 ± 0.12; Reid et al. 2011)[13] and inclination ($\theta = 27.1 \pm 0.8$; Orosz et al. 2011) distributions. The best-fit result is taken as the median of the one-dimensional posterior distributions and the uncertainties are reported as the range between the median and the 15th percentile (-), and the 85th percentile and the median (+), corresponding approximately to 1σ errors. Our best-fit parameters are displayed in Table 4.1 and Figure 4.6.

---

[13]The reader is reminded that there is a discrepancy between this radio parallax distance used in these calculations and the *Gaia* DR2 distance of 2.37 ± 0.18 kpc (Gaia Collaboration et al., 2018; Gandhi et al., 2018).

Table 4.1: Best fit jet parameters for Cyg X-1

Parameter	Best-fit result
Γ	$2.59^{+0.79}_{-0.61}$
ϵ	$0.40^{+0.05}_{-0.05}$
l_{vlba} (mas)	$5.69^{+1.52}_{-1.62}$
$\beta^{\dagger}$	$0.92^{+0.03}_{-0.06}$

† β represents the bulk jet speed and is not a fitted parameter (see §4.4.2 for details). We instead fit for the bulk Lorentz factor, $\Gamma = (1 - \beta^2)^{-1/2}$, and estimate the distribution of the corresponding bulk jet speeds by performing Monte Carlo simulations sampling from the posterior Γ distribution 10000 times.
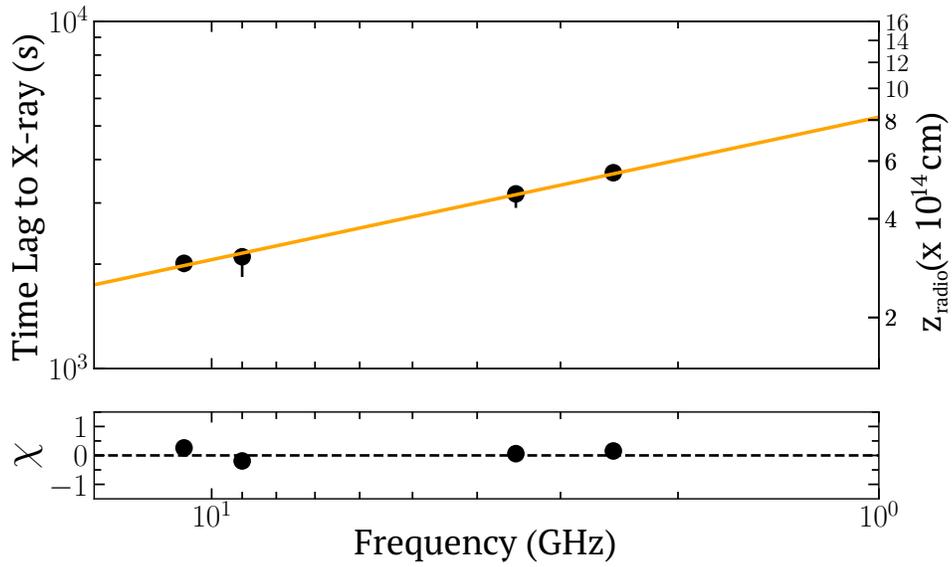
Figure 4.6: Time lags between the radio and X-ray bands, as a function of radio frequency. The *top* panel displays the time lag measurements from our CCFs (black markers), and our best-fit model (orange solid line). The *bottom* panel displays the residuals of the fit, where residual=(data-model)/(measurement errors). The right vertical axis indicates the corresponding jet size scale for the time lags on the left most vertical axis and our best-fit parameters (using Equation 4.1; units of $\times 10^{14}$ cm).

Prior to this study, the compact jet speed in BHXBs had never been directly measured (although Casella et al. 2010 have placed direct lower limits on the jet speed, see below). Past studies using indirect methods (e.g., scatter in radio/X-ray correlation, spread in accretion state transition luminosities; Gallo et al. 2003; Maccarone 2003; Gleissner et al. 2004) to infer limits on the compact jet speed, estimate that $\beta < 0.8$ (corresponding to a bulk Lorentz factor of $\Gamma < 2$). In turn, it is typically thought that compact jets are inherently less relativistic than the other form of jets detected in these systems, discrete jet ejecta (displaying bulk speeds as high as $\Gamma > 2$ measured through VLBI imaging; Hjellming et al. 2000b; Hjellming & Rupen 1995; Fender et al. 2009). However, Fender (2003) has shown that Γ depends strongly on the assumed distance to the source (which is not known accurately in most BHXBs), and Miller-Jones et al. (2006) show that if the jets are not externally confined, the intrinsic Lorentz factors of BHXB jets could be as high as in AGN (up to $\Gamma \sim 10$). The compact jet speed measurement we present here for Cyg X-1 shows a reasonably high bulk Lorentz factor of $\Gamma \sim 2.6$. Additionally, a previous study on the compact jet in GX 339-4 also presented potential evidence for similarily high bulk Lorentz factors inferred from infrared/X-ray lags ($\Gamma > 2$; Casella et al. 2010). Since the compact jet speed is likely to vary during an outburst (Fender et al., 2004a, 2009), it is possible that our Cyg X-1 jet speed measurement samples the jet speed at the high end of the distribution in this source (rather than the mean). In this sense, jet speed constraints from different stages of an outburst in a single BHXB source are needed to understand the degree to which compact jet speed can change during an outburst. Similarly, jet speed constraints for a number of sources are needed to constrain the distribution of compact jet speeds across the BHXB population (as well as help determine if Cyg X-1 is an outlier in terms of higher compact jet speed).

Moreover, our time lag modelling also reveals that the size scale as a function of radio frequency in the Cyg X-1 jet seems to deviate from the expected

$z \propto 1/\nu$ relationship predicted by simple jet models (Blandford & Königl, 1979). In particular, we find that a shallower relationship ($z \propto 1/\nu^{0.4}$) is needed to explain our observed time lags.

Further, for a conical jet, the opening angle can be estimated based on the axial and transverse size scales of the jet according to,

$$\phi = \tan^{-1}\left(\frac{z_{\mathrm{trans}}}{z_{\mathrm{axial}}}\right) \tag{4.4}$$

Therefore, through applying estimates of z_{axial} (via our measured time-lags) and z_{trans} (via timescales derived from our Fourier analysis that may trace the transverse jet size scale), we can use Equation 4.4 to place constraints on the opening angle of the Cyg X-1 jet. Considering the size scales in the region of the jet sampled by the 11 GHz radio band, Equation 4.1 yields $z_{\mathrm{axial}} = 3.1 \times 10^{14}$ cm, and we estimate $z_{\mathrm{trans}} = (0.1-1)\times10^{13}$ cm based on the smallest timescales over which we observe significant power in the PDS (0.03 Hz; see Figure 4.3) and the timescales at which we observe a significant drop in coherence in our 9/11 GHz cross-spectral analysis (0.003 Hz; see Figure 4.5). With these size scale estimates, we estimate the opening angle to be $\phi \sim 0.4 - 1.8$ degrees. This constraint is consistent with both the VLBI upper limit (< 2 degrees) and the work of Heinz (2006), the latter who present analytical expressions for jet parameters in Cyg X-1 (see Equation 9 of Heinz 2006 for the opening angle expression).

We reiterate that all the results in this section hinge on the accuracy of our time lag measurements (see §4.3.2 for a discussion on the uncertainty in the time lags for the lower frequency radio bands) and the assumption that the bulk jet speed is constant. Therefore, the reader is cautioned that, while our results are intriguing, they come with caveats.

4.5 Summary

In this paper, we present the results of our simultaneous multi-band radio and X-ray observations of the BHXB Cyg X-1, taken with the VLA and *NuS-TAR*. With these data, we extracted high time resolution light curves, probing timescales as short as seconds. The light curves display small amplitude flaring events, where the lower frequency radio emission appears to lag the higher frequency radio emission and any variability is much more smoothed out at the lowest radio frequencies. This emission pattern is consistent with emission from a compact jet, where higher radio frequencies probe closer to the black hole.

To better characterize the compact jet variability we observe in our light curves, and probe how this variability propagates down the jet, we performed timing analyses on our data, including Fourier domain analyses (PSDs and cross-spectral analyses between radio bands), as well as cross-correlation analyses. We summarize the key results of this analysis below.

Our radio PSDs show a monotonically decreasing trend with frequency, with no significant power at Fourier frequencies > 0.03 Hz (< 30 sec timescales). Over the Fourier frequencies that we sample, we do not observe a turnover in the radio PSDs, as was seen in recent studies analyzing infrared/optical PSDs of compact jet emission from the BHXB GX 339-4. However, upon comparing our radio PSDs to a past study probing longer timescales, we find that it is plausible that such a turnover in the PSDs could occur in the currently unsampled $10^{-5} - 10^{-3}$ Hz Fourier frequency range. As this turnover is thought to reflect the physical size scale of the emitting region in the jet, future studies with a set of longer (> 3 hours) radio observations present the opportunity to detect such a turnover, and in turn use it to map out the jet size scale in different regions of the jet flow.

Our cross spectral analyses reveals that the higher frequency radio bands

(9/11 GHz) are highly correlated over the same Fourier frequency range where we observe significant radio variability amplitude in our PSDs (Fourier frequencies < 0.01 Hz), and a roughly constant time-lag is observed with Fourier frequency between these bands. These results are consistent with a propagation model whereby the higher frequency radio signal is delayed and the variability at higher Fourier frequencies is smoothed out as the signal propagates down the jet. However, in the lower frequency radio bands (2/3 GHz) we observed very little correlation across all timescales. While this loss of coherence could be a result of the smoothing effect described above (which we expect to be more severe at the lowest radio frequencies), we discuss several other mechanisms that could also cause a loss of coherence: turbulence in the jet flow on timescales shorter than the propagation time between emitting regions, a strong noise contribution in the radio light curves, other sources of emission contributing to our radio signals (e.g., interaction with ISM, stellar wind absorption), and non-linear processes acting on the radio signals (e.g., shocks within the jet flow or at jet-ISM impact sites).

Our cross-correlation functions confirm the presence of a correlation between the radio and X-ray emission in Cyg X-1. We detect time lags of tens of minutes between the X-ray and radio bands, and use these measurements to solve for a jet speed of $\beta = 0.92^{+0.03}_{-0.06}$ ($\Gamma = 2.59^{+0.79}_{-0.61}$). Additionally, we also constrain how the jet size scale changes with frequency, finding a shallower relation than predicted by simple jet models ($z \propto 1/\nu^{0.4}$), as well as estimate the jet opening angle to be $\phi \sim 0.4 - 1.8$ degrees.

Overall, in this paper we have presented a detailed study of rapid compact jet variability (probing second to hour timescales) at radio frequencies in a BHXB. Our work here shows the power of time domain analysis in probing jet physics and displays the need for longer (> 3 hours) continuous observations of BHXB jets across a range of electromagnetic frequency bands (especially including > 11 GHz radio and sub-mm frequencies to bridge the gap to the

infrared/optical bands). The combination of the techniques and tools developed in this study, as well as the improved capabilities of planned next generation instruments (such as the ngVLA and ALMA-2030), will make more of these radio time domain studies possible, not just in BHXBs, but in other transient phenomena as well.

4.6 Appendix

4.6.1 Radio Calibrator Light Curves

Given the flux variations we detected in our VLA radio frequency data of Cyg X-1, we wished to check the flux calibration accuracy of all of our observations on short timescales and ensure that the variations observed in Cyg X-1 represent intrinsic source variations rather than atmospheric or instrumental effects. Therefore, we created time resolved light curves of our calibrator source (see Figure 4.7).

We find that our calibrator source displays a relatively constant flux throughout our observations in all the sampled bands, with any variations ($<1\%$ of the average flux density at all bands[14]) being a very small fraction of the variations we see in Cyg X-1. Based on these results, we are confident that our light curves of Cyg X-1 are an accurate representation of the rapidly changing intrinsic flux of the source.

---

[14]Note that the way in which calibrations are applied to interferometric data (see Equation 1.6 in Chapter 1 of this thesis) means that this multiplicative value is the critical value when checking calibration accuracy.
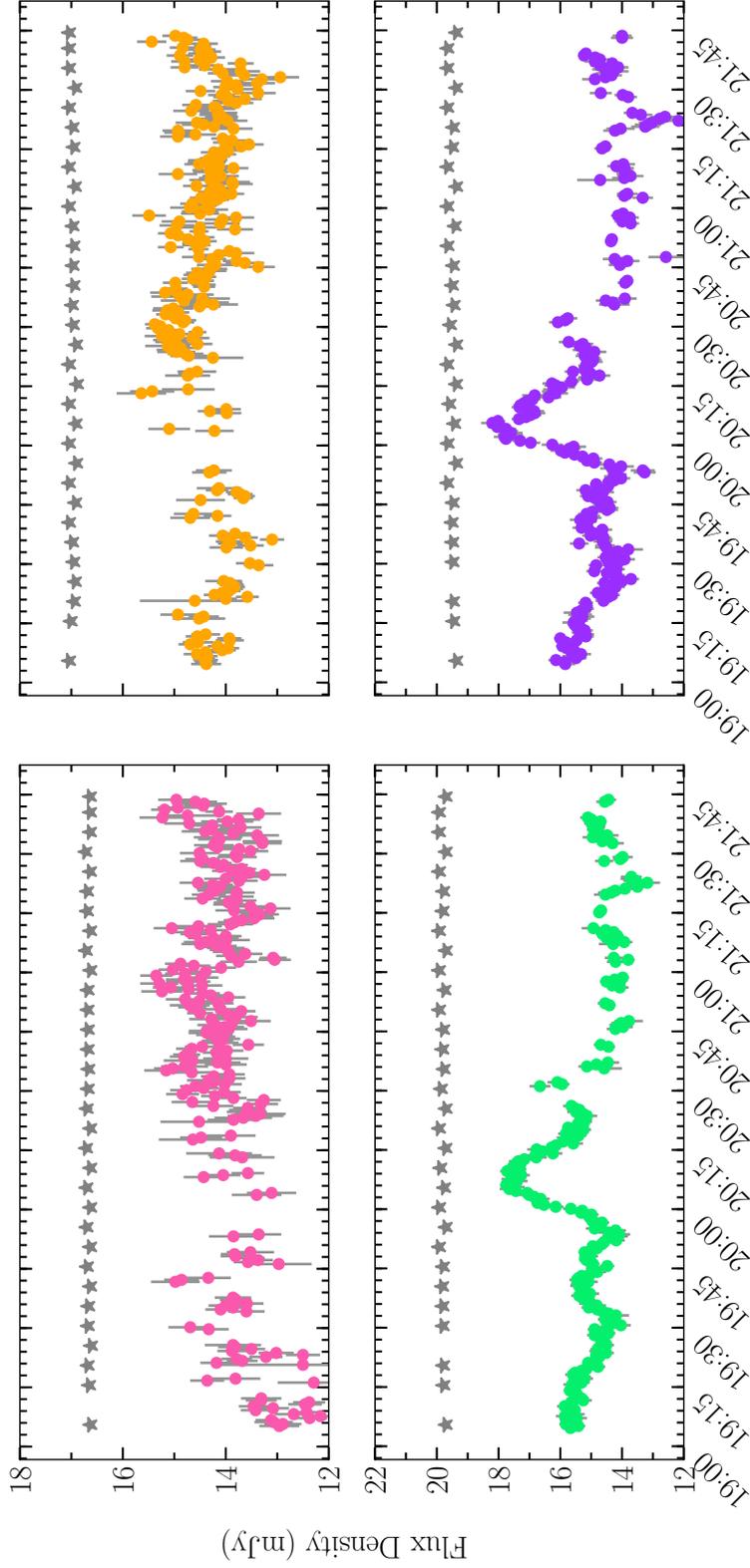
Figure 4.7: Multi-frequency light curves of Cyg X-1 and our calibrator source (J2015+3710); 2 GHz (*top left*), 3 GHz (*top right*), 9GHz (*bottom left*), and 11 GHz (*bottom right*) bands. In all panels, the calibrators are plotted as gray star symbols and the total flux of the calibrators are scaled down for clarity in the plots (the average flux densities of J2015+3710 are 2916.4, 3481.5, 3963.3, and 3803.9 mJy in the 2, 3, 9, and 11 GHz bands). The calibrator observations in all bands display a relatively constant flux throughout our observations, indicating that the variations we observe in Cyg X-1 are most likely intrinsic to the source, rather than due to atmospheric or instrumental effects.

4.6.2 X-ray Light curves

In this section we display an extended version of our *NuSTAR* X-ray light curves covering the full observation period, including the period prior to the overlap with our VLA radio observations (see Figure 4.8).

4.6.3 PSD white noise subtraction

In this section we display the radio PSDs prior to white noise subtraction, and indicate the measured white noise levels (see Figure 4.9). To determine whether the white noise could be intrinsic to the source (and in turn if subtracting the white noise in our PSDs is a valid practice in this case), we compared the white noise levels shown in Figure 4.9 to the rms noise levels in the individual time-bin images that make up each light curve. We find that the white noise levels closely match the average rms noise levels in the images at each radio frequency band. This indicates that the source of the white noise in the PSDs is likely not intrinsic to the source but rather due to atmospheric/instrumental effects (which govern the rms noise levels in radio frequency images).
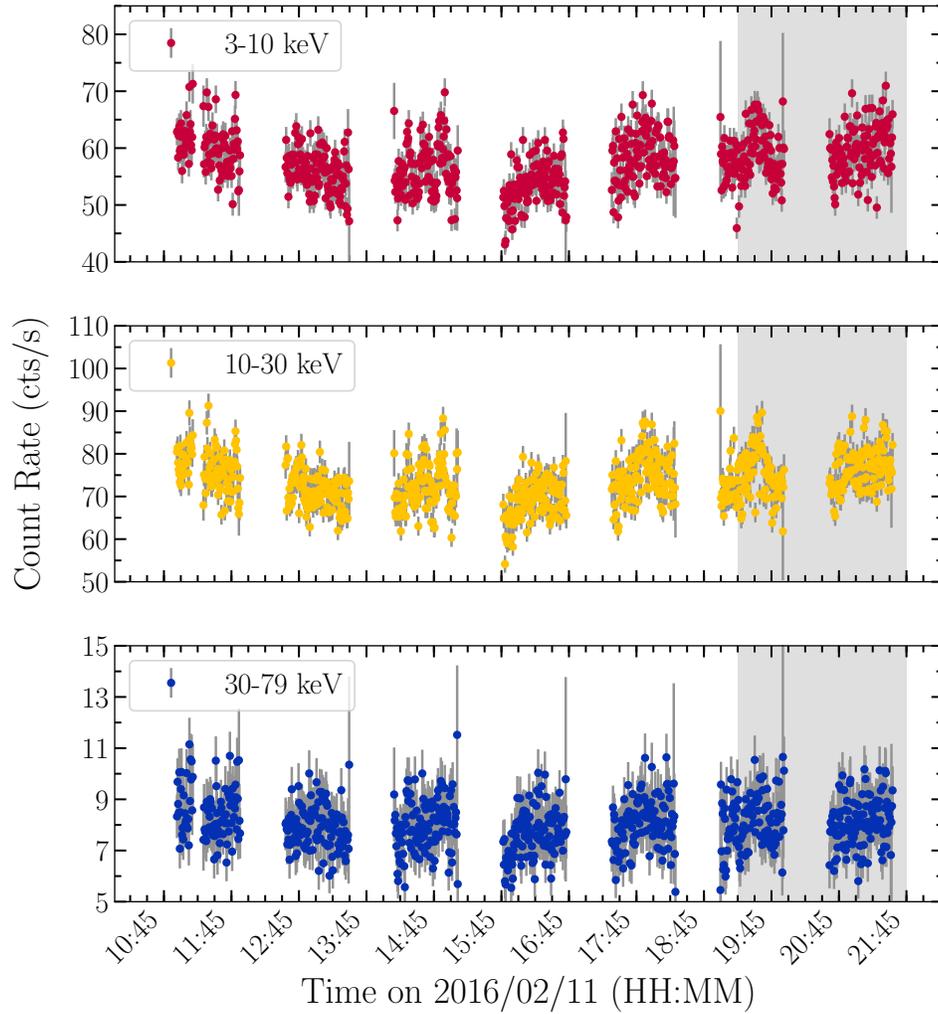
Figure 4.8: Extended version of Figure 4.1, where our complete *NuSTAR* X-ray frequency light curves of the BHXB Cyg X-1 are shown (with 30 sec time-bins). The gray shading represents the period of overlap between the VLA and *NuSTAR* observations, in which simultaneous X-ray and radio data were obtained.
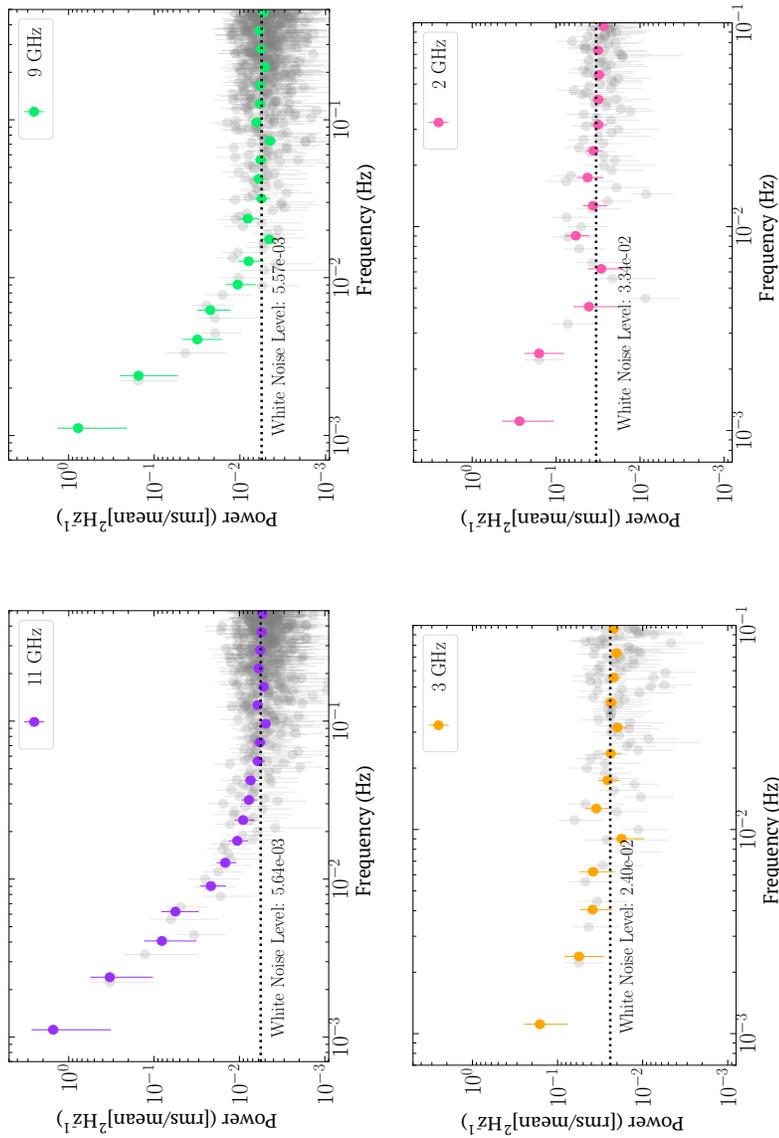
Figure 4.9: Radio PSDs of Cyg X-1 prior to white noise subtraction. In each panel, the gray-scale markers represent the PSDs before re-binning in frequency, and the coloured markers represent the PSDs after re-binning. The white noise level is also indicated in each panel. The PSDs in the 9/11 GHz bands are created from data imaged with 1 sec time-bins, while the 2/3 GHz PSDs are created from data imaged with 5 sec time-bins.

Chapter 5

Extreme jet ejections from the black hole X-ray binary V404 Cygni

This chapter details the work published Tetarenko, A.J. et al. 2017, "Extreme jet ejections from the black hole X-ray binary V404 Cygni", *MNRAS*, 469, 3141-3162, describing detailed Bayesian multi-frequency modelling of emission from rapid jet ejection events launched by the black hole X-ray binary V404 Cygni.

Abstract

We present simultaneous radio through sub-mm observations of the black hole X-ray binary (BHXB) V404 Cygni during the most active phase of its June 2015 outburst. Our 4 hour long set of overlapping observations with the Karl G. Jansky Very Large Array, the Sub-millimeter Array, and the James Clerk Maxwell Telescope (SCUBA-2), covers 8 different frequency bands (including the first detection of a BHXB jet at $666\,\mathrm{GHz}/450\mu m$), providing an unprecedented multi-frequency view of the extraordinary flaring activity seen during this period of the outburst. In particular, we detect multiple rapidly evolving

flares, which reach Jy-level fluxes across all of our frequency bands. With this rich data set we performed detailed MCMC modeling of the repeated flaring events. Our custom model adapts the van der Laan synchrotron bubble model to include twin bi-polar ejections, propagating away from the black hole at bulk relativistic velocities, along a jet axis that is inclined to the line of sight. The emission predicted by our model accounts for projection effects, relativistic beaming, and the geometric time delay between the approaching and receding ejecta in each ejection event. We find that a total of 8 bi-polar, discrete jet ejection events can reproduce the emission that we observe in all of our frequency bands remarkably well. With our best fit model, we provide detailed probes of jet speed, structure, energetics, and geometry. Our analysis demonstrates the paramount importance of the mm/sub-mm bands, which offer a unique, more detailed view of the jet than can be provided by radio frequencies alone.

5.1   Introduction

Black hole X-ray binaries (BHXBs), the rapidly evolving, stellar-mass counterparts of active galactic nuclei, are ideal candidates with which to study accretion and accretion-fed outflows, such as relativistic jets. These transient binary systems, containing a black hole accreting mass from a companion star, occasionally enter into bright outburst phases lasting days to weeks, providing a real-time view of the evolving relativistic jets (probed by radio through IR frequencies) and accretion flow (probed at X-ray frequencies).

BHXBs display two different types of relativistic jets, dependent on the mass accretion rate in the system (Fender et al., 2004a). At lower mass accretion rates ($< 10^{-1}L_{\mathrm{Edd}}$)[1], during the hard accretion state (see Remillard & McClintock 2006 and Belloni 2010 for a review of accretion states in BHXBs), a steady,

---

[1]The Eddington luminosity is the theoretical limit where, assuming ionized hydrogen in a spherical geometry, radiation pressure balances gravity. This limit corresponds to $L_{\mathrm{Edd}} = 1.26 \times 10^{38} M/M_{\odot} \, \mathrm{ergs}^{-1}$, where M is the black hole mass.

compact synchrotron-emitting jet is believed to be present in all BHXBs. It has also been shown that the compact jet is not only present during outburst phases, but can persist down into quiescence, at $< 10^{-5}L_{\mathrm{Edd}}$ (Gallo et al., 2005a; Plotkin et al., 2013, 2015, 2016). At higher mass accretion rates, during the transition between accretion states, discrete jet ejecta are launched (e.g., Mirabel & Rodríguez 1994; Hjellming & Rupen 1995; Corbel et al. 2002; Miller-Jones et al. 2012), and the compact jet may become quenched (Fender et al., 1999b; Corbel et al., 2001; Russell et al., 2011; Coriat et al., 2011b; Rushton et al., 2016). A small number of BHXBs have been observed to display multiple jet ejection events within a single outburst (e.g., Mirabel & Rodríguez 1994; Hjellming & Rupen 1995; Tingay et al. 1995; Fender et al. 1999a; Kuulkers et al. 1999; Brocksopp et al. 2002, 2013).

Compact jets are characterized by a flat to slightly inverted optically thick spectrum ($\alpha > 0$; where $f_\nu \propto \nu^\alpha$; Fender 2001), extending from radio up to sub-mm or even infrared frequencies (Corbel & Fender, 2002; Casella et al., 2010; Tetarenko et al., 2015d). Around infrared frequencies the jet emission becomes optically thin ($\alpha \sim -0.7$; Russell et al. 2013b), resulting in a spectral break. Each frequency below this break probes emission (from the optical depth, $\tau = 1$ surface) coming from a narrow range of distances downstream in the jet, where higher frequencies originate from regions along the jet axis that are closer to where the jet is launched (Blandford & Königl, 1979; Falcke & Biermann, 1995). The exact spectral shape (i.e., spectral index, location of the spectral break) is believed to evolve with changing jet properties such as geometry, magnetic field structure, and particle density profiles (Heinz & Sunyaev, 2003; Markoff et al., 2005; Casella & Pe'er, 2009; Russell et al., 2013c; van der Horst et al., 2013; Russell et al., 2014), as well as the plasma conditions in the region where the jet is first accelerated (Polko et al., 2010, 2013, 2014; Koljonen et al., 2015).

In contrast to the compact jets, jet ejecta are characterized by an optically thin spectrum ($\alpha < 0$), give rise to bright flaring activity, and can be routinely

resolved with Very Long Baseline Interferometry (VLBI; e.g., Fender 2006). The accompanying flares typically have well defined rise and decay phases, where the flares are usually optically thick in the rise phase, until the self-absorption turnover in the spectrum has passed through the observing band. These jet ejection events are believed to be the result of the injection of energy and particles to create an adiabatically expanding synchrotron emitting plasma, threaded by a magnetic field (i.e., van der Laan synchrotron bubble model, hereafter referred to as the vdL model; van der Laan 1966; Hjellming & Johnson 1988; Hjellming & Han 1995). In this model, as the source expands the evolving optical depth results in the distinct observational signature of the lower frequency emission being a smoothed, delayed version of the higher frequency emission. The ejection events have been linked to both X-ray spectral and timing signatures (e.g., Fender et al. 2009; Miller-Jones et al. 2012; Russell et al. 2014; Kalemci et al. 2016), although a definitive mechanism or sequence of events leading to jet ejection has not yet been identified.

Additionally, an extremely rare jet phenomenon, so called jet oscillation events, has also been observed in two BHXBs, GRS 1915+105 (radio, mm, IR; Pooley & Fender 1997) and V4641 Sgr (optical band; Uemura et al. 2004). Such rare events seem to occur only when the accretion rate is at very high fractions of the Eddington rate. These quasi-periodic oscillations (see Fender & Belloni 2004 for a review) show lower frequency emission peaking at later times (consistent with the vdL model for expanding discrete jet ejecta), rise and decay times of the repeated flares that are similar at all frequencies, and time lags between frequencies that vary within a factor of two. Moreover, no discrete moving components were resolved with VLBI during these oscillation events (although we note this could very well be due to sensitivity limits or the difficulty of synthesis imaging of fast-moving, time-variable components). As such, the exact nature of these events remains unclear, with theories including discrete plasma ejections, internal shocks in a steady flow, or variations in the

jet power in a self-absorbed, conical outflow (e.g., Fender & Pooley 1998, 2000; Collins et al. 2003). In GRS 1915+105 , these oscillations have also been clearly associated with dips in hard X-ray emission, possibly linking the launching of jet ejecta to the ejection and refilling of the inner accretion disc or coronal flow (Mirabel et al., 1998; Belloni et al., 1997; Vadawale et al., 2001).

While several transient BHXBs may undergo an outburst period in a given year, in which the jet emission becomes bright enough for detailed multi-wavelength studies, only rare (e.g., once per decade) outbursts probe the process of accretion and the physics of accretion-fed outflows near (or above) the Eddington limit. Observing the brightest and most extreme phases of accretion during these outbursts presents us with a unique opportunity to study jet and accretion physics in unprecedented detail. On 2015 June 15, the BHXB V404 Cygni entered into one of these rare near-Eddington outbursts. In this paper we report on our simultaneous radio through sub-mm observations of V404 Cygni during the most active phase of this outburst.

5.1.1 V404 Cygni

V404 Cygni (aka GS 2023+338; hereafter referred to as V404 Cyg) is a well studied BHXB that has been in a low-luminosity quiescent state since its discovery with the Ginga satellite in 1989 (Makino, 1989). This source has been observed to undergo a total of three outbursts prior to 2015; most recently in 1989 (Han & Hjellming, 1992; Terada et al., 1994; Oosterbroek et al., 1997), and two prior to 1989 which were recorded on photographic plates (Richter, 1989). V404 Cyg is known to display bright X-ray luminosities and high levels of multi-wavelength variability, both in outburst and quiescence (Tanaka & Lewin, 1995; Hynes et al., 2002b; Hjellming & Han, 1989; Kitamoto et al., 1989). The prolonged quiescent period of V404 Cyg, and high quiescent luminosity ($L_X \sim 1 \times 10^{33} \, \mathrm{erg \, s^{-1}}$; Corbel et al. 2008), has allowed the complete characterization of the system. The optical extinction is low, with $E(B - V) = 1.3$,

enabling the study of the optical counterpart, and the determination of the mass function as $6.08 \pm 0.06\,M_\odot$ (Casares et al., 1992; Casares & Charles, 1994). Subsequent modelling determined the black hole mass to be $9.0^{+0.2}_{-0.6}\,M_\odot$, with an inclination angle of $67°^{+3}_{-1}$, and an orbital period of 6.5 days (Khargharia et al., 2010; Shahbaz et al., 1994). However, we note that this inclination angle estimate is dependent on the assumed level of accretion disc contamination in the optical light curves being modelled. Khargharia et al. (2010) assumed $< 3\%$ accretion disc contamination, but given that V404 Cyg is known to be variable in quiescence in the optical, it is plausible that the accretion disc contamination may be larger (Zurita et al., 2003; Bernardini et al., 2016b), which would imply a larger inclination angle. Further, the faint, unresolved radio emission from the quiescent jets was used to determine a model-independent parallax distance of 2.39 ± 0.14 kpc (Miller-Jones et al., 2009), making V404 Cyg one of the closest known BHXBs in the Galaxy. The close proximity, well-determined system parameters, and bright multi-wavelength activity make this system an ideal target for jet and accretion studies.

On 2015 June 15[2], V404 Cyg entered into its fourth recorded outburst period. The source began exhibiting bright multi-wavelength flaring activity (e.g., Ferrigno et al. 2015b; Gandhi et al. 2015; Gazeas et al. 2015; Mooley et al. 2015; Motta et al. 2015a,b; Tetarenko et al. 2015a,b) immediately following the initial detection of the outburst in X-rays (Barthelmy et al., 2015; Negoro et al., 2015; Kuulkers et al., 2015), and swiftly became the brightest BHXB outburst seen in the past decade. This flaring behaviour was strikingly similar to that seen in the previous 1989 outburst (Terada et al., 1994; Oosterbroek et al., 1997; Zycki et al., 1999). Towards the end of June the flaring activity began to diminish across all wavelengths (e.g., Ferrigno et al. 2015a; Martin-Carrillo et al. 2015; Oates et al. 2015; Scarpaci et al. 2015; Tetarenko et al. 2015c; Tsubono et al.

---

[2]Bernardini et al. (2016b) serendipitously detected an optical precursor to this outburst on June 8/9, approximately one week prior to the first X-ray detection.

2015), and the source began to decay (Sivakoff et al., 2015b,c), reaching X-ray quiescence[3] in early to mid August (Sivakoff et al., 2015a; Plotkin et al., 2017). V404 Cyg also showed a short period of renewed activity from late December 2015 to early January 2016 (e.g., Lipunov et al. 2015; Trushkin et al. 2015; Beardmore et al. 2015; Malyshev et al. 2015; Tetarenko et al. 2016a; Motta et al. 2016), and Muñoz-Darias et al. (2017) present radio, optical, and X-ray monitoring during this period.

We organized simultaneous observations with the Karl G. Jansky Very Large Array (VLA), the Sub-millimeter Array (SMA), and the James Clerk Maxwell Telescope (JCMT) on 2015 June 22 (approximately one week following the initial detection of the outburst), during which time some of the brightest flaring activity seen in the entire outburst was observed. This comprehensive data set gives us an unprecedented multi-frequency view of V404 Cyg, in turn allowing us to perform detailed multi-frequency light curve modelling of the flaring events. In §5.2 we describe the data collection and data reduction processes. §5.3 describes the custom procedures our team developed to extract high time resolution measurements from our data. In §5.4 we present our multi-frequency light curves, outline our model, and describe the modelling process. A discussion of our best fit model is presented in §5.5, and a summary of our work is presented in §5.6.

5.2 Observations and Data Analysis

5.2.1 VLA Radio Observations

We observed V404 Cyg with the VLA (Project Code: 15A-504) on 2015 June 22, with scans on source from 10:37:24–14:38:39 UTC (MJD = $57195.442 - 57195.610$) in both C ($4 - 8\,\mathrm{GHz}$) and K ($18 - 26\,\mathrm{GHz}$) band. The array was in

---

[3]V404 Cyg entered optical quiescence in mid October 2015 (Bernardini et al., 2016a).

its most extended A configuration, where we split the array into 2 sub-arrays of 14 (sub-array A) and 13 (sub-array B) antennas. Sub-array A observed the sequence C-K-C, while sub-array B observed the sequence K-C-K, with an 80 second on target and 40 second on calibrator cycle, in order to obtain truly simultaneous observations across both bands. All observations were made with an 8-bit sampler, comprised of 2 base-bands, with 8 spectral windows of 64 2 MHz channels each, giving a total bandwidth of 1.024 GHz per base-band. Flagging, calibration, and imaging of the data were carried out within the Common Astronomy Software Application package (CASA; McMullin et al. 2007) using standard procedures. We used 3C48 (0137+331) as a flux calibrator, and J2025+3343 as a phase calibrator for both sub-arrays. No self-calibration was performed. Due to the rapidly changing flux density of the source, we imaged the source (with natural weighting; see the Appendix 5.7.1 for details on our choice of weighting scheme) on timescales as short as the correlator dump time (2 seconds) using our custom CASA timing scripts (see §5.3.1 for details).

5.2.2   SMA (Sub)-Millimetre Observations

We observed V404 Cyg with the SMA (Project Code: 2015A-S026) on 2015 June 22, with scans on source from 10:16:17–18:20:47 UTC (MJD = 57195.428−57195.764), and the correlator tuned to an LO frequency of 224 GHz. The array was in the sub-compact configuration with a total of 7 antennas (out of a possible 8 antennas). These observations were made with both the ASIC and SWARM (Primiani et al., 2016) correlators active, to yield 2 side-bands, with 48 spectral windows of 128 0.8125 MHz channels (ASIC) and an additional 2 1.664 GHz spectral windows (SWARM), giving a total bandwidth of 8.32 GHz per side-band. The SWARM correlator had a fixed resolution of 101.6 kHz per channel, and thus originally 16383 channels for each SWARM spectral window. Given the continuum nature of these observations, we performed spectral averaging, to yield 128 13 MHz channels in both SWARM spectral windows, to

match the number of channels in the ASIC spectral windows, and in turn make it easier to combine ASIC and SWARM data. We used 3C454.3 (J2253+1608) as a bandpass calibrator, MWC349a and J2015+3710 as phase calibrators, and Neptune and Titan as flux calibrators[4]. We note that only the second IF (spectral windows 25-50) was used for flux calibration in the upper side-band due to a CO line that was present in both flux calibrators at 230.55 GHz. Our observing sequence consisted of a cycle of 15 min on target and 2.5 min on each of the two phase calibrators. As CASA is unable to handle SMA data in its original format, prior to any data reduction we used the SMA scripts, sma2casa.py and smaImportFix.py, to convert the data into CASA MS format, perform the T_{sys} corrections, and spectrally average the two SWARM spectral windows. Flagging, calibration, and imaging of the data were then performed in CASA using procedures outlined in the CASA Guides for SMA data reduction[5]. Due to the rapidly changing flux density of the source, we imaged the source (with natural weighting; see the Appendix 5.7.1 for details on our choice of weighting scheme) on timescales as short as the correlator dump time (30 seconds) using our custom CASA timing scripts (see §5.3.1 for details).

5.2.3 JCMT SCUBA-2 (Sub)-Millimetre Observations

We observed V404 Cyg with the JCMT (Project Code: M15AI54) on 2015 June 22 from 10:49:33–15:12:40 UTC (MJD $= 57195.451 - 57195.634$), in the $850\mu m$ (350 GHz) and $450\mu m$ (666 GHz) bands. The observation consisted of eight ~ 30 min scans on target with the SCUBA-2 detector (Chapin et al., 2013; Holland et al., 2013). To perform absolute flux calibration, observations of the calibrator CRL2688 were used to derive a flux conversion factor (Dempsey et al., 2012). The daisy configuration was used to produce 3 arcmin maps

---

[4]The SMA calibrator list can be found at `http://sma1.sma.hawaii.edu/callist/callist.html`.

[5]Links to the SMA CASA Guides and these scripts are publicly available at `https://www.cfa.harvard.edu/sma/casa`.

of the target source region. During the observations we were in the Grade 3 weather band with a 225 GHz opacity of 0.095–0.11. Data were reduced in the STARLINK package using both standard procedures outlined in the SCUBA-2 cookbook[6] and SCUBA-2 Quickguide[7], as well as a custom procedure to create short timescale maps (timescales shorter than the 30 minute scan timescale) to extract high time resolution flux density measurements of the rapidly evolving source (see §5.3.2 for details).

5.3   High Time Resolution Measurements

5.3.1   VLA and SMA

To obtain high time resolution flux density measurements of V404 Cyg from our interferometric data sets (VLA and SMA) we developed a series of custom scripts that run within CASA. A detailed account of the development and use of these scripts will be presented in Tetarenko & Koch et al. 2017, in prep., although we provide a brief overview of the capabilities here.

Our scripts split an input calibrated CASA Measurement Set into specified time intervals for analysis in the image plane or the uv-plane. In the image plane analysis, each time interval is cleaned and the flux density of the target source is measured by fitting a point source in the image plane with the native CASA task imfit. All imaging parameters (e.g., image size, pixel size, number of *clean* iterations, *clean* threshold) can be fully specified. In the uv-plane analysis, the UVMULTFIT package (Marti-Vidal et al., 2014) is used to measure flux density of the target source. In either case, an output data file and plot of the resulting light curve are produced. These scripts are publicly available on github[8], and are being implemented as a part of an interactive service our

---

[6]http://starlink.eao.hawaii.edu/devdocs/sc21.htx/sc21.html
[7]https://www.eaobservatory.org/jcmt/instrumentation/continuum/scuba-2/data-reduction/reducing-scuba2-data
[8]https://github.com/Astroua/AstroCompute_Scripts

team is developing to run on Amazon Web Services Cloud Resources.

All VLA and SMA flux density measurements output from this procedure (fitting only in the image plane) are provided in a machine readable table online, which accompanies this paper. Additionally, to check that the variability we observed in V404 Cyg is dominated by intrinsic variations in the source and not due to atmospheric or instrumental effects, we also ran our calibrator sources through these scripts (see the Appendix 5.7.2 for details).

5.3.2 JCMT SCUBA-2

To obtain high time resolution flux density measurements of V404 Cyg from our JCMT SCUBA-2 data we developed a custom procedure to produce a data cube, containing multiple maps of the target source region, at different time intervals throughout our observation.

We run the STARLINK Dynamic Iterative Mapmaker tool on each of the target scans, using the bright compact recipe, with the addition of the shortmap parameter. The shortmap parameter allows the Mapmaker to create a series of maps, each of which will include data from a group of adjacent time slices. The number of time slices included in each map is equivalent to the shortmap parameter value. At $850\mu m$ we use shortmap $= 200$ to produce 362 time slices for a 32 minute scan, resulting in 5 second time bins. At $450\mu m$ shortmap $= 400$ would produce the same number of time slices, where a factor of 2 is applied as the default pixel size is 2 arcsec at $450\mu m$ and 4 arcsec at $850\mu m$. However, as the noise is higher at $450\mu m$, we use shortmap $= 4800$ to produce 32 time slices for a 32 minute scan, resulting in 60 second time bins. The `stackframes` task is then used to combine all of the short maps into a cube for each scan. The sort $=$ True and sortby $=$ MJD $-$ AVG parameters ensure the maps are ordered chronologically in time, with the resulting cube having the dimensions, position X (pixels), position Y (pixels), time (MJD). Using the `wcsmosaic` task we then combined the cubes from all the scans. We calibrated the combined

cube into units of Jy using the `scuba2checkcal` and `cmult` tasks. Finally, the combined cube can be viewed in `Gaia`, and converted to FITS format with the `ndf2fits` task.

To extract flux densities from each time slice in the combined cube, we fit a 2D gaussian[9] with the size of the beam (FWHM of 15.35 arcsec at $850\mu m$ and 10.21 arcsec at $450\mu m$; derived using the task `scuba2checkcal`) to each slice of the cube. All JCMT SCUBA-2 flux density measurements output from this procedure are provided in a machine readable table online, which accompanies this paper. As with our interferometric data sets, to check that the variability we observed in V404 Cyg is dominated by intrinsic variations in the source and not due to atmospheric or instrumental effects, we also ran this procedure on our calibrator source scans (see the Appendix 5.7.2 for details).

5.4   Results

5.4.1   Multi-frequency Light Curves

A composite light curve of all of our VLA, SMA and JCMT observations from June 22 is presented in Figure 5.1. We observe rapid multi-frequency variability in the form of multiple large scale flares, reaching Jy flux levels. In the SMA data, the largest flare (at $\sim$ 13:15 UTC) rose from $\sim$ 100 mJy to a peak of $\sim$ 5.6 Jy on a timescale of $\sim$ 25 min. The JCMT SCUBA-2 data appear to track the SMA data closely, with the largest flare at 350 GHz rising from $\sim$ 400 mJy to a peak of $\sim$ 7.2 Jy on a timescale of $\sim$ 18 min. This is the largest mm/sub-mm flare ever observed from a BHXB, far surpassing even the brightest events in GRS 1915+105 (Fender & Pooley, 2000). The VLA radio data lag the mm/sub-mm (where the lag appears to be variable among the flares; $\sim$20–45 min & $\sim$40–75 min between 350 GHz and the 18–26 GHz & 4–8

---

[9]The python package GAUSSFITTER is used in the gaussian fitting; `https://github.com/keflavich/gaussfitter`
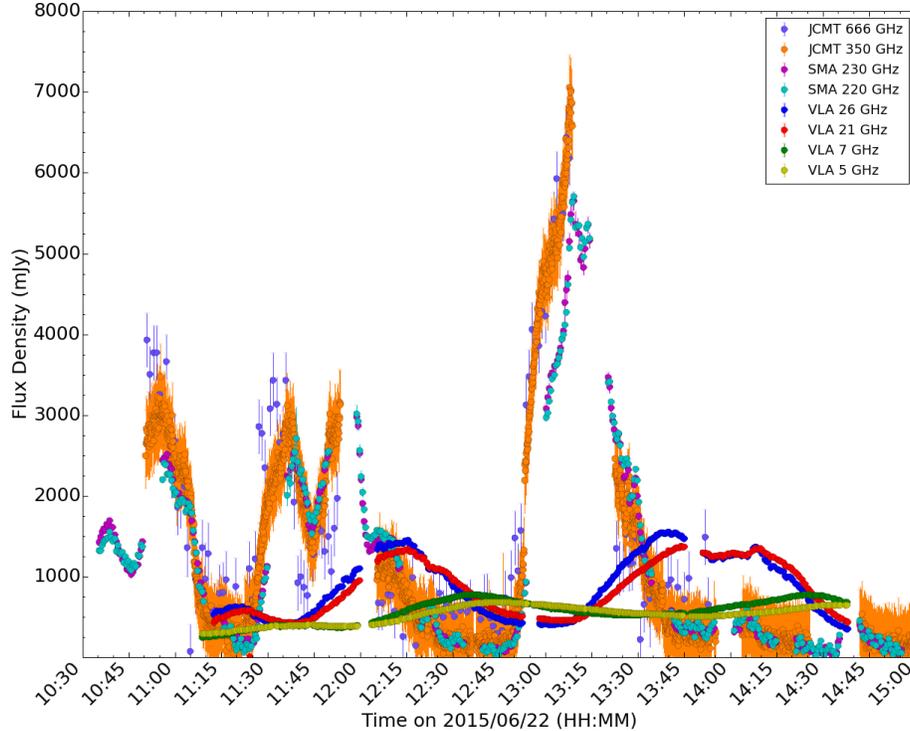
Figure 5.1: Simultaneous radio through sub-mm light curves of the BHXB V404 Cygni during the most active phase of its June 2015 outburst. These light curves sample the brightest flares at these frequencies over the entire outburst. All light curves are sampled at the finest time resolution possible, limited only by the correlator dump time (and the sensitivity for JCMT data). The VLA light curves have 2 second time bins, the SMA light curves have 30 second time bins, the JCMT SCUBA-2 350 GHz ($850\,\mu m$) light curve has 5 second time bins, and the JCMT SCUBA-2 666 GHz ($450\,\mu m$) light curve has 60 second time bins. The mm/sub-mm regime samples a much more extreme view of the flaring activity than the radio regime, with detailed sub-structure detected only in the mm/sub-mm light curves.

GHz bands, respectively), with flares in the 18–26 GHz band rising to a peak of ~ 1.5 Jy on a timescale of ~ 35 min, and flares in the 4–8 GHz band rising to a peak of ~ 780 mJy on a timescale of ~ 45 min.

Upon comparing the multi-frequency emission, it is clear that the mm/sub-mm data provide a much more extreme view of the flaring activity than the radio emission. In particular, there is more structure present in the mm/sub-mm light curves when compared to the radio light curves. As such, while not immediately apparent in the radio light curves, the mm/sub-mm data suggest

132

that each of the three main flares in the light curves is actually the result of the superposition of emission from multiple flaring components. Additionally, the lower frequency emission in the light curves appears to be a smoothed, delayed version of the high frequency emission (with the flares showing longer rise times at lower frequencies). This emission pattern is consistent with an expanding outflow structure, where the mm/sub-mm emission originates in a region (with a smaller cross-section) closer to the black hole, and has thus not been smoothed out to as high a degree as the radio emission, as the material expands and propagates outwards. Therefore, all of these observations suggest that the emission in our light curves could be dominated by emission from multiple, expanding, discrete jet ejection events (van der Laan, 1966).

Further, we notice that the baseline flux level at which the flaring begins at each frequency in our light curves appears to vary. This suggests that there is an additional frequency-dependent component contributing to our light curves, on top of the discrete jet ejecta. In an effort to determine the origin of this extra emission, assuming that the baseline emission is constant in time, we create a spectrum of this emission by estimating the baseline flux level at each frequency (we performed iterative sigma clipping and take the minimum of the resulting sigma clipped data). This spectrum[10] is presented in Figure 5.2, where it appears as though the baseline emission could be described by a broken power-law or a single power-law (with higher frequency emission displaying a lower baseline level than lower frequency emission). This spectral shape, combined with the fact that we observe a strong compact core component (in addition to resolved ejecta components) within simultaneous high resolution radio imaging (Miller-Jones, et al. 2018, in prep., also see Chapter 7 of this thesis), suggests that the baseline emission originates from an underlying compact jet that was not fully quenched.

---

[10]We note that these are only empirical initial estimates of the baseline flux at each frequency, and do not necessarily represent the flux of the compact jet in our model presented in §5.4.2.
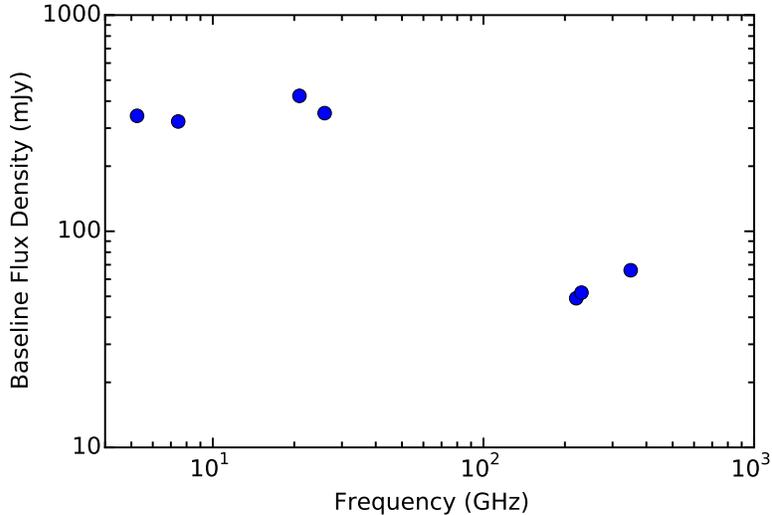
Figure 5.2: Estimated radio through sub-mm spectrum of the baseline flux component seen in our light curves.

5.4.2 V404 Cyg Jet Model

Given the morphology of our light curves outlined in the previous section, we have constructed a jet model for V404 Cyg that is capable of reproducing emission from multiple, repeated, discrete jet ejection events, on top of an underlying compact jet component. We define two coordinate frames, the observer frame and the source frame (at rest with respect to the ejecta components). We will compute our model primarily in the source frames, and then transform back to the observer frame. All variables with the subscript *obs* are defined in the observer frame. Schematics displaying the geometry of our model from different viewpoints are displayed in Figures 5.3 & 5.4.

In our model, the underlying compact jet is characterized by a broken power-law spectrum, where the flux density is independent of time and varies only with frequency according to,

$$F_{\nu,\mathrm{cj}} = \begin{cases} F_{\mathrm{br,cj}}(\nu/\nu_{\mathrm{br}})^{\alpha_1} & , \nu < \nu_{\mathrm{br}} \\ F_{\mathrm{br,cj}}(\nu/\nu_{\mathrm{br}})^{\alpha_2} & , \nu > \nu_{\mathrm{br}} \end{cases} \tag{5.1}$$
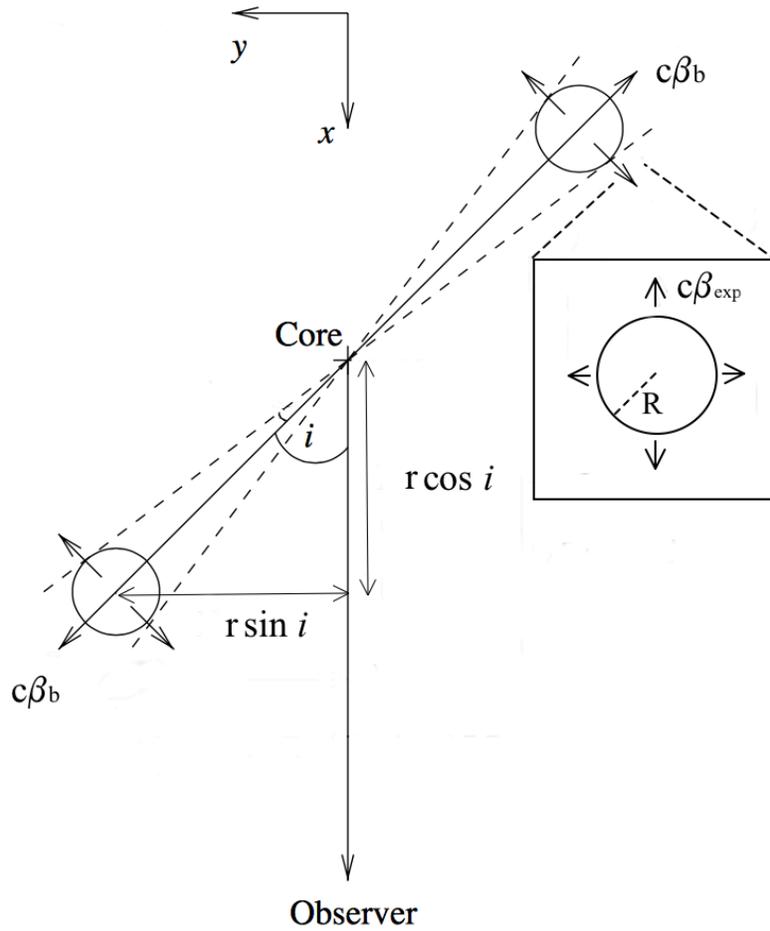
Figure 5.3: Schematic of the geometry for our jet model in a plane defined by our line-of-sight and the central axis of the jets (i.e., bird's eye view). The inset panel displays the ejecta component seen from the source frame (at rest with respect to the ejecta). All parameters are defined within the accompanying text. This figure was adapted from its original form in Miller-Jones et al. 2006.
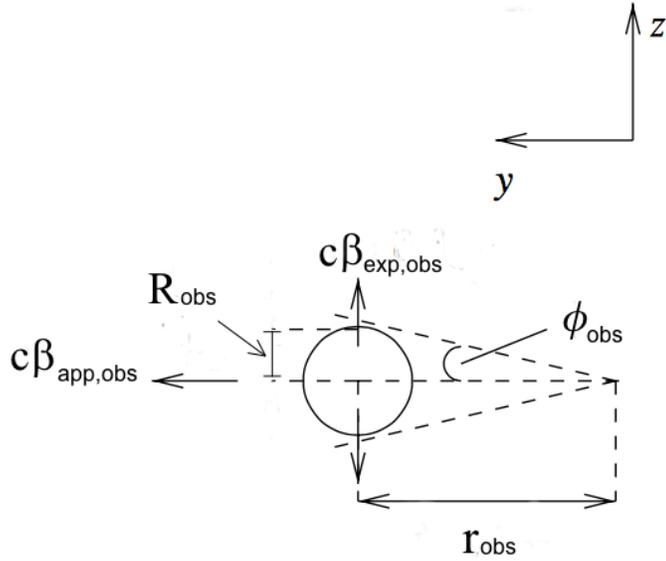
Figure 5.4: Schematic of the geometry of the discrete jet ejections in our model, as seen by the observer. All parameters are defined within the accompanying text. This figure was adapted from its original form in Miller-Jones et al. 2006.

Here ν_{br} represents the frequency of the spectral break, $F_{\mathrm{br,cj}}$ represents the amplitude of the compact jet at the spectral break frequency, α_1 represents the spectral index at frequencies below the break, and α_2 represents the spectral index at frequencies above the break. In the case where the spectral break frequency is located below the lowest sampled frequency band, or above the highest sampled frequency band, the underlying compact jet can be characterized by a single power-law spectrum, where $F_{\nu,\mathrm{cj}} = F_{0,\mathrm{cj}} \left(\frac{\nu}{\nu_0} \right)^{\alpha}$. Here $F_{0,\mathrm{cj}}$ represents the amplitude of the compact jet at ν_0, and α represents the spectral index.

On top of the compact jet, we define a discrete ejection event as the simultaneous launching of two identical, bi-polar plasma clouds (an approaching and receding component). Each of these clouds evolve according to the vdL model (van der Laan, 1966). In this model, a population of relativistic electrons, with a power-law energy distribution ($N(E)dE = KE^{-p}dE$), is injected

136

into a spherical cloud threaded by a magnetic field. The cloud is then allowed to expand adiabatically, while the electrons and magnetic field are assumed to be kept in equipartition. As a result of the expansion, this model predicts the flux density of each cloud will scale as,

$$F_{\nu,\text{ej}} = F_0 \left(\frac{\nu}{\nu_0}\right)^{5/2} \left(\frac{R}{R_0}\right)^3 \frac{1 - \exp(-\tau_\nu)}{1 - \exp(-\tau_0)}. \tag{5.2}$$

Here R indicates the time-dependent radius of the cloud, and the synchrotron optical depth, τ_ν, at a frequency, ν, scales as,

$$\tau_\nu = \tau_0 \left(\frac{\nu}{\nu_0}\right)^{-(p+4)/2} \left(\frac{R}{R_0}\right)^{-(2p+3)}. \tag{5.3}$$

Note that the subscript 0 in all our equations indicates values at the reference frequency[11], at the time (or radius) of the peak flux of the component.

Taking the derivative of Equation 5.2 with respect to time[12] (or radius), allows us to relate the optical depth at which the flux density of the reference frequency reaches a maximum, τ_0, to the power-law index of the electron energy distribution, p,

$$e^{\tau_0} - (2p/3 + 1)\tau_0 - 1 = 0. \tag{5.4}$$

Equation 5.4 has no analytic solution and thus must be solved numerically. Therefore, we choose to leave our model in terms of τ_0, and solve for p after the fitting process.

To describe the time-dependence of the cloud radius, a linear expansion model is used, according to,

$$R = R_0 + \beta_{\exp} c \, (t - t_0). \tag{5.5}$$

---

[11] We defined our reference frequency as the upper-sideband in our SMA data (230 GHz).
[12] Our expression in Equation 5.4 differs from that of van der Laan (1966), as he takes the derivative with respect to ν instead of time, yielding $e^{\tau_0} - ([p+4]/5)\tau_0 - 1 = 0$.

Here $\beta_{\mathrm{exp}}c$ represents the expansion velocity of the cloud, while R_0 can be expressed in terms of the distance to the source, d, peak flux, F_0, and optical depth, τ_0, of the cloud at the reference frequency (Yusef-Zadeh et al., 2008),

$$R_0 \propto \left[\frac{F_0 d^2}{\pi} \frac{1}{1 - \exp(-\tau_0)} \right]^{1/2} . \tag{5.6}$$

At the same time that the clouds are expanding, they are also propagating away from the black hole at bulk relativistic velocities, along a jet axis that is inclined to the observer's line of sight (see Figure 5.3). As such, the emission we observe will have been affected by projection effects, relativistic beaming, and a geometric time delay between the approaching and receding clouds in each ejection event.

To account for these effects, we first assume that the clouds are travelling at a constant bulk velocity, $\beta_b c$, and that the jet has a conical geometry (with an observed opening angle, ϕ_{obs}). In turn, the apparent observed velocity across the sky (derived via the transverse Doppler effect) is represented as (Mirabel & Rodríguez, 1999),

$$\beta_{\mathrm{app,obs}} = \begin{cases} \dfrac{r\sin i}{c\,(t-t_{\mathrm{ej}}) - r\cos i} & \rightarrow \text{approaching} \\[4mm] & , \\[2mm] \dfrac{r\sin i}{c\,(t-t_{\mathrm{ej}}) + r\cos i} & \rightarrow \text{receding} \end{cases} \tag{5.7}$$

where $r = \beta_b c(t - t_{\mathrm{ej}})$ is the distance travelled by the cloud away from the black hole, t_{ej} represents the ejection time, c represents the speed of light, and i represents the inclination angle of the jet axis to the line of sight.

Equation 5.7 can be simplified by substituting in our expression for r to yield,

$$\beta_{\mathrm{app,obs}} = \beta_b \Gamma \delta_{\mp} \sin(i), \tag{5.8}$$

where the Doppler factor and bulk Lorentz factor are given by $\delta_{\mp} = \Gamma^{-1}[1 \mp \beta_b \cos i]^{-1}$ and $\Gamma = (1 - \beta_b^2)^{-1/2}$, respectively. The sign convention in the Doppler

factor indicates that a δ_- should be used for the approaching cloud and a δ_+ should be used for the receding cloud.

From Figures 5.3 & 5.4,

$$\tan\phi_{\rm obs} = \frac{R_{\rm obs}}{r_{\rm obs}} = \frac{\delta_\mp\,\beta_{\rm exp}\,c\,(t-t_{ej})_{\rm obs}}{\beta_{\rm app,obs}\,c\,(t-t_{\rm ej})_{\rm obs}} = \frac{\delta_\mp\,\beta_{\rm exp}}{\beta_{\rm app,obs}}. \tag{5.9}$$

Combining Equations 5.8 & 5.9, and solving for the bulk Lorentz factor, Γ, yields,

$$\Gamma = \left(1 + \frac{\beta_{\rm exp}^2}{\tan^2\phi_{\rm obs}\sin^2 i}\right)^{1/2}. \tag{5.10}$$

Rearranging Equation 5.10 (and substituting in $1-\Gamma^2 = -\Gamma^2\beta_b^2$) gives the expansion velocity (to be input into Equation 5.5) in terms of only the bulk velocity and jet geometry (inclination and opening angle), such that,

$$\beta_{\rm exp} = \tan\phi_{\rm obs}[\Gamma^2\{1-(\beta_b\cos i)^2\}-1]^{1/2}. \tag{5.11}$$

Further, we wish to write our model in terms of only the ejection time $(t_{\rm ej})$, rather than the time of the peak flux at the reference frequency (t_0), without introducing any additional parameters. Using our definition that $R = R_0$ at the instant $t = t_0$, the two timescales are related by,

$$t_0 = t_{\rm ej} + \frac{R_0}{\beta_{\rm exp}c}. \tag{5.12}$$

Lastly, we correct for relativistic beaming by applying a factor of $\delta_\mp^3$ (Longair, 2011) to our flux density in Equation 5.2, according to,

$$F_{\nu,{\rm ej,obs}} = \delta_\mp^3 F_{\nu,{\rm ej}}. \tag{5.13}$$

Here $F_{\nu,{\rm ej,obs}}$ indicates the flux density of the cloud in the observer frame, at the observing frequency $\nu_{\rm obs}$, at the observed times since the zero point of our observations, $\Delta t_{\rm obs}$, while $F_{\nu,{\rm ej}}$ indicates the flux density of the clouds in

the source frame, at the frequency, $\nu = \delta_{\mp}^{-1}\nu_{\text{obs}}$, at the times, $\Delta t = \delta_{\mp}\Delta t_{\text{obs}}$.

All of the ejection events we model are not correlated, and thus evolve independently of each other. The total observed flux density in our model is represented as,

$$F_{\nu,\text{obs,tot}} = \sum_i \delta_-^3 (F_{\nu,\text{i,app}}) + \sum_i \delta_+^3 (F_{\nu,\text{i,rec}}) + F_{\nu,\text{cj}}. \qquad (5.14)$$

5.4.2.1 Jet Precession

In addition to our VLA, SMA, and JCMT observations, we also obtained simultaneous high angular resolution radio observations with the Very Long Baseline Array (VLBA). Through imaging the VLBA data set in short 2 minute time bins, we resolve multiple discrete ejecta. Our analysis of these VLBA images has shown clear evidence of jet precession, where the position angle of the resolved ejecta change by up to 40 degrees on an hourly timescale (this result will be reported in detail in Miller-Jones et al. 2018, in prep., also see Chapter 7 of this thesis). As the emission predicted by our model is highly dependent on the inclination angle of the jet axis, we account for the effect of this rapid, large scale jet precession in our model by allowing our inclination parameter, i, to vary between ejection events.

5.4.2.2 Accelerated Motion

While we have assumed that the jet ejecta are travelling at constant bulk velocities, it is possible that they undergo some form of accelerated motion. To test this hypothesis we generalized our model to allow the input of a custom bulk velocity profile, where we implemented simple velocity profiles to mimic a finite acceleration period where the cloud would approach a terminal velocity (e.g., a linear ramp function, a body subject to a quadratic drag force). However, in all cases, our best fit model either tended towards a constant velocity profile, or would not converge. This result, while not ruling out the possibility of accel-

erated motion, suggests that any potential acceleration period may have only lasted for a short enough period of time that we are not able to discern the difference between the resulting light curves for the accelerated and constant bulk motion.

5.4.2.3 Sub-Conical Jet Geometry

While we have assumed that the jet in our model is conical (constant opening angle), it is possible that the jet geometry could deviate from a strictly conical shape (especially on the AU size scales we are probing), where the opening angle (and in turn the expansion speed of the ejecta) could change with time. In particular, if we assume that the jet confinement mechanism is external, then the jet geometry will depend on the adiabatic indices of the two media (i.e., the jet and its surrounding medium). A relativistic plasmon confined by the internal pressure of a terminal spherical wind (made up of a $\Gamma = 5/3$ gas) will expand sub-conically, according to $R \propto r^{5/6}$. To test this scenario, we modified our model to use the above sub-conical expansion expression in place of Equation 5.5. In doing this we find that our best fit model still tends toward constant expansion speed/opening angle profiles for all the ejecta. This result, while not ruling out a non-conical jet geometry, could suggest that any deviations from a conical jet shape only occur on sub-AU size scales, probing timescales before the sub-mm emission peaks, and thus we are not able to discern the difference between the resulting light curves for conical/sub-conical jet geometry.

5.4.2.4 Bi-polar vs. Single-Sided Ejections

Our jet model assumes that each ejection event takes the form of two identical, oppositely directed plasmons. However, in principle our light curves could also be fit with a collection of single-sided ejections. These unpaired components could occur as a result of Doppler boosting of highly relativistic plasmons

causing us to observe only the approaching component of an ejecta pair, or intrinsically unpaired ejecta. Our simultaneous VLBA imaging (see Chapter 7 of this thesis) may help distinguish between these two scenarios. We resolve both paired and (possibly[13]) unpaired ejecta components in our VLBA images, which could suggest that the emission in our light curves is produced by a combination of bi-polar and single-sided ejection events. Using these VLBA results to include stricter constraints within our model on ejecta numbers, type (single/bi-polar), and ejection times, is beyond the scope of this work, but will be considered in a future iteration of the model.

5.4.3 Modelling Process and Best Fit Model

Due to the large number of free parameters in our model, we use a Bayesian approach for parameter estimation. In particular, we apply a Markov-Chain Monte Carlo algorithm (MCMC), implemented with the EMCEE package (Foreman-Mackey et al., 2013), to fit our light curves with our jet model. This package is a pure-Python implementation of Goodman & Weare's Affine Invariant MCMC Ensemble Sampler (Goodman & Weare, 2010), running a modified version of the commonly used Metropolis-Hastings Algorithm, whereby it simultaneously evolves an ensemble of "walkers" through the parameter space. We use 500 walkers ($10 \times$ the number of dimensions in our model) for our MCMC runs.

---

[13]Given the rapid timescales of the ejections, multiple ejecta can become blended together in these images, making it difficult at times to conclusively identify and track individual components.

Table 5.1: V404 Cyg Jet Model Parameters and Priors

Parameter[a,b]	Description	Prior Distribution[c]	Prior Minimum	Prior Maximum
$F_{0,cj}$	amplitude of compact jet component at ν_0 in mJy	uniform	10	1000
α	spectral index	truncated normal ($\mu = -0.5$, $\sigma = 0.1$)	-1	0
*t_{ej}	ejection time of bi-polar components in seconds[d,e]	uniform	$t_g - 1000$	$t_g + 1000$
*i	inclination angle of the jet axis in degrees	truncated normal ($\mu = 67$, $\sigma = 20$)	0	90
*ϕ_{obs}	observed opening angle in degrees	uniform	1	20
*τ_0	optical depth at the reference frequency	truncated normal ($\mu = 2.0$, $\sigma = 0.3$)	1	3
*F_0	peak flux density at the reference frequency in mJy	truncated normal ($\mu = 3000$, $\sigma = 1000$)	0	6000
*β_b	bulk jet speed in units of c	inverse gamma ($a = 3$)[f]	0	1

[a] Note that the emission from the underlying compact jet portion of our model is best fit by a single power-law rather than a broken power-law. Therefore, only the parameters describing the single power-law version of the compact jet in our model are shown here.
[b] Parameters marked with a * indicate those which are allowed to vary between ejection events.
[c] Justification of our use of these priors is presented in the text of §5.4.3.
[d] For simplicity, when modelling we convert our times to units of seconds past the zero point of MJD 57195.41806.
[e] t_g represents the initial guess of the ejection time, see §5.4.3 for details.
[f] The inverse gamma distribution takes the form, $f(x) = \frac{x^{(-a-1)}}{\Gamma(a)} \exp(-1/x)$, where Γ represents the gamma function not the bulk Lorentz factor. This distribution is a common prior used for small number parameters defined to be < 1.

Prior distributions used for all of our parameters are listed in Table 5.1. We choose physically informative priors that reflect our knowledge of V404 Cyg (or commonly assumed values for BHXBs) where possible, and wide uninformative uniform priors when we have no pre-defined expectation for a specific parameter. For instance, the prior for the inclination angle is set as a truncated normal distribution, centered on 67 degrees (the measured inclination angle of the system), with boundaries of 0 and 90 degrees (allowed values of the inclination angle). On the other hand, the prior for the ejection time is simply a uniform distribution, sampling a wide range of possible times around our best initial guess.

Before running the MCMC, the initial position of the walkers in the parameter space needs to be defined. As the performance of the EMCEE algorithm tends to benefit heavily from well defined initial conditions, we do an initial exploration of the parameter space using a harmony search global optimization algorithm[14]. This metaheuristic algorithm, that is similar to, but much more efficient than a brute force grid search method (which would not be computationally feasible in this case), yields a reasonable initial guess for our model, and we place our walkers in a tight ball around this initial guess in the parameter space.

As our jet model can predict emission at multiple frequencies, to reduce the degeneracy in our model, we choose to simultaneously fit all of our multi-frequency data sets, except for the JCMT 666 GHz data set, due to its sparser sampling and larger uncertainty in flux calibration (see the Appendix 5.7.3 for details). To do this, we use an iterative process whereby we start with our reference frequency data set, run the MCMC (the walkers are evolved over a series of steps, where the first 500 step "burn in" period is not retained) until convergence is reached, and use the final position of the walkers for the first

---

[14]Implemented in the python package, PYHARMONYSEARCH; `https://github.com/gfairchild/pyHarmonySearch`.

144

run as the initial guess for the next run of the MCMC, which will include increasingly more data sets in the fit. To monitor the progress of the MCMC and ensure that correct sampling was occurring, we checked that the acceptance fraction stayed within the suggested bounds (between 0.25 and 0.75). Our criteria for convergence requires that the positions of the walkers are no longer significantly evolving. We determine whether this criteria is met by monitoring the chains of each of the walkers through the parameter space, and ensuring that, for each parameter, the intra-chain variance across samples is consistent with the inter-chain variance at a given sample.

Using the multi-dimensional posterior distribution output from the converged MCMC solution, we create one dimensional histograms for each parameter. The best fit result is taken as the median of these distributions, and the uncertainties are reported as the range between the median and the 15th percentile (-), and the 85th percentile and the median (+), corresponding approximately to 1σ errors. All of the best-fit parameters and their uncertainties are reported in Table 5.2. Figure 5.5 & 5.6 show the best fit model overlaid on our multi-frequency light curves. Additionally, with our multi-dimensional posterior distribution we can explore the possible two-parameter correlations for our model, where a significant correlation between a pair of parameters can indicate a model degeneracy or a physical relationship between the parameters. In the Appendix 5.7.5 section we show correlation plots (Figure 5.11), along with the one-dimensional histograms, for pairs of parameters for which we find a correlation, and discuss the significance of such a correlation.

Within the Bayesian formalism, the uncertainties reported in Table 5.2 are purely statistical, and only represent the credible ranges of the model parameters under the assumption that our model is correct. Given the residuals with respect to the optimal model (Figure 5.5 bottom panel), the observations contain physical or observational effects not completely accounted for in our model. To factor in how well our chosen model represents the data, we estimated an

additional systematic error for our parameters (displayed in Table 5.3 of the Appendix 5.7.4). To do this we rerun our MCMC, starting from the best fit solution, with an extra variance parameter (effectively modelling all the physical/observational effects not included in our model) in our log probability for each frequency band. This variance is equivalent to the square of the mean absolute deviation of the residuals with respect to our optimal model at each frequency (difference between the best fit model and the data). The resulting uncertainties in the parameters after this extra MCMC run will reflect the full (statistical + systematic) uncertainties.

Our broad frequency coverage, in particular the high sub-mm frequencies, is crucial to the success of our modelling. Detailed substructure detected in the sub-mm bands can be used to separate out emission from different ejections, where their lower frequency counterparts are smoothed out and blended together. As such, modelling the lower frequency emission would not be possible without the critical information the high frequency sub-mm emission provides and vice versa.

Table 5.2: V404 Cyg Jet Model Best Fit Parameters during the 2015 June 22 Epoch

Compact Jet Parameters[a]

$F_{0,cj}$ (mJy)	α
$56.22^{+0.19}_{-0.21}$	$-0.46^{+0.03}_{-0.03}$

Individual Jet Ejecta Parameters

Ejection	t_{ej} (HH:MM:SS.S)	t_{ej} (MJD)	i (degrees)	ϕ_{obs} (degrees)	τ_0	p^b	F_0 (mJy)	β_b (v/c)	β_{exp} (v/c)[c]
1	$10{:}23{:}42.4^{+8.5}_{-8.0}$	$57195.4331^{+0.0001}_{-0.0001}$	$39.73^{+1.64}_{-1.57}$	$4.06^{+0.24}_{-0.22}$	$1.96^{+0.01}_{-0.01}$	$3.18^{+0.03}_{-0.03}$	$986.8^{+6.2}_{-5.4}$	$0.290^{+0.006}_{-0.006}$	$0.014^{+0.001}_{-0.001}$
2	$10{:}36{:}09.4^{+3.6}_{-3.4}$	$57195.4418^{+0.0001}_{-0.0001}$	$58.80^{+1.37}_{-2.04}$	$9.86^{+0.73}_{-0.47}$	$2.60^{+0.01}_{-0.01}$	$5.69^{+0.01}_{-0.01}$	$1672.6^{+8.3}_{-9.3}$	$0.115^{+0.005}_{-0.007}$	$0.017^{+0.002}_{-0.001}$
3	$11{:}21{:}35.1^{+50.9}_{-46.6}$	$57195.4733^{+0.0006}_{-0.0005}$	$87.98^{+0.06}_{-0.07}$	$5.36^{+0.03}_{-0.03}$	$1.28^{+0.03}_{-0.03}$	$1.54^{+0.01}_{-0.01}$	$3909.1^{+95.1}_{-108.3}$	$0.574^{+0.011}_{-0.013}$	$0.066^{+0.002}_{-0.003}$
4	$11{:}28{:}58.2^{+7.5}_{-7.3}$	$57195.4785^{+0.0001}_{-0.0001}$	$68.47^{+1.33}_{-1.42}$	$4.63^{+0.44}_{-0.39}$	$1.58^{+0.02}_{-0.02}$	$2.15^{+0.01}_{-0.01}$	$2050.1^{+8.5}_{-8.3}$	$0.392^{+0.006}_{-0.006}$	$0.032^{+0.003}_{-0.003}$
5^d	$12{:}30{:}42.6^{+94.2}_{-99.6}$	$57195.5213^{+0.0011}_{-0.0012}$	$75.23^{+0.06}_{-0.05}$	$5.15^{+0.07}_{-0.07}$	$1.72^{+0.01}_{-0.01}$	$2.51^{+0.03}_{-0.03}$	$5496.2^{+186.8}_{-175.8}$	$0.861^{+0.003}_{-0.003}$	$0.148^{+0.003}_{-0.003}$
6	$12{:}32{:}47.6^{+87.4}_{-90.3}$	$57195.5228^{+0.0010}_{-0.0010}$	$85.51^{+0.08}_{-0.08}$	$6.06^{+0.03}_{-0.03}$	$1.71^{+0.01}_{-0.01}$	$2.48^{+0.02}_{-0.02}$	$2404.7^{+73.5}_{-65.0}$	$0.606^{+0.010}_{-0.010}$	$0.081^{+0.002}_{-0.002}$
7	$12{:}39{:}39.5^{+8.8}_{-9.4}$	$57195.5275^{+0.0001}_{-0.0001}$	$87.86^{+0.42}_{-0.28}$	$6.95^{+0.17}_{-0.17}$	$1.20^{+0.05}_{-0.03}$	$1.40^{+0.01}_{-0.01}$	$1756.4^{+11.8}_{-11.9}$	$0.186^{+0.005}_{-0.005}$	$0.023^{+0.001}_{-0.001}$
8	$12{:}42{:}43.2^{+6.6}_{-6.9}$	$57195.5297^{+0.0001}_{-0.0001}$	$87.84^{+0.12}_{-0.20}$	$7.72^{+0.33}_{-0.21}$	$2.10^{+0.01}_{-0.01}$	$3.60^{+0.03}_{-0.04}$	$1491.9^{+13.8}_{-14.6}$	$0.085^{+0.002}_{-0.004}$	$0.012^{+0.001}_{-0.001}$

[a] The emission from the underlying compact jet portion of our model is best fit by a single power-law rather than a broken power-law.
[b] The index of the electron energy distribution, p, is not a fitted parameter but rather is solved for using values of τ_0 and Equation 4.
[c] The expansion velocity, β_{exp}, is not a fitted parameter but rather is solved for using values of β_b, i, ϕ_{obs} and Equation 11.
[d] We note that the receding component for this ejection is not well constrained, as it is modelled primarily by the SMA data at later times when the VLA observations had stopped (see Figure 5.6). Therefore, the parameters for this ejection should be treated with caution.
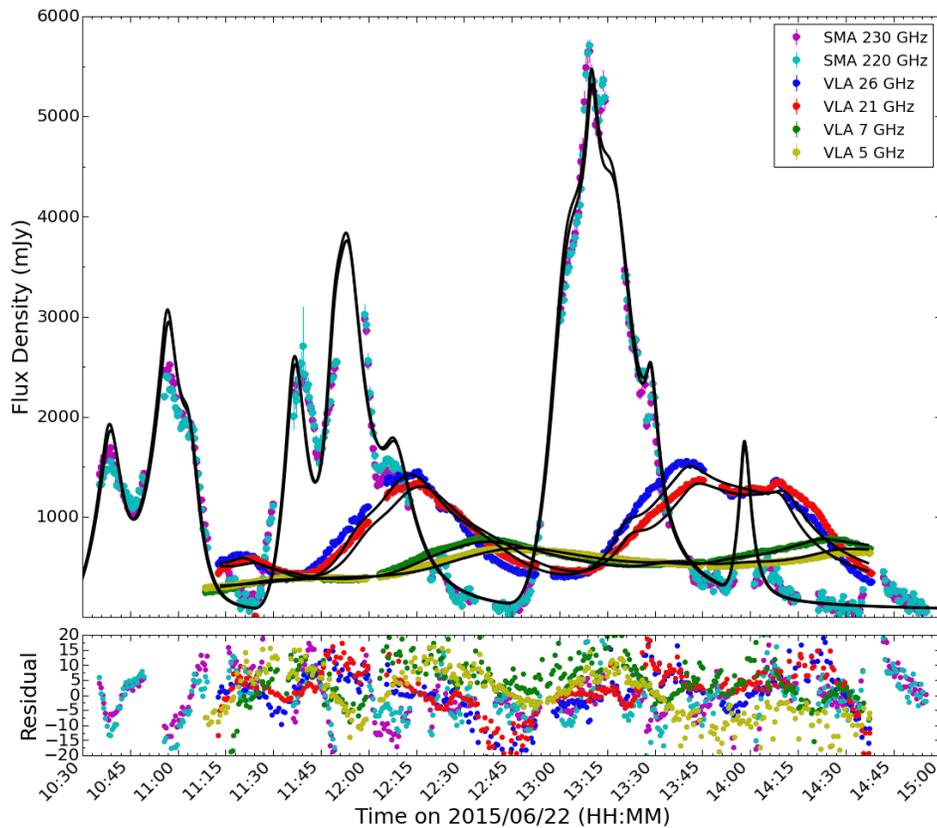
Figure 5.5: Radio through sub-mm light curves of V404 Cyg on 2015 June 22. In the top panel we have overlaid the predicted best fit model at each frequency (black solid lines) on top of the light curves. The residuals are shown in the bottom panel, where, residual=(data-model)/(observational uncertainties). The JCMT 350 GHz data are not shown in this figure even though they are included in the fit. We do this for the sake of clarity in the figure, due to the small time lag between the JCMT and SMA data (see Figure 5.6 for the JCMT 350 GHz light curve and model). With a total of 8 bi-polar ejection events, our model can reproduce the emission we observe from V404 Cyg at all of our sampled frequencies remarkably well.
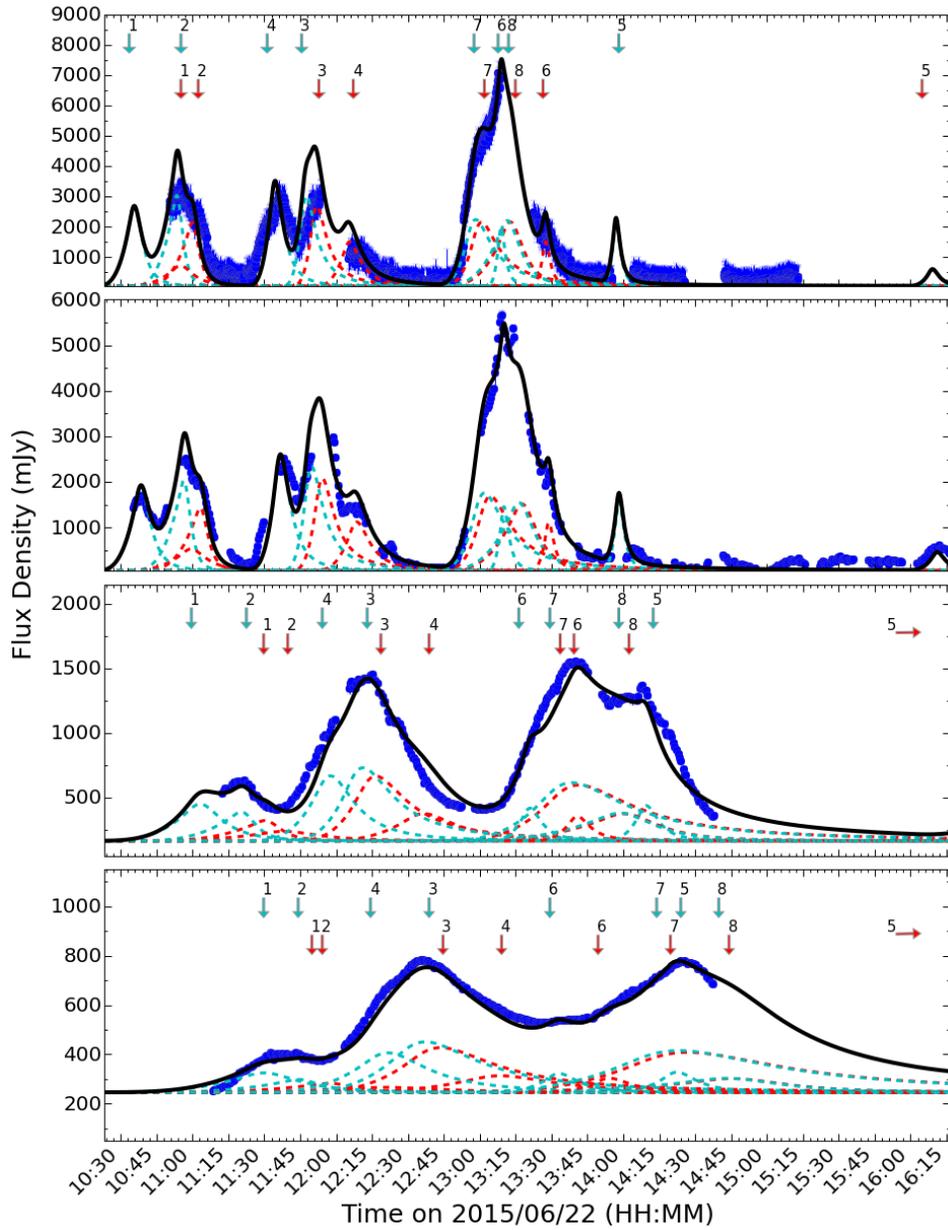
Figure 5.6: V404 Cyg light curves at representative frequencies; 350 GHz (top), 230 GHz (2nd from top), 26 GHz (third from top), and 7 GHz (bottom). In all panels, the black solid line indicates the total model, and the dotted lines indicate the approaching (cyan) and receding (red) components of the individual ejection events. The arrows (cyan for approaching, red for receding) identify which flares correspond to which ejection number from Table 5.2. Note that we do not attempt to model all of the sub-mm emission at times after the VLA observations had stopped.

5.5 Discussion of the Best Fit Model

Our jet model for V404 Cyg, with a total of 8 bi-polar ejection events on top of an underlying compact jet, is able to reproduce the emission in all of our observed frequency bands, matching the flux levels, time lags between frequencies, and the overall morphology remarkably well. With such a large sample of jet ejecta, we can probe the intrinsic ejecta properties, and the distribution of these properties between the different ejection events. In particular, our model characterizes the bulk speeds, peak fluxes, the electron population injected during each event, and the jet geometry, all of which we find can vary between events, with bulk speeds of $0.08 < \beta_b < 0.86$ c, peak fluxes of $986 < S_0 < 5496$ mJy, electron energy distribution indices of $1.4 < p < 5.6$ (corresponding to $1.2 < \tau_0 < 2.6$), and observed opening angles of $4.06 < \phi_{\rm obs} < 9.86°$. In the following sections we discuss these ejecta parameters and what they can tell us about jet speeds, energetics, mass loss, and geometry. Additionally, we draw comparisons between the V404 Cyg ejection events and the jet oscillation events in GRS 1915+105, as well as other multi-wavelength observations of V404 Cyg.

5.5.1 Jet Speeds

The bulk speeds of jet ejecta measured in BHXBs[15] can vary from system to system (e.g., $\Gamma \sim 1$ in SS 433; Hjellming & Johnson 1981, $\Gamma \sim 2$ in V4641 Sgr; Hjellming et al. 2000b), where some systems that are known to enter high luminosity states, like V404 Cyg, have been shown to launch jet ejecta with $\Gamma > 2$ (e.g., GRO J1655-40; Hjellming & Rupen 1995). However, in V404 Cyg we find that the bulk speeds of our modelled ejecta are quite low, with bulk

---

[15]An important caveat when considering the value of the bulk Lorentz factor (Γ), estimated using proper motions of discrete jet ejecta, is that Γ depends strongly on the assumed distance to the source (Fender, 2003). While the distance is well known for V404 Cyg, this is not the case for the majority of BHXBs, and as a result constraints on Γ in these systems typically represent lower limits.

Lorentz factors of only $\Gamma \sim 1 - 1.3$ (excluding ejection 5; see footnote c in Table 5.2 for details).

Moreover, V404 Cyg shows bulk speeds that vary substantially between ejection events, on timescales as short as minutes to hours. There is some evidence in the literature that jet speeds can vary within a BHXB[16] source. For example, Blundell & Bowler (2005) find small variations in jet speed up to 10% in SS 433, jet speeds have been reported to vary between outbursts of H1743-322 (Corbel et al. 2005; Miller-Jones et al. 2012), and varying proper motions have been measured in GRS 1915+105 (Miller-Jones et al., 2007a). However, no other source has shown variations as large, or on as rapid timescales as V404 Cyg.

Performing a Monte Carlo Spearman's rank correlation test, we find no correlation between jet speed and ejection time, where, for instance, the bulk speed of the ejections (i.e., $\beta_b c$) increased or decreased throughout our observation period. However, we find a potential correlation (Spearman coefficient of 0.83 ± 0.07 with a p-value of 0.01) between bulk speed and peak flux of our modelled ejecta, where brighter ejecta tend to have higher speeds. This correlation is consistent with what was seen in H1743-322, where higher bulk ejecta speeds corresponded to higher radio luminosity measurements (Corbel et al. 2005; Miller-Jones et al. 2012).

The factors that govern jet speed in BHXBs are not well understood, but our measurements of surprisingly slow speeds, which can vary between sequential jet ejection events, suggest that the properties of the compact object (i.e., black hole mass) or peak luminosity of the outburst are likely not the dominant factors that affect jet speed.

Additionally, given the varying bulk speeds between the ejection events, it is plausible that later, faster ejections could catch up to earlier, slower ejections.

---

[16]There is also evidence of jet speeds varying in neutron star XBs, most notably, Sco X-1 (Fomalont et al., 2001b,a) and Cir X-1 (Tudose et al., 2008).

Such a collision between ejecta may result in a shock that could be as bright or even brighter than the initial ejections, and in turn produce a flaring profile that could mimic a new ejection event. While including ejecta collisions in our model is beyond the scope of this work, we briefly consider the possibility here by examining the bulk motion of all of the ejections. We find that a collision between ejection 3 and ejection 2 would occur at $\sim 11:30$ (if they were ejected at the same PA), which is very close to the predicted ejection time of ejection 4. Moreover, ejection 4 has a bulk speed which is in between the bulk speeds of ejection 2 and 3, as we might expect for the bulk motion of the plasmon after such a collision. However, given that the jet appears to be rapidly precessing in V404 Cyg (Miller-Jones et al. 2018, in prep., also see Chapter 7 of this thesis), ejection 2 and ejection 3 are launched at very different inclination angles, which would prevent such a collision from occurring. Therefore, given the precessing jet, we find this collision scenario unlikely.

5.5.2 Jet Energetics, Mass Loss, and Particle Acceleration

In our model we assumed that the radiating electrons follow a power-law energy distribution. The power-law index of this distribution, p, informs us about the population of accelerated electrons initially injected into each discrete jet component, where the value of this energy index is governed by the electron acceleration mechanism. Fermi acceleration by a single shock can produce values of $p \sim 2 - 3$, which are typically found in XBs (Blandford & Eichler, 1987; Bell, 1978; Markoff et al., 2001). However, the energy index can take on a wider range of values under certain conditions, where for example, lower values of p (which result in a more asymmetric flare profile) can be produced if the acceleration occurs in multiple shocks (Melrose & Pope, 1993), or if the electrons carry away kinetic power from the shock (Drury & Volk, 1981), and higher values

of p could be produced in the presence of oblique shocks (although this case requires highly relativistic shocks to produce large p values; Ballard & Heavens 1992). Distributions with values of $p > 4$ are nearly indistinguishable from a thermal (Maxwellian) distribution, which in the shock acceleration paradigm, implies very little acceleration has occurred (a shock essentially takes an input thermal distribution of electrons and builds a power-law distribution up over time). Magnetic reconnection in a relativistic plasma is another viable mechanism that can accelerate electrons into distributions with similar p values to shock acceleration. In this case, smaller p values can be produced in the case of a strongly magnetized plasma ($\sigma > 10$; where $\sigma \equiv B^2/4\pi nmc^2$ represents the magnetization parameter), and larger p values can be produced in a weakly magnetized plasma ($\sigma \sim 1$; Sironi & Spitkovsky 2014; Guo et al. 2014; Sironi et al. 2016). In either theory of particle acceleration, we would expect a link between the speed (for shock acceleration) or magnetization (for magnetic reconnection), and the energy index, p.

The energy indices of our modelled ejecta appear to vary between sequential ejection events, with $1.4 < p < 5.6$ (where we find no clear correlation between p values and jet speed). These p values could be produced by shock acceleration or magnetic reconnection (under the right conditions), although we would need to invoke different mechanisms to produce distributions in both the very low and very high p regimes (e.g., 1.4 in ejection 7, and 5.7 in ejection 2), which is not entirely physical for a single source. Further, this significant range seen in our energy indices suggests that our model may not be capturing all of the complexities of these ejection events, where the more extreme values of the energy index could be mimicking the effect of physics that has not been included in our model. For instance, the vdL model assumes equipartition, but as the plasmons expand they must do work, which will result in some of the magnetic field dissipating into kinetic or thermal pressure, and in turn, the assumption of equipartition may break down. Simplifications in our model such as this could

153

also explain the lack of expected correlation between our energy indices and the speed of the ejecta. A more rigorous treatment, which, for example, calculates the full synchrotron flux (and does not rely on the equipartition assumption), is beyond the scope of this work, but will be considered in future iterations of this model.

For synchrotron emitting clouds of plasma injected with our measured electron distributions, we estimate that the minimum energy[17] needed to produce each of our modelled ejection events range from $5.0 \times 10^{35} < E_{\min} < 3.5 \times 10^{38}$ erg, with minimum energy magnetic fields[18] on the order of a few Gauss ($1 < B_{\min} < 35$ G). Taking into account the duration of each event, these energies correspond to a mean power into each event ranging from $4.0 \times 10^{32} < P_{\min} < 2.5 \times 10^{35}$ erg s^{-1}. Due to the slow bulk speeds of the ejecta, including the kinetic energy from the bulk motion (in an electron-positron plasma $E_{\mathrm{KE}} = (\Gamma - 1)E_{\min}$) yields only slightly higher values of $4.1 \times 10^{32} < P_{\mathrm{tot}} < 2.6 \times 10^{35}$ erg s^{-1}. The minimum energy and power released within each of our modelled ejection events is comparatively lower than estimated for other major ejection events in BHXBs ($E_{\min} \sim 1 \times 10^{43}$ erg; e.g., Fender et al. 1999a and $P_{\mathrm{tot}} \sim 10^{36} - 10^{39}$ erg s^{-1}; e.g., Fender et al. 1999a; Brocksopp et al. 2007; Curran et al. 2014). This difference is dominated by the difference in the estimated size of the emitting region, where the radii of our modelled ejecta are smaller than is normally estimated for major ejection events, and the low bulk speeds, which result in a much smaller kinetic energy contribution. Considering that the flaring activity in V404 Cyg lasted ~ 2 weeks (and assuming our obser-

---

[17]In our minimum energy calculations, we perform the full calculations outlined in Longair (2011), where we integrate the electron energy distribution from $\nu_{\min} = 150$ MHz to $\nu_{\max} = 666$ GHz. The minimum frequency represents the lowest radio detection with LOFAR on June 23 & 24 (Broderick et al., 2015), and the maximum frequency represents our highest frequency sub-mm detection. When we consider an electron-proton plasma, we assume the ratio of the energy in the protons over that of the electrons is $\frac{\epsilon_p}{\epsilon_e} = 1$.

[18]We note that while these calculation assume equipartition, the system could be far from equipartition. In this case the magnetic field would not necessarily be equivalent to the minimum energy field, but rather could be either much higher or much lower.

vations to be representative of this entire period), we estimate that the the total (minimum) energy (radiative + kinetic) released into jet ejections over the full flaring period is $\sim 3.2 \times 10^{40}$ erg, which is more on par with typical energies estimated for major ejection events in BHXBs. This total energy is also comparable to that carried by the accretion disc wind ($\sim 10^{41}$ erg)[19].

If we assume that the jet ejecta contain some baryonic content, in the form of one cold proton for every electron, we calculate that the mean power into each event (including the kinetic energy from bulk motion) ranges from $6.2 \times 10^{32} < P_{\text{tot}} < 3.8 \times 10^{35} \, \text{erg} \, \text{s}^{-1}$. In this baryonic case, we estimate a total mass lost through the jet in our observation period of $9.4 \times 10^{-13} \, M_\odot$ (corresponding to $7.2 \times 10^{-11} \, M_\odot$ over the 2 week flaring period). To compare this jet mass loss to the mass accreted onto the black hole, we follow a procedure similar to Muñoz-Darias et al. (2016), using simultaneous INTEGRAL X-ray observations (only including the harder ISGRI bands, ranging from 25-200 keV) to calculate the total energy radiated (integrated X-ray luminosity) during our observations. To do this we convert the count rate into flux in the 10–1000 keV band using a power law model with photon index $\Gamma_p \sim 1-2$, and approximating the integral as a sum ($\int L_X dt \approx \sum_i L_i \delta t = \bar{L} \Delta T$, where $\bar{L}$ is the weighted mean, δt is size of the time bins, and ΔT is the total observation time). Assuming an accretion efficiency of 0.1, we calculate a total mass accreted during our observations of $M_{\text{acc,BH}} = 3.4 \times 10^{-11} - 7.8 \times 10^{-11} \, M_\odot$. Therefore, the mass lost in the jet is a small fraction of the total mass accreted, $M_{\text{jet}} = (1-3) \times 10^{-2} \, M_{\text{acc,BH}}$, and much less than the mass estimated to be lost in the accretion disc wind ($\sim 1000 M_{\text{acc,BH}}$; Muñoz-Darias et al. 2016).

---

[19]A rough estimate of the energy lost in the accretion disc wind is equivalent to $E_{\text{wind}} \sim (1/2) M_{\text{wind}} v_{\text{wind}}^2$. Using $M_{\text{wind}} \sim 10^{-8} \, M_\odot$ and $v_{\text{wind}} \sim 1000 \, \text{km} \, \text{s}^{-1}$ (Muñoz-Darias et al., 2016), we estimate $E_{\text{wind}} \sim 10^{41}$ erg.

5.5.3 Jet Geometry and Ejecta Size Scale

Measurements of jet geometry in BHXBs, in particular the observed opening angle, only exist for a handful of systems, where all but one are upper limits (e.g., see Table 1 in Miller-Jones et al. 2006, as well as Yang et al. 2010 and Rushton et al. 2017 for recent measurements in XTE J1752-223 and XTE J1908+094). Our simultaneous light curve modelling technique allows us to directly derive the first measurements of the jet geometry in V404 Cyg, where we model observed jet opening angles of $4.06 < \phi_{\mathrm{obs}} < 9.86°$. These measurements are consistent with the opening angle estimates for the other BHXB systems with constraints, where the majority show $\phi_{\mathrm{obs}} \lesssim 10°$.

With the opening angles, we can estimate the level of confinement of the jets in V404 Cyg by solving for the intrinsic expansion speed (using Equation 5.11; see last column of Table 5.2) of our modelled ejecta ($\beta_{\mathrm{exp}}c = \frac{c}{\sqrt{3}}$ indicates freely expanding components, where $\frac{c}{\sqrt{3}}$ represents the speed of sound in a relativistic gas). We find intrinsic expansion speeds of $0.01 < \beta_{\mathrm{exp}} < 0.1$ c, indicating a highly confined jet in V404 Cyg. There are many possible mechanisms that could be responsible for confining the jets in V404 Cyg. In particular: the jet could be inertially confined (Icke et al., 1992), where the ram pressure of the strong accretion disc wind detected in V404 Cyg (Muñoz-Darias et al., 2016) could inhibit the jet ejecta expansion[20]; the jet could be magnetically confined by a toroidal magnetic field (Eichler, 1993); the jet could contain cold protons, which may impede the jet ejecta expansion (Miller-Jones et al., 2006); or a combination of these different mechanisms could be at work.

Further, as we alluded to in the previous section, the initial radii of the jet ejecta (i.e., the radii of the ejecta at the time the sub-mm emission peaks)

---

[20]Although, we note that if the confinement is external, this would suggest that a very large amount of pressure surrounds the ejections. If this is supplied solely by the ram pressure from an accretion disc wind, then the mass-loss rate (proportional to the velocity ratio of the ejections to the wind) would be unrealistically large (i.e., greater then the mass accretion rate).

estimated by our model are noticeably smaller than those typically estimated for major ejection events in other BHXBs. This is likely a result of the much slower expansion velocities ($\beta_{\mathrm{exp}} << 1$) we find for the V404 Cyg ejecta. In particular, we infer a range of initial radii for our ejecta ranging from $(0.6 - 1.3) \times 10^{12}$ cm. These radii appear to remain similar (to within a factor of 2) between ejection events.

5.5.4 Underlying Compact Jet

In addition to the jet ejecta component, we observe an extra constant flux component in our light curves, which varies with frequency. Due to the shape of our estimated spectrum of this emission (see Figure 5.2) and the strong compact core jet present throughout the span of our simultaneous VLBA imaging (Miller-Jones et al. 2018, in prep., also see Chapter 7 of this thesis), we interpret this extra flux term as emission from an underlying compact jet. We believe that this compact jet was switched on during the launching of the multiple discrete ejection events. In our best fit model, this compact jet emission is characterized by a single power-law spectrum, with an optically thin spectral index of $\alpha = -0.46^{+0.03}_{-0.03}$.

Our suggestion of a compact jet, that has not been fully quenched, is in agreement with the findings of Sánchez-Fernández et al. (2017), who show that V404 Cyg never fully reached a soft accretion state (where we would likely expect strong quenching of the compact jet; e.g., Rushton et al. 2016), but rather remained in either a harder intermediate or very high state during our observations. Under this interpretation, based on our lowest radio frequency measurement, we place limits on the optically thick to thin jet spectral break frequency of $\nu_{\mathrm{br}} < 5.25$ GHz, and flux at the spectral break of $S_{\mathrm{br}} > 318$ mJy. However, we note that simultaneous VLITE observations (Kassim et al., 2015) detect V404 Cyg at a total time-averaged flux density of 186 ± 6 mJy at 341 MHz. Given that our best fit model predicts a maximum jet ejecta flux

component of ~ 100 mJy at 341 MHz, it is clear that the 341 MHz compact jet component cannot lie along the single power-law stated above. As such, the spectral break would therefore occur within the range of $0.341 < \nu_{\mathrm{br}} < 5.25$ GHz, which is significantly lower than previous estimates for V404 Cyg made during the hard accretion state ($\nu_{\mathrm{br}} = 1.82 \pm 0.27 \times 10^5$ GHz; Russell et al. 2013b,c). This evolution in the location of the spectral break is consistent with the pattern suggested by recent observations (e.g., Corbel et al. 2013; van der Horst et al. 2013; Russell et al. 2014) and MHD simulations (Polko et al., 2014), where, as the mass accretion rate increases during softer accretion states of BHXB outbursts (which usually occur at high luminosities; Koljonen et al. 2015), the jet spectral break moves toward lower radio frequencies prior to the jet switching off (or at least fading below our detection limits).

Up to now we have only considered the compact jet and the ejection events as separate entities. In the presence of explosive, energetic ejection events, we might expect a compact jet to be disrupted. In particular, as the ejecta collide with the pre-existing compact jet, a shock would likely develop, due to the difference in bulk speeds between the two. In this situation, if the compact jet rapidly re-establishes itself after being destroyed by ejecta (before the ejecta propagate far enough away from the black hole to be resolved), we would observe a compact core jet which appears to never shut off. Therefore, we believe it is plausible that a compact jet is being repeatedly destroyed and re-established (on rapid timescales) following ejection events in V404 Cyg. Further, the emission from such a shock interaction could display an optically thin spectrum (similar to the interaction between the discrete ejecta and the surrounding ISM; e.g., Corbel et al. 2004), like the one we observe for our baseline emission component. Thus, while we interpreted the baseline emission in our light curves as originating only from a compact jet, emission from a possible interaction of the jet ejecta with this compact jet, and/or continuous lower-level, fainter jet ejecta that never get resolved, could also be contributing

158

to the baseline flux level we observe.

Moreover, in our model we have assumed that the compact jet flux component is constant in time. However, as the accretion rate (and in turn the jet power) changes, the flux of a compact jet is expected to change as well (Russell et al., 2014). If we consider the erratic X-ray behaviour observed in the source (which presumably traces a rapidly changing accretion rate), it is plausible that the compact jet component could in fact be variable as well. Exploring the possibility of a variable compact jet component in our model is left for future work.

5.5.5 Ejecta Time Lags

Our model predicts that the intrinsic time lag (in the source frame) between a certain frequency (ν) and the reference frequency (ν_0), is represented by,

$$t_{\nu-\nu_0,\mathrm{src}} = \left(\frac{R_0}{\beta_{\mathrm{exp}}}\right)\left\{\left(\frac{\nu_0}{\nu}\right)^{\frac{p+4}{4p+6}} - 1\right\} \tag{5.15}$$

where the observed time lag can be obtained through the transformation, $t_{\nu-\nu_0,\mathrm{obs}} = \frac{t_{\nu-\nu_0,\mathrm{src}}}{\delta_{\mp}}$.

Figure 5.7 shows the observed time lags, predicted by our model, between each frequency band and the ejection time, for the approaching (top panel) and receding (bottom panel) components. The time lags are clearly variable between different ejection events (e.g., $\sim 10 - 30$ min between the ejection and our reference frequency, 230 GHz), which is a result of the varying ejecta properties (i.e., β_{exp}, p, R_0).

Further, it is interesting to note that, for a different flaring event that occurred ~ 2 days after our data set, Shahbaz et al. (2016) measured a time lag of 2.0 hours & 3.8 hours between the predicted ejection time (indicated by an r'-band polarization flare, which these authors suggest could be the signature of the launching of a major jet ejection event) and the flare peaks at 16 GHz
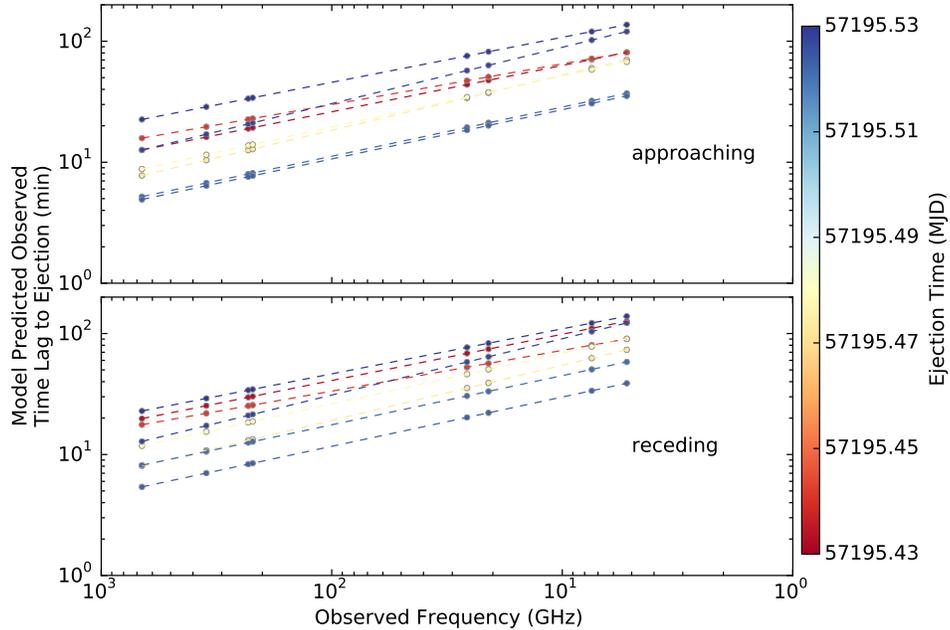
Figure 5.7: Observed time lag, predicted by our model, between our sampled frequency bands and the time of ejection, for the approaching (top panel) and receding (bottom panel) components of each ejection event. The data points are coloured by ejection time, where the colour bar indicates the ejection time of the event in MJD.

& 5 GHz, respectively. These lags are slightly higher than predicted for the approaching components of our modelled ejection events, but appear to share a similar slope across frequencies.

5.5.6 Comparison to GRS 1915+105

GRS 1915+105 is the only other BHXB in which a similar multi-frequency variability pattern to that seen in V404 Cyg has been reported. While flaring activity has been seen in other systems, it is often only detected in one frequency band (e.g., V4641 Sgr in optical; Uemura et al. 2004), or the flares in question evolved over much longer (days rather than minutes/hours) timescales (e.g., 4U 1630-47 in radio/X-ray; Hjellming et al. 1999). GRS 1915+105 has displayed some correlated radio, sub-mm, and IR flares (with lower frequency emission delayed from higher frequency emission), which repeated every $\sim$ 20

160

minutes for a ≥ 10 day period (Fender & Pooley, 2000). While no discrete components were resolved with VLBI during the events, the similar rise and decay times of flares at different frequencies suggest that adiabatic energy losses, likely during the expansion of discrete components, played a key role in determining the flaring profiles of these events. In fact, Mirabel et al. (1998) found that the timing of the radio emission during these events was consistent with synchrotron emission from adiabatically expanding plasma clouds, where each event required an energy input of $\sim 10^{39}$ erg, and carried an estimated mass of $\sim 10^{18}$ g. Many studies of these jet ejection events suggest that they occur as a result of instabilities causing the repeated ejection and refilling of the inner accretion disc or coronal flow (e.g., Belloni et al. 1997; Nandi et al. 2001; Vadawale et al. 2001).

In V404 Cyg our modelled ejection times appear to occur on a similar rapid timescale as seen in GRS 1915+105, where we observe groups of 2-4 ejections (separated by at most ~ 20 minutes), followed by longer periods of up to ~ 1 hour between groups (see Figure 5.8). Each group of ejections seems to correspond to a large flaring event in the light curves. Our estimates of the energetics and mass-loss of the V404 Cyg events (§5.5.2) are also similar to those estimated for the oscillation events in GRS 1915+105, where both are consistent with being smaller-scale analogues of major ejection events seen in other BHXBs. Further, Naik et al. (2001) suggested that multiple ejections in GRS 1915+105 could manifest as a single radio flare, similar to the ejection groupings we see in V404 Cyg. However, a noticeable difference in the timing of the V404 Cyg and GRS 1915+105 events is that the V404 Cyg events are not as quasi-periodic (i.e., they do not occur on as regular intervals) when compared to the GRS 1915+105 events, which occurred every ~ 20 min (Fender & Pooley, 2000). The absence of quasi-periodicity in the V404 Cyg events could indicate that the jet production process is not as stable in V404 Cyg as it was during the GRS 1915+105 events.

The similarity between the morphology, duration and energetics of the rapid ejection periods in V404 Cyg and GRS 1915+105 suggests that the events may have a common origin, possibly in the repeated ejection and refilling of some reservoir in the inner accretion flow. This hypothesis is consistent with the recent finding of Radhika et al. (2016), who report the non-detection of the disc component in the X-ray spectra following major radio flares in V404 Cyg. Although, given the large intrinsic absorption (Motta et al., 2017a) seen in V404 Cyg during the outburst, it is conceivable that we may not have been able to detect the soft disc component, even if it was present. Nevertheless, as both V404 Cyg and GRS 1915+105 are long period systems, with large accretion discs, a key ingredient in fuelling rapid, repeated ejection events may be a large accretion disc (as suggested by Kimura et al. 2016; Muñoz-Darias et al. 2016).

5.5.7 Alternative Emission Models

Other than the vdL model, an alternative emission model that has been used to reproduce flaring light curves in XBs is the shock-in-jet model (Marscher & Gear, 1985; Bjornsson & Aslaksen, 2000; Turler et al., 2000). This analytical model, while traditionally favoured for extragalactic sources, has been successfully applied to flaring events in Cyg X–3 (Lindfors et al., 2007; Miller-Jones et al., 2009), GRO J1655−40 (Stevens et al., 2003), and GRS 1915+105 (Turler et al., 2004). The shock-in-jet model considers a shock wave travelling downstream in a jet flow as the source of each flare in the light curve. Each shock wave will evolve through three different phases; (1) Compton losses dominate, (2) synchrotron losses dominate, and (3) adiabatic losses dominate. The main differences between the shock-in-jet model and the vdL model are that the shock-in-jet model considers an initial phase where Compton losses dominate over adiabatic losses, all shock wave events are self-similar, and the electron energy scales differently when compared to the vdL model (shock-in-jet flow

expands in 2D, $E \propto R^{-2/3}$; vdL cloud expands in 3D, $E \propto R^{-1}$). These differences will result in a different flare profile between models, where for the same electron population (i.e., same p value), the shock-in-jet model flares will show a much shallower decay, and the peak fluxes at frequencies that are initially optically thin (likely IR and above) will be smaller than predicted by the vdL model (which will over predict peak fluxes at these frequencies).

As our adapted vdL model is able to reproduce all our light curves (at 7 different frequencies) remarkably well, and simultaneous VLBA imaging resolves multiple, discrete components (Miller-Jones et al. 2018, in prep., also see Chapter 7 of this thesis), we favour the expanding plasmon model over the shock-in-jet model for the V404 Cyg events (although we can not rule out the shock-in-jet model).

However, for the GRS 1915+105 oscillation events, the emission has been shown to be consistent with both an expanding plasmon model (Mirabel et al. 1998; although we note that these authors only model a single flaring event, and did not include any relativistic/projection effects in their model) and a shock-in-jet model (Turler et al., 2004). If the GRS 1915+105 events are in fact a result of shock waves rather than expanding plasmons, this could explain the notable differences to the V404 Cyg events, namely the quasi-periodicity and the lack of VLBI resolved components[21]. Additionally, as Turler et al. (2004) point out, the shock-in-jet model is still consistent with the scenario that these oscillation events originated with instabilities in the inner accretion disc, as these instabilities could be the catalyst that leads to an increased injection rate of material at the base of the jet, and in turn a downstream shock wave.

---

[21]Although, we note that these GRS 1915+105 oscillation events were only observed with MERLIN (Fender et al., 1999a), which does not have the resolution to see ejection events of a few mas in size (like those of V404 Cyg).

5.5.8 Connection to X-ray & OIR

If the jet ejection events in V404 Cyg are linked to processes occurring in the accretion flow, we might expect our predicted ejection times to correlate well with X-ray/OIR emission. For instance, in GRS 1915+105, IR and radio flares (which are presumably tracers of the ejection events) followed an X-ray peak and occurred during a period of spectral softening (dips in hard X-ray emission). However, the connection is not as clear in V404 Cyg. Figure 5.8 displays our predicted ejection times on top of simultaneous X-ray[22] (Rodriguez et al., 2015) and OIR (Kimura et al., 2016) emission.

Flares in the OIR light curve appear to coincide with flares in the X-ray light curves. However, an unfortunate gap in the OIR coverage makes it difficult to confirm that such a pattern holds for the final X-ray flare. In terms of our modelled ejection times, we may be able to tentatively match groups of ejections with specific X-ray/OIR peaks, and possibly local dips in hardness (where the start/end of a steep gradient in hardness appears to correspond to ejections). But it is puzzling that the group which contains the largest number of ejections and produces the largest sub-mm flares appears to be connected to the X-ray flare with the smallest amplitude (although, if an X-ray flare is indicative of a strong dissipative process, more energy dissipated in the X-ray implies less energy would be available to the jets, and vice versa). Further, the second X-ray flare appears to have no jet ejecta counterpart.

Given the extremely high intrinsic absorption during this time period (Motta et al., 2017a), it is entirely possible that the flaring in the X-ray light curves is not always dominated by intrinsic source variation, but rather dependent on how much of the inner accretion flow is obscured. This effect was seen in the 1989 outburst, where large changes in column density were determined to be the origin of some of the extreme X-ray variability observed (Oosterbroek

---

[22]All X-ray data presented in this paper are taken from the INTEGRAL public data products available at `http://www.isdc.unige.ch/integral/analysis#QLAsources`.

et al., 1997; Zycki et al., 1999). Thus, even if the jet ejections are linked to processes in the accretion flow, we may not expect to see a clear correlation between our jet ejections and the X-ray/OIR emission. On the other hand, if the high absorption reduced the X-ray flux artificially, we would expect the high energy bands (60-200 keV) to be less affected than the lower energy bands (5-10 keV), which does not seem to be the case here. Therefore, the nature of the connection (if any) between our jet ejections and the X-ray/OIR emission is still not fully understood.

5.5.9 The Critical Sub-mm Perspective

Traditionally XB jet studies have been dominated by radio frequency observations, such that there only exists a limited set of XBs that have been observed at mm/sub-mm frequencies (e.g., Paredes et al. 2000; van der Horst et al. 2013; Russell et al. 2013c; Fender et al. 2001; Tetarenko et al. 2015d). When considering time-resolved (< 1 day cadence) mm/sub-mm observations this number decreases to two (i.e., GRS 1915+105; Pooley & Fender 1997, Cygnus X-3; Baars et al. 1986; Fender et al. 1995). However, our work in this paper has clearly shown the vital importance of high time resolution mm/sub-mm data in XB jet studies. In particular, the mm/sub-mm bands can be used to isolate emission from different flaring events in the light curves, while the lower frequency counterparts of these events tend to be smoothed out and blended together. As such, we find that radio frequency observations alone can often be misleading, especially in terms of identifying and pinpointing the timing of individual rapidly variable flaring events. Including mm/sub-mm monitoring during future XB outbursts will continue to add key insight to our understanding of jet behaviour.
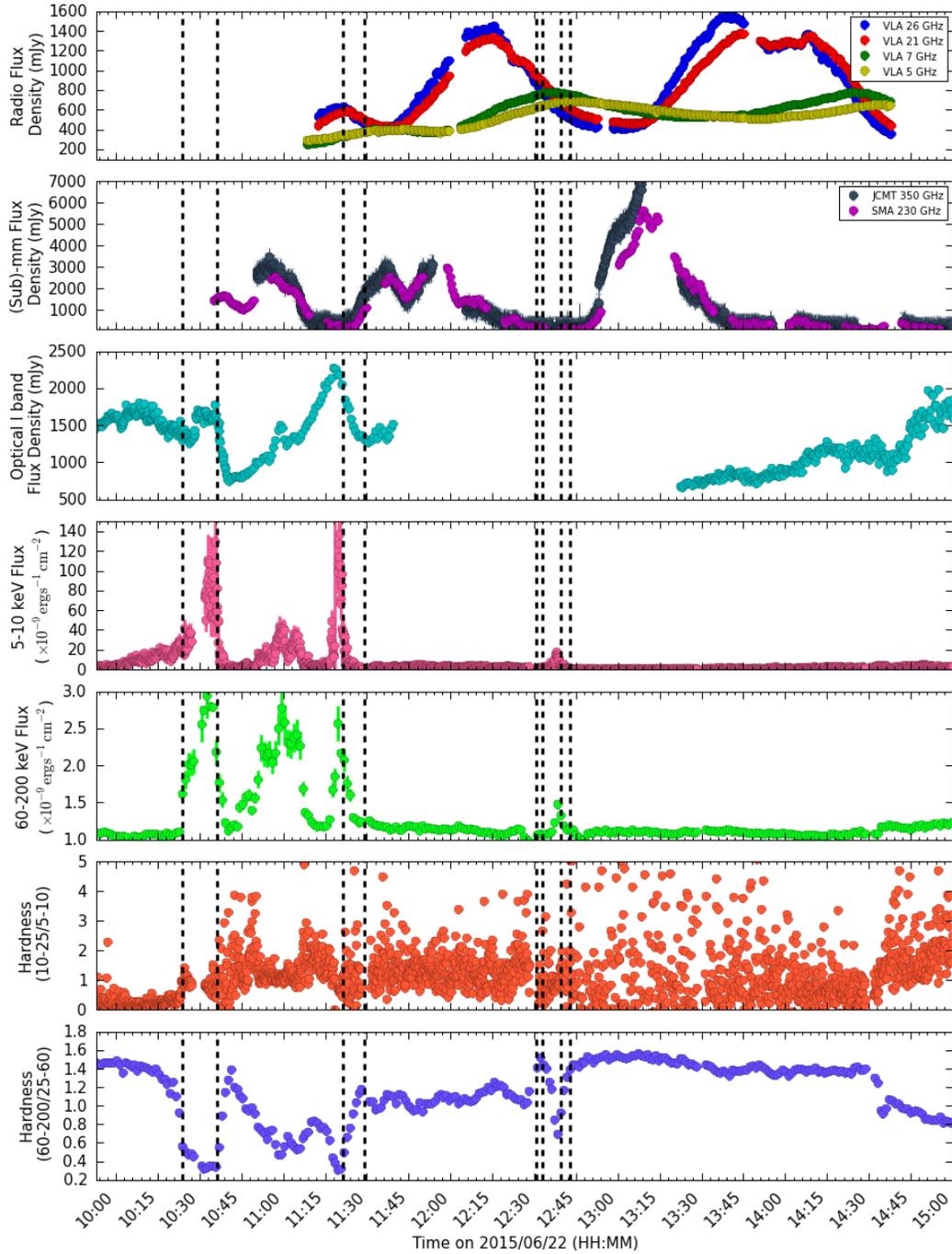
Figure 5.8: The evolution of the emission properties of V404 Cyg on June 22. Top to bottom the panels represent radio light curves, (sub)-mm light curves, optical light curve (Kimura et al., 2016), soft and hard X-ray light curves, and the 10-15/5-10 keV and 60-100/25-60 keV hardness ratios (Rodriguez et al., 2015). Our modelled ejection times are shown by the dotted vertical lines, where the uncertainties on the ejection times are smaller than the line thickness.

5.6 Summary

In this paper we present the results of our simultaneous radio through sub-mm observations of the BHXB V404 Cyg during its June 2015 outburst, with the VLA, SMA and JCMT. Our comprehensive data set, taken on 2015 June 22 ($\sim$ 1 week following the initial detection of the outburst), extends across 8 different frequency bands (5, 7, 21, 26, 220, 230, 350, and 666 GHz). Using custom procedures developed by our team, we created high time resolution light curves of V404 Cyg in all of our sampled frequency bands. In these light curves, we detect extraordinary multi-frequency variability in the form of multiple large amplitude flaring events, reaching Jy level fluxes.

Based on the overall morphology, we postulate that our light curves were dominated by emission from a relativistic jet. To understand the source of the emission we constructed a detailed jet model for V404 Cyg. Our model is capable of reproducing emission from multiple, discrete, bi-polar plasma ejection events, which travel at bulk relativistic speeds (along a jet axis inclined to the line of sight), and evolve according to the van der Laan synchrotron bubble model (van der Laan, 1966), on top of an underlying compact jet. Through implementing a Bayesian MCMC technique to simultaneously fit all of our multi-frequency light curves with our jet model, we find that a total of 8 bi-polar ejection events can reproduce the emission we observe in all of our sampled frequency bands.

Using our best fit model to probe the intrinsic properties of the jet ejecta, we draw the following conclusions about the ejection events in V404 Cyg:

- The intrinsic properties of the jet ejecta (i.e., speeds, peak fluxes, electron energy distribution indices, opening angles) vary between different ejection events. This results in varying time lags between the flares produced by each ejection at different frequencies.

- The ejecta require (minimum) energies on the order of $10^{35} - 10^{38}$ erg.

When taking into account the duration of each event, these energies correspond to a mean power into the ejection events of $10^{32} - 10^{35}\,\mathrm{erg\,s^{-1}}$.

- The ejecta carry very little mass ($\sim 1\%\ M_{\mathrm{acc,BH}}$), especially when compared to that carried by the other form of outflow detected in V404 Cyg, the accretion disc wind ($\sim 1000\ M_{\mathrm{acc,BH}}$). However, despite carrying much less mass, we estimate that the ejecta carry similar energy to that of the accretion disc winds.

- We place the first constraints on jet geometry in V404 Cyg, where we find that V404 Cyg contains a highly confined jet, with observed opening angles of the ejecta ranging from $4.06 - 9.86°$. While we can not pin down the main jet confinement mechanism in V404 Cyg, it is possible that the ram pressure of the strong accretion disc wind detected in V404 Cyg (Muñoz-Darias et al., 2016) could contribute to inhibiting the jet ejecta expansion, and thus be a key cause of the highly confined jet in this system.

- The ejecta travel at reasonably slow bulk speeds, that can vary substantially between events, on timescales as short as minutes to hours ($\Gamma \sim 1 - 1.3$).

- Brighter ejections tend to travel at faster bulk speeds.

- Our modelled ejection events appear to occur in groups of 2-4 ejections (separated by at most ~ 20 minutes), followed by longer periods of up to ~ 1 hour between groups.

- The rapid timescale of the ejections is similar to the jet oscillation events observed in GRS 1915+105. Although the V404 Cyg events do not occur on as regular intervals as the GRS 1915+105 events, possibly suggesting the jet production process is not as stable in V404 Cyg.

- We can tentatively match groups of ejections with peaks in simultaneous X-ray/OIR emission. However, the nature of the connection (if any) between our modelled ejection events and X-ray/OIR emission is still not completely clear.

Based on these conclusions, it appears as though the V404 Cyg ejection events are smaller-scale analogues of major ejection events, typically seen during the hard to soft accretion state transition in BHXBs. Given the similarity between these rapid ejection events in V404 Cyg and those seen in GRS 1915+105, we postulate that the ejection events in both systems may have a common origin, in the repeated ejection and refilling of some reservoir in the inner accretion flow. This suggests that, in agreement with the findings of Kimura et al. (2016) & Muñoz-Darias et al. (2016), the presence of a large accretion disc in both systems may be a key ingredient in producing these rare, rapid ejection events.

Overall, the success of our modelling has shown that, multiple expanding plasmons, on top of a compact jet, is a good match to the emission we observe from V404 Cyg in multiple frequency bands. However, it is also apparent from our results that some simplifications within our model may not fully capture all of the physics of these ejection events (e.g., assuming equipartition, assuming a constant flux from the compact jet), and future iterations of this model will work to address these assumptions and explore their effect on the ejecta properties.

In this work we have demonstrated that simultaneous multi-band photometry of outbursting BHXBs can provide a powerful probe of jet speed, structure, energetics, and geometry. Additionally, our analysis has revealed that the mm/sub-mm bands provide a critical new perspective on BHXB jets (especially in the time-domain) that can not be achieved with radio frequency observations alone. Future high time resolution, multi-band observations of more systems, including the mm/sub-mm bands, have the potential to provide

invaluable insights into the underlying physics that drives jet behaviour, not only in BHXBs but across the black hole mass and power scale.

5.7   Appendix

5.7.1   Image Weighting Scheme

As we are imaging the source on very short timescales, the *uv*-coverage in each time-bin will be limited. While we do not need to worry about the lack of *uv*-coverage affecting the fidelity of the images, as the source is point-like at the VLA and SMA resolutions, the side-lobe levels may be a concern. In particular, if the amplitude is changing significantly in each time bin, this implies that we cannot deconvolve the side-lobes properly. As such, the choice of weighting scheme used while imaging could affect the quality of the images, and in turn the flux density measurements for each time bin. While the side-lobe level is not much of a concern for the VLA, which has reasonably good instantaneous *uv*-coverage, the SMA is only an 8-element interferometer. In this case, imaging the source with a more uniform weighting scheme minimizes the side-lobe level, and could improve the quality of the images in each time bin. On the other hand, imaging with a natural weighting scheme would maximize sensitivity, leading to lower rms noise levels. After testing different weighting schemes we find that the choice of weighting had very little effect on the output SMA light curves, where any differences in the flux measurements in each time bin were well within the rms noise. We find that the natural weighting scheme led to lower rms noise and slightly higher dynamic range in the majority of the time bin images. Therefore, we opted to use natural weighting, as the side-lobe level/rms noise trade-off appears to be optimized for natural weighting.

5.7.2 Calibrator Light Curves

Given the large flux variations we detected in our data of V404 Cyg, we wished to check the flux calibration accuracy of all of our observations on short time scales, and ensure that the variations we observed in V404 Cyg are dominated by intrinsic variations and not atmospheric or instrumental effects. Therefore, we ran our custom procedures to extract high time resolution measurements from our data (see §5.3 for details) on all of our calibrator sources. Figure 5.9 displays target & calibrator light curves at all frequencies.

We find that all of our interferometric calibrator sources and our JCMT 350 GHz calibrator display relatively constant fluxes throughout our observations, with any variations ($< 5\%$/$< 10\%$ of the average flux density at radio/(sub)-mm frequencies) being a very small fraction of the variations we see in V404 Cyg. However, our JCMT 666 GHz calibrator scan shows noticeably larger scale variations ($\sim 30\%$ of its average flux level). While these larger variations are not unexpected at this high frequency, as the atmosphere is much more opaque, when combined with the fact that higher noise levels at this frequency prevent us from sampling timescales shorter than 60 seconds, we choose to not include the 666 GHz data set in our modelling (although see Appendix 5.7.3 below for a discussion of how well our best fit model agrees with the 666 GHz data).

Overall, based on these results, we are confident that the high time resolution light curves of V404 Cyg used in our modelling are an accurate representation of the rapidly changing intrinsic flux of the source.
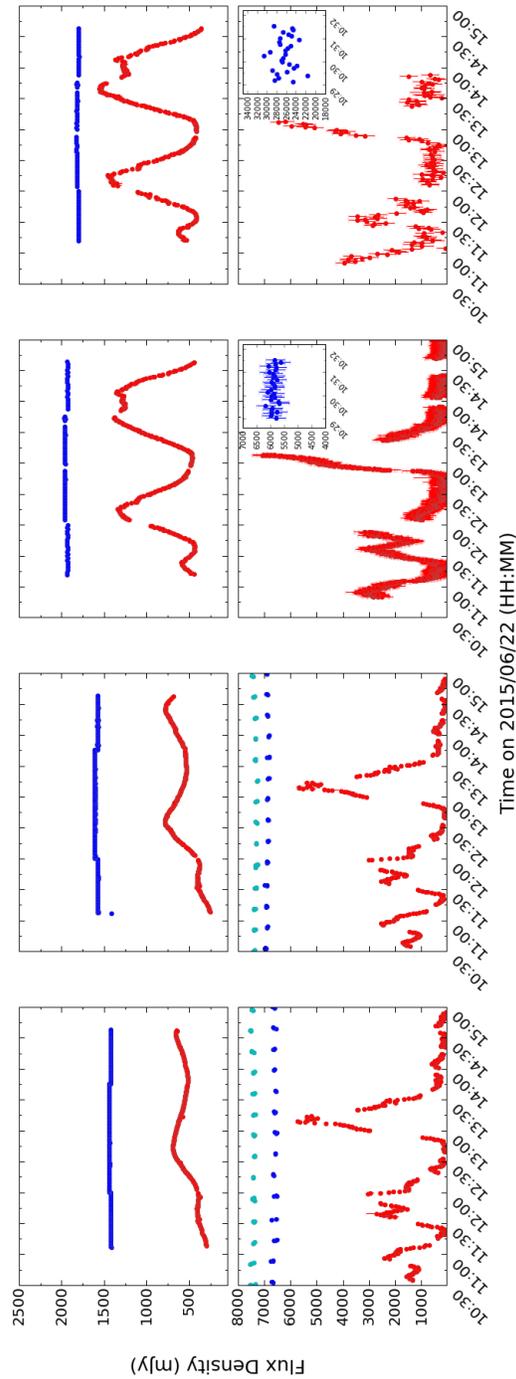
Figure 5.9: Multi-frequency light curves of V404 Cyg and our calibrator sources. *(top)* Left to right the panels represent 5 GHz, 7GHz, 21 GHz, 26 GHz. *(bottom)* Left to right the panels represent 220 GHz, 230 GHz, 350 GHz, and 666 GHz. In all panels, the calibrators are plotted in blue/cyan, while the V404 Cyg data are plotted in red. In the SMA data, the calibrator light curves are scaled up (5000 mJy added to total flux of the two calibrators) for clarity in the plot. In the JCMT data, the calibrator light curves are shown in inset panels as the calibrator scans were taken prior to the target scans.

172
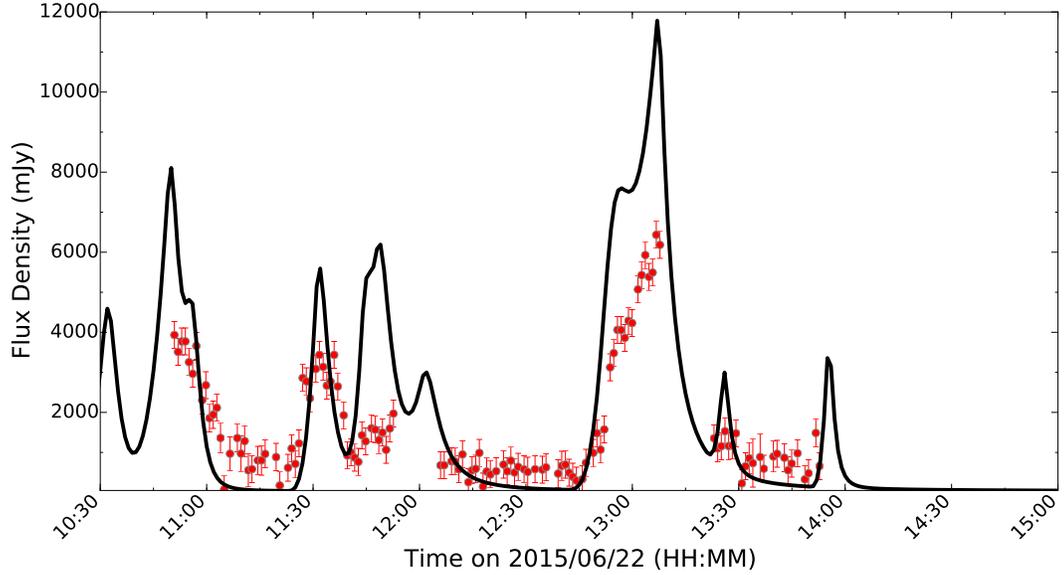
Figure 5.10: JCMT light curve of V404 Cyg in the 666 GHz band on 2015 June 22. The black solid line represents our predicted best fit model in the 666 GHz band.

5.7.3 JCMT SCUBA-2 666 GHz Model Comparison

While we did not include the JCMT SCUBA-2 666 GHz data in our model fitting, it is still of interest to compare our best fit model prediction for the 666 GHz band to the data (see Figure 5.10). While our best fit model appears to match the timing of the flares in the 666 GHz data quite well, the model tends to over predict flux in some areas when compared to our data. It is possible that the deviations between the best fit model and the data are dominated by the higher flux calibration uncertainty in this band, especially when considering such short timescales. On the other hand, our model (and the vdL model) are only capable of predicting emission at frequencies which are initially self-absorbed (i.e. optically thick). Thus the deviations between the best fit model and the data could also suggest that the emission we observe from the jet ejecta in the 666 GHz band is optically thin.

5.7.4 Systematic Errors

As described in §5.4.3, we estimated additional uncertainties on our best fit parameters, to factor in how well our chosen model represents the data. Table 5.3 displays these uncertainties (+ for upper confidence interval, − for lower confidence interval) for each fitted parameter.

Table 5.3: Full (Statistical + Systematic) errors on V404 Cyg Jet Model Best Fit Parameters during the 2015 June 22 Epoch

Compact Jet Parameters

$F_{0,cj}$ (mJy)	α
+3.5, −2.0	+0.05, −0.06

Individual Jet Ejecta Parameters

Ejection	t_{ej} (sec)	t_{ej} (MJD)	i (degrees)	ϕ_{obs} (degrees)	τ_0	F_0 (mJy)	β_b (v/c)
1	+25.8, −37.5	+0.0003, −0.0004	+3.01, −6.72	+1.00, −0.34	+0.07, −0.05	+35.4, −40.0	+0.027, −0.047
2	+33.7, −27.3	+0.0004, −0.0003	+1.60, −1.88	+0.43, −0.41	+0.01, −0.01	+45.2, −37.4	+0.011, −0.010
3	+122.7, −98.8	+0.0014, −0.0011	+0.13, −0.14	+0.16, −0.13	+0.03, −0.03	+325.4, −342.5	+0.017, −0.024
4	+28.3, −27.9	+0.0003, −0.0003	+2.45, −3.54	+0.83, −0.51	+0.03, −0.02	+59.5, −87.1	+0.016, −0.019
5	+331.5, −388.6	+0.0038, −0.0045	+0.26, −0.25	+0.35, −0.29	+0.13, −0.11	+389.0, −280.3	+0.013, −0.013
6	+263.8, −378.5	+0.0031, −0.0044	+0.20, −0.18	+0.73, −0.92	+0.14, −0.11	+483.8, −291.9	+0.036, −0.026
7	+27.4, −26.7	+0.0003, −0.0003	+1.22, −0.72	+0.29, −0.23	+0.01, −0.01	+51.1, −51.6	+0.009, −0.010
8	+45.9, −55.5	+0.0005, −0.0006	+0.48, −0.96	+0.62, −0.90	+0.05, −0.05	+85.2, −118.0	+0.007, −0.006

5.7.5 Two-Parameter Correlations

With the multi-dimensional posterior distribution output from our MCMC runs, we explored possible two-parameter correlations for our model. A significant correlation between a pair of parameters, that is common to all of the ejecta, could indicate a model degeneracy or a physical relationship between the two parameters. Out of the possible two-parameter pairs, we find interesting correlations involving the i, ϕ_{obs}, F_0, and β_b parameters. Figure 5.11 displays the correlation plots, along with the one-dimensional histograms of the parameters[23]. The correlation between i and ϕ_{obs} (first column) indicates a known degeneracy in the vdL model. The correlation between F_0 and β_b (second column) likely indicates a physical relationship between the parameters, where faster ejecta tend to have brighter fluxes. We find the same relationship when we look at the distribution of bulk speeds and fluxes across all the ejecta, and this relationship has been seen in other sources (see §5.5.1 for details). The final four correlations (columns 3 through 6) seem to indicate a degeneracy between all four parameters (or at least a sub-set of them), where different combinations of the four parameters could potentially produce similar flaring profiles.

---

[23]We make use of the CORNER python module to make these correlation plots; `https://github.com/dfm/corner.py`
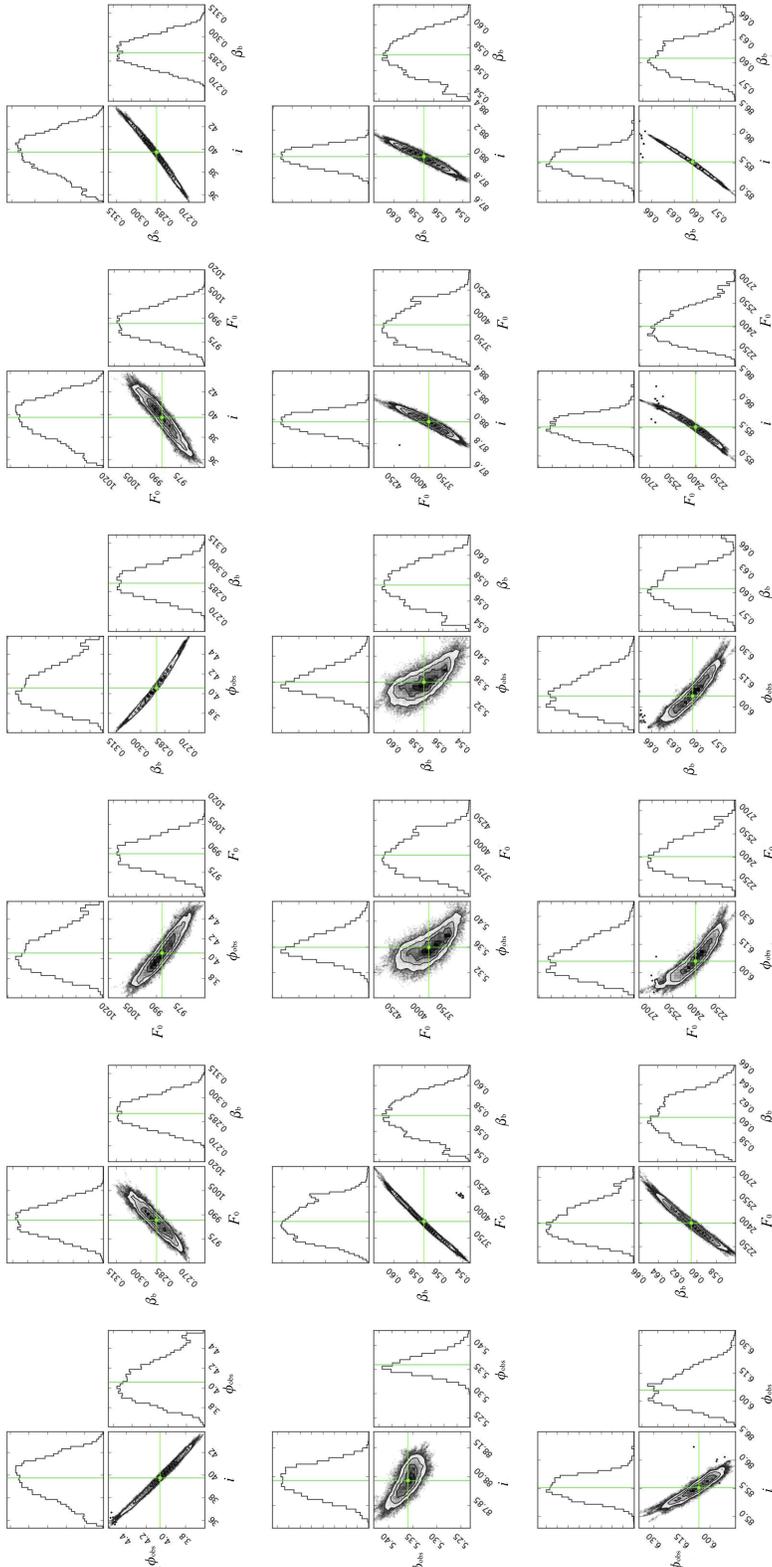
Figure 5.11: Two-parameter correlation plots for pairs of parameters in our model that show a significant relationship. While all the ejection events display the correlations shown, for clarity we only display the correlation plots for three events, which sample a range of i, $\phi_{\rm obs}$, F_0, and β_b values, and are spread out in time throughout our observations; ejection 1 (top row), ejection 3 (middle row), ejection 6 (bottom row). The histograms represent the one dimensional posterior distributions of the parameters, and the green lines/squares indicate the best fit value of the parameters.

177

Chapter 6

Tracking the variable jets of V404 Cygni during its 2015 outburst

This chapter details the work submitted to the *Monthly Notices of the Royal Astronomical Society (MNRAS)* journal as Tetarenko, A.J. et al. 2018, "Tracking the variable jets of V404 Cygni during its 2015 outburst", describing a multi-frequency photometric study of the variable jet emission from the black hole X-ray binary V404 Cygni.

Abstract

We present multi-frequency monitoring observations of the black hole X-ray binary V404 Cygni throughout its June 2015 outburst. Our data set includes radio and mm/sub-mm photometry, taken with the Karl G. Jansky Very Large Array, Arc-Minute MicroKelvin Imager Large Array, Sub-millimeter Array, James Clerk Maxwell Telescope, and the Northern Extended Millimetre Array, combined with publicly available infrared, optical, UV, and X-ray measurements. With these data, we report detailed diagnostics of the spectral and variability properties of the jet emission observed during different stages of this

outburst. These diagnostics show that emission from discrete jet ejecta dominated the jet emission during the brightest stages of the outburst. We find that the ejecta became fainter, slower, less frequent, and less energetic, before the emission transitioned (over 1-2 days) to being dominated by a compact jet, as the outburst decayed toward quiescence. While the broad-band spectrum of this compact jet showed very little evolution throughout the outburst decay (with the optically thick to thin synchrotron jet spectral break residing in the near-infrared/optical bands; $\sim 2 - 5 \times 10^{14}$ Hz), the emission still remained intermittently variable at mm/sub-mm frequencies. Additionally, we present a comparison between the radio jet emission throughout the 2015 and previous 1989 outbursts, confirming that the radio emission in the 2015 outburst decayed significantly faster than in 1989. Lastly, we detail our sub-mm observations taken during the December 2015 mini-outburst of V404 Cygni, which demonstrate that, similar to the main outburst, the source was likely launching jet ejecta during this short period of renewed activity.

6.1 Introduction

Black hole X-ray binaries (BHXBs) contain a stellar mass black hole accreting matter from a companion star, where a portion of the accreted material can be transported back outwards in the form of a relativistic jet. These systems are typically transient in nature, evolving from periods of inactivity into a bright out-bursting state lasting days to months. BHXB jet emission can span many decades in frequency, and during these outbursts, the intensity, morphology, spectral, and temporal properties of the jet emission are known to vary with accretion state (Fender et al., 2004a; Belloni, 2010).

In quiescence and the hard accretion state, there exists a steady, compact synchrotron-emitting jet, which primarily emits at radio, sub-mm, and optical/infrared (OIR) frequencies (Fender, 2001; Corbel & Fender, 2002; Chaty

et al., 2011; Russell et al., 2006; Tetarenko et al., 2015d; Gallo et al., 2005a; Russell et al., 2013c; Plotkin et al., 2013, 2015, 2016). This compact jet displays a characteristic flat to slightly-inverted broad-band spectrum ($\alpha \geq 0$, $f_\nu \propto \nu^\alpha$; Blandford & Königl 1979; Falcke & Biermann 1995; Fender 2001) extending up to OIR frequencies (Corbel & Fender, 2002; Casella et al., 2010; Chaty et al., 2011), where it breaks to an optically thin spectrum ($\alpha \sim -0.7$; Russell et al. 2013b). The location of the spectral break marks the most compact region of the jet, where particles are first accelerated to high energies (Markoff et al., 2001, 2005; Chaty et al., 2011), and has only been directly observed in a few BHXBs ($\nu_{\mathrm{break}} \sim 10^{11-14}\,\mathrm{Hz}$; e.g. Russell et al. 2013b,c).

As the system evolves through the rising hard state, where the X-ray luminosity (and, in turn the mass accretion rate) increases, the compact jet spectrum also evolves. In particular, the location of the spectral break has been observed to shift to lower frequencies (toward the radio regime), as the source transitions into a softer accretion state (van der Horst et al., 2013; Russell et al., 2014). This spectral evolution cannot be driven solely by optical depth effects, which predict an opposite scaling for the spectral break frequency ($\nu_{\mathrm{break}} \propto \dot{M}^{2/3}$; Falcke & Biermann 1995). Alternatively, recent work (Koljonen et al., 2015), which shows a correlation between the location of the spectral break and the photon index of the X-ray spectrum, suggests that the particle acceleration properties within jets (traced by the flux density and frequency of the spectral break) may instead be connected to the properties of the plasma close to the black hole.

During the transition between the hard and soft accretion state, the jet emission can switch from being dominated by a compact jet to arising from discrete jet ejections (e.g., Mirabel & Rodríguez 1994; Hjellming & Rupen 1995; Kuulkers et al. 1999; Corbel et al. 2002; Miller-Jones et al. 2012; Brocksopp et al. 2013; Tetarenko et al. 2017). These ejecta have an optically thin spectrum ($\alpha < 0$) above the self-absorption/free-free absorption turnover frequency (Miller-Jones

et al., 2004), display highly variable emission, and their expansion/bulk motion can be resolved and tracked with Very Long Baseline Interferometry (VLBI; e.g., Hjellming & Rupen 1995; Tingay et al. 1995; Miller-Jones et al. 2004). Once the source reaches the soft state, jet emission is believed to be quenched altogether (or faint enough to be below the detection thresholds of current instruments; Fender et al. 1999b; Corbel et al. 2001; Russell et al. 2011; Coriat et al. 2011b; Rushton et al. 2016), with any residual radio emission usually attributed to an interaction between the jet ejecta and the surrounding medium (e.g., Corbel et al. 2004).

By tracking spectral, temporal, and morphological changes in the jet emission over an outburst, physical conditions in the jet can be linked to the properties of the accretion flow (probed at X-ray frequencies), potentially revealing which accretion flow properties govern the launching, evolution, and quenching of jets (Russell et al., 2013c, 2014, 2015). Therefore, multi-frequency studies of these jets during outburst, which track jet emission properties at different physical scales along the jet axis, are essential in understanding the mechanisms that govern BHXB jet behaviour. Within the BHXB population, V404 Cygni (aka GS 2023+338; hereafter referred to as V404 Cyg) is an optimal candidate for multi-frequency jet studies due to its proximity (2.39 ± 0.14 kpc; Miller-Jones et al. 2009), low extinction ($E(B-V) = 1.3$; Casares et al. 1993), and high X-ray luminosity levels in outburst ($L_X \sim 1 \times 10^{39}\,\mathrm{erg\,s^{-1}}$; Motta et al. 2017b) and quiescence ($L_X \sim 1 \times 10^{33}\,\mathrm{erg\,s^{-1}}$; Corbel et al. 2008).

V404 Cyg was first discovered in outburst in 1989 (Makino, 1989), after which it remained in a low-luminosity quiescent state for ~ 26 years. During this prolonged quiescent state, V404 Cyg displayed a spectrum that was measured to be flat across the radio band ($\alpha = -0.05 \pm 0.15$, where $f_\nu \propto \nu^\alpha$ and $\nu = 1.4 - 8.4$ GHz), likely extending up to IR frequencies, where it breaks to an optically thin spectrum ($\alpha < 0$; Hynes et al. 2009). This radio spectrum is consistent with originating from a partially self-absorbed synchrotron jet

(Blandford & Königl, 1979). While optical and UV emission in the quiescent spectrum of V404 Cyg are well described by blackbody emission from the known K0IV companion star, Muno & Mauerhan (2006) report a mid-IR (4.5μm and 8μm) excess above the level expected from the companion star. This mid-IR excess could originate from the accretion disc (Muno & Mauerhan, 2006; Hynes et al., 2009), the compact jet (Gallo et al., 2007), or a combination of the two. The average radio flux density of the jet in quiescence is ~ 0.3 mJy (Gallo et al., 2003), although the emission is known to be highly variable (Hynes et al. 2009; Plotkin et al. in prep.), reaching up to ~ 1.5 mJy (Hjellming et al., 2000a). The quiescent jet of V404 Cyg is unresolved with the global VLBI array, but Miller-Jones et al. (2009) placed an upper limit on the compact jet size scale of < 1.4 AU at 22 GHz.

During its discovery outburst in 1989, V404 Cyg displayed bright X-ray flaring activity. This highly variable emission was found to not always be intrinsic to the source, but at times be caused by large changes in column density, where the accretion flow became obscured (Terada et al., 1994; Oosterbroek et al., 1997; Zycki et al., 1999). V404 Cyg displayed a variety of radio behaviour during this outburst (Han & Hjellming, 1992), where the radio spectrum evolved from steep ($\alpha < 0$) to inverted ($\alpha > 0$) in a matter of days. Further, significant radio flux variability on timescales as short as tens of minutes was observed, and there were hints of coupled radio, optical, and X-ray emission. However, the instruments available during this 1989 outburst did not have the capabilities to perform the simultaneous, multi-frequency, time-resolved observations needed to fully understand this rapidly evolving jet source.

In June 2015, V404 Cyg entered a new outburst (Barthelmy et al., 2015; Negoro et al., 2015; Kuulkers et al., 2015; Bernardini et al., 2016b), providing a unique opportunity to study the evolving jet with observational coverage that was not possible during the 1989 outburst. During this new outburst, V404 Cyg exhibited bright multi-frequency variability, in the form of large-amplitude

flaring events (e.g., Ferrigno et al. 2015b; Gandhi et al. 2015; Gazeas et al. 2015; Mooley et al. 2015; Motta et al. 2015a,b; Tetarenko et al. 2015a,b), for a ~ 2 week period, before the flaring activity ceased at all wavelengths, and the source began to decay (Sivakoff et al., 2015b,c; Plotkin et al., 2017) back towards quiescence. Additionally, in late December 2015 V404 Cyg entered a short mini-outburst period, during which it displayed renewed flaring activity (e.g., Lipunov et al. 2015; Trushkin et al. 2015; Beardmore et al. 2015; Malyshev et al. 2015; Tetarenko et al. 2016a; Motta et al. 2016; Muñoz-Darias et al. 2017; Kajava et al. 2018).

In this paper, we present multi-frequency monitoring of V404 Cyg during this 2015 outburst, including radio and mm/sub-mm photometry, combined with publicly available OIR, UV, and X-ray measurements. Radio frequency data were taken with NSF's Karl G. Jansky Very Large Array (VLA) and the Arc-Minute MicroKelvin Imager Large Array (AMI-LA), while the mm/sub-mm frequency data were taken with the Sub-millimeter Array (SMA), the Sub-millimetre Common User Bolometric Array-2 instrument on the James Clerk Maxwell Telescope (JCMT SCUBA-2), and the Institute de Radioastronomie Millimétrique's Northern Extended Millimetre Array (IRAM NOEMA). Our observations span a time period from hours after the initial X-ray detection of the outburst, until late in its decay back toward quiescence. While our team's earlier work (Tetarenko et al. 2017, also see Chapters 5 and 6 of this thesis) probed the jet emission during a portion of the brightest flaring period (on 2015 June 22) of the outburst, this work aims to track the spectral and temporal changes in the jet emission as the system transitioned away from the flaring state and began to decay back into quiescence. In §6.2 we describe the data collection and data reduction processes. In §6.3 we present multi-frequency light curves and broad-band spectra. In §6.4, we use this series of observations to discuss the jet properties in V404 Cyg, as well as draw comparisons to the previous 1989 outburst, and the December 2015 mini-outburst. A summary of

our work is presented in §6.5.

6.2 Observations and Data Analysis

6.2.1 VLA Radio Frequency Observations

We observed V404 Cyg with the VLA (project codes 15A-504 and 15A-509) from 2015 July 02 to July 12 (MJD $57205 - 57215$) in the L $(1 - 2\,\text{GHz})$, C $(4 - 8\,\text{GHz})$, Ku $(12 - 18\,\text{GHz})$, and K $(18 - 26\,\text{GHz})$ bands. The array was in its most extended A-configuration for all observations, where we split the array into 2 or 3 sub-arrays to obtain strictly simultaneous observations across multiple bands. All observations were made with the 8-bit samplers, generating 2 base-bands, each with 8 spectral windows of 64 2 MHz channels, giving a total bandwidth of 1.024 GHz per base-band (see Table 6.3 for a summary of the array setup of all the observations). Flagging, calibration, and imaging (with natural weighting chosen to maximize sensitivity) of the data were carried out within the Common Astronomy Software Application package (CASA v4.3.1; McMullin et al. 2007) using standard procedures outlined in the CASA Guides[1] for VLA data reduction (i.e., a priori flagging, setting the flux density scale, initial phase calibration, solving for antenna-based delays, bandpass calibration, gain calibration, scaling the amplitude gains, and final target flagging). We used J2025+3343 as a phase calibrator for all epochs, and 3C48 (0137+331) as a flux calibrator in all epochs but July 11 (MJD 57214), where 3C147 (0542+498) was used. When imaging the lower-frequency bands $(1 - 2\,\text{GHz}$ and $4 - 8\,\text{GHz})$, we placed outlier fields on other bright sources within the primary beam to ensure that their side-lobes did not affect our flux density measurement of V404 Cyg. Flux densities of the source were measured by fitting a point source in the image plane (using the `imfit` task) and, as

---

[1] `https://casaguides.nrao.edu`

is standard for VLA L/C/Ku/K band data, systematic errors of 1/1/3/3% were added (Perley & Butler, 2017). All VLA flux density measurements are reported in Table 6.6. Given the rapidly changing radio flux density observed in this outburst, we also imaged the source on shorter timescales (less than the full observation period), using our custom CASA variability measurement scripts[2] (see §3.1 of Tetarenko et al. 2017 or Chapter 5 §5.3.1 of this thesis for a detailed description of the capabilities of these scripts).

6.2.2 AMI-LA Radio Frequency Observations

V404 Cyg was observed with the AMI-LA (Zwart et al., 2008) radio telescope throughout the 2015 outburst. Observations were carried out with the analogue lag correlator using 6 frequency channels spanning 13.5–18.0 GHz. The raw data were binned to 8×0.625 GHz channels and processed (RFI excision and calibration) with a fully-automated pipeline, AMI-REDUCE (e.g. Davies et al., 2009; Perrott et al., 2013). Daily measurements of 3C48 and 3C286 were used for the absolute flux calibration, which is good to about 10%. The calibrated and RFI-flagged data were then imported into CASA for imaging. In this paper, we use a sub-set of the AMI-LA observations taken during this outburst (complete data set will be published in Fender et al., in prep.). Our analysis includes AMI-LA data that were taken simultaneously with our NOEMA mm/sub-mm observations; from 2015 June 26–30 and July 11–12.

6.2.3 NOEMA (Sub)-mm Frequency Observations

We observed V404 Cyg with the NOEMA (project codes S15DE and D15AB) between 2015 June 26 and July 13 (MJD $57199 - 57216$), in the 3mm (tuning frequency of 97.5 GHz) and 2mm (tuning frequency of 140 GHz) bands. These

---

[2]These scripts are publicly available on github; `https://github.com/Astroua/AstroCompute_Scripts`.

observations were made with the WideX correlator, to yield 1 base-band, with a total bandwidth of 3.6 GHz per polarization (see Table 6.4 for a summary of the correlator and array setup of all the observations). We used J2023+336 as a phase calibrator, and MWC349 as a flux calibrator, in all epochs. The bandpass calibrator varied between epochs; 3C273 (57199 at 3mm), 3C454.3 (57200/57203 at 2mm), J1749+096 (57202 at 3mm and 57200/57201 at 2mm) and J2013+370 (57215/57216 at 2mm and 3mm). As CASA is unable to handle NOEMA data in its original format, flagging and calibration of the data were first performed in GILDAS[3] using standard procedures, then the data were exported to CASA[4] for imaging (with natural weighting to maximize sensitivity). Flux densities of the source were measured by fitting a point source in the image plane (using the `imfit` task). All NOEMA flux density measurements can be seen in Table 6.7. Given the rapidly changing (sub)-mm flux density observed in this outburst, we also imaged the source on shorter timescales (less than the full observation period), using our custom CASA variability measurement scripts.

6.2.4 SMA (Sub)-mm Frequency Observations

We observed V404 Cyg with the SMA (project code 2015A-S026) between 2015 June 16 and July 02 (MJD 57189 − 57215). All of our observations utilized the ASIC and/or SWARM correlators, tuned to an LO frequency of 224 GHz (see Table 6.5 for a summary of the correlator and array setup of all the observations). We performed all flagging, calibration, and imaging (with natural weighting to maximize sensitivity) of the data within CASA, using the same procedures and calibrators outlined in §2.2 of Tetarenko et al. 2017 (Chapter 5 §5.2.2 in this thesis). Flux densities of the source were measured by fit-

---

[3] http://www.iram.fr/IRAMFR/GILDAS
[4] To convert a NOEMA data set for use in CASA, we followed the procedures outlined at https://www.iram.fr/IRAMFR/ARC/documents/filler/casa-gildas.pdf.

ting a point source in the image plane (using the `imfit` task). All SMA flux density measurements are reported in Table 6.7. Given the rapidly changing (sub)-mm flux density observed in this outburst, we also imaged the source on shorter timescales (less than the full observation period), using our custom CASA variability measurement scripts.

6.2.5 JCMT SCUBA-2 (Sub)-mm Frequency Observations

We observed V404 Cyg with the JCMT (project code M15AI54) on 2015 June 17 and July 02 (MJDs 57190 and 57205), in the 850μm (350 GHz) and 450μm (666 GHz) bands. On June 17 the observation consisted of five ~ 30 min scans on target with the SCUBA-2 detector (Chapin et al., 2013; Holland et al., 2013), from 11:13:12–14:19:05 UTC (MJD 57190.468 − 57190.597). On July 02 the observation consisted of eight ~ 30 min scans on target with the SCUBA-2 detector from 09:01:23–13:42:29 UTC (MJD 57205.376−57205.571). During the observations on June 17 we were in the Grade 4 weather band with a 225 GHz opacity of 0.1–0.2, while on July 02 we were in the Grade 3 weather band with a 225 GHz opacity of 0.08–0.1. Data were reduced in the STARLINK package, using the same procedures and calibrators outlined in §2.3 of Tetarenko et al. 2017 (Chapter 5 §5.2.3 in this thesis). JCMT flux densities of the source in both epochs are reported in Table 6.7. We note that we only detect the source at 350 GHz in these epochs; however, 3σ upper limits in the 666 GHz band are provided in the table. Given the rapidly changing (sub)-mm flux density observed in this outburst, we also attempted to create maps of the source on shorter timescales (less than the full observation period). To do this, we used a custom procedure we developed to produce a data cube, containing multiple maps of the target source region, at different time intervals throughout our observation (see §3.2 of Tetarenko et al. 2017 or Chapter 5 §5.3.2 of this thesis

for the details of this procedure). In both epochs we were only able to measure the flux density on timescales as short as the 30 min scan timescale, as V404 Cyg was too faint, and the noise was too high to accurately measure the flux density on shorter timescales.

6.2.5.1   December 2015/January 2016 Mini-outburst

As V404 Cyg displayed renewed activity in December 2015/January 2016, we also observed V404 Cyg with the JCMT (project code M15BI036) on 2016 January 1 and 2 (MJDs 57388 and 57389). Each observation consisted of one ~ 30 min scan on target with the SCUBA-2 detector (using the daisy configuration), from 19:48–20:20 UTC (MJD 57388.825–57388.847) on January 1, and 19:59-20:32 UTC (MJD 57389.833–57389.856) on January 2. CRL2688 was used for absolute flux calibration on January 1, and Mars was used on January 2. During both observations we were in the Grade 1 weather band, with a 225 GHz opacity of 0.04/0.05 on January 1/2. These later epochs were also reduced in the STARLINK package, following the same procedures as in §6.2.5. V404 Cyg transits during the daytime at this time of year, therefore, the JCMT was operating in an specialized extended observing mode at the time of our observations. Given the rapidly changing (sub)-mm flux density observed in V404 Cyg, we searched for variability within the January 1 observation by splitting the scan into two maps. The first half of the observation shows an average flux density of 58 ± 19 mJy and the second half shows an average flux density of 38 ± 10 mJy. The source was not bright enough, and the noise was too high to accurately measure the flux density on shorter timescales. For the same reasons we were unable to obtain flux density measurements on timescales less than the 30 min scan timescale in the January 2 epoch. JCMT flux densities of the source in these later epochs are also reported in Table 6.7.

6.2.6 IR/Optical/UV/X-ray Observations

We have compiled publicly available OIR, UV, and X-ray (*Chandra*; Plotkin et al. 2017, and Swift/XRT; Sivakoff et al. 2015c) photometric observations that were quasi-simultaneous with our radio through sub-mm observations (i.e., < 1 day separation from our observations). Observational details and flux densities from these data are reported in Table 6.8, where data in this table have been de-reddened (when required) using the prescription in Cardelli et al. (1989), with an $E(B - V) = 1.3 \pm 0.2$ (Casares et al., 1993). Additionally, in our analysis we include time-resolved OIR data from Kimura et al. 2016 and AAVSO[5], as well as INTEGRAL X-ray data (5-10 keV and 60-200 keV bands; Rodriguez et al. 2015)[6], all occurring simultaneously with our radio/sub-mm data sets.

The *Swift/XRT* data were all taken in photon counting (PC) mode, and we analyzed the data using the HEASOFT software package. We first reprocessed the data using `xrtpipeline`, and then we extracted source and background spectra using standard procedures in `xselect`. Due to the presence of dust scattering halos around V404 Cyg in many of these observations (e.g., Beardmore et al. 2016; Heinz et al. 2016), background spectra were extracted from regions where no halos were detected. We fit the 0.5–10 keV X-ray spectra with an absorbed power-law (`TBABS*PEGPWRLW`); here we used abundances from Wilms et al. (2000) and cross sections from Verner et al. (1996). We tied the power-law photon index ($\Gamma = 1.8 \pm 0.3$; 90% confidence interval) together, but allowed the hydrogen absorption column to vary between observations ($N_H \sim 0.5$–$3 \times 10^{22}\,\mathrm{cm}^{-2}$). We report the flux densities arising from these fits at 5 keV ($1.21 \times 10^{18}\,\mathrm{Hz}$).

---

[5]Kafka, S., 2018, Observations from the AAVSO International Database, `https://www.aavso.org`

[6]All INTEGRAL X-ray data presented in this paper are taken from the INTEGRAL public data products available at `http://www.isdc.unige.ch/integral/analysis#QLAsources` (Kuulkers 2015, PI: Rodriguez).

6.3   Results

6.3.1   Light Curves

Daily timescale light curves of all of our radio through sub-mm observations of V404 Cyg are presented in the top two panels of Figure 6.1[7]. Throughout our month long-monitoring of the source, we observe the radio/sub-mm flux to vary by over 3 orders of magnitude, ranging from Jy levels at its brightest to sub-mJy levels at its faintest. In the sub-mm bands, the emission in our first epoch (taken hours after the first detection of the outburst in X-rays) is relatively bright compared to the mm/sub-mm flux densities typically seen in BHXBs (i.e., ~ 100 mJy vs < 50 mJy), but rapidly drops by an order of magnitude within the next 24 hours. Following our first two detections, the sub-mm flux likely continues to rise, approaching a peak on MJD 57195. The source then begins to decay, where this decay is initially quite rapid (i.e., the flux density drops at least an order of magnitude between MJD 57195 and 57199), before the emission appears to plateau for a few days around MJD 57204, and then proceeds to decay at a much slower rate as the source heads towards quiescence. The radio emission tracks the sub-mm emission closely, and both show a potential secondary peak in the light curves around MJD 57200.

The bottom panel of Figure 6.1 displays the radio through sub-mm spectral indices (where a single power-law is fit across radio/sub-mm frequencies), for epochs where at least 2 different bands were sampled. We find that the spectral indices appear to vary between steep ($\alpha < 0$) and inverted ($\alpha \geq 0$) during the MJD 57189–57204 period, but then remain flat to inverted for the rest of our monitoring period.

---

[7]All the fluxes presented in this figure are measured through imaging the source over the full observation period, except for the AMI 16 GHz data, where a weighted mean of time-resolved measurements (100 sec time-bins) is taken.
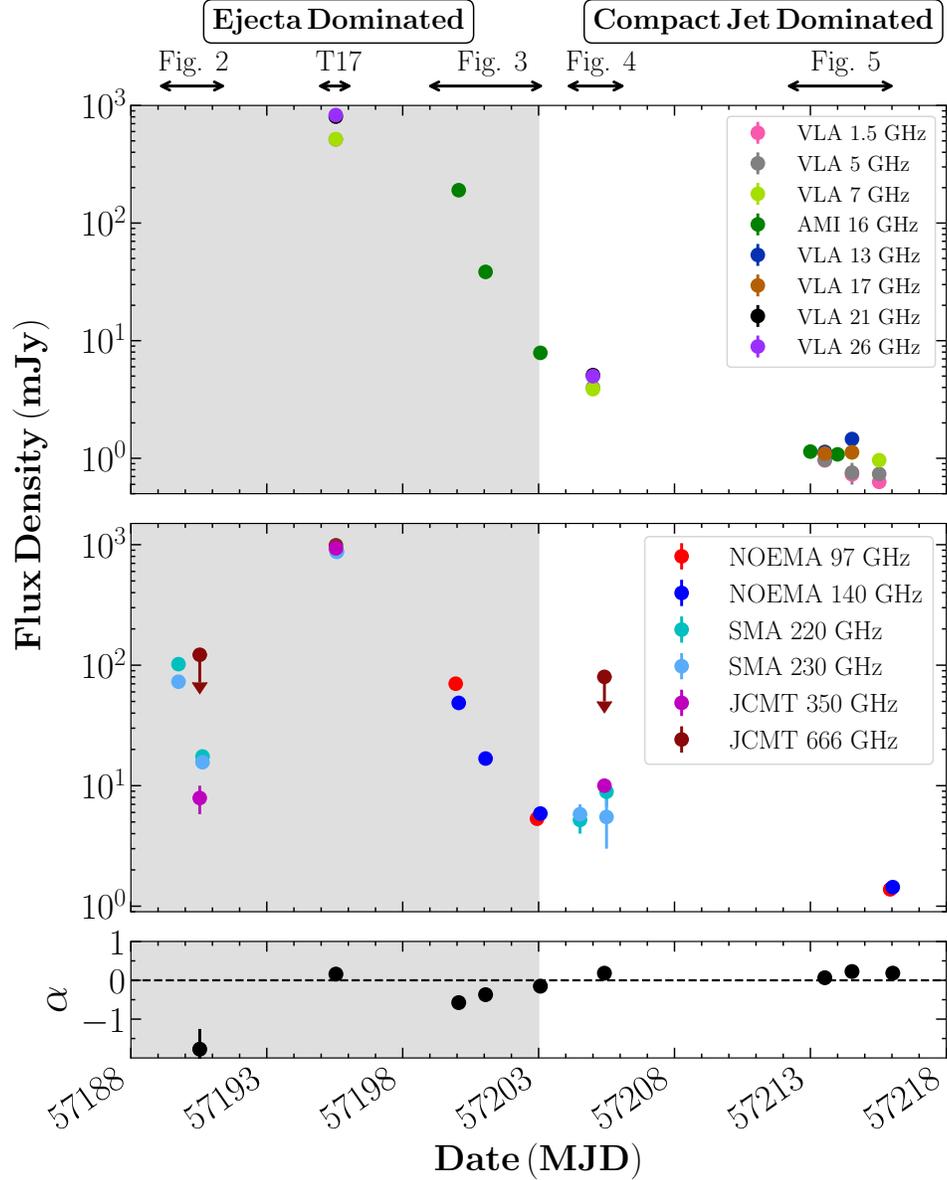
Figure 6.1: Day-timescale light curves of V404 Cyg during its June 2015 outburst. The *top* panel displays the radio frequency bands, the *middle* panel displays the (sub)-mm frequency bands, and the *bottom* panel displays the radio–sub-mm spectral indices, in epochs where at least two different bands were sampled (using the convention $f_\nu \propto \nu^\alpha$, where α represents the spectral index; dotted line indicates $\alpha = 0$). The (un-)shaded regions represent time-periods where the jet emission was likely dominated by jet ejecta or a compact jet (as labelled above the top panel). The figures displaying time-resolved measurements of these data are indicated at the top of the figure (T17 indicates Tetarenko et al. 2017 or Figure 5.1 in Chapter 5 of this thesis). Over our month long monitoring period of V404 Cyg, we find that the jet emission is highly variable, where the radio through sub-mm fluxes vary by ~ 3 orders of magnitude, and the spectral index varies between steep ($\alpha < 0$) and inverted ($\alpha > 0$).

As V404 Cyg is known to be significantly variable regardless of its brightness, these day-timescale light curves and spectral indices will only display the overall average trend in the data. Therefore, we opted to also search for intra-observation variability in our data. To do this, we created time-resolved light curves (and simultaneous spectral index measurements) of all of our radio through sub-mm observations. These time-resolved light curves, along with simultaneous optical and X-ray data (when available), are displayed in Figures 6.2, 6.3, 6.4, and 6.5. To ensure that any short timescale variations we observe from V404 Cyg are dominated by intrinsic variations, and not atmospheric or instrumental effects, we extracted high time resolution measurements from our calibrator sources as well. We find that the majority of our calibrator observations show relatively constant fluxes (variations $< 10\%$ of the average flux density), except for the SMA data taken on MJD 57189 (see discussion below).

To characterize the amplitude of any intra-observation variability and compare between epochs, we use the fractional RMS statistic,

$$F_{\mathrm{var}} = \sqrt{\frac{S^2 - \bar{\sigma}_{\mathrm{err}}^2}{\bar{x}^2}} \tag{6.1}$$

where $\bar{x}$ represents the weighted mean of the flux measurements, the sample variance $S^2 = \frac{1}{N-1} \sum_{i=1}^{N} (x_i - \bar{x})^2$, and the mean square measurement error $\bar{\sigma}_{\mathrm{err}}^2 = \frac{1}{N} \sum_{i=1}^{N} \sigma_{\mathrm{err,i}}^2$ (Vaughan et al., 2003). For this paper, we consider $F_{\mathrm{var}} < 20\%$ as not significantly variable, $20\% < F_{\mathrm{var}} < 50\%$ as mildly variable, and $F_{\mathrm{var}} > 50\%$ as highly variable.

In our first epoch on MJD 57189, the sub-mm emission is highly variable over the short ~ 1.5 hour observation, with a $F_{\mathrm{var}} = 71.0 \pm 1.4\%$ at 224 GHz. Although, we note that this variability appears to be very stochastic (especially when compared to the next epoch taken ~ 24 hours later), rather than showing smooth or structured variations that we might expect to see from this high

frequency emission probing close to the jet base (e.g., see Tetarenko et al. 2017 and Chapter 5 of this thesis). Upon examining the calibrator light curve for this observation, we noticed that the calibrator source shows an atypically high level of variability within the first half of the observation (i.e., prior to ~18:00 UT), likely due in large part to the very low elevations of these observations (as low as 15 degrees). Therefore, all of the V404 Cyg variability observed in this epoch may not be intrinsic to the source. Less than a day later, the variability amplitude decreases, along with the average flux level, to just above mildly variable at $F_{\mathrm{var}} = 51.9 \pm 0.8\%$ at 224 GHz. While we are only able to sample the sub-mm spectral index in two time bins on MJD 57190, both show a steep spectral index in this epoch, consistent with that observed from the daily average data (see Figures 6.1 and 6.2).

Our next epoch, taken approximately a week later (MJD 57195), displayed large scale, structured flaring activity, with lower frequency emission appearing as a smoothed and delayed version of high frequency emission. We have shown that this emission can be well modelled by a series of bi-polar, adiabatically expanding jet ejections (details of this data set are reported in Tetarenko et al. 2017 and Chapter 5 of this thesis). This structured flaring activity (tracing repeated jet ejection events) likely continued intermittently up to MJD 57199, where we sample a final, large radio flare (peaking at $\sim$ 200 mJy), coinciding with rapid flaring activity at optical and X-ray frequencies (see Figure 6.3). Following this large flare, the radio through optical emission remains highly variable for another 1–2 days ($F_{\mathrm{var}} = 71.6 \pm 0.2\%$ at 140 GHz on MJD 57200), displaying multiple smaller amplitude flaring events, before the flaring activity ceases, and the variability amplitude drops to mildly variable ($F_{\mathrm{var}} = 39.0 \pm 0.2\%$ at 140 GHz on MJD 57202/57203). The spectral indices during the flaring activity between MJD 57199–57201 oscillate between steep and inverted on hourly timescales, consistent with the evolving optical depth of adiabatically expanding jet ejecta. After the flaring activity had ceased, the spectral index

is much more stable over time, and close to flat.

In the following two days, the sub-mm variability amplitude once again increases to highly variable with $F_{\mathrm{var}} = 85 \pm 5\%$ at 224 GHz on MJD 57204, before declining to the point where any variance in the data is much less than the measurement errors on MJD 57205 (see Figure 6.4). The optical and X-ray emission at this time are not significantly variable ($F_{\mathrm{var}} < 10\%$), while the spectral index is stable, and remains inverted across radio through sub-mm bands. While small scale variability is seen in the soft X-ray light curves during these epochs, the variations are not seen in the hard X-rays. Therefore, these soft X-ray variations are likely due to the highly variable absorption (Motta et al., 2017a), and not intrinsic source variations. A week later (MJD 57213), both the radio and sub-mm flux has dropped by another order of magnitude, while the X-ray flux has remained relatively constant since MJD 57201 (see Figure 6.5). All the radio bands are not significantly variable, displaying $F_{\mathrm{var}} < 20\%$ (similar to that observed in later radio observations taken in late July and early August; Plotkin et al. 2017), and the sub-mm variability amplitude is similar to that seen on MJD 57202/57203. The spectral indices remain flat to slightly inverted during the MJD 57213–57216 period.
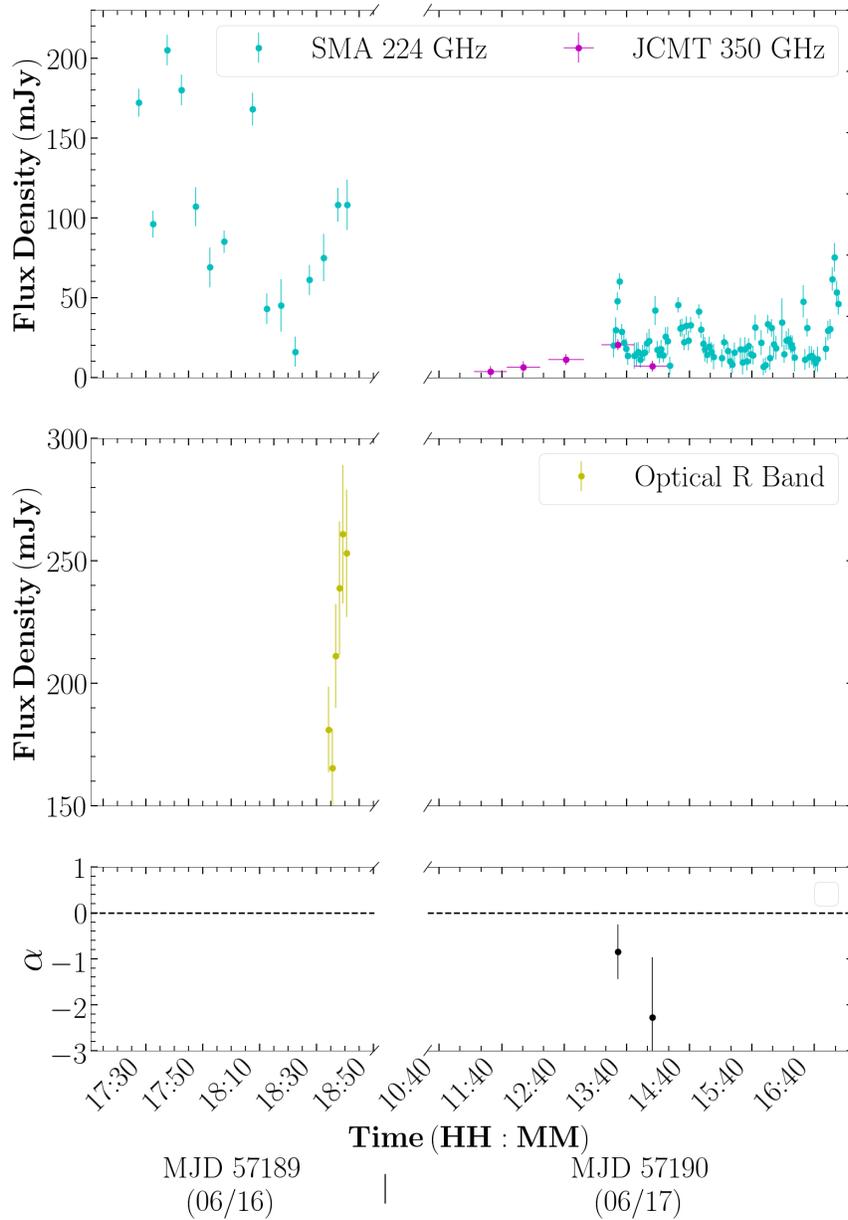
Figure 6.2: Time-resolved light curves and spectral indices of V404 Cyg during the first two days of our monitoring of the outburst (June 16 and 17, MJD 57189 and 57190). The data shown have varying time-bin sizes; 224 GHz (5/2 min June 16/17), 350 GHz (30 min), Optical R band (75 sec; Kimura et al. 2016). Here we have combined the two SMA sidebands (cyan data points), in order to gain a higher signal to noise in our time-resolved light curves. The horizontal error bars on the JCMT measurements (magenta data points) represent the time range of the 30 minute SCUBA-2 scans. The dotted line in the bottom panel indicates a spectral index of $\alpha = 0$. In less than 24 hours, between these two epochs, both the sub-mm flux levels and variability amplitude change dramatically.
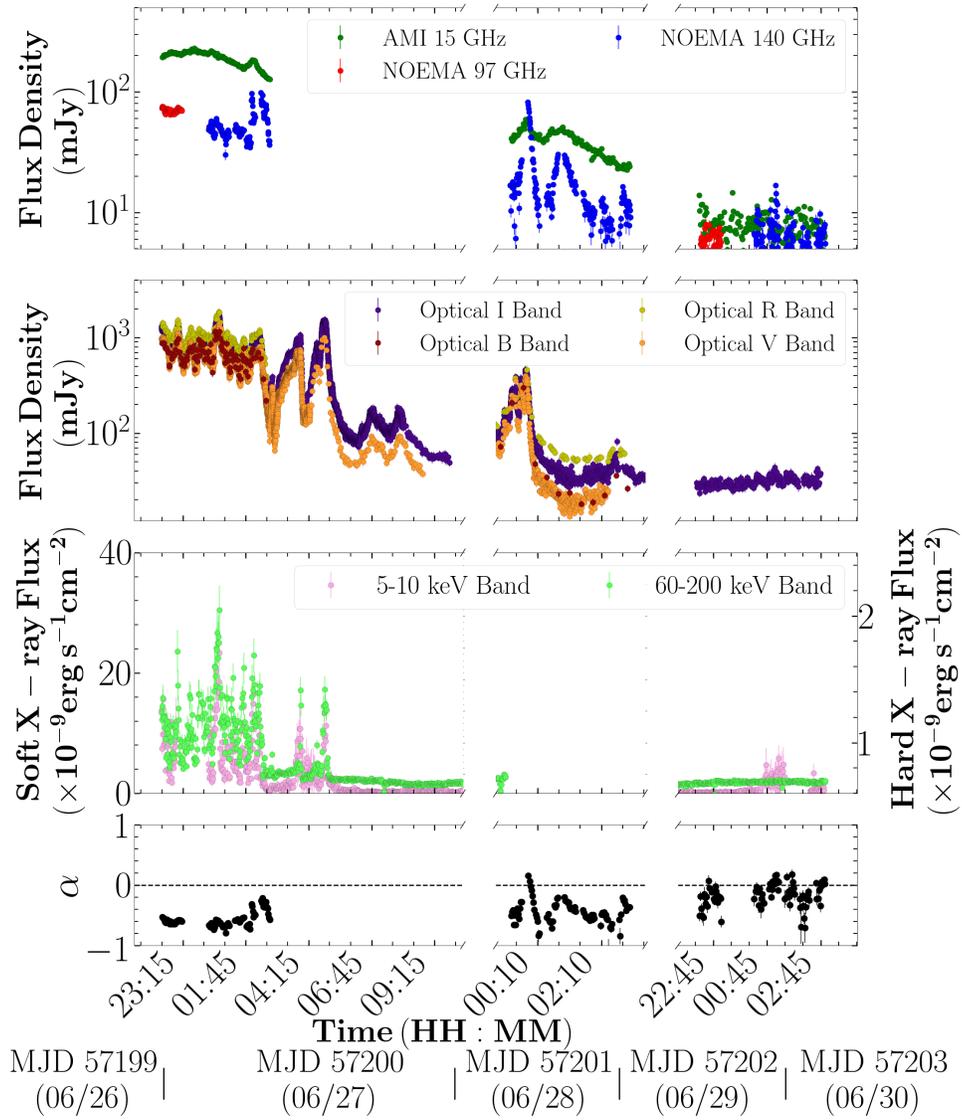
Figure 6.3: Time-resolved light curves and spectral indices of V404 Cyg between June 26 and 30 (MJD 57199–57203). The data shown have varying time-bin sizes; 15 GHz (100 sec), 97–140 GHz (45 sec), Optical I, R, B,V bands (75 sec; Kimura et al. 2016), INTEGRAL 5–10 keV (64 sec), INTEGRAL 60–200 keV (64 sec). The dotted line in the bottom panel indicates a spectral index of $\alpha = 0$. We initially detect rapid flaring activity at radio through X-ray frequencies, which drops in amplitude, becomes less frequent, and eventually stops all together, over this four day period.
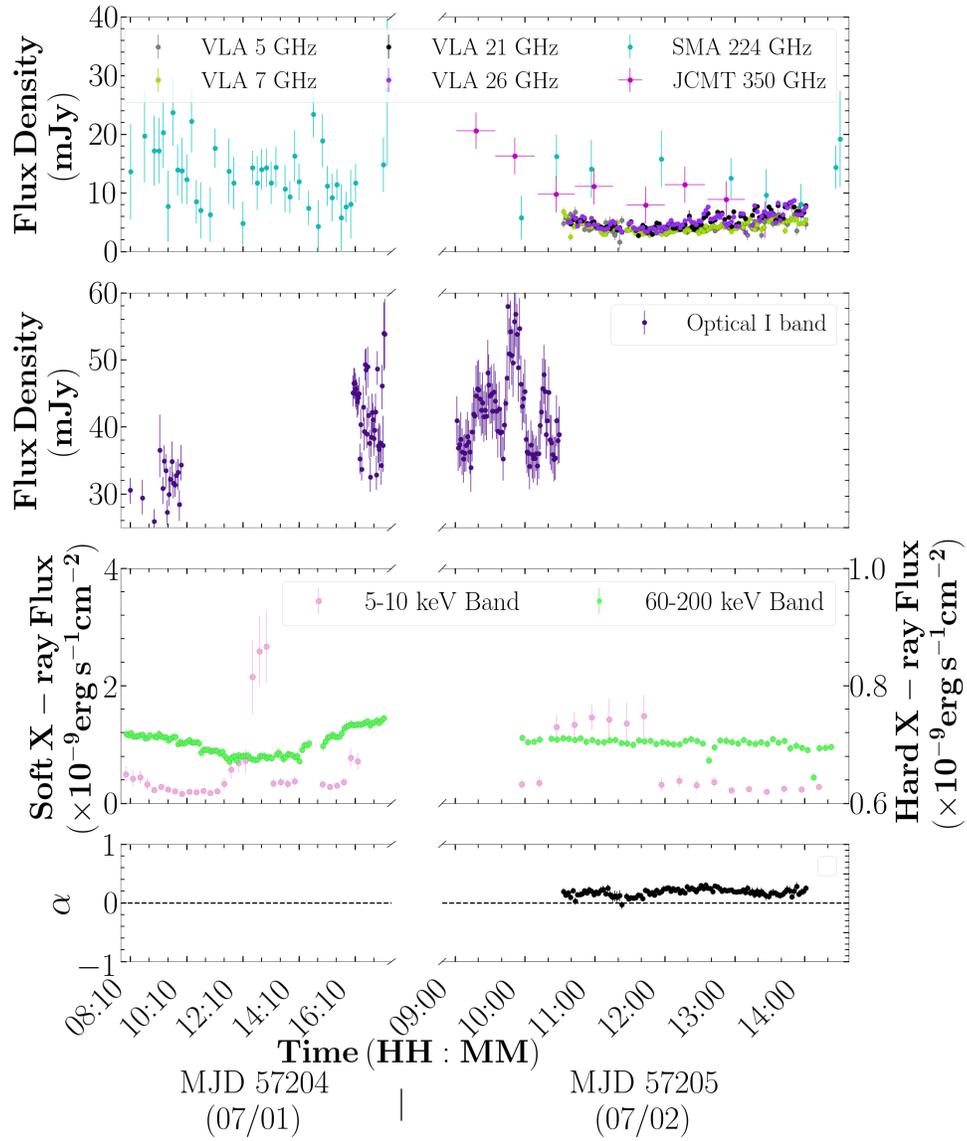
Figure 6.4: Time-resolved light curves and spectral indices of V404 Cyg on July 01 and 02 (MJDs 57204 and 57205). The data shown have varying time-bin sizes; 5–26 GHz (2 min), 224 GHz (10/30 min on July 1/2), 350 GHz (30 min), Optical I band (100/75 sec on July 01/02; AAVSO/ Kimura et al. 2016), INTEGRAL 5–10 keV (15 min), INTEGRAL 60–200 keV (5 min). Here we have combined the two SMA sidebands, in order to reduce the noise in our short timescale light curves. The horizontal error bars on the JCMT measurements represent the range of the 30 minute SCUBA-2 scans. The dotted line in the bottom panel indicates a spectral index of $\alpha = 0$. While no structured flaring activity is observed, the sub-mm emission remains highly variable on July 01, before becoming much more stable a day later.
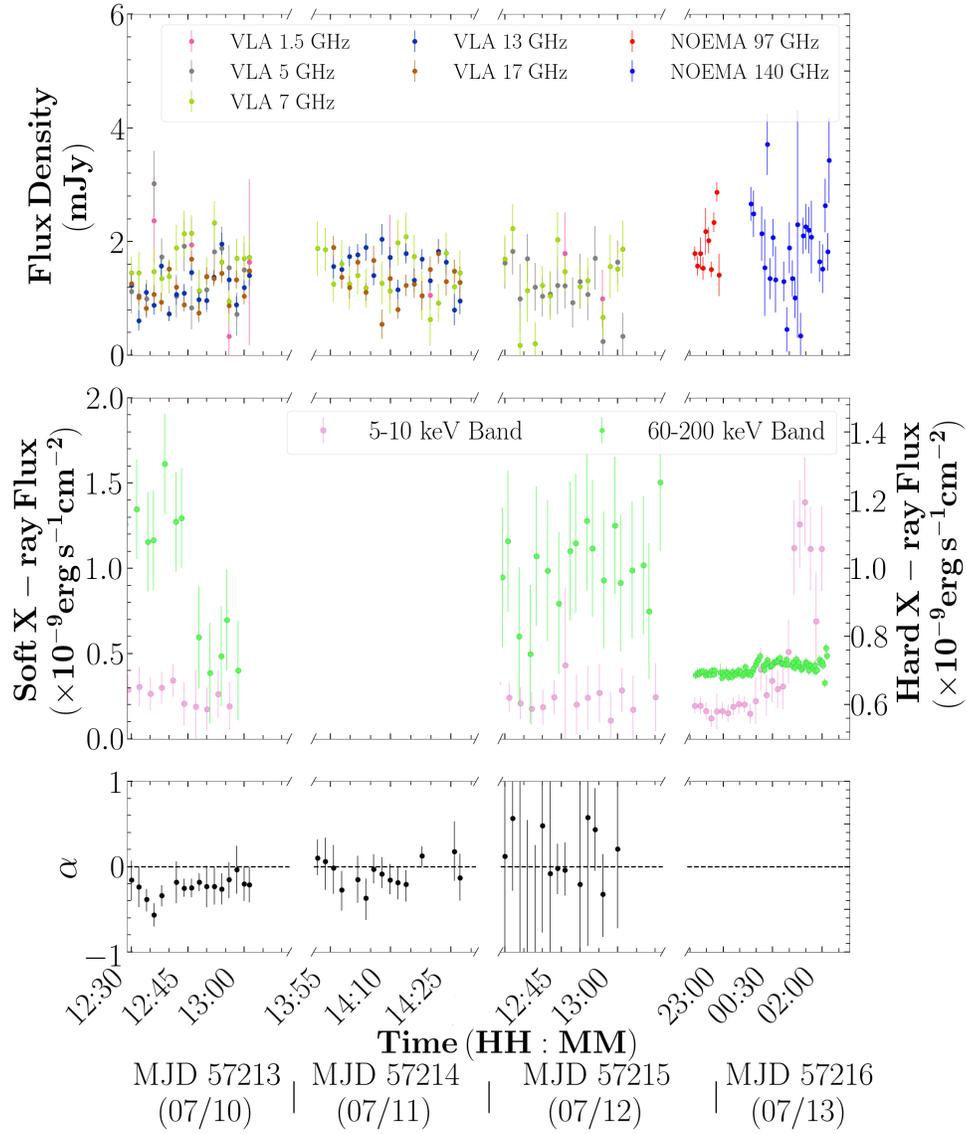
Figure 6.5: Time-resolved light curves and spectral indices of V404 Cyg between July 10 and 13 (MJD 57213–57216). The data shown have varying time-bin sizes; 1.5 GHz (10 min), 5–17 GHz (2 min), 97–140 GHz (5 min), INTEGRAL 5–10 keV (3 min), INTEGRAL 60–200 keV (1.5 min). The dotted line in the bottom panel indicates a spectral index of $\alpha = 0$. The radio through sub-mm flux densities are much more constant in these epochs, when compared to our observations one week earlier (see Figure 6.4).

6.3.2 Modelling the Flaring Activity

Out of all the time resolved light curves shown in Figures 6.2 – 6.5, the radio and sub-mm light curves between MJD 57199 and 57201 show a distinct morphology. During these days we observe rapid, multi-frequency flaring activity (with the lower frequency emission appearing to be a smoothed, delayed version of the higher frequency emission; see Figure 6.3). Given the striking similarity between these data and our earlier work on multi-frequency flaring activity from MJD 57195 (Tetarenko et al. 2017 and Chapter 5 of this thesis), we opted to apply the jet model we developed for that data set to the MJD 57199–57201 light curves.

While a detailed description of our jet model is provided in §4.2 of Tetarenko et al. (2017) (and Chapter 5 §5.4.2), we provide a brief summary here. Our V404 Cyg jet model reproduces emission from multiple, discrete, ballistically moving jet ejection events, on top of a constant compact jet component with a power-law spectrum. Each of the ejection events consists of the simultaneous launching of identical bi-polar plasma clouds, both of which evolve under the van der Laan (van der Laan, 1966) synchrotron bubble formalism. Additionally, our model folds in both projection and relativistic effects (e.g., relativistic beaming, geometric time delays) for each ejection event.

Here we use the same modelling process detailed in §4.3 of Tetarenko et al. 2017 (and Chapter 5 §5.4.3), where we implement a Markov-Chain Monte Carlo (MCMC) algorithm to fit our light curves on MJD 57200/57201 (Foreman-Mackey et al., 2013). The best fit parameters and their uncertainties[8] for this fit are shown in Table 6.1, and Figure 6.6 displays the best fit model overlaid on our light curves (see also Figure 6.11). With our best fit model, we find that

---

[8]The uncertainties reported in Table 6.1 are purely statistical, only representing confidence intervals on our parameters under the assumption that our model completely represents the data. However, given the residuals with respect to our best-fit model, it is possible that there are physical/instrumental effects in the data that cannot be reproduced by our model. See §4.3 of Tetarenko et al. (2017) (and Chapter 5 §5.4.3) for a more detailed discussion on this point.

a total of 5 bi-polar ejection events can reproduce the overall morphology and flux densities of the emission we observe in the June 27/28 (MJD 57200/57201) epoch. Further, our modelling suggests that the inclination angle of the jet axis changes by up to ∼ 40 degrees during this series of ejections, which is consistent with the magnitude of jet axis precession independently estimated from a series of resolved jet ejecta observed in an earlier epoch with the VLBA (Miller-Jones et al. 2018, in prep., also see Chapter 7 of this thesis). Therefore, overall our modelling shows that the flaring emission observed on June 27/28 (MJD 57200/57201) is consistent with emission originating from multiple, discrete jet ejection events. While we also observe multi-frequency flaring in the 2015 June 26/27 (MJD 57199/57200) epoch, there is limited overlap between the mm/sub-mm and radio observations, which makes it difficult to reliably fit this data set with our model.
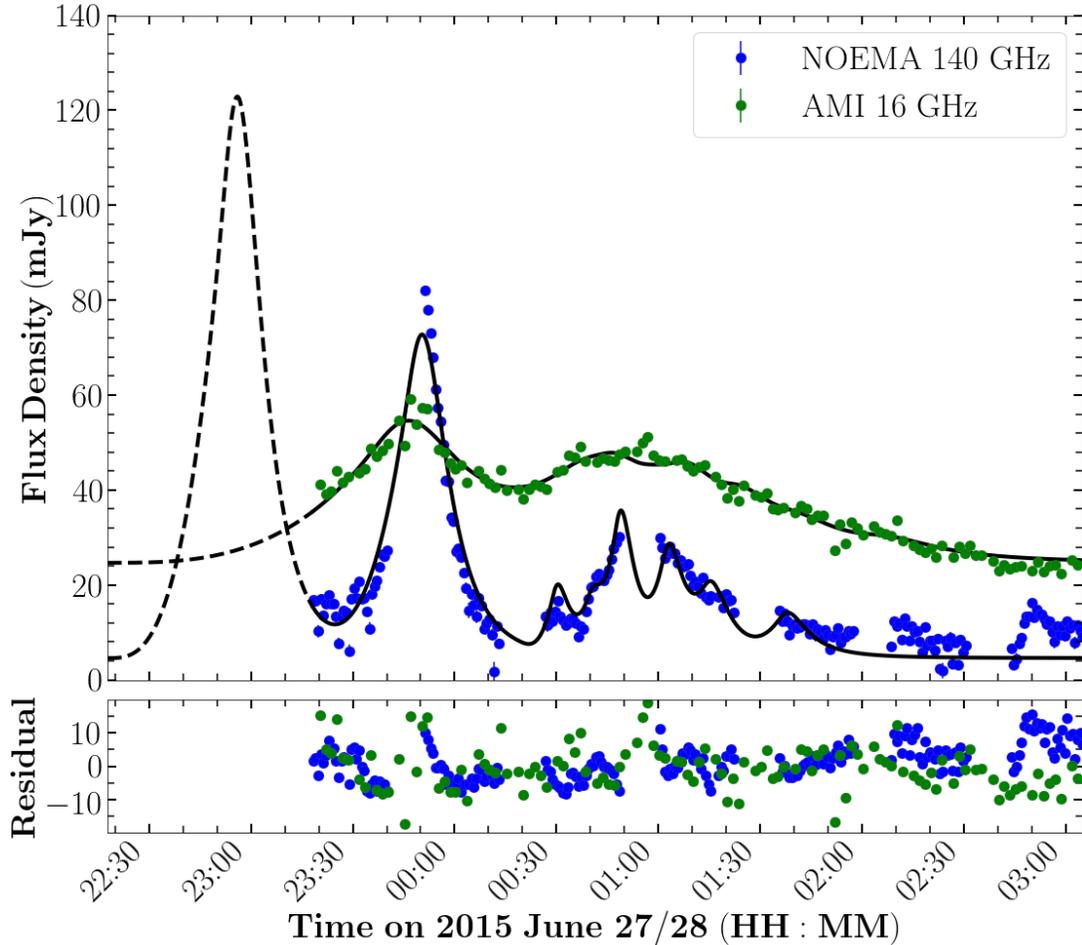
Figure 6.6: Radio (AMI 16 GHz) and mm/sub-mm (NOEMA 140 GHz) light curves of V404 Cyg on 2015 June 27/28 (MJD 57200/57201). In the *top* panel, we have overlaid our predicted best fit jet model at each frequency on the light curves (black lines, where our model contains contributions from both approaching and receding components for each ejection event). The residuals are shown in the *bottom* panel, where residual=(data–model)/(observational errors). Our best fit model, which contains a total of 5 bi-polar ejection events, can reproduce the overall morphology and flux levels of the emission we observe from V404 Cyg, indicating that this flaring emission is consistent with emission originating from multiple, discrete jet ejection events. Note that we do not attempt to model all of the peaks and wiggles in the mm/sub-mm emission past 02:00 UT, as we do not have the radio frequency coverage to constrain any additional components in the model past this point. See Figure 6.11 for a version of this figure where we decompose the full model into individual approaching and receding components.

Table 6.1: V404 Cyg Jet Model Best Fit Parameters during the 2015 June 27/28 Epoch

Baseline Flux Parameters[a]

Epoch	$F_{0,\mathrm{cj}}$ (mJy)	α
June 27/28	$4.59^{+0.06}_{-0.06}$	$-0.75^{+0.004}_{-0.004}$

Individual Jet Ejecta Parameters[b]

Ejection	t_{ej} (HH:MM:SS.S)	t_{ej} (MJD)	i (degrees)	ϕ_{obs} (degrees)	τ_0	p[c]	F_0 (mJy)	β_{b} (v/c)	β_{exp} (v/c)[d]
1	06-27 22:17:56.8$^{+49.13}_{-53.84}$	57200.9291$^{+0.0006}_{-0.0006}$	44.07$^{+1.98}_{-1.62}$	4.55$^{+0.18}_{-0.17}$	2.09$^{+0.02}_{-0.02}$	3.59$^{+0.08}_{-0.07}$	59.48$^{+0.82}_{-0.78}$	0.037$^{+0.001}_{-0.001}$	0.0020$^{+0.0001}_{-0.0001}$
2	06-27 23:14:19.3$^{+12.56}_{-11.48}$	57200.9683$^{+0.0001}_{-0.0001}$	53.45$^{+1.49}_{-1.62}$	5.86$^{+0.20}_{-0.16}$	1.99$^{+0.01}_{-0.01}$	3.27$^{+0.04}_{-0.04}$	34.29$^{+0.20}_{-0.20}$	0.020$^{+0.001}_{-0.001}$	0.0017$^{+0.0001}_{-0.0001}$
3	06-28 00:23:46.5$^{+16.64}_{-16.66}$	57201.0165$^{+0.0002}_{-0.0002}$	34.56$^{+2.46}_{-2.84}$	6.47$^{+0.73}_{-0.53}$	1.50$^{+0.01}_{-0.01}$	1.99$^{+0.01}_{-0.01}$	12.60$^{+0.24}_{-0.27}$	0.050$^{+0.002}_{-0.002}$	0.0032$^{+0.0004}_{-0.0003}$
4	06-28 00:42:13.7$^{+13.14}_{-12.60}$	57201.0293$^{+0.0002}_{-0.0001}$	63.30$^{+1.23}_{-1.55}$	2.37$^{+0.15}_{-0.12}$	1.51$^{+0.03}_{-0.01}$	2.01$^{+0.06}_{-0.02}$	24.09$^{+0.60}_{-0.96}$	0.107$^{+0.004}_{-0.005}$	0.0040$^{+0.0004}_{-0.0003}$
5	06-28 01:08:23.2$^{+62.68}_{-133.28}$	57201.0475$^{+0.0007}_{-0.0015}$	19.54$^{+1.06}_{-1.10}$	4.74$^{+0.29}_{-0.25}$	1.56$^{+0.04}_{-0.04}$	2.12$^{+0.09}_{-0.10}$	10.23$^{+0.52}_{-0.30}$	0.067$^{+0.003}_{-0.002}$	0.0018$^{+0.0002}_{-0.0001}$

[a] The baseline flux (representing contributions from a compact jet) is best fit by a single power-law, with amplitude $F_{0,\mathrm{cj}}$ at 140 GHz, and spectral index α.

[b] Ejecta parameters are defined as follows: ejection time (t_{ej}), inclination angle of the jet axis (i), jet opening angle (ϕ_{obs}), synchrotron optical depth (at 140 GHz) at the time of peak flux density (τ_0), peak flux density of the ejecta component (F_0), and the bulk ejecta speed (β_{b}).

[c] The index of the electron energy distribution, p, is not a fitted parameter but rather is solved for using values of τ_0. Similar to the situation discussed in our earlier modelling work (Tetarenko et al. 2017), the large range of energy indices (p) for the ejecta found here is not entirely physical for a single source. We believe that more extreme values of the energy index could be mimicking the effect of physics that has not been included in our model.

[d] The expansion velocity, β_{exp}, is not a fitted parameter but rather is solved for using values of β_{b}, i, ϕ_{obs}.

6.3.3 Cross-correlation analysis

To search for time lags between different frequency bands, we computed cross-correlation functions (CCFs) of our time-resolved light curves in all epochs, using the z-transformed discrete correlation function (ZDCF; Alexander 1997, 2013, this technique was also used in Chapter 4 of this thesis). We chose to use the ZDCF algorithm, as this method has been shown to provide a more robust estimate of the CCFs for sparse, unevenly sampled light curves, when compared to the classic discrete correlation function (DCF; Edelson & Krolik 1988) or the interpolation method (Gaskell & Peterson, 1987). To obtain an estimate of the CCF peak (indicating the strongest positive correlation, and thus the best estimate of any time-lag between the light curves from different frequency bands), with corresponding uncertainties, we utilize the maximum likelihood method[9] described in Alexander (2013). Additionally, to estimate the significance level of any peak in the CCF, we perform a set of simulations (as described in Chapter 4 §4.3.2), allowing us to quantify the probability of false detections in our CCFs, by accounting for stochastic fluctuations and intrinsic, uncorrelated variability within each radio light curve.

While we performed the above CCF analysis for all of the radio through X-ray data sets for which we had overlapping, time-resolved data, we only find clear evidence of time lags during the July 02 (MJD 57205) epoch (see Figure 6.7). In particular, we measure a time lag between the 26 GHz radio band and the 5 GHz radio band of $12.0^{+3.7}_{-4.2}$ minutes. However, the measured time lags between the 26 GHz band and the 7/21 GHz bands are consistent with a zero lag within the uncertainty limits (where the $1\,\sigma$ upper limits for the 26 GHz to 7/21 GHz lags are < 10 min and < 5 min, respectively). Further, the

---

[9]This method estimates a fiducial interval rather than the traditional confidence interval. The approach taken here is similar to Bayesian statistics, where the normalized likelihood function (fiducial distribution) is interpreted as expressing the degree of belief in the estimated parameter, and the 68% interval around the likelihood function's maximum represents the fiducial interval (68% of the likelihood-weighted ensemble of all possible CCFs reach their peaks within this interval).

optical I band flaring activity observed in this epoch (see Figure 6.4) is unlikely to be correlated with this radio emission, as a simple jet model ($z_0 \propto 1/\nu$, where z_0 represents the distance down the jet axis from the black hole) paired with our our detected radio lag predicts a ~ 15 min lag between the I band and 5 GHz, rather than the hours between the optical and radio flaring observed in the light curves (see Figures 6.4 and 6.7). However, as the radio and I band light curves do not overlap in this epoch, we can not conclusively rule out a correlation between the two. Therefore, we are unable to conclusively determine if a trend with frequency, where the lower frequency bands always lag the higher frequency bands (and the lag increases as the frequency decreases in the comparison band), exists in our CCFs. Such a trend is expected from emission originating in a compact jet, as lower frequency emission is expected to originate from a region further down the jet axis from the black hole, and these time lags between radio bands could trace the propagation of material downstream along the jet (Malzac et al., 2003; Casella et al., 2010; Gandhi et al., 2017; Vincentelli et al., 2018).

As the jet model we used in §6.3.2 can predict lags between different frequency bands for each jet ejection event, it is of interest to compare the model predicted lags from data on MJD 57200/57201 and the CCF predicted lags from data on MJD 57205. In particular, our best-fit jet model from MJD 57200/57201 predicts time lags between 26 and 5 GHz of 24–59 min, between 26 and 7 GHz of 17–44 min, and between 26 and 21 GHz of 2–5 min, for different ejection events. Therefore, the jet model predicted lags between 26 and 5 GHz are all larger than our CCF measured lag. These differing lags likely indicate varying jet properties at different phases of the outburst (i.e., decline from a major flare vs. flat-spectrum compact jet emission at a much lower level), such as bulk speed, inclination angle, opening angle, or electron energy distributions, between the MJD 57200 and 57205 epochs.
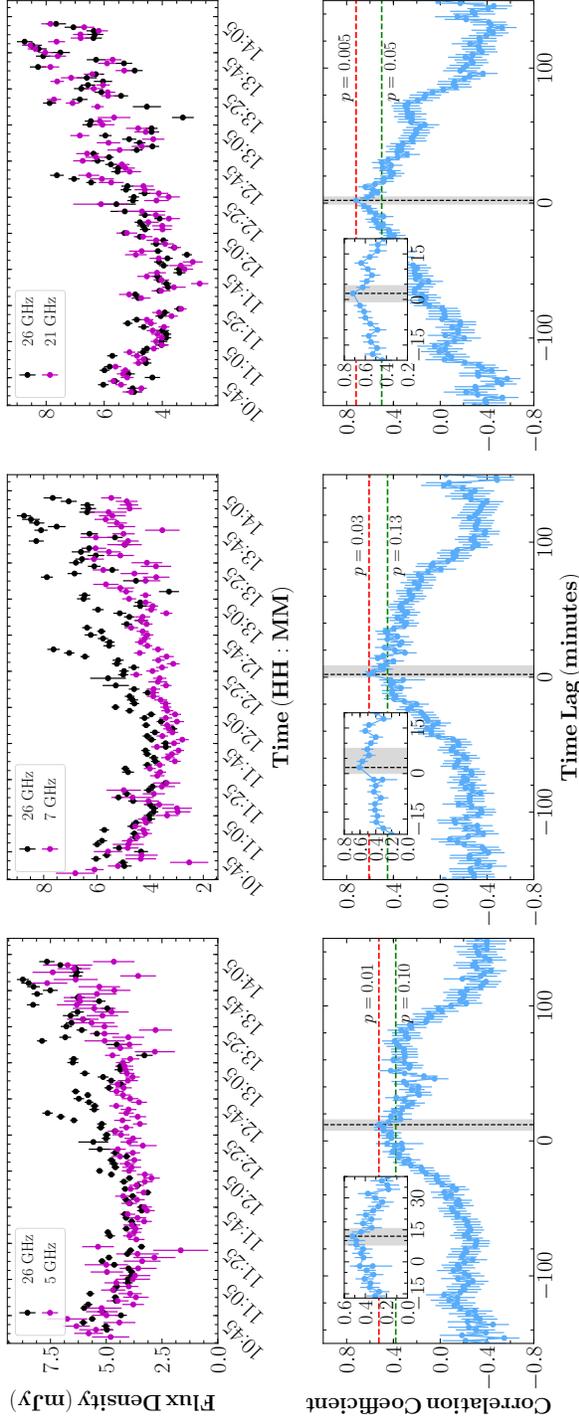
Figure 6.7: Radio light curves (zoomed in versions of Figure 6.4; *top panels*) and cross-correlation functions (CCFs; *bottom panels*) between the VLA radio frequency bands on July 02 (MJD 57205). The peak of each CCF (indicating the strongest positive correlation) is shown by the black dotted line, with the 68% fiducial confidence interval indicated by the shaded grey region, and different significance levels indicated by the red and green dotted lines (see §6.3.3 for details). The insets in each panel display a zoomed view of the region surrounding the peak of each CCF. A positive time lag indicates that the lower frequency band lags behind the higher frequency band. We observe a clear time lag between the 26 GHz and 5 GHz bands (*bottom left*; $12.0^{+3.7}_{-4.2}$ min), however, our measured lags between the 26 GHz and the 7 GHz (*bottom middle*) / 21 GHz (*bottom right*) bands are consistent with zero lag.

6.3.4 Broad-band Spectra

In the epochs following the structured flaring activity (MJD 57203–57216), where the emission is much more constant (showing minimal flux variability within an observation), we constructed broad-band spectra to track the spectral evolution of the jet emission as V404 Cyg decayed towards quiescence (including additional radio data from the Giant Metrewave Radio Telescope reported in Chandra & Kanekar 2017, to add lower frequency coverage at 0.235, 0.610, and 1.280 GHz). We fit these radio through optical/UV broad-band spectra with a phenomenological multi-component model, consisting of a broken power law (representing compact jet emission), a black-body ($R_\star = 5.71R_\odot$, $T_\star = 0.784T_\odot$, representing the known companion star; Gallo et al. 2007), and in two epochs, an additional single power law (representing emission from fading jet ejecta). To fit these spectra we use a MCMC algorithm (Foreman-Mackey et al., 2013), where the best fit result is taken as the median of the one-dimensional posterior distributions, and the uncertainties are reported as the range between the median and the 15th percentile (-), and the 85th percentile and the median (+), corresponding approximately to 1σ errors. These broad-band spectra are displayed in Figure 6.8, and the best-fit model parameters are reported in Table 6.2. We note that while accretion disc emission has been known to contribute to the optical/UV emission in broad-band spectra of BHXBs (Khargharia et al. 2010 estimate $< 3\%$ accretion disc contamination during quiescence for V404 Cyg, although the accretion disc is much brighter in outburst than in quiescence; Bernardini et al. 2016b), we do not include an accretion disc component in our model presented here (e.g., Hynes et al. 2002a; Hynes 2005). While we could reasonably reproduce the optical/UV emission in our broad-band spectra with a cool ($T \sim 3000$ K), highly truncated ($R \sim 10^4 R_g$), viscous disc (where irradiation is not necessary to describe the spectral shape), the integrated flux over this disc emission implies a physically improbable mass transfer rate (e.g., on MJD 57205 $\sim 2 \times 10^{-9} M_\odot/\mathrm{yr}^{-1}$)

through the disc for this scenario. Therefore, we favour a model where the jet dominates the optical/UV emission in our broad-band spectra.

The broad-band spectra constructed from data on MJD 57202–57205, are well fit by a broken power-law, where we detect the spectral break in the near-IR bands. The OIR emission from the companion star is fainter than the jet emission on MJDs 57204 and 57205, contributing little to the overall broad-band spectra (although the jet and companion star show similar flux levels in the OIR on MJD 57202/57203). However, on MJDs 57202/57203, and 57204, we require an additional power-law component, to account for the excess emission at radio frequencies[10]. The broken power-law emission is characteristic of a compact jet, while the additional power-law component could originate in emission from fading jet ejecta, potentially launched during the flaring period 2–3 days prior to these epochs. Further, while we see very little evolution in the location of the spectral break across these three broad-band spectra, the optically thin spectral index may steepen over time, while the optically thick spectral index may flatten over time (although, given the large uncertainties in some epochs, it is difficult to determine if we see an evolutionary trend in this spectral index; e.g., MJD 57204, where we only sample the optically thick part of the spectrum in two closely placed sub-mm bands).

The broad-band spectra constructed from data on MJD 57213–57216, are also well fit by a broken power-law, where we detect the spectral break at frequencies as high as the optical bands. This indicates that the spectral break has moved to higher frequencies over the ~ 1 week timescale between these epochs and the previous three epochs. Further, during these later epochs, the jet emission has faded by $\sim$ an order of magnitude, and thus the emission from the companion star contributes much more to the overall spectral shape

---

[10]Note that we have fixed the spectral index of this jet ejecta component to a typical value of -0.7 in the MJD 57202/57203 epoch, as we only have a single radio data point to constrain this component. However, as we have three radio data points in the MJD 57204 epoch, we allow this parameter to vary in the fit for that epoch.

in these broad-band spectra.

We note that all of the above conclusions are dependent upon the assumption that other emission sources (e.g., accretion disc emission, irradiation of the companion star by X-rays), are not significantly contaminating the OIR/UV bands in our broad-band spectra. For instance, X-rays emitted during the final major flaring event of the outburst (occurring a few days prior to the spectra presented in this work) could have potentially caused the emission from the companion star to be much brighter than normal (through the irradiation process), and in turn contribute more to the OIR/UV part of the broad-band spectrum. In this case, we would expect a smaller jet contribution to the OIR/UV emission. In fact, this scenario may explain the larger deviations between the radio/sub-mm data and our best-fit model on MJD 57213. The presence of a hotter companion star component, producing more OIR/UV flux, would allow for a flatter jet spectrum at lower frequencies, that would be more representative of the radio/sub-mm data in this epoch.

Further, given the high spectral break frequency measured here, it is of interest to explore whether the synchrotron jet emission could be dominating the emission in the X-ray bands during our sampled epochs. To test this scenario, we have also included the available quasi-simultaneous *Swift XRT/Chandra* X-ray flux measurements (in the 0.5-10 keV band) within our broad-band spectra (Figure 6.8 and Table 6.8). Simply extrapolating the optically thin part of the jet spectrum to the X-ray bands in the X-ray sampled epochs (blue dotted lines on Jun 29/30 & July 02, and gray shading representing a range of expected optically thin spectral indexes between $\alpha = -0.6$ and $\alpha = -0.8$ on July 10 & 11) clearly over-predicts the X-ray flux. Therefore, we consider the possibility where a second break, representing a synchrotron cooling break[11] (due to the highest-energy electrons losing their energy through radiation on timescales

---

[11]We note that to the best of our knowledge the synchrotron cooling break has only been detected in the broad-band spectra of one BHXB so far (MAXI 1836–194), where the cooling break was found in the optical bands between $(3 - 4.5) \times 10^{14}$ Hz (Russell et al., 2014).

faster than the dynamical time scale; Sari et al. 1998; Pe'er & Markoff 2012; Russell et al. 2013b, 2014), occurs between the UV and X-ray bands in the synchrotron spectrum. To place constraints on the location of the cooling break in this case, we consider the July 02 (MJD 57205) epoch, as this is the only epoch in which we have data sampling the optically thin part of the jet spectrum, no contribution from jet ejecta, and an X-ray measurement. Through refitting the July 02 spectrum, including the X-ray data point, adding a cooling break (where the spectral index after the cooling break is steeper by $\Delta\alpha = 0.5$; Sari et al. 1998; Russell et al. 2014) in the model, and keeping all other parameters fixed at the original best-fit values, we find $\nu_{\mathrm{coolbr}} = (1.5^{+0.7}_{-0.5}) \times 10^{16}$ Hz (where the cooling break version of the model is displayed as a red dot-dashed line in the middle-left panel of Figure 6.8). Given this cooling break measurement, and estimates of the optically thin spectral index (we assume spectral indexes between $\alpha = -0.6$ and $\alpha = -0.8$ in epochs where we have no constraint on this parameter), we also extrapolate the synchrotron spectrum to the X-ray bands in the June 29/30, as well as the July 10 & 11 epochs (displayed as red shading in the top-left, middle-right, and bottom-left panels of Figure 6.8). Overall, we find that the jet synchrotron emission could reasonably be producing a significant fraction of the X-ray flux in these epochs. Further discussion of the plausibility of this scenario is presented in §6.4.2.
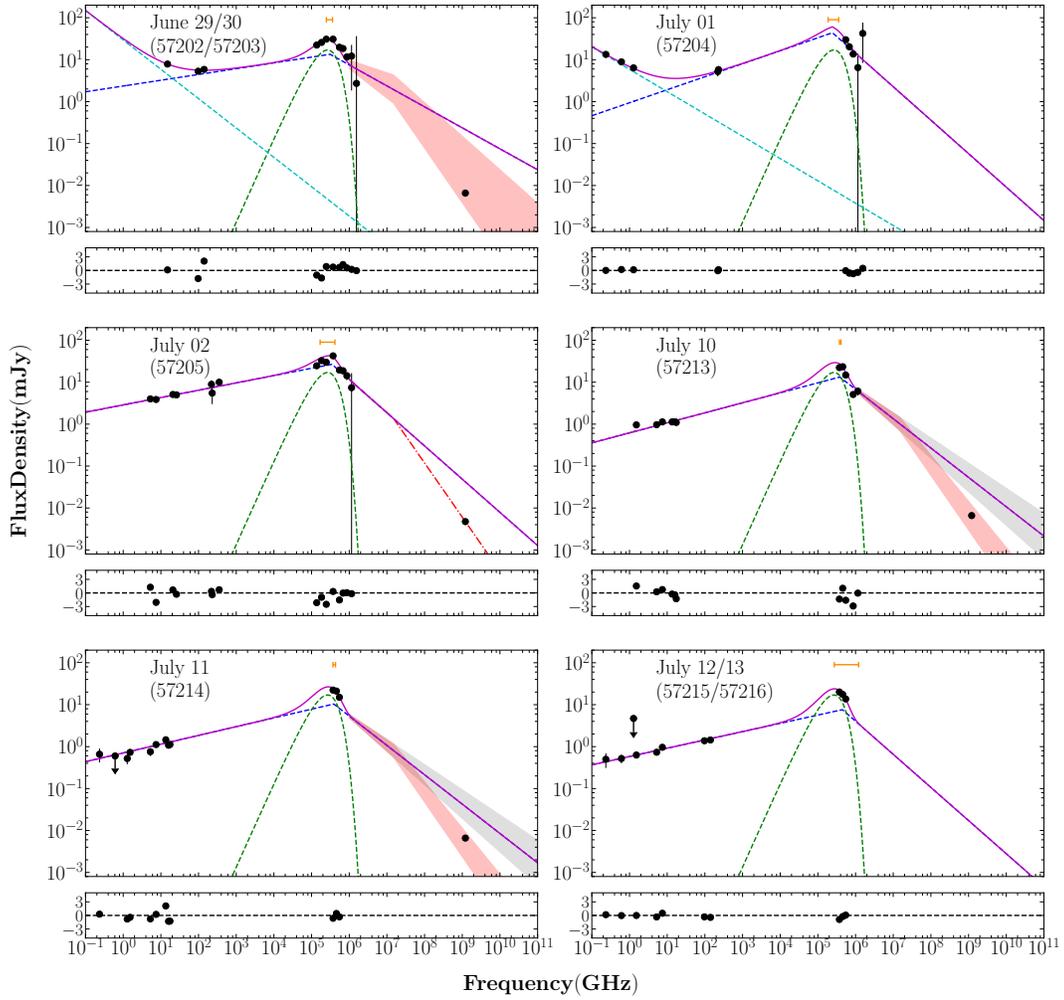
Figure 6.8: Broad-band spectra of V404 Cyg during the decay of the 2015 outburst. The *top* panel in each broad-band spectra displays the broad-band photometric data (black markers), and the best-fit model (where the *Swift/XRT* and *Chandra* X-ray data points are not included in these fits), in each epoch. The solid purple line represents the total model, and the dotted lines represent the model components (green is the companion star component, dark blue is the compact jet component, and cyan is the fading jet ejecta component). The orange bars/arrows represent constraints on the location of the spectral break. The dash-dotted red line and shaded red/gray regions represent constraints on the synchrotron jet contribution to the X-ray emission (where our jet model over-predicts X-ray flux unless a sychrotron cooling break is considered in the spectrum; see §6.3.4 for details). The *bottom* panel of each broad-band spectra represents the residuals, where residual=(data-model)/(observational errors). The emission in these broad-band spectra is consistent with being dominated by emission from a compact jet, with a spectral break in the near-IR and optical frequency bands.

Table 6.2: Best-fit parameters for broad-band spectral modelling during the decay of the 2015 outburst of V404 Cyg

Date	$\nu_{\rm break}$ (GHz)	$F_{\rm break}$ (mJy)	$\alpha_{\rm thick}$	$\alpha_{\rm thin}$	$L_{\rm jet}$ (erg s^{-1})	$F_{\rm 15\,GHz}$ (mJy)	$\alpha_{\rm thin,2}$
June 29/30	$(3.10^{+0.50}_{-0.63}) \times 10^{5}$	$13.48^{+0.53}_{-0.90}$	$0.14^{+0.01}_{-0.01}$	$-0.50^{+0.22}_{-0.29}$	$(5.47^{+1.14}_{-0.97}) \times 10^{35}$	$4.45^{+0.25}_{-0.32}$	-0.70
July 01	$(2.44^{+1.12}_{-0.57}) \times 10^{5}$	$43.97^{+0.50}_{-0.29}$	$0.31^{+0.11}_{-0.03}$	$-0.80^{+0.18}_{-0.10}$	$(1.42^{+0.33}_{-0.28}) \times 10^{36}$	$1.33^{+0.56}_{-0.69}$	$-0.53^{+0.11}_{-0.16}$
July 02	$(3.48^{+0.69}_{-1.79}) \times 10^{5}$	$26.71^{+2.10}_{-4.14}$	$0.17^{+0.02}_{-0.01}$	$-0.79^{+0.37}_{-0.18}$	$(9.45^{+2.81}_{-2.91}) \times 10^{35}$	$\cdots$	$\cdots$
July 10	$(3.81^{+0.06}_{-0.31}) \times 10^{5}$	$13.27^{+0.92}_{-1.56}$	$0.24^{+0.01}_{-0.01}$	-0.70	$(5.25^{+0.92}_{-0.81}) \times 10^{35}$	$\cdots$	$\cdots$
July 11	$(3.89^{+0.44}_{-0.20}) \times 10^{5}$	$10.38^{+1.59}_{-1.64}$	$0.20^{+0.02}_{-0.02}$	-0.70	$(4.22^{+1.10}_{-0.79}) \times 10^{35}$	$\cdots$	$\cdots$
July 12/13	$(4.48^{+7.58}_{-1.75}) \times 10^{5}$	$7.62^{+1.21}_{-2.67}$	$0.19^{+0.04}_{-0.02}$	-0.70	$(3.03^{+1.19}_{-1.05}) \times 10^{35}$	$\cdots$	$\cdots$

[a] Columns from left to right: spectral break frequency, flux at the spectral break, optically thick spectral index, optically thin spectral index, integrated compact jet power ($L_{\rm jet} = 4\pi D^2 \int \nu L_\nu \, d\nu$, from 1.5–1.2×10^6 GHz) given our best-fit model, flux (at 15 GHz) and spectral index of additional optically thin power law component. The radius and temperature of the companion star were fixed in all fits ($R_\star = 5.71 R_\odot$, $T_\star = 0.784 T_\odot$; Gallo et al. 2007).
[b] Note that we fix the optically thin spectral index to a value of -0.7 for the July 10, July 11 and July 12/13 epochs, as we do not have sufficient data to place accurate constraints on this parameter in our fitting.

6.4 Discussion

Throughout the June 2015 outburst of V404 Cyg, the jet emission we observe displays a wide range of intensities (spanning over 3 orders of magnitude between the brightest and faintest epochs), and the spectral and variability properties of the jet emission change dramatically throughout the outburst (on timescales of minutes to days). In this work, we have presented detailed diagnostics of this jet emission, and in the following sections we discuss jet properties and evolution in V404 Cyg, as well as draw comparisons to the jet emission observed in the 1989 outburst, and the December 2015/January 2016 mini-outburst.

6.4.1 Jet ejecta behaviour

For the first $\sim$ 13 days of the June 2015 outburst, the jet emission from V404 Cyg appears to be dominated by emission from discrete jet ejections, as evidenced by the structured multi-frequency flaring activity in the light curves, and the rapidly oscillating radio through sub-mm spectral indices (consistent with the evolving optical depth of these expanding ejecta; see Figure 6.1 & 6.3). In recent work (Tetarenko et al. 2017 and Chapter 5 of this thesis), we developed a jet ejecta model for V404 Cyg that could reproduce the brightest multi-frequency flaring emission detected during the outburst (on MJD 57195), and in turn allow us to probe jet speeds, energetics, and geometry. To examine how the jet ejecta properties could evolve throughout the outburst, in this paper we have presented model fits to another multi-frequency flaring data set, occurring 5 days following the brightest epoch. We find that these later multi-frequency flaring episodes can also be well represented by emission from a series of jet ejections (Figure 6.6). Upon comparing the jet ejecta properties between our modelled data sets, the later epochs tend to show fainter ejecta (tens to hundreds of mJy, rather than thousands of mJy), with lower bulk speeds

212

($< 0.1c$), and longer periods between ejections (on the order of hours, rather than minutes). This suggests that the ejecta properties changed throughout the flaring period, becoming slower, less energetic, and less frequent as the outburst progressed, before the discrete jet ejections stopped all together.

If the jet ejecta launched from V404 Cyg are powered by the accretion flow, then the radio/sub-mm emission we observe should be correlated with the optical/X-ray emission. In particular, we might expect to observe optical/X-ray flaring counterparts preceding our radio/sub-mm flares. Interestingly, the beginning of the optical flaring complex observed on June 27 at $\sim$ 23:00 UT coincides with the predicted ejection time for the largest mm/sub-mm flare observed in this epoch. Further, while we were unable to model the radio/sub-mm flaring on June 26, if we assume similar delay timescales ($\sim 10 - 40$ min between mm/sub-mm and optical/X-ray) from our modelled epoch, it seems plausible that the rapid optical/X-ray activity on June 26 could also be related to the radio/sub-mm flaring we observe during this epoch (see Figure 6.3). Therefore, these observations provide hints of a possible correlation between radio/sub-mm and optical/X-ray emission during jet ejection events in V404 Cyg.

6.4.2 Compact jet behaviour

Following the flaring period, the jet emission from V404 Cyg switches to being dominated by a compact jet, as evidenced by the flat/inverted (radio through sub-mm) spectral indices, and the absence of large-scale flaring activity in the time-resolved light curves in all bands (see Figures 6.4 & 6.5).

Through applying a phenomenological model to the broad-band emission at this stage in the outburst, we find that the compact jet is the dominant source of emission in V404 Cyg from the radio through optical/UV bands (see Figure 6.8, where the broad-band spectra can be well fit by a broken power law, characteristic of compact jet emission). With this modelling, we initially

directly detect the optically thick to thin synchrotron jet spectral break in the near-IR bands ($\sim 2 - 3 \times 10^{14}$ Hz), and find that the spectral break could reach as high as the optical bands in our final epochs (4.48×10^{14} Hz). This high spectral break frequency is atypical for BHXBs (typical values for the spectral break in BHXBs are 10^{11-14} Hz; Russell et al. 2013b), but consistent with data from the 1989 outburst, which also display a high spectral break frequency ($\sim 1.8 \times 10^{14}$ Hz; Russell et al. 2013b). These results are also in agreement with the recent work of Maitra et al. (2017), who present several lines of evidence to suggest that the optical emission was dominated by the compact jet on MJD 57200, and theorize the spectral break lies above the optical V band at this time ($\sim 5.5 \times 10^{14}$ Hz). As the spectral break probes the jet base (where jet particles are first accelerated to high energies), Maitra et al. (2017) suggest that a spectral break at such a high frequency suggests the jet base was very compact and energetic at this point in the outburst. If this is the case, our spectral break measurements suggest these conditions persisted as the system faded toward quiescence.

Measuring a spectral break in the optical bands in the V404 Cyg jet spectrum could also have important implications regarding the jet contribution to the X-ray emission in this system. In particular, with such a high spectral break frequency, the optically thin synchrotron emission from the jet could be dominating the emission in the X-ray bands (e.g., in XTE J1550-564 the jet has been shown to dominate the X-ray bands during the outburst decay; Russell et al. 2010). In §6.3.4 and Figure 6.8 we have shown that a synchrotron spectrum (with a cooling break between the UV and X-ray bands) extrapolated to the X-ray bands can reasonably reproduce the X-ray fluxes observed during the decay of this V404 Cyg outburst. This indicates that the jet could be producing a large portion of the X-ray flux at this point in the outburst. However, to confirm this theory, a more detailed X-ray analysis (possibly examining hard/soft lags, reflection features, or the presence of iron lines) would need to

be performed to verify that the X-ray emission is indeed more consistent with synchrotron from a jet rather than Comptonization in a hot inner flow. Such an X-ray analysis is beyond the scope of this work. However, we note that X-ray spectral studies (Motta et al., 2017b) of this stage of the outburst find photon indexes ($\Gamma \sim 1.5 - 1.7$) consistent with our estimated optically thin synchrotron spectral indices ($\alpha \sim -0.6 - -0.8$, where $\Gamma = 1 - \alpha$). This suggests that the X-ray spectrum may show a similar slope to the optically thin part of the compact jet spectrum, and thus be indicative of a synchrotron origin for this X-ray emission.

Further, we see limited evidence for evolution in the broad-band spectra across our sampled epochs during the outburst decay. For instance, the optically thin spectral index stays relatively constant (within error) across the epochs where it is measured, the optically thick spectral index may only flatten slightly over time, and the spectral break resides in the near-IR/optical bands across all of our sampled epochs (see Table 6.2). Additional radio observations occurring after our sampled epochs (in late July and early August) also show a similar trend, where the shape of the radio spectrum (i.e., spectral index) remains relatively constant over time (Plotkin et al., 2017). Limited jet spectral evolution may suggest the jet properties are not changing significantly as the jet emission fades during these epochs (e.g., the jet spectral shape can be sensitive to many parameters, such as the magnetic field strength at the base of the jet, jet geometry, inclination of the system, the particle acceleration process, and the electron energy distribution injected into the jets; Pe'er & Casella 2009; Kaiser 2006; Jamil et al. 2010; Malzac 2014). Interestingly, Chandra & Kanekar (2017) have reported the detection of a spectral break in the radio band at $\nu_{\mathrm{break}} = 1.8$ GHz on MJD 57199/57200. This finding is consistent with our previous work (Tetarenko et al. 2017 and Chapter 5 §5.5.4 of this thesis), where we found evidence of a compact jet with a spectral break between $0.341 < \nu_{\mathrm{break}} < 5.25$ GHz on MJD 57195. Therefore, while we

observe little spectral break evolution in broad-band spectra sampling epochs later than MJD 57202 in this work, combining these two results may suggest that the spectral break rapidly shifted from the radio to near-IR bands over the span of a few days (between MJD 57199–57202).

Moreover, we find that the compact jet emission during the outburst decay can also be highly variable (on minute to hour timescales), similar to the conditions observed in the quiescent V404 Cyg jet. While the variability amplitude at radio/sub-mm frequencies appears to follow an average trend, where the variability amplitude decreases as the intensity of the jet emission decreases, interestingly we also find that the variability amplitude can sporadically increase in certain time periods. For example, on MJD 57204 the sub-mm emission displays a large variability amplitude of $F_{var} \sim 85\%$, while the epochs taken ~ 24 hours prior to and following the MJD 57204 epoch, show little to no variability (see Figure 6.4). Maitra et al. (2017) have suggested that strong optical frequency variability (also probing the jet base region, but closer to the black hole than probed by sub-mm frequencies) occurring a few days earlier on MJD 57200, could be caused by a disruption in the feeding of the jet. In this situation, the mass outflow rate changes sporadically in response to a change in the mass inflow rate through the disc. Alternatively, the high variability amplitude detected on MJD 57204 could be tracing the re-establishment of the compact jet, following the last major flaring episodes occurring a few days earlier. In either case, if the jet flow was unstable in the MJD 57204 epoch, this could also explain the origin of the time lags we detect between the radio bands in the MJD 57205 epoch. In particular, these time lags could be tracking a disturbance in the jet flow, that was injected into the jet base sometime between the MJD 57204/57205 epochs, and has since propagated downstream (to lower frequencies) in the jet.

6.4.3   Comparison to the 1989 Outburst

V404 Cyg underwent three outbursts prior to 2015: 1938 (when the optical counterpart was observed and originally identified as Nova Cygni; Wagner et al. 1989), 1956 (as discovered on photographic plates; Richter 1989), and 1989 (when the transient X-ray counterpart was first identified by the Ginga satellite; Makino 1989). The 1989 outburst was monitored at multiple frequencies, including X-ray, optical, and radio frequencies (Han & Hjellming, 1992). While both the 1989 and 2015 outburst have been shown to exhibit similar X-ray behaviour (e.g., bright X-ray flaring activity that is not always intrinsic to the source), a detailed comparison between the radio jet behaviour during these different outbursts has not yet been presented. Radio frequencies offer the distinct advantage of providing a cleaner view of the system, when compared to the X-ray regime, as the high column density/external obscuration effects (Motta et al., 2017a) do not apply in the radio regime. As such, given our well-sampled radio coverage, in this section we compare the radio jet behaviour between the 1989 and 2015 outbursts (see Figure 6.9 for the radio frequency light curves and radio spectral indices for both outbursts).

The radio jet behaviour in the 1989 and 2015 outbursts display many similarities; both outbursts reach similar peak intensities (~ 1 Jy), the spectral indices show similar evolution (progresses from steep, to flat, to inverted, in ~ 20 days), both outbursts spend ~ 15 days in a high luminosity flaring accretion state before transitioning into a hard accretion state (where the jet emission is dominated by a compact jet; red and blue shading in Figure 6.9), the radio emission remained variable throughout the outburst (regardless of flux level), and there are hints of coupling between radio, optical, and X-ray emission (Han & Hjellming 1992; Tetarenko et al. 2017; Plotkin et al. 2017, and Chapter 5 §5.5.8 of this thesis). However, the radio emission in the 2015 outburst decays significantly faster than the radio emission in the 1989 outburst (~ 30 days in 2015 vs. ~ 300 days in 1989, to reach sub-mJy levels), and

no mini-outburst is observed at radio frequencies in 1989 (Muñoz-Darias et al., 2017). However, given the duration of the 2015 mini-outburst, and the sampling timescale between the 1989 radio epochs, it is entirely possible that such a mini-outburst was simply missed in 1989. Interestingly, the 2015 outburst also decayed much more quickly in X-rays when compared to the 1989 outburst (~ 60 days in 2015 vs ~ 160 days in 1989; Terada et al. 1994; Oosterbroek et al. 1997; Zycki et al. 1999; Plotkin et al. 2017).

Several works (Gallo et al., 2003; Corbel et al., 2008; Gallo et al., 2014; Plotkin et al., 2017; Gallo et al., 2018) have shown that the radio luminosity of V404 Cyg is linked to the X-ray luminosity through a robust disc-jet coupling relationship (radio luminosity is proportional to the X-ray luminosity, $L_R \propto L_X^\beta$, where $\beta \sim 0.54$ for V404 Cyg; see also Chapters 2 and 3 of this thesis for a detailed discussion on this correlation). This relationship was shown to hold across a wide range of X-ray luminosities ($L_X \sim 10^{32} - 10^{37} \, \mathrm{erg \, s^{-1}}$), and is valid for both the 1989 and 2015 outbursts (Plotkin et al., 2017). Therefore, as the X-ray luminosity can be thought of a proxy for mass accretion rate, the more rapid drop in radio luminosity in the 2015 outburst could be the result of a more rapid drop in the average mass accretion rate after the peak of the outburst, when compared to the 1989 outburst. Muñoz-Darias et al. (2016) have suggested that the strong accretion disc wind detected during the 2015 outburst may be a factor that regulates outburst duration, as these winds can significantly deplete the mass in the accretion disc (and potentially cause drastic and rapid changes in mass accretion rate). As such, it is possible that the faster decay seen in our radio light curves in the 2015 outburst indicates that the mass loss rate in the winds was much higher in the 2015 outburst, leaving less matter in the disc to fuel the jets. Along the same lines, the length of the quiescent period prior to each outburst may also be a contributing factor to the more rapid radio decay. In particular, as the quiescent period prior to the 1989 outburst was longer than the quiescent period prior to the 2015 outburst

(33 vs 26 years), the system had more time to build up mass in the disc (to fuel the jets) before the 1989 outburst.
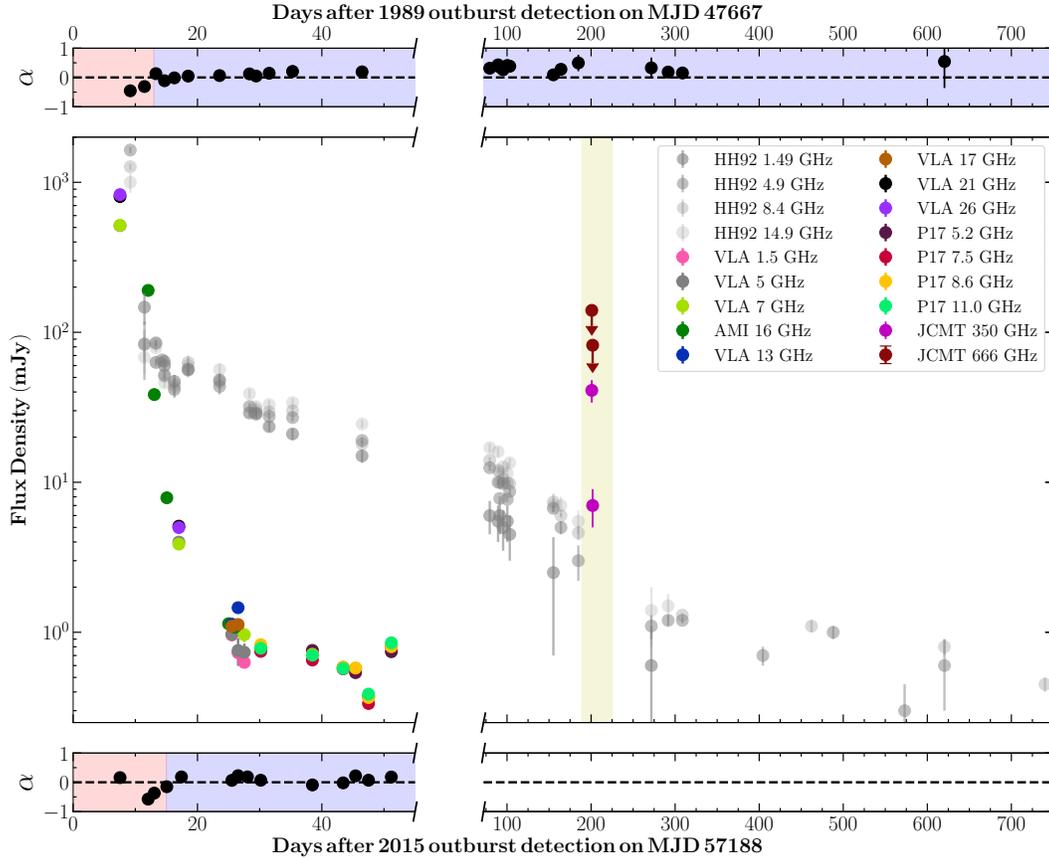
Figure 6.9: Radio frequency light curves of the 1989 (gray-scale data points) and 2015 (coloured data points) outbursts of V404 Cyg. The 1989 radio frequency data is taken from Han & Hjellming (1992) (HH92), and we supplement our 2015 radio frequency coverage with the measurements reported in Plotkin et al. (2017) (P17). The *top* and *bottom* panels indicate the radio spectral indices (in epochs where at least two radio bands were observed) in 1989 and 2015, respectively. The shaded regions in the *top* and *bottom* panels represent the time periods in which the radio emission was likely dominated by jet ejecta emission (red; $\alpha < 0$) or compact jet emission (blue; $\alpha \geq 0$). We also include our JCMT sub-mm coverage of the 2015 mini-outburst-burst in this plot, where the yellow shading in the *middle* panel indicates the duration of the 2015 mini-outburst period (MJD 57377–57413; Muñoz-Darias et al. 2017). While both outbursts reach similar peak intensities and show similar radio spectral index evolution, the radio emission from the 2015 outburst appears to decay much faster than in the 1989 outburst.

6.4.4 The December 2015 Mini-outburst

Following the June 2015 outburst of V404 Cyg, renewed X-ray activity was detected from the system in December 2015 (MJD 57377, $\sim$ 189 days after the first detection of the June outburst; Lipunov et al. 2015; Trushkin et al. 2015; Beardmore et al. 2015; Malyshev et al. 2015; Motta et al. 2016). Recent work (Muñoz-Darias et al., 2017; Kajava et al., 2018) has shown that while this "mini-outburst" was in general fainter across all sampled frequencies when compared to the June outburst, it showed similar phenomenology; strong flaring activity, fast accretion disc wind, highly variable column density.

This mini-outburst phenomenon has been seen in other BHXB sources following bright outbursts (e.g., GRO J0422+32, XTE J1650-500, MAXI J1659-152, GRS 1739-278; Yan & Yu 2017 and references within). However, with the exception of one source (Swift J1753.5-0127; Plotkin et al. 2017), these mini-outbursts have only been monitored at X-ray and optical frequencies.

Muñoz-Darias et al. (2017) present AMI radio monitoring of this mini-outburst period, where they detect flaring radio emission for a 10 day period following the mini-outburst detection. This flaring period ended with a large radio flaring episode on December 31/January 1, after which the radio emission began to decay (similar to the final radio flare on June 26 in the main outburst). We obtained JCMT SCUBA-2 sub-mm observations on January 1 and 2, in which we observe a decreasing flux density trend in both the time-resolved measurements on January 1 and between the two JCMT epochs (see Figure 6.10). This trend, combined with the timing of our measurements near the large radio flare, suggests that we may have caught the tail end of a brighter flare in our JCMT observations. Radio and sub-mm flaring accompanied repeated jet ejection events during the main June outburst (Chapter 5 of this thesis and Figure 6.3). Therefore, our measurements corroborate the theory suggested by Muñoz-Darias et al. (2017), that despite the fainter nature of the mini-outburst, V404 Cyg was still launching discrete jet ejecta during this time
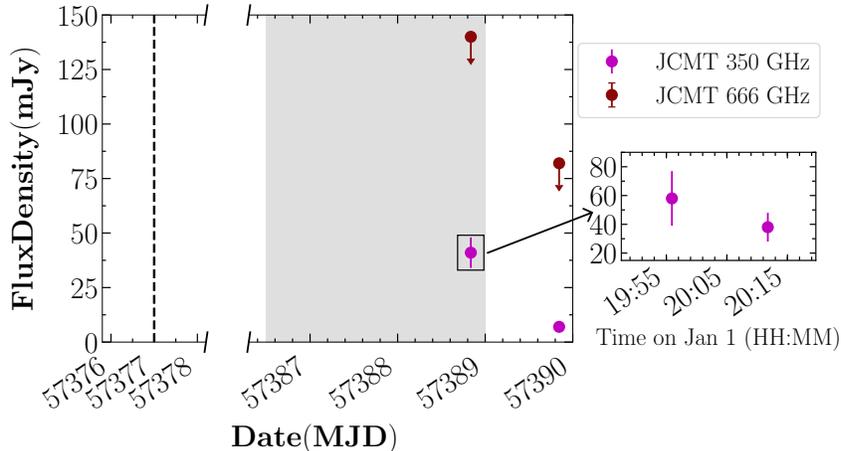
Figure 6.10: JCMT sub-mm light curves of V404 Cyg during the December 2015 mini-outburst. The vertical dotted line indicates the start of the mini-outburst on MJD 57377, while the shaded grey region indicates the most active flaring phase of the mini-outburst (MJD 57386.5–57389; as identified by Muñoz-Darias et al. 2017). The *right panel* displays a time-resolved analysis of the 2016 January 1 (MJD 57388) observation, where we split the 30 minute scan into two segments. The decreasing flux trend observed in the daily light curve (*main panel*) and time resolved measurements (*right panel*), as well as the timing of our measurements near the end of the active flaring period, suggests that we may have caught the tail end of a brighter flare in these JCMT sub-mm observations.

period, and in turn, jet ejecta are not exclusive to the highest luminosity states in V404 Cyg.

6.5 Summary

In this paper, we present the results of our multi-frequency monitoring observations of the 2015 outburst of the BHXB V404 Cyg. We observed the source at radio and mm/sub-mm frequencies, with the VLA, AMI, SMA, JCMT, and NOEMA, and collected publicly available OIR, UV, and X-ray measurements to supplement our coverage. With this well-sampled data set, we created detailed diagnostics of the jet emission in V404 Cyg, tracking the spectral and variability properties throughout different stages of the outburst (e.g., time-resolved light curves and spectral indices, broad-band spectra, CCFs, variability amplitude

measurements).

Using these diagnostics we find that the jet emission was originally dominated by emission from discrete jet ejecta during the brightest stages of the outburst. These ejecta appeared to become fainter, slower, less frequent, and less energetic, before the emission abruptly (over 1–2 days) transitioned to being dominated by a compact jet. While the broad-band spectrum of this compact jet showed very little evolution throughout the outburst decay (despite the intensity of the jet emission fading by an order of magnitude), the emission still remained intermittently variable at mm/sub-mm frequencies. Further, through phenomenological modelling of the broad-band emission from this compact jet, we directly detect the optically thick to thin synchrotron jet spectral break in the near-IR and optical bands ($\sim 2 - 5 \times 10^{14}$ Hz), and postulate that the compact jet could have been significantly contributing to the X-ray emission observed during the outburst decay.

Additionally, we compared the radio jet emission throughout the 2015 and previous 1989 outbursts. While the radio jet emission in both outbursts show many similarities (e.g., peak flux, spectral index evolution), we show that the radio emission in the 2015 outburst decayed significantly (~ 10 times) faster than in the 1989 outburst. We postulate that, given the robust disc-jet coupling relationship found between these two outbursts (Plotkin et al., 2017), this difference could indicate that the average mass accretion rate dropped (possibly due to the strong accretion disc wind) much quicker following the peak of the 2015 outburst, when compared to the 1989 outburst.

Lastly, we report on sub-mm observations during the December 2015 minioutburst of V404 Cyg. These sub-mm observations display a decreasing flux trend, that most likely samples the tail end of a larger flaring episode. As sub-mm flaring coincided with jet ejection episodes during the main outburst, these observations support previous claims (Muñoz-Darias et al., 2017) that, similar to the main outburst, the source was most likely launching powerful jet

ejecta during this period of renewed activity.

Overall, our work here has demonstrated the importance of simultaneous, multi-frequency, time-resolved observations, to fully understand the rapidly evolving jet sources in BHXBs.

6.6 Appendix

6.6.1 Observation Setup

In this section we provide details on the correlator and array setup of all of our radio through mm/sub-mm interferometric observations; VLA (Table 6.3), NOEMA (Table 6.4), SMA (Table 6.5).

6.6.2 Observational Data

In this section we provide data tables of all the day-timescale multi-frequency photometry measurements presented in this work; radio (Table 6.6), mm/sub-mm (Table 6.7), and OIR/UV/X-ray (Table 6.8).

Table 6.3: VLA observations summary of our V404 Cyg data during the 2015 outburst

Date (2015)	MJD	Sub-array	Scans (UTC)	Band(s)[a]	Number of Antennas
July 02	57205	A	10:02:14–14:01:32	C-K-C	14
		B	10:05:14–14:01:32	K-C-K	13
July 10	57213	A	12:03:02–13:01:50	C	8
		B	12:04:02–13:01:52	L	9
		C	12:02:02–13:01:50	Ku	9
July 11	57214	A	13:29:52–14:27:40	L	9
		B	13:28:52–14:27:40	C	8
		C	13:27:52–14:27:40	Ku	9
July 12	57215	A	12:04:02–13:01:52	L	8
		B	12:03:02–13:01:50	C	9
		C[b]	⋯	Ku	8

[a] This column indicates the frequency bands observed with each sub-array. When multiple bands are present, the entry in this column indicates the temporal sequence with which the bands were observed by the sub-array.
[b] A technical error occurred during observing and no data was taken for this sub-array.

225

Table 6.4: NOEMA observations summary of our V404 Cyg data during the 2015 outburst

Date (2015)	MJD	Array Config.	Scans (UTC)	Band	Number of Antennas
Jun 26	57199	6Dq-E03+E12	22:24:02–23:12:58	3 mm	6
Jun 27	57200	6Dq-E03+E12	00:15:35–02:42:31	2 mm	6
Jun 27/28	57200/57201	6Dq-E03+E12	23:17:37–03:05:34	2 mm	6
Jun 29	57202	6Dq	22:13:50–23:02:47	3 mm	6
Jun 30	57203	6Dq	00:14:51–02:55:10	2 mm	6
Jul 12	57215	6Dq	22:03:27–22:52:23	3 mm	6
Jul 12/13	57215/57216	6Dq	23:45:19–02:12:09	2 mm	6

Table 6.5: SMA Observations summary of our V404 Cyg data during the 2015 outburst

Date (2015)	MJD	Array Config.	Scans (UTC)	Total Bandwidth (GHz)	Correlator	Correlator Setup[a] (N_{spw}, N_{C}, $\Delta\nu$ MHz)[b]	Number of Antennas
Jun 16	57189	sub-compact	17:22:33–18:40:43	8.32	ASIC+SWARM	(48, 128, 0.8125) + (2, 128, 13)[c]	7
Jun 17	57190	sub-compact	13:25:04–17:03:14	4.992	ASIC	(48, 128, 0.8125)	6
July 01	57204	compact	07:50:28–17:18:53	2.080	ASIC	(20, 32, 3.250)	6
July 02	57205	compact	09:26:57–14:30:42	2.496	ASIC	(24, 32, 3.250)[d]	6

[a] Our SMA project is a ToO program, with highly constrained start times, needed to obtain simultaneous observations with other facilities. Therefore, due to the continuum nature of our observations, our program is often run immediately before or after other SMA observing programs, which results in the wide variety of correlator setups seen here.
[b] The correlator setup; number of spectral windows, number of channels, and channel width, for each of the two side-bands.
[c] The SWARM correlator had a fixed resolution of 101.6 kHz per channel, with 16383 channels for each SWARM spectral window. Given the continuum nature of these observations, we performed spectral averaging, to yield 128 13 MHz channels in both SWARM spectral windows (matching the number of channels in the ASIC spectral windows), to make it easier to combine ASIC and SWARM data.
[d] Three of the 24 spectral windows were set up with a higher spectral resolution in this observation; 512 0.203 MHz channels. As such, we spectrally averaged these channels to match the other spectral windows with 32 3.250 MHz channels.

Table 6.6: Flux densities of V404 Cyg at radio frequencies

Telescope	Date (2015)	MJD	Freq. (GHz)	Flux Density[a] (mJy)
VLA	June 22	57195	5.25	514.5 ± 5.1
VLA	June 22	57195	7.45	516.9 ± 5.2
VLA	June 22	57195	20.8	803.5 ± 18.1
VLA	June 22	57195	25.9	827.7 ± 18.3
AMI	June 26/27	57199/57200	16.0	190.23 ± 0.03
AMI	June 27/28	57200/57201	16.0	38.44 ± 0.03
AMI	June 29/30	57202/57203	16.0	7.88 ± 0.02
GMRT[†]	July 01	57204	1.280	6.39 ± 0.67
GMRT[†]	July 01	57204	0.610	8.88 ± 0.94
GMRT[†]	July 01	57204	0.235	13.4 ± 2.4
VLA	July 02	57205	5.25	3.99 ± 0.06
VLA	July 02	57205	7.45	3.87 ± 0.05
VLA	July 02	57205	20.8	5.10 ± 0.16
VLA	July 02	57205	25.9	4.99 ± 0.15
VLA	July 10	57213	1.52	0.96 ± 0.09
VLA	July 10	57213	5.24	0.97 ± 0.09
VLA	July 10	57213	7.45	1.13 ± 0.08
VLA	July 10	57213	13.5	1.13 ± 0.05
VLA	July 10	57213	17.4	1.10 ± 0.05
AMI	July 10	57213	16.0	1.14 ± 0.07
GMRT[†]	July 11	57214	1.280	0.52 ± 0.14
GMRT[†]	July 11	57214	0.610	< 0.6
GMRT[†]	July 11	57214	0.235	0.66 ± 0.24
VLA	July 11	57214	1.52	0.73 ± 0.05
VLA	July 11	57214	5.24	0.76 ± 0.16
VLA	July 11	57214	7.45	1.12 ± 0.10
VLA	July 11	57214	13.5	1.46 ± 0.07
VLA	July 11	57214	17.4	1.13 ± 0.07
AMI	July 11	57214	16.0	1.08 ± 0.07
GMRT[†]	July 12	57215	1.280	< 4.7
GMRT[†]	July 12	57215	0.610	0.52 ± 0.12
GMRT[†]	July 12	57215	0.235	0.50 ± 0.19
VLA	July 12	57215	1.52	0.63 ± 0.04
VLA	July 12	57215	5.24	0.74 ± 0.11
VLA	July 12	57215	7.45	0.96 ± 0.10
VLA	July 12[⋆]	57215	13.5	$\ldots$
VLA	July 12[⋆]	57215	17.4	$\ldots$

[a] The VLA measurements include the standard VLA systematic errors.
[⋆] A technical error occurred during observing, and thus no data was taken for this sub-array.
[†] Giant Metrewave Radio Telescope (GMRT) data is taken from Chandra & Kanekar (2017).

Table 6.7: Flux densities of V404 Cyg at mm/sub-mm frequencies

Telescope	Date (2015)	MJD	Freq. (GHz)	Flux Density (mJy)
SMA	June 16	57189	220.25	102.0 ± 1.6
SMA	June 16	57189	230.25	72.9 ± 1.5
SMA	June 17	57190	220.25	17.5 ± 0.6
SMA	June 17	57190	230.25	15.7 ± 0.6
JCMT	June 17	57190	350	7.9 ± 2.1
JCMT	June 17	57190	666*	< 122
SMA	June 22	57195	220.25	878.0 ± 32.0
SMA	June 22	57195	230.25	872.0 ± 32.0
JCMT	June 22	57195	350	932.8 ± 6.9
JCMT	June 22	57195	666	988.6 ± 30.0
NOEMA	June 26/27	57199/57200	97.5	70.16 ± 0.09
NOEMA	June 26/27	57199/57200	140	48.62 ± 0.07
NOEMA	June 27/28	57200/57201	140	16.80 ± 0.05
NOEMA	June 29/30	57202/57203	97.5	5.32 ± 0.09
NOEMA	June 29/30	57202/57203	140	5.87 ± 0.07
SMA	July 01	57204	220.25	5.2 ± 1.2
SMA	July 01	57204	230.25	5.8 ± 1.2
SMA	July 02	57205	220.25	8.9 ± 2.2
SMA	July 02	57205	230.25	5.5 ± 2.5
JCMT	July 02	57205	350	10.0 ± 1.4
JCMT	July 02	57205	666*	< 80
NOEMA	July 12/13	57215/57216	97.5	1.38 ± 0.09
NOEMA	July 12/13	57215/57216	140	1.44 ± 0.12
JCMT	January 01†	57388	350	41 ± 7
JCMT	January 01†	57388	666*	< 140
JCMT	January 02†	57389	350	7 ± 2
JCMT	January 02†	57389	666*	< 82

* Note that data in the 666 GHz (450μm) band was obtained simultaneously with the 350 GHz (850 μm) band, but the source was not always significantly detected at 666 GHz. The values reported here represent 3σ upper limits.
† These data were taken during the late December 2015 mini-outburst of V404 Cyg.

Table 6.8: Flux densities of V404 Cyg at OIR/UV/X-ray frequencies

Band[a]	Date (2015)	MJD	Freq. (GHz)	Flux Density (mJy)	Ref.[b]
R	June 16	57189	4.56×10^5	212.2 ± 22.9	[5]
J	June 26/27	57199/57200	2.45×10^5	46.6 ± 4.9	[1]
H	June 26/27	57199/57200	1.84×10^5	50.5 ± 5.0	[1]
K	June 26/27	57199/57200	1.37×10^5	37.6 ± 2.9	[1]
U	June 26/27	57199/57200	8.65×10^5	25.7 ± 1.0	[2]
J	June 27/28	57200/57201	2.45×10^5	98.7 ± 8.6	[3]
H	June 27/28	57200/57201	1.84×10^5	77.9 ± 8.5	[3]
K	June 27/28	57200/57201	1.37×10^5	67.4 ± 6.6	[3]
V	June 27/28	57200/57201	5.48×10^5	19.1 ± 1.9	[2]
B	June 27/28	57200/57201	6.82×10^5	16.1 ± 2.4	[2]
UV1	June 27/28	57200/57201	1.15×10^6	2.2 ± 9.1	[2]
J	June 29/30	57202/57203	2.45×10^5	30.7 ± 0.6	[4]
H	June 29/30	57202/57203	1.84×10^5	25.8 ± 0.6	[4]
K	June 29/30	57202/57203	1.37×10^5	22.3 ± 0.5	[4]
I	June 29/30	57202/57203	3.72×10^5	30.9 ± 2.7	[5]
V	June 29/30	57202/57203	5.48×10^5	19.9 ± 2.0	[2]
B	June 29/30	57202/57203	6.82×10^5	18.4 ± 2.4	[2]
U	June 29/30	57202/57203	8.65×10^5	11.4 ± 2.3	[2]
UV1	June 29/30	57202/57203	1.15×10^6	12.7 ± 10.7	[2]
UV2	June 29/30	57202/57203	1.55×10^6	2.9 ± 35.2	[2]
XRT	June 30	57203	1.21×10^9	$(6.6^{+0.5}_{-0.4}) \times 10^{-3}$	[6]
V	July 1	57204	5.48×10^5	29.8 ± 1.7	[2]
B	July 1	57204	6.82×10^5	20.4 ± 1.9	[2]
U	July 1	57204	8.65×10^5	13.8 ± 2.3	[2]
UV1	July 1	57204	1.15×10^6	5.7 ± 7.9	[2]
UV2	July 1	57204	1.55×10^6	41.0 ± 33.3	[2]
J	July 2	57205	2.45×10^5	29.9 ± 2.6	[1]
H	July 2	57205	1.84×10^5	31.8 ± 2.9	[1]
K	July 2	57205	1.37×10^5	24.3 ± 2.1	[1]
I	July 2	57205	3.72×10^5	42.5 ± 4.0	[5]
V	July 2	57205	5.48×10^5	19.6 ± 2.1	[2]
B	July 2	57205	6.82×10^5	18.9 ± 2.4	[2]
U	July 2	57205	8.65×10^5	14.5 ± 3.1	[2]
UV1	July 2	57205	1.15×10^6	7.3 ± 9.7	[2]
XRT	July 2	57205	1.21×10^9	$(4.7^{+0.3}_{-0.3}) \times 10^{-3}$	[6]
I	July 10	57213	3.72×10^5	22.3 ± 2.0	[8]
R	July 10	57213	4.56×10^5	23.4 ± 0.4	[8]
V	July 10	57213	5.48×10^5	14.8 ± 0.8	[8]
U	July 10	57213	8.65×10^5	5.1 ± 0.6	[2]
UV1	July 10	57213	1.15×10^6	6.1 ± 1.3	[2]
XRT	July 10	57213	1.21×10^9	$(1.0^{+0.2}_{-0.1}) \times 10^{-3}$	[6]
I	July 11	57214	3.72×10^5	22.3 ± 2.0	[8]
R	July 11	57214	4.56×10^5	21.1 ± 1.1	[8]
V	July 11	57214	5.48×10^5	15.0 ± 0.4	[8]
Chandra	July 11	57214	1.21×10^9	$(1.2^{+0.02}_{-0.01}) \times 10^{-3}$	[7]
I	July 12	57214	3.72×10^5	20.1 ± 1.0	[8]
R	July 12	57214	4.56×10^5	17.6 ± 1.6	[8]
V	July 12	57214	5.48×10^5	13.7 ± 0.8	[8]

[a] Filters/instruments used for each observation; U (UVOT U band), B (UVOT B band), V (UVOT/Optical V band), UV1 (UVOT UVW1 band), UV2 (UVOT UVW2 band), R (optical R band), I (optical I band), J (infrared J band), H (infrared H band), K (infrared K band), *Swift* X-ray Telescope (XRT; 0.5-10 keV), *Chandra* (0.5-10 keV). Data shown in this table have been de-reddened (when required) using the prescription in Cardelli et al. (1989), with an $E(B-V) = 1.3 \pm 0.2$ (Casares et al., 1993).
[b] **References:** [1] Arkharov et al. 2015; [2] Oates et al. 2015; [3] Shaw 2015; [4] Carrasco et al. 2015; [5] Kimura et al. 2016; [6] Sivakoff et al. 2015c; [7] Plotkin et al. 2017; [8] AAVSO; Kafka, S., 2018, Observations from the AAVSO International Database, https://www.aavso.org.

6.6.3 Jet Modelling Results

In this section we display an alternate version of Figure 6.6 (Figure 6.11), in which we decompose the total jet model into the individual approaching and receding components.
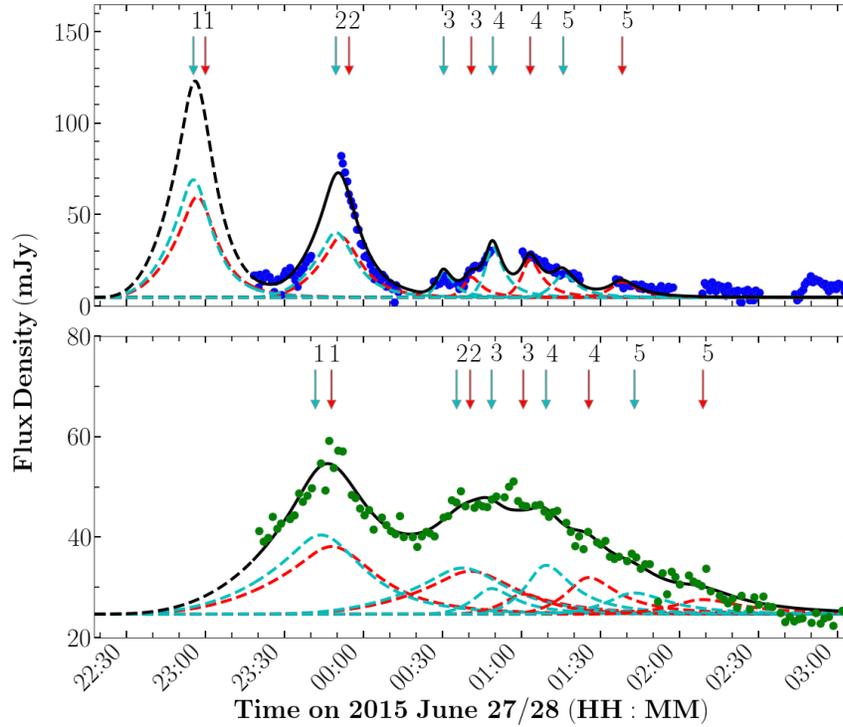
Figure 6.11: Radio (AMI 16 GHz) and mm/sub-mm (NOEMA 140 GHz) light curves of V404 Cyg on 2015 June 27/28 (MJD 57200/57201). In both panels, the black lines represents our predicted best fit jet model at each frequency, and the dotted lines indicate the approaching (cyan) and receding (red) components of the individual ejection events. The arrows at the top of each panel (cyan for approaching, red for receding) identify which flares correspond to which ejection number from Table 6.1.

Chapter 7

Rapidly-precessing relativistic jets from the stellar-mass black hole V404 Cygni

This chapter is based on a manuscript in preparation, to be submitted to the *Nature* journal as Miller-Jones, J.C.A., Tetarenko, A.J. et al. 2018, "Rapidly-precessing relativistic jets from the stellar-mass black hole V404 Cygni", describing a high angular resolution radio imaging study of the jets launched from the black hole X-ray binary V404 Cygni.

Abstract

We present Very Long Baseline Array (VLBA) radio frequency observations of the black hole X-ray binary V404 Cygni, taken during its June 2015 outburst. With these data, we create a series of high angular resolution images of the jets in V404 Cygni, in which we detect and track the motion of multiple discrete jet ejection events launched from the system. The orientation of the jet axis during these events varies on timescales as short as minutes, indicating that the jet is rapidly precessing in V404 Cygni. We show that this jet precession could originate from Lense-Thirring precession of a vertically-extended accretion disc,

arising from a super-Eddington accretion rate in V404 Cygni. Ultimately, our findings demonstrate that the dynamics of a precessing inner accretion disc can play a key role in either directly launching or redirecting jets within the inner few hundred gravitational radii of the black hole.

7.1 Introduction

Accreting black holes are known to launch powerful relativistic jets, however, we still lack a fundamental understanding of the mechanisms involved in launching these jets and their bulk properties. While jets are thought to be launched on size scales comparable to the black hole event horizon and magnetic fields are expected to play a key role in accelerating and collimating the jets, the reservoir from which energy is extracted to power the jets (e.g., rotational energy of the accretion disc; Blandford & Payne 1982, or the spin energy of the black hole; Blandford & Znajek 1977; Punsly & Coroniti 1990) and the sequence of events leading to jet launching, are not well understood.

In accreting systems that harbor a stellar-mass black hole (black hole X-ray binaries or BHXBs), both the jet launching region and the the accretion flow cannot be directly imaged. However, X-ray variability studies of BHXBs can provide an alternative means of understanding the conditions in these regions. For instance, X-ray variability properties have provided evidence that the inner accretion flow can precess in BHXBs (Ingram et al., 2016). In the situation where the black hole spin axis is misaligned with the orbital plane of the binary (Martin et al., 2008; Maccarone, 2002), frame-dragging around the black hole causes material out of the equatorial plane to precess (Lense & Thirring, 1918), thereby enhancing the amplitude of X-ray variability at the precession period (detected in the form of quasi-periodic oscillations). Recent magneto-hydrodynamic (MHD) simulations suggest that jets launched from or redirected by the accretion flow should be significantly affected by this pre-

cession (Liska et al., 2018), however, the interplay between the dynamics of the accretion flow and the launching of these jets has not been well-studied observationally.

High resolution radio imaging studies of BHXBs with Very Long Baseline Interferometry (VLBI) can be used to directly measure jet properties (e.g., speed, geometry, and structure; Dhawan et al. 2000; Stirling et al. 2001; Miller-Jones et al. 2009), and probe the connection between jet launching and the accretion flow (e.g., Miller-Jones et al. 2012; van der Horst et al. 2013; Russell et al. 2014). In particular, VLBI can image the jets launched from BHXBs down to AU size scales, allowing us to directly resolve compact jets along the axial direction and jet ejecta launched from these systems. The unique ability of this VLBI technique to resolve the jet ejecta, presents the opportunity to track and model the motion of the ejecta in VLBI images, and in turn pinpoint the moment of jet ejection. Therefore, VLBI studies have a distinct advantage over photometric studies (which can only track changes in brightness of a flare accompanying the ejection) when attempting to connect the moment of jet ejection to conditions in the accretion flow.

On 2015 June 15, a new outburst of the BHXB V404 Cygni (hereafter V404 Cyg) was detected (Barthelmy et al., 2015; Negoro et al., 2015; Kuulkers et al., 2015). This particular BHXB system is an ideal laboratory for VLBI studies, due to its close proximity (2.39±0.14 kpc; Miller-Jones et al. 2009) and bright jet emission (showing mJy level fluxes in quiescence and Jy level fluxes in outburst; Han & Hjellming 1992; Gallo et al. 2003; Hynes et al. 2009; Hjellming et al. 2000a; Tetarenko et al. 2017). During its 2015 outburst, V404 Cyg was observed to undergo two weeks of multi-frequency flaring activity, where the radio emission was consistent with originating from a series of bi-polar, discrete jet ejection events (see Chapters 5 and 6 of this thesis). My team triggered high-angular resolution radio frequency VLBI observations with the Very Long Baseline Array (VLBA) amid this period of intense flaring, with the goal of

detecting and tracking the motion of the jet ejection events launched from V404 Cyg. Through tracking the motion of these jet ejecta, we aimed to study the sequence of events that lead to jet launching and work to link conditions in the accretion flow to the jet launching process.

In §7.2 we describe details of the VLBA observations, as well as the data reduction and imaging procedures. In §7.3 we present a sequence of high resolution radio frequency images of the source, in which we resolve multiple jet ejecta components whose brightness and morphology vary with time. Through detailed modelling of the bulk motion of these jet ejecta (accounting for atmospheric and instrumental effects), we measure proper motions and ejection times for each component, as well as infer jet speeds and the orientation of the jet axis during the ejection events. We present a discussion and interpretation of our results in §7.4.

7.2 VLBA observations, data reduction, and imaging

We observed V404 Cyg with the VLBA between 2015 June 17 and July 11 in the 8.4, 15.2, and 22.4 GHz bands, for a total of 15 epochs (see Table 7.1 for a detailed log of all the observations). During the observations of duration ≥ 3 hours, we spent 30 min at the beginning and end of the runs observing a selection of bright calibrator sources spread across the sky (i.e. geodetic blocks). This enabled us to better account for unmodeled clock and tropospheric phase errors, thereby improving the success of the phase calibration of the data.

All the VLBA data were reduced and calibrated using standard procedures within the Astronomical Image Processing System (AIPS; Greisen 2003). We first applied corrections for the updated Earth orientation parameters and ionospheric effects, used the system temperatures at each antenna to calibrate the amplitude scale, and derived instrumental phase solutions using the fringe

finder source (either J1800+3858 or J2253+1608, depending on the individual observation). Fringe fitting was then performed on a bright, nearby phase reference calibrator (J2025+3343), which was subjected to iterative imaging and self-calibration. The final image of the phase reference calibrator was then used as a model for bandpass calibration, before transferring bandpass, amplitude and phase solutions to the target source. Following the calibration process, the final calibrated data was written out for imaging.

My earlier work (Chapter 5 of this thesis and Tetarenko et al. 2017) showed that V404 Cyg displayed high amplitude variability at radio frequencies during the time of our VLBA observations. This variability complicates the imaging process as it violates one of the fundamental assumptions of aperture synthesis, namely that the target source should remain constant over the period of imaging. Therefore, we broke the VLBA data down into shorter segments for imaging, such that the overall amplitude would not change by more than 10% in each segment. This process equated to 103 scan-based segments (of duration 70 s) in the 15-GHz data from June 22 and two-scan segments (of duration 310 s) in the lower-frequency 8.4-GHz data from the other epochs. However, the sparse uv-coverage in each individual segment introduces other complexities into the imaging process, as we could not reliably image complex structures in any individual snapshot segment. Therefore, we worked to minimize the number of degrees of freedom during our deconvolution and imaging process by performing uv-model fitting to create a source model (using the DIFMAP software package; Shepherd 1997), rather than the standard *clean* algorithm. With this approach, we modelled the source with a number (≤ 6) of point source components in each snapshot segment, including one component representing a strong core jet component, and multiple jet ejecta components. Following multiple rounds of phase-only self-calibration and a final single round of amplitude and phase self-calibration within DIFMAP, the final calibrated image from each snapshot was written out as a FITS file.

Since the DIFMAP package does not provide uncertainties on its fitted model parameters, we converted the self-calibrated data to measurement sets, which were then read in to the Common Astronomy Software Application package (CASA; McMullin et al. 2007). Within CASA, we performed the *uv*-model fitting procedure again (with the UVMULTIFIT software tool; Marti-Vidal et al. 2014), using the DIFMAP model fit results to define the number of point sources used for each snapshot, and the initial guesses for the point source positions and flux densities.

Further, we took additional steps to ensure the fidelity of our final images. After all our snapshot segments of V404 Cyg had been imaged with the procedure described above, we individually inspected them for consistency between adjacent frames. Only a small minority of frames showed inconsistent structure, in which case we re-processed those frames taking into account our prior knowledge of what the adjacent frames showed. In a few cases, we processed longer chunks of data (10–15 min) into a single image to assess the fidelity of the structures with better *uv*-coverage.

Overall, we find that the flux densities and positions of our final set of source components in each segment evolve smoothly with time (e.g., see Figures 7.1 and 7.7), giving us confidence in the fidelity of our images.

Table 7.1: VLBA observing log of our observations during the 2015 outburst of V404 Cyg

Date	Time (UTC)[a]	MJD	Proposal Code	Frequency (GHz)
2015 June 17	09:30–12:30	57190.46±0.06	BM421A	8.4
2015 June 22	10:30–14:30	57195.52±0.08	BS249	15.2
2015 June 23	10:30–13:30	57196.50±0.06	BM421B	8.4
2015 June 24	10:30–13:30	57197.50±0.06	BM421C	8.4
2015 June 26	12:25–14:25	57199.56±0.04	BM421D	8.4
2015 June 27	07:52–09:51	57200.37±0.04	BM421E	8.4
2015 June 30	06:10–08:10	57203.30±0.04	BM421F	8.4
2015 July 1	10:05–12:05	57204.46±0.04	BM421G	8.4
2015 July 2	09:32–11:32	57205.44±0.04	BM421H	8.4
2015 July 4	07:24–09:24	57207.35±0.04	BM421I	8.4
2015 July 5	07:00–09:00	57208.33±0.04	BM421J	8.4
2015 July 6	10:46–12:46	57209.49±0.04	BM421K	8.4
2015 July 7	06:12–10:12	57210.34±0.08	BM421L	22.4
2015 July 8	08:58–10:54	57211.41±0.04	BM421M	8.4
2015 July 11	04:28–07:26	57214.25±0.06	BM421N	4.9

[a] Times denote the on-source time and do not include the 30-min geodetic blocks at the start and end of the longer ($\geq$ 3-hour) observations.
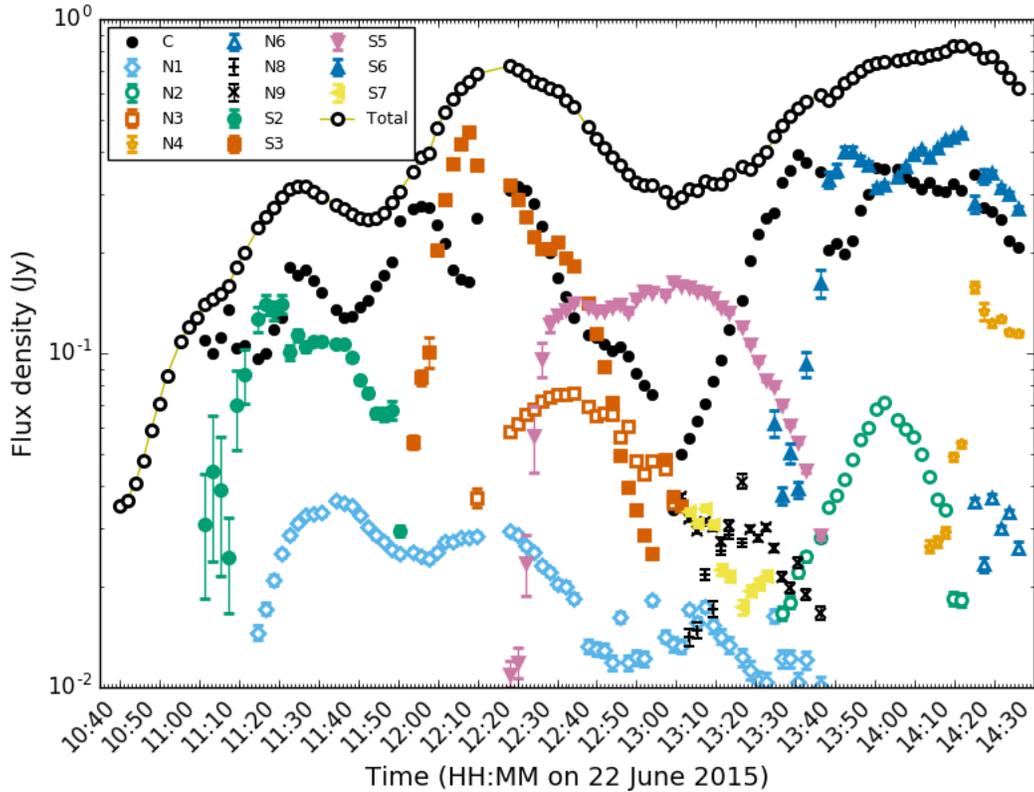
Figure 7.1: Light curves of the individual source components detected in our images, as a function of time on 2015 June 22. Colored markers represent the ejecta components (where empty markers represent northern components and filled markers represent southern components; N and S) and the solid black markers represent the core component (C). The topmost curve of empty black circles indicates the total integrated 15.4-GHz light curve of all the components. The light curves of all the source components evolve smoothly with time, other than occasional jumps when a new component appears or a blend of two components separates.

7.3 Results

7.3.1 Jet morphology and orientation

We imaged the jets of V404 Cyg across fifteen different VLBA observations (between 2015 June 17 and July 11; see Table 7.1) during its 2015 outburst. Within this series of images we observe that both the morphology and brightness of these jets vary on timescales as short as minutes.

Images made from the 2015 June 17, 23, 24, 26, 27, and 30 VLBA observations all revealed resolved jets that were extended on size scales of up to 5 mas, corresponding to a physical size scale of 12 AU at a distance of 2.39 kpc (see Figure 7.2). As these epochs were taken at 8.4 GHz, the lower angular resolution only allowed us to detect a single ejection event during each of these observations. Images made from the 2015 July 1–July 11 observations (after the flaring activity had ceased, see Chapter 6 of this thesis for details) only revealed an unresolved core jet component and no jet ejecta components.

Further, a series of higher angular resolution images made from the 2015 June 22 observations (taken at 15.4 GHz) reveal that multiple jet ejecta were launched from the system within a matter of hours during this epoch. These ejecta appear to propagate ballistically away from the core, persisting for several tens of minutes before fading below our detectability limits (see Figures 7.3–7.5, and see a movie of these VLBA images[1]).

The orientation of the extended jets on the plane of the sky (i.e., position angles or PAs) were observed to vary over time, ranging between -30.6 and $+5.9$ degrees east of north (Figure 7.6 and Table 7.2). Further, within the four-hour 2015 June 22 epoch, the series of ejecta we detected showed a similar range of orientations as the extended jets, implying extremely rapid changes in the orientation of the jet axis.

---

[1]`https://www.dropbox.com/s/yfpep4qpmalt5uf/v404_movie.mp4?dl=0`
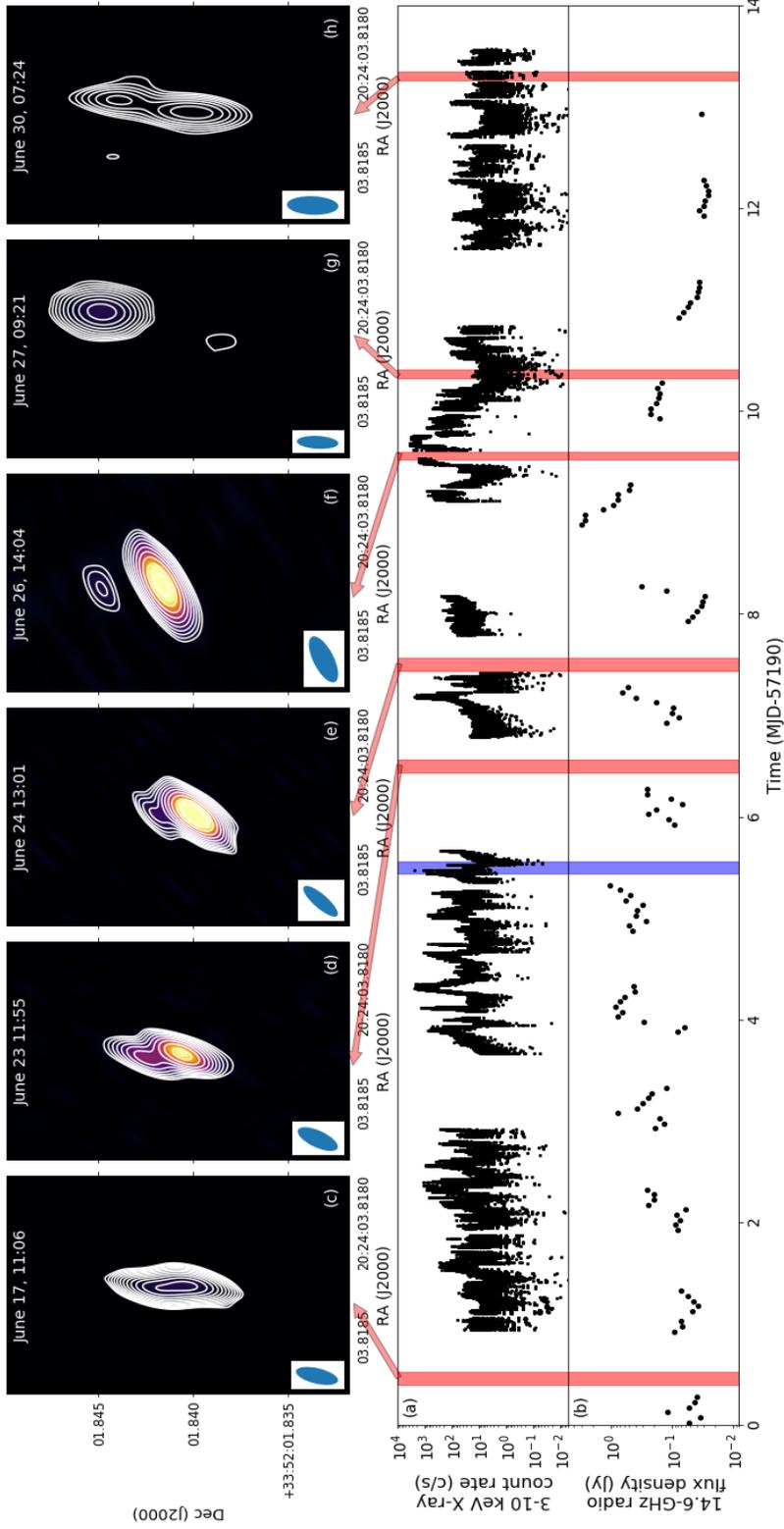
Figure 7.2: VLBI, X-ray, and radio frequency monitoring of V404 Cyg during the two weeks of extreme flaring activity seen in the 2015 outburst. The top panels display our VLBA monitoring of the radio jets at 8.4-GHz; left to right are VLBA snapshots from June 17 (panel c), June 23 (panel d), June 24 (panel e), June 26 (panel f), June 27 (panel g), and June 30 (panel h). Blue ellipses in the VLBA panels display the VLBA synthesized beam shape. The bottom two panels show the 3–10 keV X-ray (panel a; Rodriguez et al. 2015) and the 15 GHz AMI radio (panel b) light curves. The red shading indicates the time range of the VLBA observations shown in the top panel, while the blue shading indicates the time range of the VLBA observations from the 2015 June 22 epoch (see Figures 7.3–7.5 for the corresponding VLBA images from this epoch). We observe multiple jet ejection events, coincident with the multi-frequency flaring activity in V404 Cyg.

241
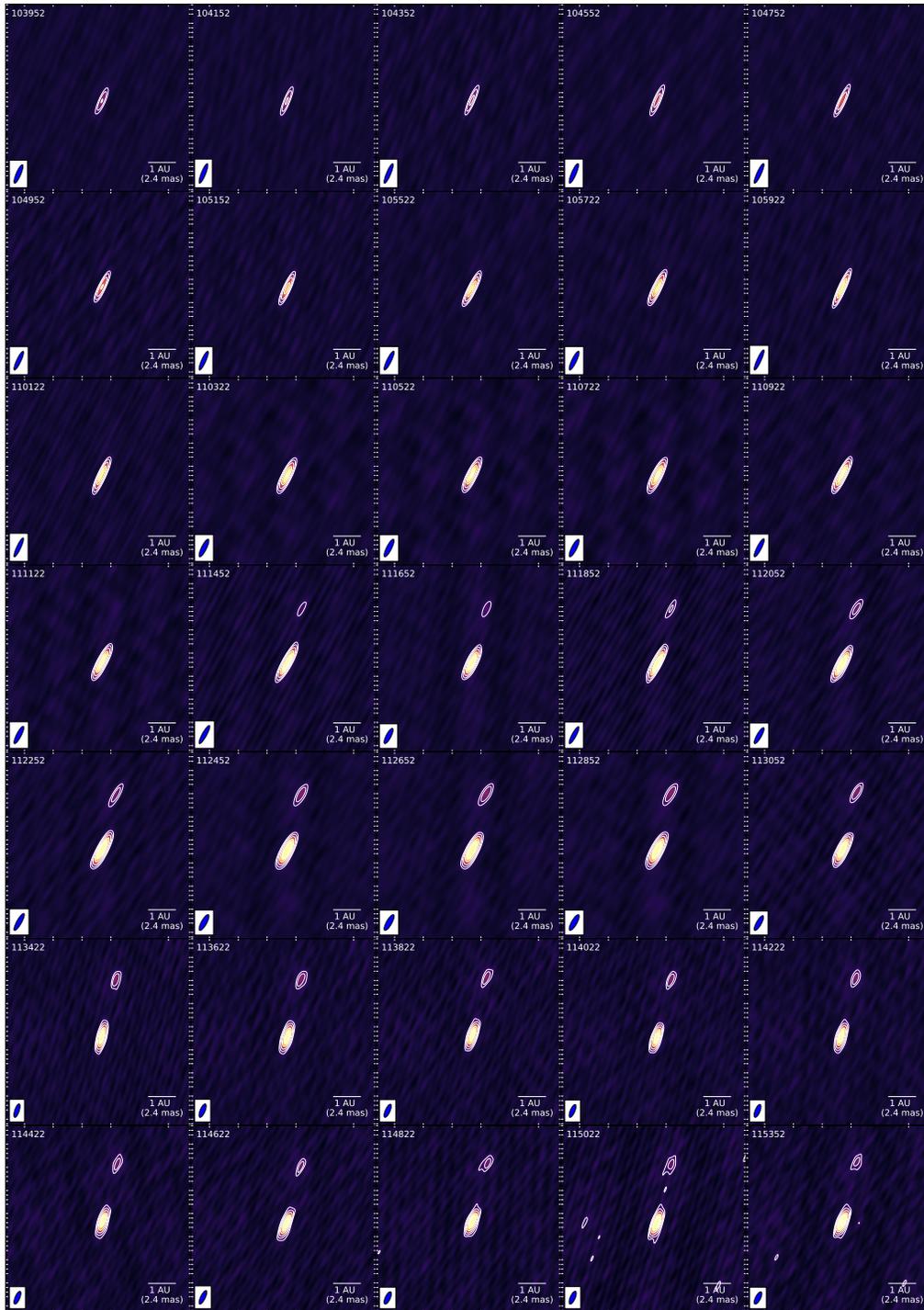
Figure 7.3: A sequence of time-resolved VLBA images of the V404 Cyg jet ejecta observed on 2015 June 22. The images are spaced by 2 minutes (except for phase calibration gaps), with the UTC time (in the format, HHMMSS) of each image given in the top left corner of each panel. Also indicated on each image are the VLBA synthesized beam shape (blue ellipse) and the size scale (white bar in the bottom right corner). A strong central core jet component is always observed, along with multiple jet ejecta which appear to propagate away from the core over time. Images are continued in Figures 7.4 and 7.5.

242
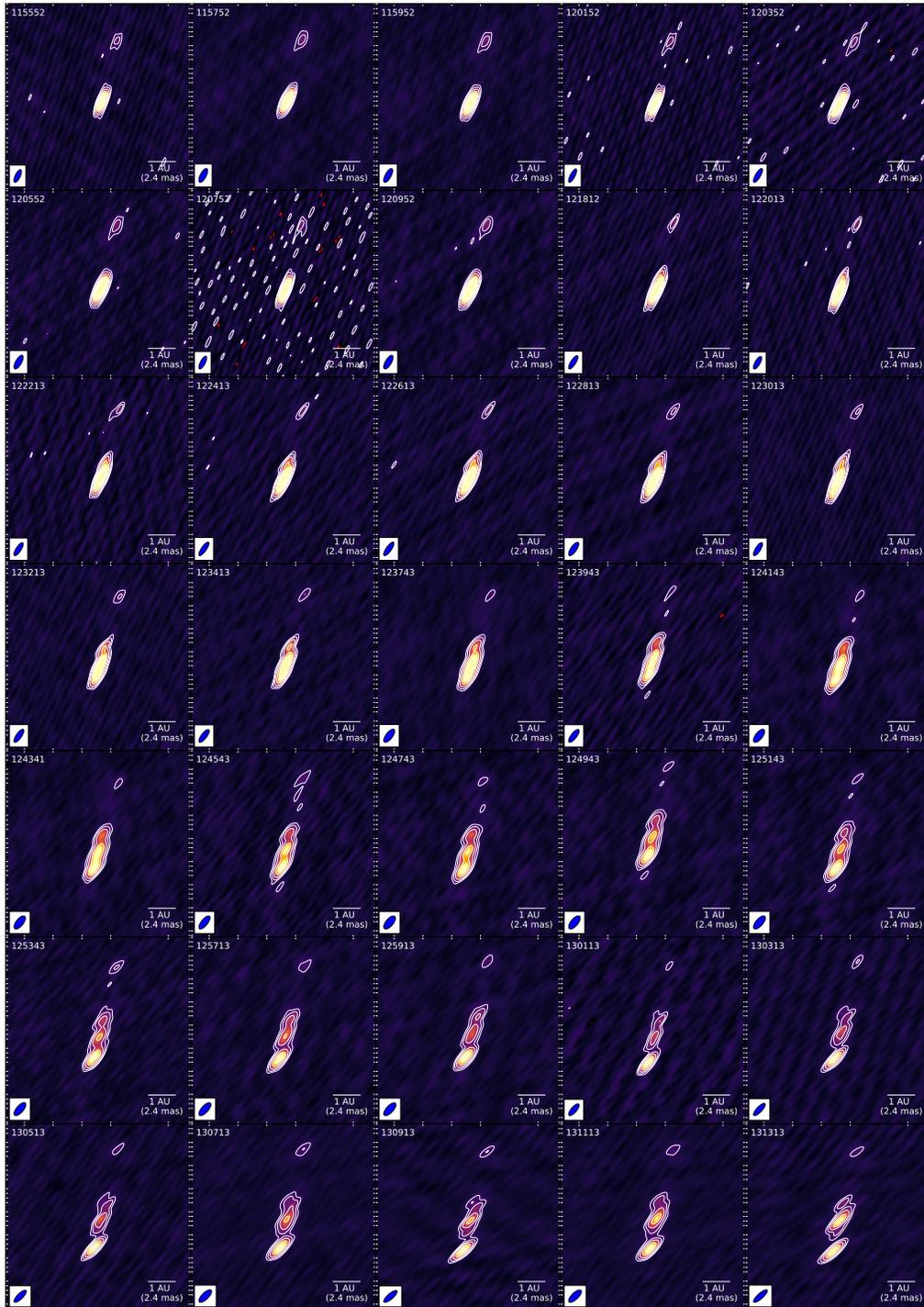
Figure 7.4: Figure 7.3 continued.
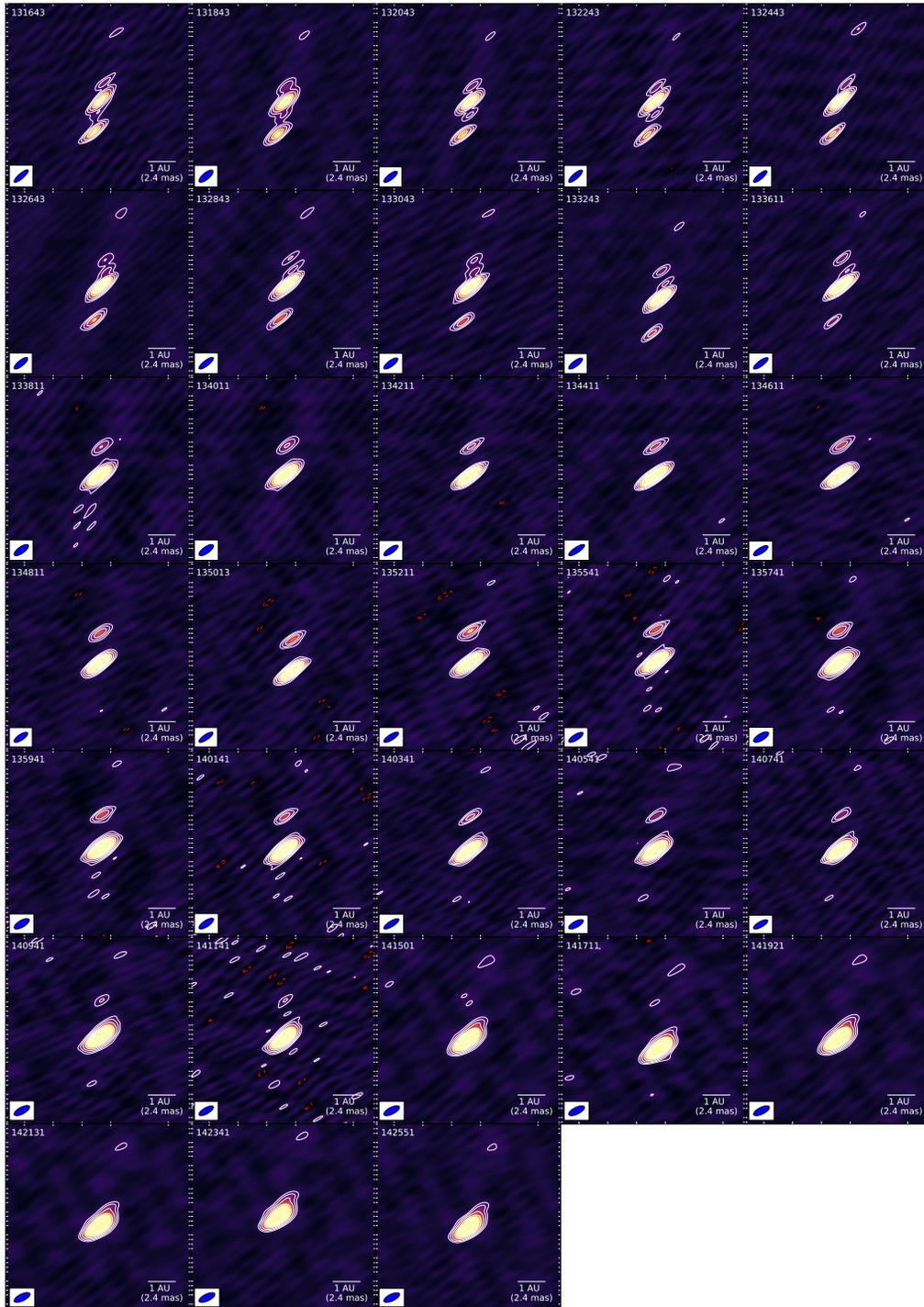
Figure 7.5: Figure 7.3 and 7.4 continued.
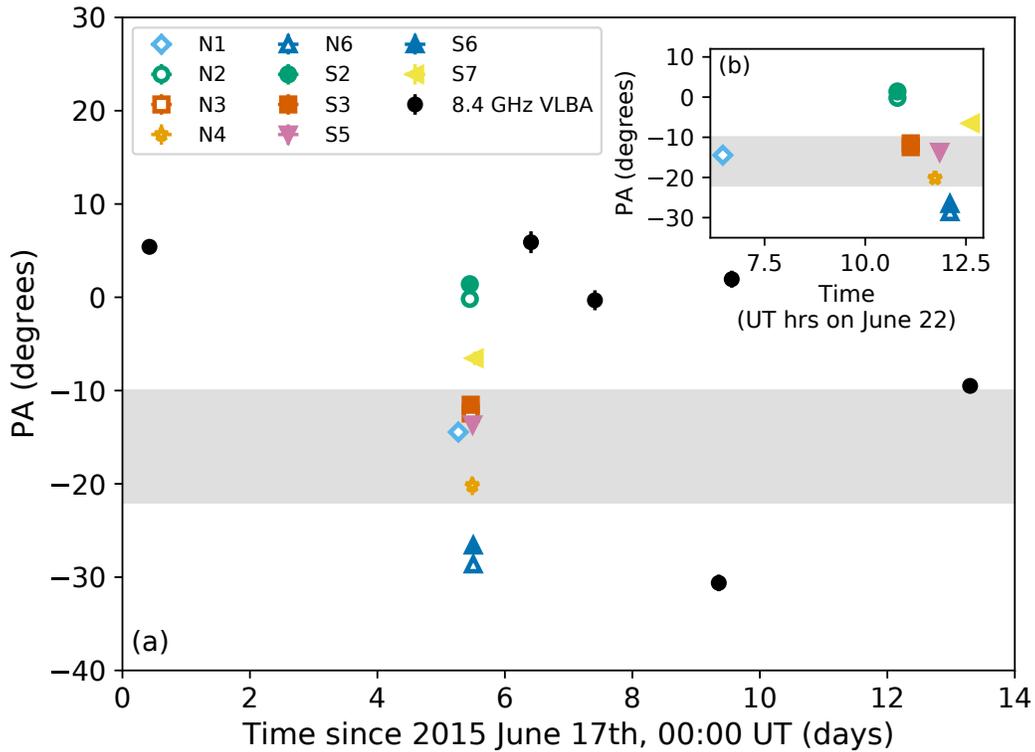
Figure 7.6: Measured position angles of the V404 Cyg jets over the course of the June 2015 outburst. In the main panel (a) the colored symbols indicate position angle measurements of the individual ejecta detected in the 2015 June 22 epoch (see §7.3.2), while the black symbols indicate the position angle measurements from all the other 8.4 GHz epochs (see Table 7.2). The inset panel (b) displays a zoom-in on the June 22 measurements. The grey shaded region in both panels indicates the position angle of the quiescent V404 Cyg jet, inferred from the polarized radio emission during the decay of the 1989 outburst (Han & Hjellming, 1992). While the position angles can vary by up to ∼ 40 degrees over different timescales, the central position angles measured during this outburst are consistent with the quiescent jet measurement.

Table 7.2: Measured position angles on the plane of the sky for the 8.4-GHz VLBA monitoring observations of V404 Cyg

Date	Position angle (degrees east of north)
2015 June 17	5.41 ± 0.80
2015 June 23	5.90 ± 1.17
2015 June 24	-0.32 ± 1.07
2015 June 26	1.94 ± 0.91
2015 June 27	-30.61 ± 0.89
2015 June 30	-9.50 ± 0.75

7.3.2 Tracking the bulk motion of the jet ejecta

The jet position angles only probe the jet orientation on the plane of the sky. However, since V404 Cyg is one of the few BHXBs with an accurate parallax distance measurement (2.39 ± 0.14 kpc; Miller-Jones et al. 2009), we are able to uniquely solve for both jet speed and the inclination angle of the jet axis to our line of sight, thereby characterizing the full three-dimensional space motion of the ejecta. To accomplish this, we need to be able to track the bulk motion of the ejecta over time and accurately measure their proper motions.

The higher resolution of our observations on 2015 June 22 allows us to separate and track the bulk motion of multiple ejecta components across a sequence of snapshot images. Further, the emission in this epoch is dominated by a stationary core component, which provides a point of reference against which to perform relative astrometry on the fainter ejecta. However, we noticed low-level positional offsets between individual snapshot images in this data set. These offsets are likely due to a combination of short-timescale tropospheric phase variations, coupled with the propensity of self-calibration to shift source positions by a small fraction of a synthesized beam. While such offsets would normally be averaged out over the few-hour durations of typical VLBI observations, they significantly affected the fitted component positions in our snapshot images (2 min imaging timescales).

To properly fit for proper motions of the individual point source components, we had to first determine the positional offsets in each snapshot. Assuming that our ejecta undergo constant bulk motion, we construct a set of linear equations with k ejecta components and i images, such that,

$$\mathrm{RA}_{ik} = \mu_{\mathrm{ra},k}(t_i - t_{\mathrm{ej},k}) + \mathrm{J}_{\mathrm{ra},i} \tag{7.1}$$

$$\mathrm{Dec}_{ik} = \mu_{\mathrm{dec},k}(t_i - t_{\mathrm{ej},k}) + \mathrm{J}_{\mathrm{dec},i} \tag{7.2}$$

The first term in these equations describes the constant bulk motion of the

ejecta, where, $\mu_{\mathrm{ra},k}$ and $\mu_{\mathrm{dec},k}$ represent the proper motions, and $t_{\mathrm{ej},k}$ represents the ejection time, of the kth ejecta component. The second term contains the jitter parameters ($J_{\mathrm{ra},i}$ and $J_{\mathrm{dec},i}$), which represent an offset in position for each ith image, allowing us to correct for the positional shift between images.

We simultaneously solved for the proper motions and ejection times of each component, as well as the jitter parameters for each image. As our data contains $k = 12$ ejecta components, and $i = 103$ images, this amounts to 24 linear equations, and 242 free parameters. Given the scale of this problem, we took a Bayesian approach for parameter estimation, by applying a Markov-Chain Monte Carlo (MCMC) algorithm implemented with the EMCEE python package (Foreman-Mackey et al., 2013). This package utilizes Goodman & Weare's Affine Invariant MCMC Ensemble Sampler (Goodman & Weare, 2010), running a modified version of the Metropolis-Hastings Algorithm, whereby it simultaneously evolves an ensemble of "walkers" through the parameter space. We used 484 walkers ($2\times$ the number of dimensions in our model) for our MCMC runs. To initialize the positions of the walkers in our parameter space, we placed them in a tight ball around the best initial guess. Prior distributions used for all of our parameters are listed in Table 7.3. Lastly, due to the large number of rapidly-moving ejecta, in some images it can be more difficult to distinguish between different components. We therefore assigned a confidence flag to each component for each image prior to the fitting (H = high, M = medium, L = low, and B = possible blended component), and weighted the data points according to these flags (H=1, M=0.7, L=0.3, and B=0.1), so that data points with lower confidence contributed less to the overall fit.

Table 7.3: Prior distributions for jitter model parameters in VLBA images[a]

Parameter	Description	Prior Distribution	Minimum	Maximum
$\mu_{\rm ra}$	RA proper motion (mas/hr)	truncated normal ($\mu = \mu_{\rm ra,g}$, $\sigma = 0.3$)	-2	2
$\mu_{\rm dec}$	Dec proper motion (mas/hr)	truncated normal ($\mu = \mu_{\rm dec,g}$, $\sigma = 0.3$)	-2	2
$t_{\rm ej}$	Ejection time (decimal hrs)	uniform	t_g-1	t_g+1
$J_{\rm ra}$	RA jitter (mas)	truncated normal ($\mu = J_{\rm ra,core}$, $\sigma = 0.5$)[b]	-3	3
$J_{\rm dec}$	Dec jitter (mas)	truncated normal ($\mu = J_{\rm dec,core}$, $\sigma = 0.5$)[b]	-3	3

[a] Values with a subscript g represent the best initial guess for the parameter values.
[b] We use the offset positions (with respect to the center of the image) of the core jet component to represent the best initial guess for the jitter parameters, and to define their priors.

We ran our MCMC by evolving the walkers over a series of steps (where the first 500 step "burn in" period is not retained) until convergence was reached. Our criterion for convergence required that the positions of the walkers were no longer significantly evolving. We determined whether this criterion was met by monitoring the chains of each of the walkers through the parameter space and ensuring that, for each parameter, the intra-chain variance across samples was consistent with the inter-chain variance for a given sample. Using the multi-dimensional posterior distribution output from the converged MCMC solution, we created one-dimensional histograms for each parameter. The best fit result was taken as the median of these distributions, and the uncertainties are reported as the range between the median and the 15th percentile (lower bound), and the 85th percentile and the median (upper bound), corresponding approximately to 1σ errors. The best fitting proper motions and ejection times for each component are reported in Table 7.4. The jitter corrected motion of the components is displayed in Figure 7.7, the best-fit proper motions of the components are displayed in Figure 7.8, and the position angles of the measured components relative to the jitter corrected centroid position are displayed in Figure 7.9. We find that the ejecta have proper motions ranging from $4.3 - 46.2$ mas day^{-1} (0.06–$0.64c$ in projection[2]; Figure 7.10), and fitted position angles between -28.6 and -0.2 degrees east of north.

Based on the similarities in ejection times and position angles, we identify three likely approaching/receding pairs of ejecta: N2/S2, N3/S3, and N6/S6. Assuming that these identifications were correct, we then re-fit the proper motion of each pair of components, forcing the ejection times of each component in a pair to be the same. These tied-ejection fits are also shown in Table 7.4, and the results of these tied fits are used in all following analysis.

---

[2]Note that the fitted proper motions of our ejecta components are well within the boundaries of our priors.

Table 7.4: Fitted component ejection times, proper motions, and position angles on the plane of the sky for the 2015 June 22 VLBA observations of V404 Cyg

Component[a,b]	Ejection time (UTC hours)	Proper motion (mas day^{-1})	Position angle (degrees east of north)
N1	6.46 ± 0.04	23.02 ± 0.14	-14.45 ± 0.19
N2	10.54 ± 0.03	18.54 ± 0.17	-0.36 ± 0.10
S2	10.36 ± 0.03	7.84 ± 0.21	$-178.56^{+0.31}_{-0.29}$
N3	10.91 ± 0.03	17.09 ± 0.24	-12.31 ± 0.38
S3	11.11 ± 0.02	10.37 ± 0.20	168.36 ± 0.49
N4	11.73 ± 0.03	4.25 ± 0.08	$-20.18^{+1.03}_{-0.98}$
S5	11.847 ± 0.004	46.23 ± 0.17	166.37 ± 0.10
N6	$10.62^{+0.91}_{-0.05}$	9.91 ± 0.16	$-28.61^{+1.14}_{-1.03}$
S6	12.26 ± 0.027	6.28 ± 0.09	153.46 ± 0.77
S7	12.62 ± 0.02	33.86 ± 0.84	$173.47^{+0.73}_{-0.70}$
N2^t	10.799 ± 0.017	20.05 ± 0.12	-0.17 ± 0.06
S2^t	10.799 ± 0.017	12.18 ± 0.29	-178.60 ± 0.15
N3^t	11.128 ± 0.010	19.43 ± 0.12	-12.45 ± 0.18
S3^t	11.128 ± 0.010	10.54 ± 0.10	168.48 ± 0.22
N6^t	12.101 ± 0.032	16.05 ± 0.19	$-28.63^{+0.82}_{-0.79}$
S6^t	12.101 ± 0.032	5.79 ± 0.08	153.39 ± 0.74

[a] N denotes north-moving ejecta, and S denotes south-moving ejecta.
[b] The tied-ejection fits of our ejecta pairs are denoted with the superscript^t, and shown in the second section of the table.
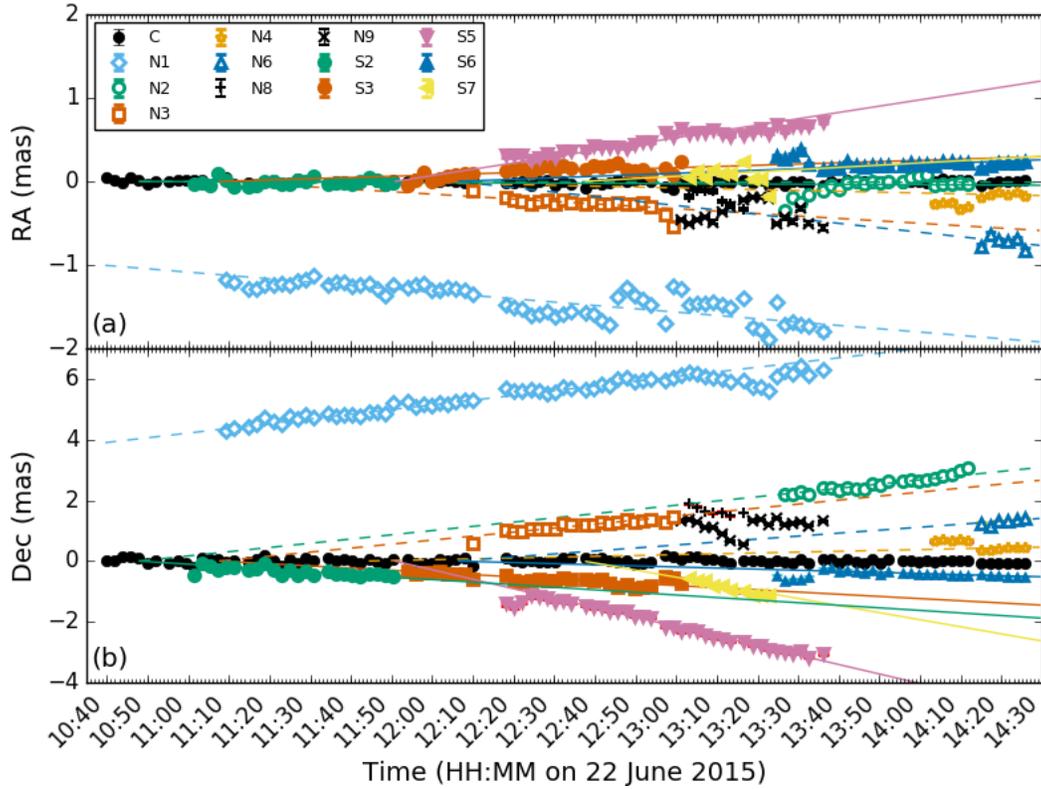
Figure 7.7: Jitter-corrected positions of the observed components over time on 2015 June 22. Panel (a) displays the motion in Right Ascension and panel (b) displays the motion in Declination. Empty coloured markers represent northern components, filled coloured markers represent southern components, and the filled black circles represent the core component. The best-fitting proper motions in both co-ordinates are shown as dashed lines (northern components) and solid lines (southern components), where the motion in declination is larger than that in right ascension for all components. With the exception of components N8 and N9 (black plus signs and crosses, respectively), all components show ballistic motion away from the core, and the core does not move systematically over time.
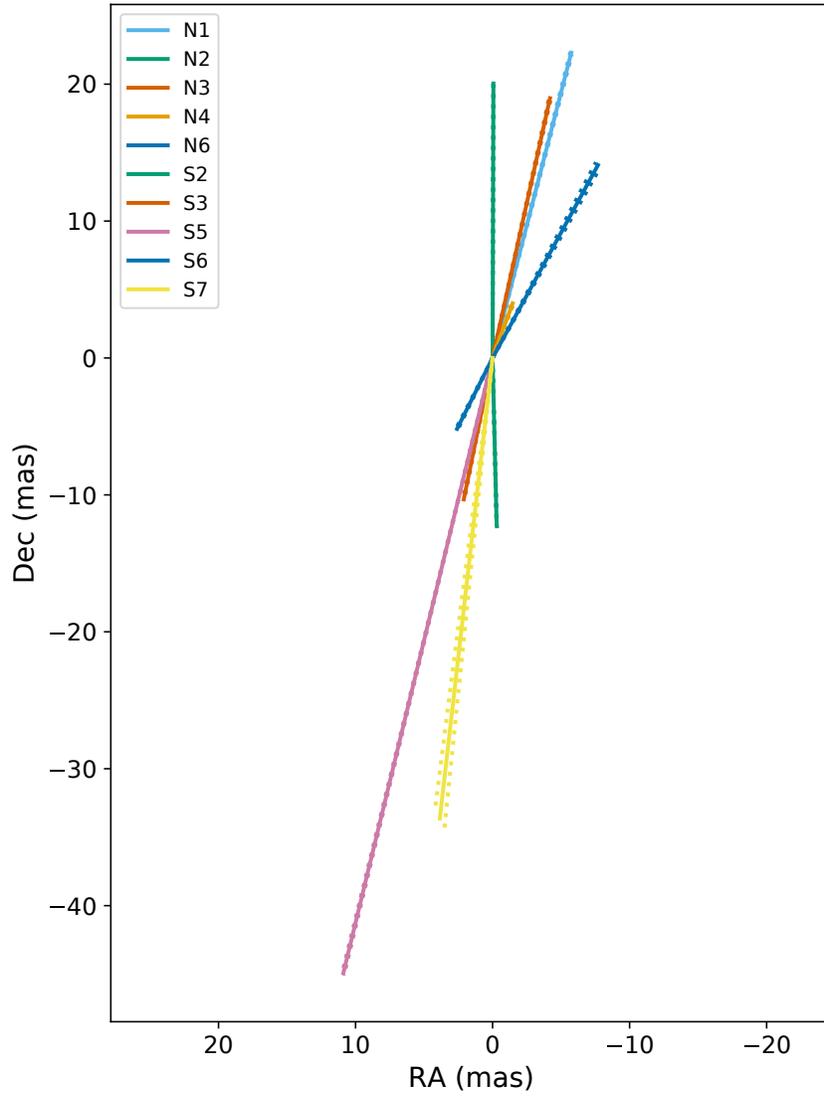
Figure 7.8: Best-fitting proper motions of the different ejecta components detected on 2015 June 22 (shown as solid lines). Corresponding pairs of components (N2/S2, N3/S3, N6/S6) are shown with the same color. The orientation of each line displays the direction of motion, and the length of each line denotes the magnitude (distance travelled in one day). Uncertainties are indicated by dotted lines (which, given the small uncertainties, merge into the solid lines). Both the orientation and lifetime of the detected ejecta clearly vary between events.
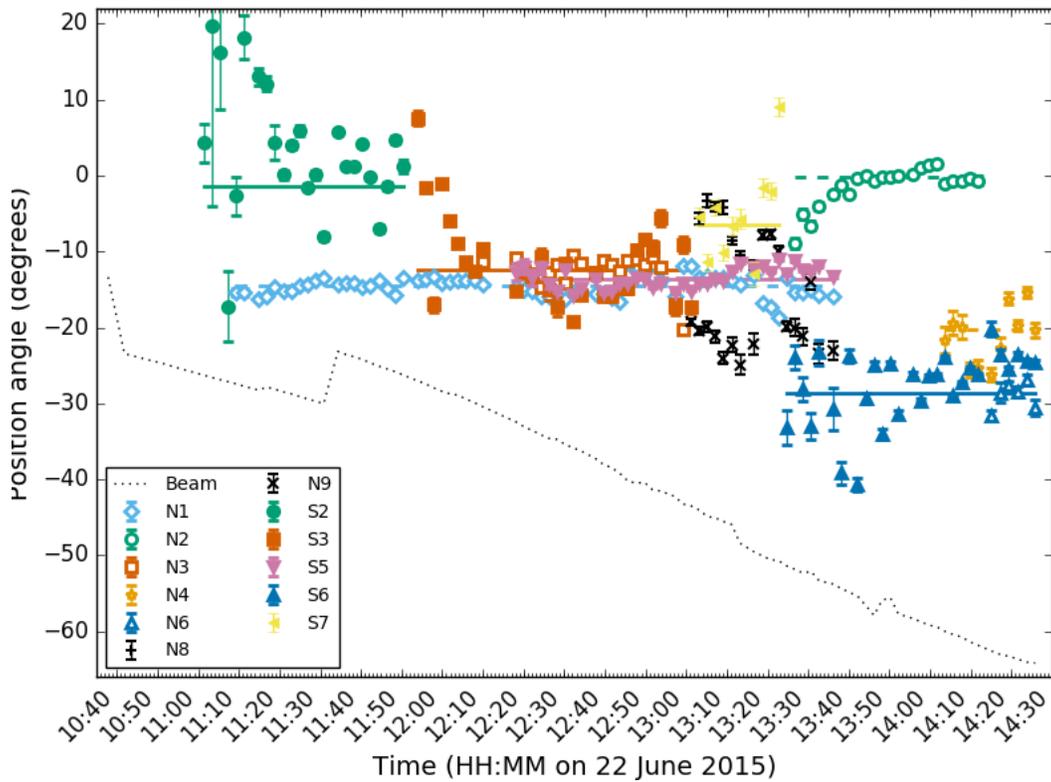
Figure 7.9: Position angles of the measured components relative to the jitter-corrected centroid position. Corresponding northern and southern component pairs (N2/S2, N3/S3, N6/S6) are identified via their consistent position angles and ejection times, and are shown with matching colors and marker shapes (empty markers for northern components and filled markers for southern components). The mean position angles of the components (as detailed in Table 7.4 and shown in Figure 7.6) are shown as dashed and solid lines for northern and southern components, respectively. The orientation of the VLBA synthesised beam is shown as the dotted black line. Discrete jumps in the beam orientation correspond to antennas entering or leaving the array (e.g., as V404 Cyg rises or sets at the different antennas). The measured position angles of the components vary from -0.2 to -28.6 degrees east of north, and do not align with the synthesized beam.
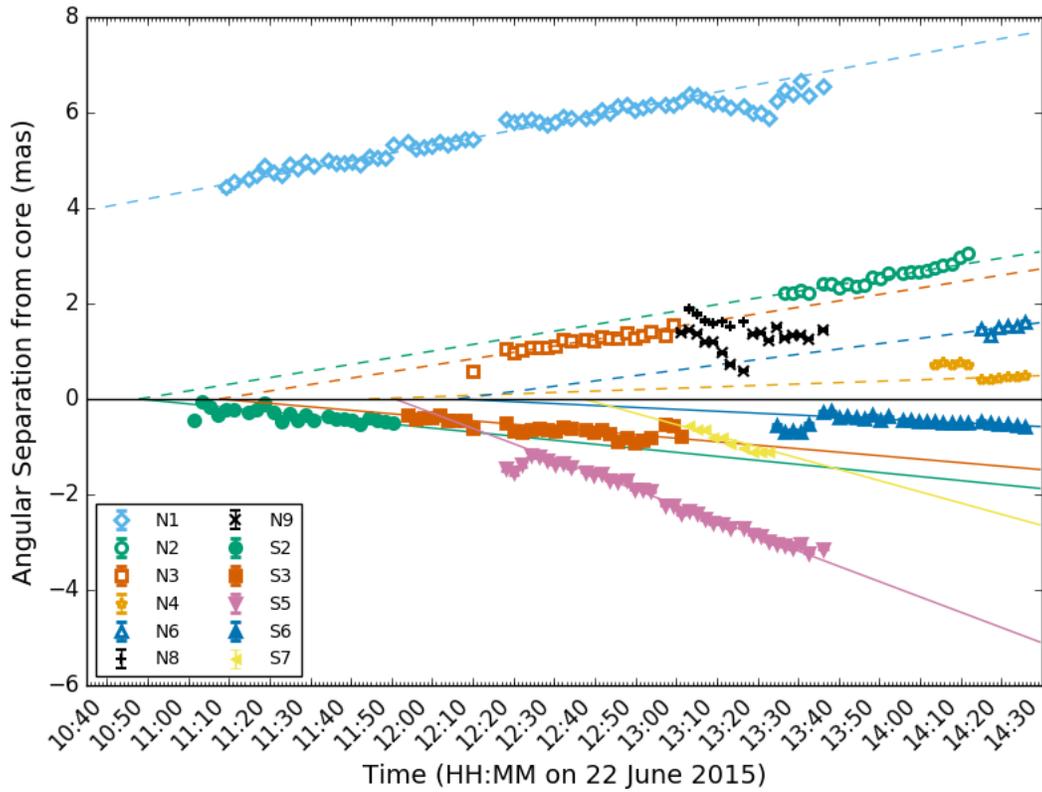
Figure 7.10: Total angular separations from the core for all the ejected components, as a function of time on 2015 June 22. Corresponding pairs of ejecta have matching colors and marker shapes, with empty markers for northern components (N) and filled markers for southern components (S). The best-fitting total proper motions are shown for all components (with the exception of the non-ballistic components, N8 and N9) as dashed lines for northern components and solid lines for southern components. The different components show a range of proper motions, from 4.3 to 46.2 mas day^{-1} (N4 and S5, respectively).

7.3.3 Jet ejecta properties

The approaching and receding proper motions of a pair of jet ejecta can be represented as,

$$\mu_{\mathrm{app}} = \frac{\beta \sin \theta}{1 - \beta \cos \theta} \frac{c}{d}, \qquad \mu_{\mathrm{rec}} = \frac{\beta \sin \theta}{1 + \beta \cos \theta} \frac{c}{d}, \qquad (7.3)$$

where $\beta = v/c$ represents the jet speed, θ represents the inclination angle of the jet axis to the line of sight, c is the speed of light, and d is the distance to the source. Assuming intrinsically symmetric jets, we can rearrange these equations to derive the following expressions,

$$\beta \cos \theta = \frac{\mu_{\mathrm{app}} - \mu_{\mathrm{rec}}}{\mu_{\mathrm{app}} + \mu_{\mathrm{rec}}}, \qquad \text{and} \qquad \tan \theta = \frac{2d}{c} \frac{\mu_{\mathrm{app}} \, \mu_{\mathrm{rec}}}{\mu_{\mathrm{app}} - \mu_{\mathrm{rec}}}. \qquad (7.4)$$

With a known distance and the measured proper motions, these two equations can be uniquely solved for jet speed and inclination angle. Further, the corresponding jet Lorentz factor, $\Gamma = (1 - \beta^2)^{-1/2}$ and the Doppler factors $\delta_{\mathrm{app,rec}} = \Gamma^{-1} (1 \mp \beta \cos \theta)^{-1}$ can also be calculated. For unpaired ejecta, we can use the known distance to solve for $\beta \cos \theta$, subject to an assumption on whether the components are approaching or receding.

For the three pairs of jet ejecta we identified in the 2015 June 22 observations (N2/S2, N3/S3, and N6/S6), we assume the northern component is the approaching component, as it has a higher proper motion in all cases. Given this constraint, Table 7.5 displays the inferred physical jet parameters for all of our identified pairs of jet ejecta, and Figure 7.11 displays constraints on the jet speed and inclination angle for both the paired and unpaired jet ejecta detected on 2015 June 22. Our measurements here show that the jet speed and inclination angle must be varying between ejection events on 2015 June 22, where the measured inclination angles from the three ejecta pairs all clearly differ from the inclination of the binary orbital plane.
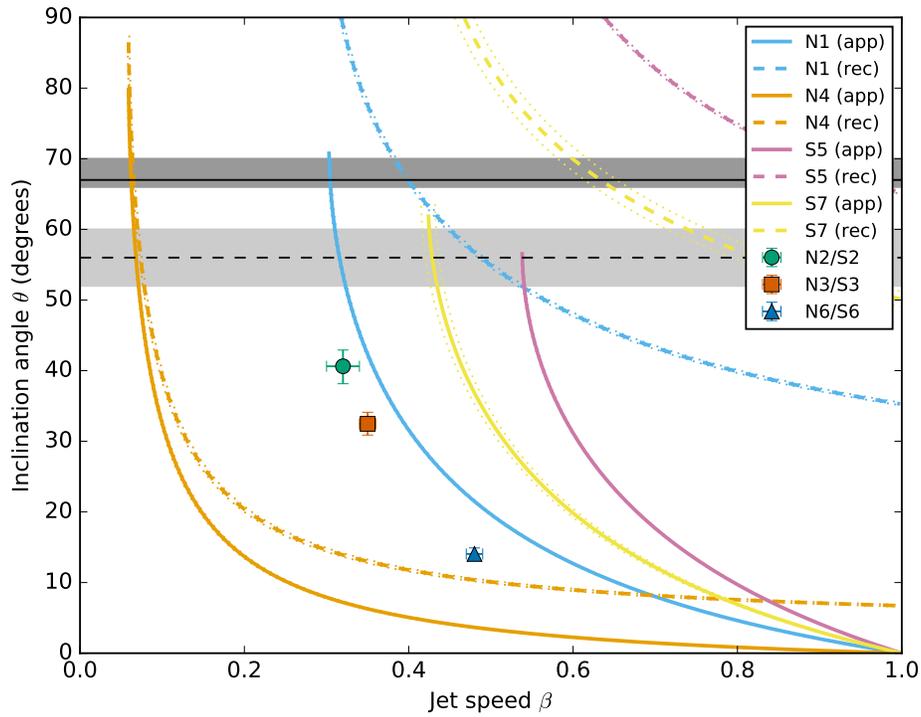
Figure 7.11: Constraints on the jet speed and inclination angle to the line of sight derived from the measured proper motions of the jet ejecta on 2015 June 22. In the three cases (N2/S2, N3/S3, N6/S6) where corresponding ejecta pairs can be identified, we can accurately determine both jet speed and inclination angle. For other un-paired components, the measured proper motion and source distance are used to constrain $\beta \cos \theta$, giving the plotted curves for both approaching (solid lines) and receding (dashed lines) scenarios. The grey shading and black lines denote the two sets of published constraints on the inclination of the binary orbital plane (Shahbaz et al., 1994; Khargharia et al., 2010). Jet speeds and inclination angles differ markedly between ejecta, and the three sets of paired ejecta give inclination angles significantly different from that of the binary orbit.

Table 7.5: Inferred physical parameters from our identified paired ejecta from 2015 June 22 VLBA observations of V404 Cyg

Ejecta pair[a]	N2/S2	N3/S3	N6/S6
μ_{app} (mas d^{-1})	20.05 ± 0.12	19.43 ± 0.12	16.05 ± 0.19
μ_{rec} (mas d^{-1})	12.18 ± 0.29	10.54 ± 0.10	5.79 ± 0.08
$\beta \cos \theta$	0.244 ± 0.011	0.297 ± 0.005	0.470 ± 0.007
β	0.321 ± 0.019	0.351 ± 0.009	0.484 ± 0.007
θ (°)	$40.6^{+2.3}_{-2.5}$	32.5 ± 1.6	14.0 ± 0.8
Γ	1.056 ± 0.005	1.068 ± 0.002	1.143 ± 0.002
δ_{app}	1.253 ± 0.020	1.331 ± 0.010	1.650 ± 0.022
δ_{rec}	0.761 ± 0.008	0.722 ± 0.003	0.595 ± 0.003

[a] Ejecta parameters are defined as follows: $\mu_{\mathrm{app,rec}}$ are the approaching and receding proper motions, β is the jet speed as a fraction of the speed of light, θ is the inclination angle of the jet axis to the line of sight, Γ is the jet bulk Lorentz factor, and $\delta_{\mathrm{app,rec}}$ are the approaching and receding jet Doppler factors. In all cases the northern component is approaching and the southern component is receding.

7.3.4 Comparison to light curve modelling results

In Chapter 5 and §7.3.3 above, we have used two independent methods (light curve modelling and high resolution imaging) to measure the V404 Cyg jet ejecta properties (e.g., ejection times, bulk speeds, inclination angle of the jet axis). While a combined analysis of all of the photometric data from Chapter 5 and the VLBA data presented in this chapter will be the subject of future work, it is of interest to briefly compare the results of these two methods here.

Upon comparing the jet ejecta properties derived from the light curve modelling and VLBA imaging, we notice both similarities and differences. In particular, both methods yield a similar number of ejection events (8 for light curve modelling, 7 for VLBA imaging), show similar low bulk speeds (the majority of the ejecta show $\beta < 0.6$), show inclination angles that clearly vary between events (by up to ~ 40 degrees) and differ from the estimates of the binary orbit (Figure 7.11 & 7.12), and show a similar trend where the ejection times appear to occur in three groupings (Figure 7.13). However, the VLBA imaging suggests the presence of un-paired ejecta (where we assume only paired ejecta in the light curve modelling), tend to show ejecta with lower inclination angles when compared to the light curve modelling events, and show ejection times that do not always coincide with light curve modelling ejection times.

Given these similarities and differences, a combined analysis including constraints from the VLBA imaging in the light curve modelling will give us an unprecedented view of these ejection events and allow us to more accurately constrain the jet ejecta properties. For instance, the VLBA 15 GHz light curve can be included in the light curve modelling, providing more data to better constrain the total model. Further, VLBA constraints on the number of ejection events, single-sided vs paired events, ejection times, bulk speeds, inclination angles, and peak fluxes, can be included as priors in the light curve modelling to further constrain the model parameters and possibly break some degeneracy between parameters (see Chapter 5 §5.7.5 of this thesis).
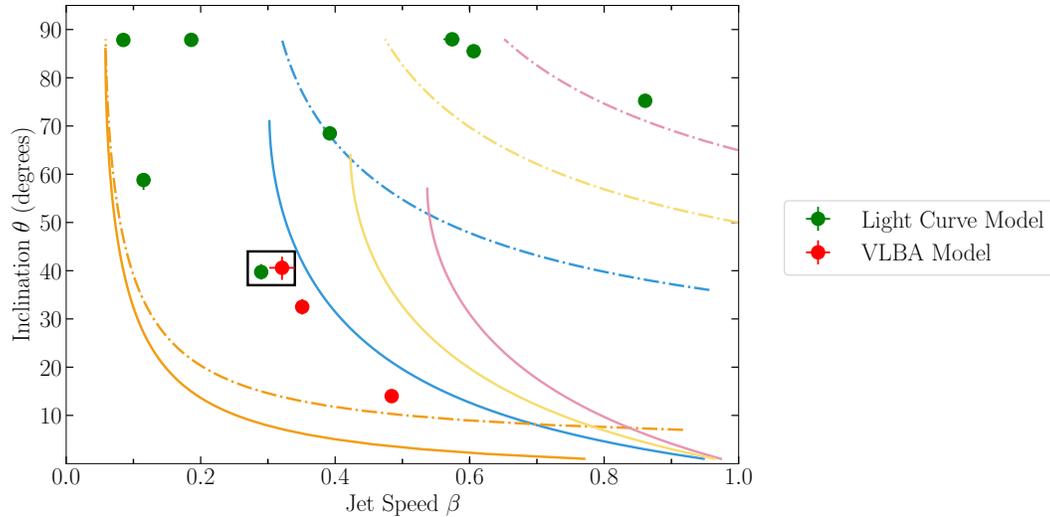
Figure 7.12: Updated version of Figure 7.11, where we include constraints on the bulk speeds and inclination angles of the jet axis for the ejection events derived from the light curve modelling work in Chapter 5 (green markers). The red markers represent constraints from the paired ejection events observed with the VLBA, while the coloured lines (following the same colour association as in Figure 7.11) represent constraints from the un-paired ejection events observed with the VLBA. The black box identifies a potential match between the light curve modelling and VLBA imaging ejection events, showing similar jet speed and inclination angles (ejection 1 from Table 5.2 and ejection pair N2/S2 from Table 7.5). Further, we may also observe potential matches between our light curve modelled events and the un-paired ejecta identified by the VLBA (for which we only have constraints on $\beta \cos \theta$, as shown by the coloured lines).
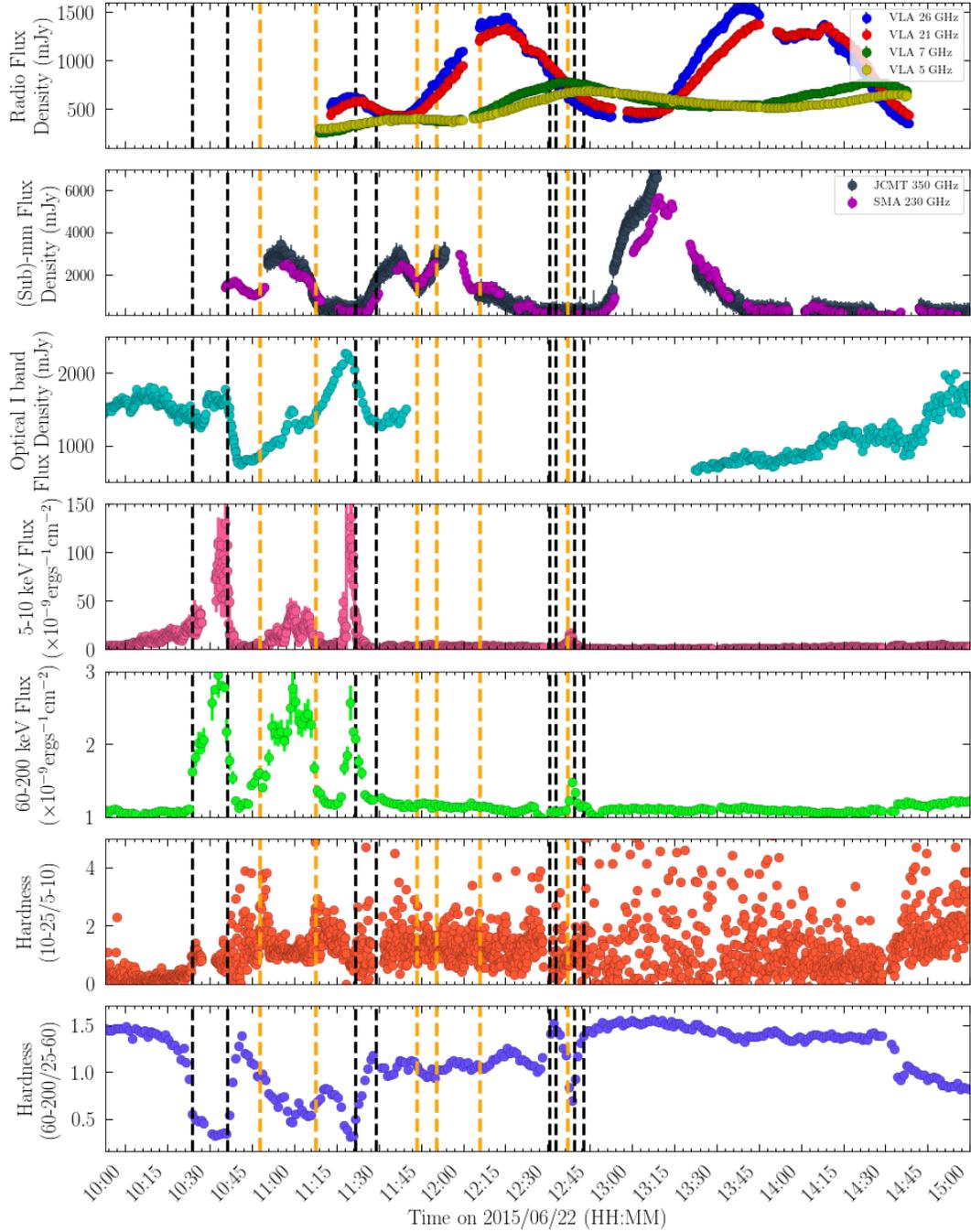
Figure 7.13: Updated version of Figure 5.8, where we include constraints on the ejection times for the jet ejecta derived from the VLBA imaging (orange dotted lines; see Table 7.4). Both the light curve modelling and VLBA imaging results show three distinct groups of ejection events. Although, we only observe a potential match in ejection times between the third group of ejection events at ~ 12:45, where the first two groups of VLBA events seem to occur 30–45 min later than the corresponding group of light curve modelling events.

261

7.4 Discussion

In this work we have presented evidence that the orientation of the jet axis differs from the inclination of the binary orbit, and is rapidly changing on timescales as short as minutes during the 2015 outburst of V404 Cyg. The most natural interpretation for the observed changes in the jet axis would be jet precession. In the following sections, we discuss the origin of this jet precession and place constraints on the precession period, precession cone opening angle, and the stability of the precession process. Additionally, we consider the occurrence of jet precession in other sources, as well as the implications jet precession has on the jet launching mechanism and the impact of these jets on the surrounding environment.

7.4.1 Origin of jet precession

In BHXBs the binary orbital plane can be misaligned with the black hole spin axis (e.g., due to formation of the black hole in an asymmetric supernova). In this situation, relativistic frame dragging should lead to Lense-Thirring precession (Lense & Thirring, 1918) of particles misaligned with the black hole equatorial plane. When considering geometrically thick accretion discs (i.e., slim discs), if the sound crossing timescale of the disc is sufficiently short, the disc will precess as a rigid body (Fragile et al., 2007). However, viscosity in the disc can act to damp the precession, leading to the alignment of the disc angular momentum axis to the black hole spin axis. Therefore, for this rigid body precession to persist in slim discs, the viscosity should be sufficiently low that the alignment timescale is longer than the precession period (thereby placing an upper limit on the outer radius of the slim disc, known as the spherisation radius; Motta et al. 2018).

In the case of V404 Cyg, since the black hole is believed to have been formed with a natal kick from a supernova (Miller-Jones et al., 2009), a mis-

alignment between the binary orbital plane and the black hole spin (Brandt & Podsiadlowski, 1995) is expected. Additionally, during its 2015 outburst, the mass accretion rate in V404 Cyg was believed to have been at, or even above, the Eddington rate, resulting in the radiation pressure in the inner part of the accretion flow creating a puffed up, geometrically thick (slim) accretion disc configuration (Motta et al., 2017b). Therefore, during its 2015 outburst, V404 Cyg possessed all the ingredients needed for Lense-Thirring precession to be occurring in a inner, geometrically thick, slim accretion disc. As this precession causes the disc orientation to vary, if the jet and disc precess together (due to the jet being directly launched from the accretion flow or spin-powered jets being re-directed along the rotational axis of the disc), this presents a plausible scenario for the origin of the jet precession in V404 Cyg.

7.4.2 Precession timescale, opening angle, and coherence

To verify the plausibility of the precession scenario we have outlined, we need to insure that the conditions in the accretion flow required to produce the observed jet precession are consistent with those observed during this outburst of V404 Cyg. In our precession scenario, the precession period and slim disc radius will depend on the black hole spin and mass accretion rate (Fragile et al., 2007; Middleton et al., 2018). In particular, the precession period for an inner super-Eddington accretion disc, rotating as a solid body, can be represented as,

$$P = \frac{\pi}{3a_*} \frac{GM}{c^3} r_{\mathrm{sph}}^3 \left[\frac{1 - (r_{\mathrm{in}}/r_{\mathrm{sph}})^3}{\ln (r_{\mathrm{sph}}/r_{\mathrm{in}})} \right] . \qquad (7.5)$$

Here M is the black hole mass, a_* is the dimensionless black hole spin parameter ($a_* = Jc/GM^2$, J represents angular momentum), c is the speed of light, G is the gravitational constant, and r_{in} and r_{sph} are the inner and outer (spherisation

radius) radii of the slim disc[3].

The inner radius of the super-Eddington accretion disc can be assumed to be located at the innermost stable circular orbit (ISCO[4]), while the structure of the outer part of a super-Eddington accretion disc is governed by the angular momentum carried away by the accretion disc wind. Therefore, the spherisation radius depends on the fraction of the radiation energy, ϵ_{w}, used to launch the accretion disc wind, and is given by (Poutanen et al., 2007),

$$\frac{r_{\mathrm{sph}}/r_{\mathrm{in}}}{\dot{m}} \approx 1.34 - 0.4\epsilon_{\mathrm{w}} + 0.1\epsilon_{\mathrm{w}}^2 - (1.1 - 0.7\epsilon_{\mathrm{w}})\dot{m}^{-2/3}. \tag{7.6}$$

Here $\dot{m}$ is the mass accretion rate in units of the Eddington accretion rate ($L_{\mathrm{edd}} = 2.2 \times 10^{-7}\,M_{\odot}\,\mathrm{yr}^{-1}$ for V404 Cyg, where $\dot{M}_{\mathrm{edd}} = L_{\mathrm{edd}}/\eta\,c^2$, and η represents the accretion efficiency), and $\epsilon_{\mathrm{w}} = (1 + L_{\mathrm{rad}}/L_{\mathrm{wind}})^{-1}$ represents the wind efficiency, where the latter is dependent upon the radiative luminosity (L_{rad}) and the wind power (L_{wind}).

To estimate the jet precession period, we can use the range of jet position angles observed within our VLBA observations (see Figure 7.6). The distribution of position angles for a precessing jet will peak at the two extremes (where the jet position angle is changing slowly). Therefore, even if each individual ejecta component observed only samples the orientation of the jet axis at the time of ejection, our observed range of position angles is most likely representative of the entire range of position angles observed within a full precession period. Given the largest swing in position angle between two ejecta pairs (~ 30 degrees between N2/S2 and N6/S6), we estimate a precession cone half opening angle of ~ 15 degrees. As the difference between the best-fitting ejection times of the N2/S2 and N6/S6 pairs is 1.3 hours, we place an upper

---

[3]All radii given here are in units of the gravitational radius, $R_{\mathrm{g}} = GM/c^2$.

[4]The innermost stable circular orbit (ISCO) represents the smallest orbit in which a test particle can stably orbit the black hole, and thus the inner boundary for an accretion disc. The radius of the ISCO is dependent upon the spin parameter, a_*, where for a non-rotating black hole $R_{\mathrm{isco}} = 6R_g$ (Frank et al., 2002).

limit of 2.6 hours on the precession period. We estimate that the lower limit for this precession period is on the order of seconds, based on the fact that we observe discrete, point source like ejecta that have not been smeared out (over the ejection timescale) in our VLBA images (see §7.4.3).

Substituting in the black hole mass of V404 Cygni ($9.0^{+0.2}_{-0.6}M_{\odot}$; Khargharia et al. 2010), $\epsilon_{\rm w} \sim 0.25 - 0.5$ for the fraction of the radiation energy used to launch the accretion disc wind (Jiang et al., 2014), a range of spin parameters[5], and possible jet precession timescales of $\leq 2.6\,\mathrm{hours}$, Equations 7.5 and 7.6 predict a mass accretion rate of a few tens of times the Eddington rate, and a consequent spherisation radius of a few hundred gravitational radii (for a precession period on the order of minutes; see Figure 7.14).

These estimates of mass accretion rate and spherisation radius needed to produce precession timescales on the order of minutes, are in line with many of the observed properties of V404 Cyg during the 2015 outburst. In particular, a super-Eddington accretion rate matches the observed peak luminosities in V404 Cyg (Motta et al., 2017b) and the calculated mass-loss rates in the accretion disc wind (10^{-8}–$10^{-5}M_{\odot}$ over 15 days implies 1.2–1200 times the Eddington accretion rate; Muñoz-Darias et al. 2016). Additionally, the spherisation radii we predict are roughly consistent with the estimated extent of the slim disc in V404 Cyg ($\sim 10^2 R_{\rm g}$; Motta et al. 2017b) and the maximum radius for rigid body precession (set by the radius at which the alignment timescale of the disc with the black hole spin becomes shorter than the precession timescale; see Figure 8 in Motta et al. 2018). Further, a precessing accretion flow is also consistent with the detection of low-frequency quasi-periodic oscillations on similar timescales to a precession period of minutes ($18\,\mathrm{mHz}$ – $1.03\,\mathrm{Hz}$;

---

[5]While Walton et al. (2017) present a spin measurement of $a_* > 0.92$ for V404 Cyg, we note that the reported constraint on the black hole spin did not account for the slim disc geometry, and assumed the disc inclination to be that of the binary orbit (which our measurements show is not always the case). Therefore, the true spin could be lower than the Walton et al. (2017) measurement.
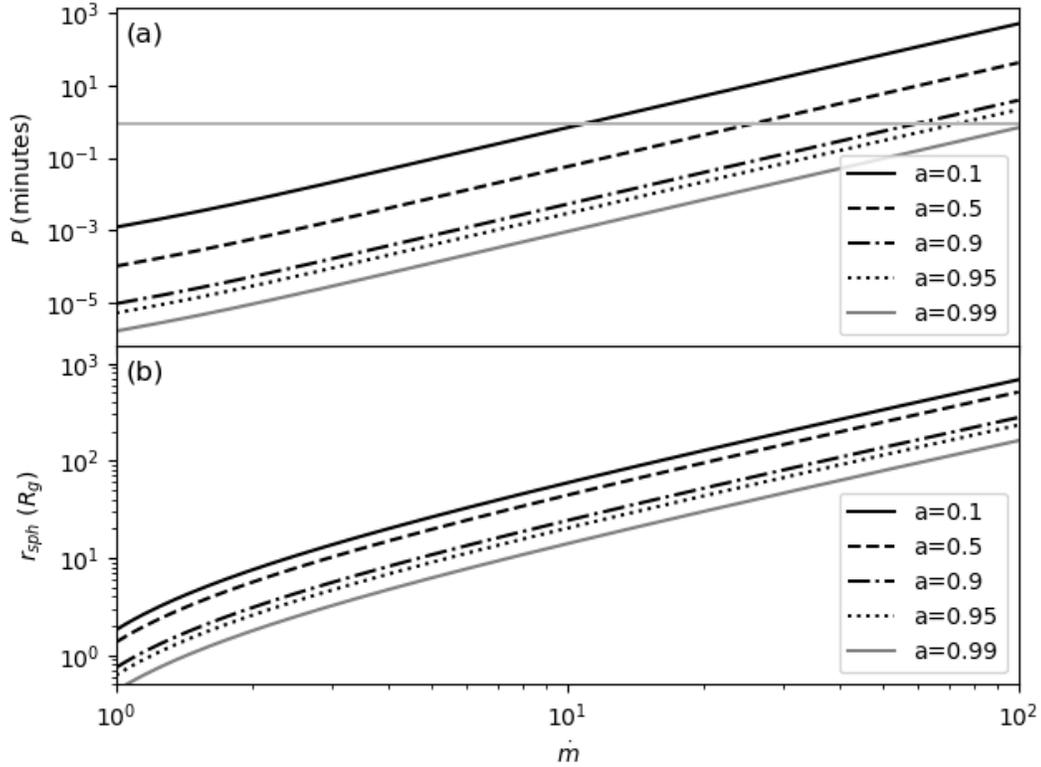
Figure 7.14: Calculated precession timescales (panel a) and spherisation radii (panel b), as a function of mass accretion rate, $\dot{m}$ (in units of the Eddington accretion rate), and the dimensionless spin parameter, a. For this plot, we set $\epsilon_w = 0.2$, although we note that changing this parameter has little effect on the precession timescales/spherisation radii relations shown here. The grey horizontal line in panel a shows the frequency of an X-ray quasi-periodic oscillation (QPO) detected during our VLBA observations on 2015 June 22 (Huppenkothen et al., 2017). For jet precession timescales of order minutes, we would need accretion rates of 10–100 times the Eddington rate, corresponding to spherisation radii of 50–100R_{g}, in the V404 Cyg accretion flow.

Huppenkothen et al. 2017). All of this complementary evidence suggests that the precession scenario we have outlined here could be occurring in V404 Cyg.

Moreover, given the high mass accretion rate required to explain the observed jet precession in V404 Cyg (tens of times the Eddington accretion rate), it is unlikely that such an mass accretion rate could be sustained over the duration of the outburst (the flaring/ejection period lasted approximately 15-days, see Chapter 6 of this thesis for details). Alternatively, the mass accretion rate is likely to have varied over the course of the outburst, which would alter both the spherisation radius and the precession period. This implies that short episodes of precession were occuring in V404 Cyg, corresponding to times of enhanced mass accretion through the disc, rather than a long-term, stable precession over the full 15 day flaring period. However, Figure 7.6 shows that the jet axis continues to vary over the full 2-week duration of our VLBA monitoring. Therefore, the precession must continue with a relatively consistent cone opening angle (presumably set by the misalignment between the axis of binary orbital plane and the black hole spin axis), even if the precession timescale and coherence vary.

7.4.3   Constraints on the jet launching timescale

The timescale over which jet ejecta are launched in BHXBs is not known. However, we can use constraints imposed by the precession timescale and estimates of the ejecta size scale to place limits on this launching timescale in V404 Cyg.

During this outburst of V404 Cyg, Gandhi et al. (2017) suggest that the base of the jet was located at a distance of 3×10^9 cm from the black hole, setting a lower limit on the jet component size at ejection. Considering that the brightest jet component detected in the 2015 June 22 VLBA epoch was unresolved to the synthesized beam (and most likely substantially smaller than the VLBA beam), the VLBA beam will set an upper limit on the jet component size at ejection of 1.3×10^{13} cm (beam size of $1.2 \times 0.4 \, \mathrm{mas}^2$ at $2.39 \, \mathrm{kpc}$). These size scales imply

light crossing times, and in turn launching timescales of 0.1s–5 min. However, the launching timescale must be less than the precession timescale, in order for us to observe discrete jet ejecta components in our VLBA images (that are not smeared out). Therefore, the upper limit on the launching timescale is likely to be less than a few minutes. Interestingly, my earlier work modelling the multi-frequency light curves as emission from a sequence of expanding spherical ejecta, suggested ejecta radii (at the peak of the sub-mm emission in each flare) of 0.6–1.3×10^{12} cm (Tetarenko et al. 2017 and Chapter 5 in this thesis). This implies light crossing times[6] of 20–40 s, which while model-dependent, is in line with our estimate here.

7.4.4   Constraints on the jet launching mechanism

The observed precession of the jet axis in V404 Cyg implies that the jets must be launched within the precessing slim disc (i.e., within the inner few hundred gravitational radii). This situation will naturally occur if the energy responsible for launching jets is extracted from the precessing slim disc (Blandford & Payne, 1982). On the other hand, if jets are powered by extracting the spin energy of the black hole (Blandford & Znajek, 1977), where the jets are initially aligned with the black hole spin axis, then they must be redirected by the precessing inner accretion flow. Recent MHD simulations have suggested that the later scenario may be plausible in BHXB systems (Liska et al., 2018). However, we note that these simulations did not include the effects of radiation pressure, and thus future, more detailed simulations are needed to validate such a scenario. Overall, while our results do not allow us to distinguish between the two competing jet launching scenarios, it is clear that the dynamics of the inner accretion disc play a key role in the jet production process.

---

[6]As the sub-mm emission in this case does not come from the jet base itself, the ejection timescale is most likely even shorter.

7.4.5 Impact and implications of jet precession

In the case of V404 Cyg, we have shown that Eddington-rate accretion from a reservoir whose angular momentum is misaligned with the black hole spin, can drive a rapidly precessing accretion disc and jet system. A handful of other Galactic XB systems have also been suggested to contain a precessing jet, namely SS 433 (Margon, 1984; Hjellming & Johnson, 1981; Fabrika, 2004), GRS 1915+105 (Rodriguez & Mirabel, 1999; Rushton et al., 2010), V4641 Sgr (Gallo et al., 2014), and Cygnus X-1 (Brocksopp et al., 1999). Many of these systems share distinct simularities with V404 Cyg, such as super-Eddington accretion rates, large accretion discs, and the tendency to display bright, multi-frequency flaring activity accompanying powerful jet ejection episodes; however, the precession timescale we measure in V404 Cyg is significantly more rapid than these other systems (e.g., minutes in V404 Cyg versus hundreds of days in SS 433 and Cyg X-1). For long precession periods (e.g., hundreds of days), the Lense-Thiring precession of a thick disc would require a physically improbable accretion rate (see Figure 7.14). Therefore, if a precessing accretion disc is driving precessing jets in these other XB systems, different processes must govern the disc precession dynamics (e.g., tidal forces from the companion star in SS 433; Fabrika 2004).

Beyond the Galactic XB population, there are various other objects that can undergo Eddington-rate accretion from a misaligned accretion flow (e.g., tidal disruption events; Komossa 2015, rapidly-accreting quasars in the early Universe; Fan et al. 2003; Wu et al. 2015, and ultra-luminous X-ray sources; Soria et al. 2010; Pakull et al. 2010; Cseh et al. 2012, 2014). As such, it is possible that the precession mechanism we have presented here could be operating in these other objects, and in turn, the accretion conditions in systems like V404 Cyg may be used to better understand the accretion flow dynamics around such objects.

Regardless of the origin of precession, all systems that launch precessing

jets will deposit their energy over larger solid angles of the surrounding medium when compared to a more directed outflow. For example, the precessing jets in SS 433 are known to have inflated a large scale-nebula surrounding the central source (Dubner et al. 1998, see also Chapter 8 §8.5.5 for more details), and the powerful jets launched from AGN are known to heat large areas of the intracluster medium (Yang & Reynolds, 2016; Vernaleo & Reynolds, 2006). Therefore, we expect jet precession to significantly increase the impact of rapidly accreting systems on their surrounding environment (see Chapter 8 of this thesis for further discussion on the effect jet sources have on their local environments).

Chapter 8

Mapping jet-ISM interactions in X-ray binaries with ALMA: a GRS 1915+105 case study

This chapter details the work published in Tetarenko, A.J. et al. 2018, "Mapping jet-ISM interactions in X-ray binaries with ALMA: a GRS 1915+105 case study", *MNRAS*, 475, 448-468, whereby astro-chemistry is used to identify and probe regions where the jets launched from the black hole X-ray binary GRS 1915+105 are colliding with the surrounding medium.

<u>Abstract</u>

We present Atacama Large Millimetre/Sub-Millimetre Array (ALMA) observations of IRAS 19132+1035, a candidate jet-ISM interaction zone near the black hole X-ray binary (BHXB) GRS 1915+105. With these ALMA observations (combining data from the 12 m array and the Atacama Compact Array), we map the molecular line emission across the IRAS 19132+1035 region. We detect emission from the ^{12}CO [$J = 2 - 1$], ^{13}CO [$\nu = 0$, $J = 2 - 1$], C^{18}O [$J = 2-1$], H$_2$CO [$J = 3_{0,3}-2_{0,2}$], H$_2$CO [$J = 3_{2,2}-2_{2,1}$], H$_2$CO [$J = 3_{2,1}-2_{2,0}$], SiO [$\nu = 0$, $J = 5 - 4$], CH$_3$OH [$J = 4_{2,2} - 3_{1,2}$], and CS [$\nu = 0$, $J = 5 - 4$]

transitions. Given the morphological, spectral, and kinematic properties of this molecular emission, we present several lines of evidence that support the presence of a jet-ISM interaction at this site, including a jet-blown cavity in the molecular gas. This compelling new evidence identifies this site as a jet-ISM interaction zone, making GRS 1915+105 the third Galactic BHXB with at least one conclusive jet-ISM interaction zone. However, we find that this interaction occurs on much smaller scales than was postulated by previous work, where the BHXB jet does not appear to be dominantly powering the entire IRAS 19132+1035 region. Using estimates of the ISM conditions in the region, we utilize the detected cavity as a calorimeter to estimate the time-averaged power carried in the GRS 1915+105 jets of $(8.4^{+7.7}_{-8.1}) \times 10^{32}\,\mathrm{erg\,s^{-1}}$. Overall, our analysis demonstrates that molecular lines are excellent diagnostic tools to identify and probe jet-ISM interaction zones near Galactic BHXBs.

8.1 Introduction

Relativistic jets launched from accreting black holes carry a significant amount of energy and matter into their surrounding environment, and thus are important sources of galactic-scale feedback. For instance, jets launched from super-massive black holes in Active Galactic Nuclei (AGN) are known to interact with the intergalactic medium (IGM) on cluster scales, carving out huge cavities in hot gas (e.g. McNamara & Nulsen 2007). These AGN jets are also thought to play a major role in galaxy formation and evolution (e.g. Magorrian et al. 1998; Croton et al. 2006; McNamara et al. 2005). Similarly, the jets launched from Galactic black hole X-ray binaries (BHXBs), the stellar-mass analogues to AGN, also have an influence on their environment. These objects release a significant portion of the liberated accretion power into their relativistic jets (Heinz & Grimm, 2005; Russell et al., 2010), injecting an estimated 1% of the time-averaged luminosity of supernovae into the surrounding ISM

(Fender et al., 2005). This injected energy heats the ISM, generates interstellar turbulence, produces high-energy cosmic rays, seeds the ISM with magnetic fields, and possibly stimulates star formation (Heinz et al., 2008; Mirabel et al., 2015).

Models of the jet-ISM interaction in BHXBs (e.g. Kaiser et al. 2004) predict that as the jet impacts the ambient medium a strong radiative shock is likely to develop. Jet particles will inflate a radio lobe, which will expand to form a bubble of shock-compressed gas containing a population of relativistic electrons, producing non-thermal emission. However, we may not see all of these predicted features at every interaction site. Both the local environment and the BHXB properties may affect how these jet-ISM interactions manifest themselves (e.g. flux, morphology, chemistry). For example, since most BHXBs are thought to propagate through a lower pressure and density environment (relative to jet power) when compared to AGN (Heinz, 2002), a local density enhancement in the surrounding medium is likely required for jet-blown lobes to form (e.g. in Cygnus X-1 the jet is believed to be moving through the tail of a dense HII region; Gallo et al. 2005b; Russell et al. 2007). Further, jets launched from sources with lower peculiar velocities (relative to the local standard of rest) are more likely to inflate jet-blown lobes at the interaction site, as these sources have a more stable jet direction over time (Miller-Jones et al., 2007b). On the other hand, sources with high peculiar velocities ($> 100 \, \mathrm{km \, s^{-1}}$) are more likely to produce trails of radio plasma, rather then a radio lobe structure, as the ram pressure of the ISM sweeps up the plasma released by the jet (Heinz et al., 2008; Wiersema et al., 2009).

Valuable information on unknown jet properties, most notably, the total jet power, radiative efficiency, jet speed, and the matter content are encoded within the properties of jet-ISM interaction regions (e.g. McNamara & Nulsen 2007; Burbidge 1959; Castor et al. 1975; Heinz 2006). For instance, Gallo et al. (2005b) used the jet-blown bubble as a calorimeter to estimate the total time-

273

averaged power in the Cygnus X-1 jets to be $9 \times 10^{35} \leq P_{\text{jet}} \leq 10^{37}\,\text{erg s}^{-1}$, by modelling the shell emission from the radio nebula as radiatively shocked gas. Further work by Russell et al. (2007) and Sell et al. (2015) narrowed these estimates using a more tightly constrained shock velocity in the region. These works clearly demonstrate that such calculations are highly sensitive to the properties of the shock and ISM (i.e. density, temperature, shock velocity). Therefore, placing improved observational constraints on these parameters in multiple jet-ISM interaction sites is crucial for such efforts.

As a jet-ISM interaction will create an environment with a unique chemistry, we expect to observe significant line emission from such a region. In particular, molecular lines provide for excellent diagnostics of shock energetics and ISM excitation as different species can trace the density (CO), temperature (H_2CO; Ginsburg et al. 2015), and presence of a shock in the gas (SiO, CS, and CH_3OH; Williams & Viti 2013). By mapping molecular line emission at potential jet impact sites near BHXBs, we can develop several lines of evidence to conclusively identify jet-ISM interaction regions, and accurately probe the ISM conditions at these sites.

To date, there are only two BHXBs (SS 433; Dubner et al. 1998, and Cygnus X-1; Gallo et al. 2005b) where confirmed jet-ISM interaction sites have been detected (i.e. a jet-blown bubble/cavity and shock excited gas are observed). However, a number of other potential jet-ISM interaction sites have been identified in the vicinity of BHXBs (1E1740–2942; Mirabel et al. 1992, GRS 1758-258; Martí et al. 2002, GRS 1915+105; Kaiser et al. 2004; Rodríguez & Mirabel 1998; Chaty et al. 2001, H1743-322;, Corbel et al. 2005, XTE J1550-564; Corbel et al. 2002; Kaaret et al. 2003; Migliori et al. 2017, XTE J1748-288; Brocksopp et al. 2007, GRO J1655-40; Hjellming & Rupen 1995; Hannikainen et al. 2000, GX 339-4; Gallo et al. 2004, 4U 1755-33; Kaaret et al. 2006, XTE J1752-223; Yang et al. 2010; Miller-Jones et al. 2011; Yang et al. 2011; Ratti et al. 2012, XTE J1650-500; Corbel et al. 2004, XTE J1908+094; Rushton et al. 2017,

GRS 1009-45; Russell et al. 2006, and LMC X-1; Cooke et al. 2007; Hyde et al. 2017) on the basis that their morphological or kinematic properties are consistent with models of jet-ISM interactions in BHXBs. Out of all of these systems, GRS 1915+105 is an ideal candidate with which to study jet-ISM interactions through molecular tracers, as this system has been in a bright outburst period for over 25 years, ejects some of the most powerful relativistic jets in the known Galactic BHXB population (Fender & Belloni, 2004), and its candidate interaction zones have existing molecular line detections (Chaty et al., 2001). In this paper, we report on our Atacama Large Millimetre/Sub-Millimetre Array (ALMA) observations of the molecular line emission in IRAS 19132+1035, one of the candidate jet-ISM interaction zones near GRS 1915+105 (see Figure 8.1).

8.1.1   GRS 1915+105

GRS 1915+105 is a BHXB that was discovered in X-rays by the GRANAT satellite in 1992 (Castro-Tirado et al., 1992). The radio counterpart to the X-ray source was found shortly after with the Very Large Array (VLA; Mirabel et al. 1993). Follow up radio-frequency observations (Mirabel & Rodríguez, 1994) revealed resolved jet components, traveling away from the central source at apparent speeds that exceeded the speed of light, marking GRS 1915+105 as the first superluminal source discovered in the Galaxy. Since its discovery, this source has remained in a bright outburst state.

Recently, Reid et al. (2014a) obtained astrometric measurements of GRS 1915+105 with the Very Long Baseline Array (VLBA), measuring a model-independent parallax distance of $8.6^{+2.0}_{-1.6}$ kpc, as well as proper motions $\mu_{\mathrm{ra}} \cos \delta = -3.19 \pm 0.03 \, \mathrm{mas \, yr^{-1}}$ and $\mu_{\mathrm{dec}} = -6.24 \pm 0.05 \, \mathrm{mas \, yr^{-1}}$, which correspond to a peculiar motion[1] with respect to a circular Galactic orbit of (U,V,W)=$(19 \pm 3,$

---

[1]Reid et al. (2014a) use the convention that U is towards Galactic centre at the location of GRS 1915+105, V is in the direction of Galactic rotation, and W is toward the north Galactic pole.

-10 ± 24, 6 ± 2) km s^{-1} (giving a total peculiar velocity of 22 ± 24 km s^{-1}). Additionally, during one of their VLBA observations, Reid et al. (2014a) tracked the motion of a resolved jet component (travelling with a proper motion of $\mu = 23.6 \pm 0.5$ mas d^{-1}, resulting in a measured bulk speed of $0.81 \pm 0.04c$), which when combined with their improved distance estimate, leads to an updated inclination angle measurement of $60 \pm 5°$.

8.1.2   Candidate interaction zones near GRS 1915+105

Rodríguez & Mirabel (1998) identified two sources of bright radio emission, coincident with IRAS sources, in the vicinity of GRS 1915+105; IRAS 19124+1106 and IRAS 19132+1035 (see left panel of Figure 8.1). Both sources are located 17 arcmin away from GRS 1915+105 on the sky, which at a distance of 8.6 kpc, corresponds to 42.5 pc. Based on their morphology and location, the authors proposed that these sources may be potential interaction zones between the GRS 1915+105 jet and the surrounding ISM. However, despite several observing campaigns (e.g. Rodríguez & Mirabel 1998; Chaty et al. 2001; Miller-Jones et al. 2007b), no definitive evidence has been presented that confirms that these IRAS sources originated as a result of (or are dominantly powered by) jet-ISM interactions. There is a plethora of circumstantial evidence both for and against IRAS 19132+1035 being a jet-ISM interaction: this source shares the same position angle as jet ejections from GRS 1915+105 observed at radio wavelengths ($\sim$130–151°, see Table 2 in Reid et al. 2014a); there is a non-thermal linear radio emission feature that is spatially coincident with the inner edge of IRAS 19132+1035 and aligned with the jet axis in GRS 1915+105 (see right panel of Figure 8.1); the highest densities in IRAS 19132+1035 are located on the side nearest to the central BHXB (Chaty et al., 2001); and a bow-shock like structure may be located on the side of IRAS 19132+1035 farthest from the central BHXB (Rodríguez & Mirabel, 1998). Furthermore, the recent parallax distance determination to GRS 1915+105 ($8.6^{+2.0}_{-1.6}$ kpc; Reid et al. 2014a) brings
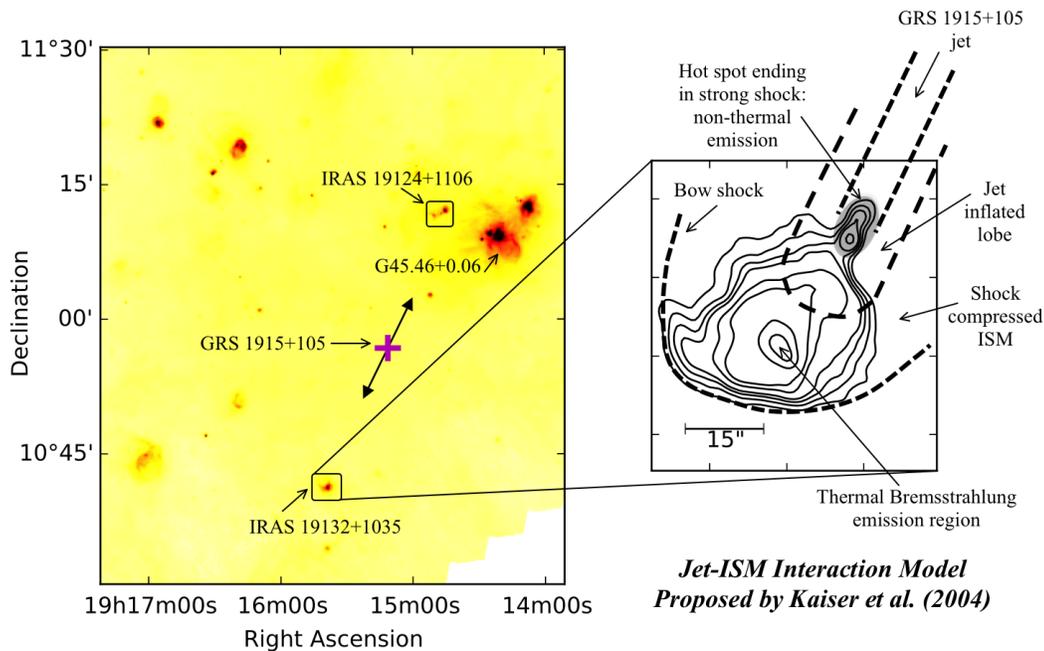
Figure 8.1: (*left*) A map of the region surrounding the BHXB GRS 1915+105, taken with the Herschel PACS continuum instrument at $70\mu m$. This map spans the extent of the previous VLA radio observations (Rodríguez & Mirabel, 1998), with which the two candidate interaction zones (IRAS 19132+1035 and IRAS 19124+1106) were first identified. Notable sources of emission are marked, including GRS 1915+105 (magenta plus sign), the position angle of the observed relativistic ejecta (solid-head arrows), the two candidate interaction zones (black squares), and a nearby compact HII region (G45.46+0.06). Our target source, IRAS 19132+1035, is southeast of GRS 1915+105. (*right*) VLA (C-configuration) radio continuum map of IRAS 19132+1035 in the 4–8 GHz band, with a schematic sketch of the XB jet-ISM interaction model (the schematic model is reproduced here to match Figure 2 in Kaiser et al. 2004). The contour levels are 0.2, 0.3, 0.4, 0.5, 0.75, 1, 2, and 3 mJy bm^{-1}. The non-thermal radio jet feature is clearly labelled (shaded grey region), and dashed lines show model features that are not directly observed in the radio continuum image.

this BHXB closer to the inferred distance of IRAS 19132+1035 (6.0 ± 1.4 kpc[2]; Rodríguez & Mirabel 1998). On the other hand, no high-velocity shock feature was seen in previous spectral line data (Chaty et al., 2001), no high-energy X-ray emission was detected at the suspected impact site (Miller-Jones et al., 2007b), and the luminosity and morphology of the region are consistent with a high mass star forming region, dominantly powered by one or more hot stars (Rodríguez & Mirabel, 1998).

To resolve this long-standing question we obtained ALMA observations to map the molecular line emission in IRAS 19132+1035, constrain ISM properties in this region, and in turn determine if there is sufficient evidence to call IRAS 19132+1035 the third conclusive site of a BHXB jet-ISM interaction in our Galaxy. In §8.2 we describe the data collection and reduction process. In §8.3 we describe our custom imaging procedure. In §8.4 we present maps of the radio/sub-mm continuum and molecular line emission in the IRAS 19132+1035 region (density tracer, CO; temperature tracer, H_2CO; and shock tracers, SiO, CS, CH_3OH, N_2D+), outline the morphological, spectral, and kinematic properties of this emission, and present constraints on the temperature, density, and column density across the region. In §8.5, we discuss the ISM conditions in the IRAS 19132+1035 region, and what these conditions reveal about the presence of a jet-ISM interaction at this site. We also present a comparison between IRAS 19132+1035, and other jet-ISM interaction zones. A summary of our work is presented in §8.6.

---

[2]This is a kinematic distance, while the GRS 1915+105 distance is a model-independent geometric parallax distance. As kinematic distances are known to be less accurate than parallax distances (Reid et al., 2014b), for all remaining calculations involving distance we will use the parallax distance, but see §8.5.7 for a discussion on the effect of distance estimates on our results.

8.2 Observations and Data Analysis

8.2.1 ALMA sub-mm observations

We observed IRAS 19132+1035 (Project Code: 2015.1.00976.S, PI: A. Tetarenko) using the ALMA 12 m array (2016 Jan 14), as well as the Atacama Compact Array (ACA) 7 m (2016 May 13, 22, and 23) and total power arrays (executions between 2016 Mar 21–2016 April 16), with the Band 6 receiver (211–275 GHz)[3]. During our observations, the 12 m array was in the most compact C36-1 configuration (with 43 antennas), and spent 34.2 min on source. We observed a 75 arcsec $\times$ 60 arcsec rectangular field centred on the coordinates (J2000) RA 19:15:39.1300, Dec 10:41:17.100 (peak of the radio continuum measured from previous VLA observations; Table 1 in Chaty et al. 2001), which consisted of 33 pointings with the 12 m array and 14 pointings with the 7 m array (see Appendix 8.7.1 for details on our choice of mosaic field). The correlator was set up to yield 4×2 GHz wide base-bands, within which we defined 9 individual spectral windows centred on our target molecular lines (see Table 8.1 for the central frequencies, bandwidth, and resolution of these spectral windows). All of the data were reduced and imaged (see §8.3 for imaging details) within the Common Astronomy Software Application package (CASA, v4.7.2; McMullin et al. 2007). Flagging and calibration of the 12 m and total power data were performed with the ALMA pipelines, while flagging and calibration of the 7 m data were performed manually using standard procedures. For the 12 m array, we used J1751+0939 as a bandpass calibrator, Pallas as a flux calibrator, and J1922+1530 as a phase calibrator. For the 7 m array, we used J1924-2914 as a bandpass calibrator, J1751+0939 as a flux calibrator, and J1922+1530 as a phase calibrator.

---

[3]Although GRS 1915+105 is a variable source, the evidence for jet-ISM interactions that we are exploring is not strongly variable on the timescales separating the different ALMA array observations.

Table 8.1: ALMA Correlator Setup

Base-band	Target Line	Central Sky Frequency (GHz)	Bandwidth ($\frac{km}{s}$ / MHz)	Resolution ($\frac{km}{s}$ / kHz)	Number of Channels
1	^{12}CO ($J = 2 - 1$)	230.48671	152 / 117.188	0.315 / 242.310	480
1	N$_2$D+ ($J = 3 - 2$)	231.27037	152 / 117.188	0.314 / 242.310	480
2	continuum / CS ($\nu = 0$, $J = 5 - 4$)	231.84934	2424 / 1875	2.507 / 1938	960
3	SiO ($\nu = 0$, $J = 5 - 4$)	217.05668	324 / 234.375	0.674 / 488.281	960
3	H$_2$CO ($J = 3_{0,3} - 2_{0,2}$)	218.17365	322 / 234.375	0.671 / 488.281	960
3	H$_2$CO ($J = 3_{2,2} - 2_{2,1}$) / CH$_3$OH ($J = 4_{2,2} - 3_{1,2}$)	218.42703	322 / 234.375	0.670 / 488.281	960
3	H$_2$CO ($J = 3_{2,1} - 2_{2,0}$)	218.71140	321 / 234.375	0.669 / 488.281	960
4	C^{18}O ($J = 2 - 1$)	219.51151	160 / 117.188	0.331 / 242.310	480
4	^{13}CO ($\nu = 0$, $J = 2 - 1$)	220.34965	159 / 117.188	0.330 / 242.310	480

8.2.2 VLA radio continuum observations

We downloaded and reduced public archival VLA observations of IRAS 19132+1035 (Project Code: 14B-482, PI: F. Mirabel). These observations were taken on 2014 Dec 06, and consisted of scans on source from 22:02:34.0–22:57:52.0 UTC (MJD 56997.9184–56997.9569), in the C (4–8 GHz) band. The array was in its C configuration during the observations. All observations were made with a 3-bit sampler, comprised of 2 base-bands, each with 16 spectral windows of 64×2 MHz channels, giving a total bandwidth of 2.048 GHz per base-band. Flagging, calibration, and imaging of the data were carried out within CASA using standard procedures. J0137+3309 was used as a flux calibrator, and J1922+1530 was used as a phase calibrator. No self-calibration was performed. We imaged the source with two Taylor terms to account for the wide bandwidth, Briggs weighting with a robust parameter of 0.5 to balance sensitivity and angular resolution, and the multi-scale *clean* algorithm (scales of $[0, 5, 20, 50] \times$ the pixel size of 0.7 arcsec) to effectively deconvolve extended emission. Flux densities from these observations are reported in Table 8.2, and are discussed in §8.4.1.

8.2.3 Other multi-wavelength observations

We compiled observations of the IRAS 19132+1035 region at other wavelengths (spanning 1.11mm – 2.73μm), taken with various instruments/surveys, including Caltech Sub-millimeter Observatory Bolocam (CSO; 1.11 mm; Ginsburg et al. 2013), Herschel Spectral and Photometric Imaging Reciever (SPIRE; 500, 350, 250 μm; Molinari et al. 2010; Griffin et al. 2010), Herschel Photometric Array Camera and Spectrometer (PACS; 70 μm; Poglitsch et al. 2010), NASA Wide-field Infrared Survey Explorer (WISE; 22 μm; Wright et al. 2010), Spitzer Galactic Legacy Infrared Mid-Plane Survey Extraordinare (GLIMPSE; 8.0 μm; Benjamin et al. 2003; Churchwell et al. 2009), and United Kingdom Infrared Telescope Infrared Deep Sky Survey (UKIRT UKIDSS; 2.37μm; Lawrence et al.

Table 8.2: Continuum Emission Properties of IRAS 19132+1035

Band	ν (GHz)	λ (μm)	$\mathbf{F_{peak}}$ (mJy bm^{-1})^c	$\mathbf{F_{integ}}$ (mJy)
Radio	6.0	5e4	2.19 ± 0.11	64.8 ± 3.3
Radio NT^a	6.0	5e4	0.66 ± 0.05	3.8 ± 0.4
Sub-mm^b	232.0	1290	1.23 ± 0.15	117 ± 15
Sub-mm	270.1	1110	554 ± 31	$(1.7 \pm 0.1) \times 10^3$
mid-IR	599.6	500	$(10.4 \pm 0.1) \times 10^3$	$(42.3 \pm 0.7) \times 10^3$
mid-IR	856.5	350	$(17.6 \pm 0.4) \times 10^3$	$(87.8 \pm 2.6) \times 10^3$
mid-IR	1199.2	250	$(26.1 \pm 1.1) \times 10^3$	$(168.5 \pm 8.4) \times 10^3$
mid-IR	4282.0	70	$(21.8 \pm 1.9) \times 10^3$	$(186 \pm 18) \times 10^3$
mid-IR	1.4e4	22	0.48 ± 0.02	6.4 ± 0.2
NIR/Opt	3.7e4	8	13.8 ± 0.8	69.1 ± 4.9
Opt/UV	1.1e5	2.73	64.9 ± 5.3	$(1.5 \pm 0.1) \times 10^3$

^{a} Fluxes reported in this row are measured over the linear non-thermal emission region only (see right panel of Figure 8.1).
^{b} Fluxes reported in this row are measured from our new ALMA observations.
^{c} The approximate beam sizes for these images are 3.7, 1.4, 33, 37, 25, 18, 6.5, 10.8, 2.5, and 0.4 arcsec at 5e4, 1290, 1110, 500, 350, 250, 70, 22, 8, and 2.73 μm.

2007; Casili et al. 2007). Flux densities from these observations are reported in Table 8.2, and are discussed in §8.4.1.

8.3 ALMA imaging process

8.3.1 Spectral line imaging

We use a custom procedure, which combines the 12 m, 7 m, and total power array data, to image all of our spectral lines. First, we split out the respective spectral windows of the line being imaged in the 12 m and 7 m data, using the CASA split task. Since the 7 m data were taken in 3 different executions, with the spectral windows slightly offset in frequency between executions, we use the mstransform task to combine the 7 m spectral windows, for each line, from each execution. We then create a template 12 m + 7 m image by running the

`clean` task with both of the 12 m and 7 m split measurement sets as input, and a single *clean* iteration. The accompanying single dish image for the spectral window (i.e. the total power array image output from the ALMA pipeline) is re-gridded to this template image using the `imregrid` task. We ensure that this re-gridded single dish image has the same primary beam response (i.e. lower in the outskirts of the image) as the 12 m + 7 m template by multiplying the re-gridded image by the primary beam template image (i.e. *.flux image in CASA). Using the `imtrans` task , we rearrange the stokes axis of the re-gridded image to be compatible with the CASA `clean` task. We then run the `clean` task with both of the 12 m and 7 m split measurement sets as input, and the re-gridded single dish image as a model image. Following this, we take the positive-only interferometer components from the *clean* model, smooth them to the synthesized beam using the `imsmooth` task, and combine the smoothed interferometer component image with the re-gridded single dish image, using the `feather` task. Lastly, we run the `clean` task again with both of the 12 m and 7 m split measurement sets as input, and the feathered single dish image as a model image. All imaging is done with natural weighting to maximize sensitivity, a pixel size of 0.2 arcsec, and the multi-scale algorithm (scales of $[0, 1, 5, 10, 15] \times$ the pixel size). See Appendix 8.7.1 (Figure 8.15) for a primary beam noise map of the region. We also tested the combination of single-dish and interferometer data directly through weighted averaging in the Fourier plane using the `feather` task in CASA only, and did not find any clear improvements in image quality.

8.3.2   Continuum imaging

To image the ALMA continuum emission, we split out the continuum spectral window in the 12 m and 7 m data, using the CASA `split` task, and then used the `mstransform` task to combine the 7 m continuum spectral windows from each execution. We then flag the channels with clear line emission in this

spectral window (determined by examining the data in `plotms`), and use the `clean` task to perform multi-frequency synthesis imaging on the combined 12 m + 7 m data. In this imaging process, we used natural weighting to maximize sensitivity, and two Taylor terms to account for the wider bandwidth. Note that the single dish data from the total power array does not have a continuum component.

8.4 Results

8.4.1 Continuum Emission from IRAS 19132+1035

The top panels of Figure 8.2 display radio continuum, radio spectral index, and sub-mm continuum emission maps of the IRAS 19132+1035 region; Figure 8.4 displays IR through UV continuum emission from the IRAS 19132+1035 region.

The radio continuum emission is mainly extended over a 43 arcsec × 41 arcsec region, and displays a unique morphology; a linear feature (dimensions of 8 arcsec × 11 arcsec) extending in the direction of the central BHXB, and a sharp edge on the opposite side of the region. The emission from the linear feature shows a steep spectral index ($\alpha \sim -0.7$, where $f_\nu \propto \nu^\alpha$) that is distinct from the flat ($\alpha \sim 0$) spectral index observed in the rest of the region. This suggests that the emission in these two zones originates from different processes. In particular, the steep spectral index is consistent with non-thermal synchrotron emission from a relativistic plasma, commonly observed from BHXB jets (Fender, 2006), while the flat-spectrum emission is consistent with thermal bremsstrahlung emission from ionized hydrogen gas. Previous work (Rodríguez & Mirabel, 1998; Kaiser et al., 2004) estimated the temperature of the ionized hydrogen gas, using the width of a hydrogen recombination line (H92α) detected in this region, to be 1.2×10^4 K. The sharp edge seen in the radio continuum emission, on the side of the IRAS 19132+1035 region furthest from the central BHXB, has previously been associated with a

potential bow-shock feature created by a jet-ISM interaction, or the ionization front from an HII region (Chaty et al., 2001).

At sub-mm frequencies, the continuum emission in IRAS 19132+1035 is confined to two regions, which are much more compact when compared with the extent of the radio continuum feature. One of these sub-mm continuum regions is consistent with the location of the peak flux density in the radio continuum (dimensions of ~ 11 arcsec $\times 13$ arcsec), and the other is located to the north of the radio continuum peak (dimensions of ~ 19 arcsec $\times 18$ arcsec). We do not detect sub-mm emission from the linear radio jet feature. This non-detection is expected, given that an extrapolation of the steep synchrotron spectrum to sub-mm frequencies predicts a flux density ($\sim 54\mu$Jy) below our ALMA detection limits ($\sim 130\mu$Jy).
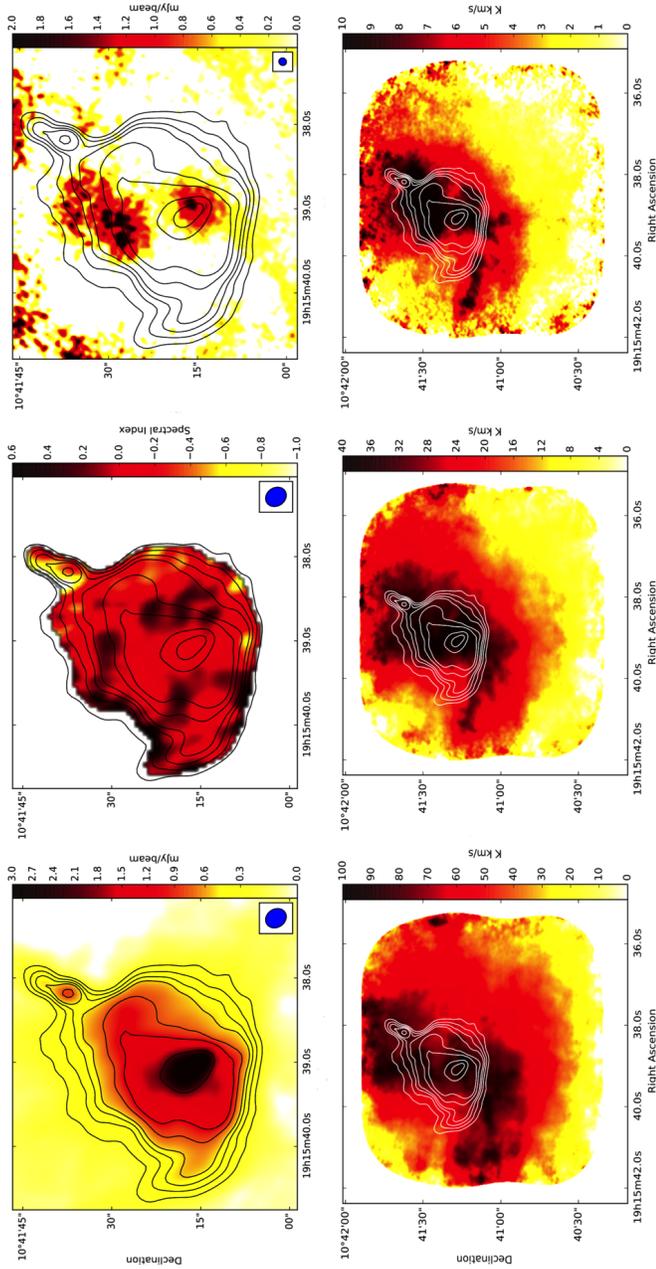
Figure 8.2: Radio through sub-mm maps of the IRAS 19132+1035 region. The *top row, left to right*, displays the VLA continuum radio frequency image in the 4–8 GHz band (contour levels of 0.2, 0.3, 0.4, 0.5, 0.75, 1, 2, and 3 mJy bm^{-1}), the radio spectral index map (using the convention $f_\nu \propto \nu^\alpha$, where α represents the spectral index), and the ALMA sub-mm continuum image in the 231.9–232.8 GHz band. The blue ellipses in the bottom right corners represent the VLA and ALMA beams. The *bottom row, left to right*, displays the ^{12}CO, ^{13}CO, and C^{18}O, integrated intensity maps; contours are the VLA radio frequency contours. The colour bars indicate the flux density in units of mJy bm^{-1} (*top left panel & top right panels*), spectral index (*top middle panel*), or integrated intensity in units of K km s^{-1} (*bottom panels*). In the IRAS 19132+1035 region, the location of bright molecular emission coincides with that of the continuum emission.

286

The bulk of the emission at mid-IR frequencies (i.e. 22–$500 \mu m$) in IRAS 19132+1035 is extended, and centred on the thermal radio continuum feature. Given the integrated fluxes reported in Table 8.2, both the sub-mm and IR continuum emission likely originate from thermal dust emission. This thermal dust emission is best modelled as a modified black-body, represented by,

$$I_\nu = \frac{2h\nu^3}{c^2} \frac{\kappa_\nu \Sigma_{\mathrm{mol}}}{\left(\exp\left[\frac{h\nu}{kT_{\mathrm{dust}}}\right] - 1\right)} \tag{8.1}$$

where we use the opacity law (Beckwith et al., 1990),

$$\kappa_\nu = 0.1 \mathrm{~cm}^2 \mathrm{~g}^{-1}, (\nu/1 \mathrm{~THz})^\beta,$$

β represents the emissivity index, T_{dust} represents the dust temperature, and Σ_{mol} represents the molecular gas surface density implied by the dust emission. Note that this value of the dust opacity includes a gas-to-dust ratio of 100 by mass.

To estimate the physical properties of the dust emission region, we fit (using a Markov Chain Monte Carlo (MCMC) algorithm) the broad-band sub-mm through IR (22–$1110 \, \mu$m; see Table 8.2) spectrum, with the modified black-body function of Equation 8.1. The best-fit parameters are displayed in Table 8.3, and the broad-band spectrum (with the best-fit dust model overplotted), is shown in Figure 8.3. We do not include our ALMA sub-mm continuum flux density measurement in the fit, as we lack single dish continuum data (we only have continuum data from the 12 m & 7 m arrays). Therefore, we do not recover all the flux from the region in these ALMA continuum observations, which leads to a lower overall integrated flux density measurement.

In the UV/optical/NIR bands (i.e. $\lambda \leq 8 \mu m$), the emission from the IRAS 19132+1035 region is dominated by compact point sources, the brightest of which coincides with the peak of the radio continuum emission. Therefore, emission in these bands appears to be mainly stellar emission.
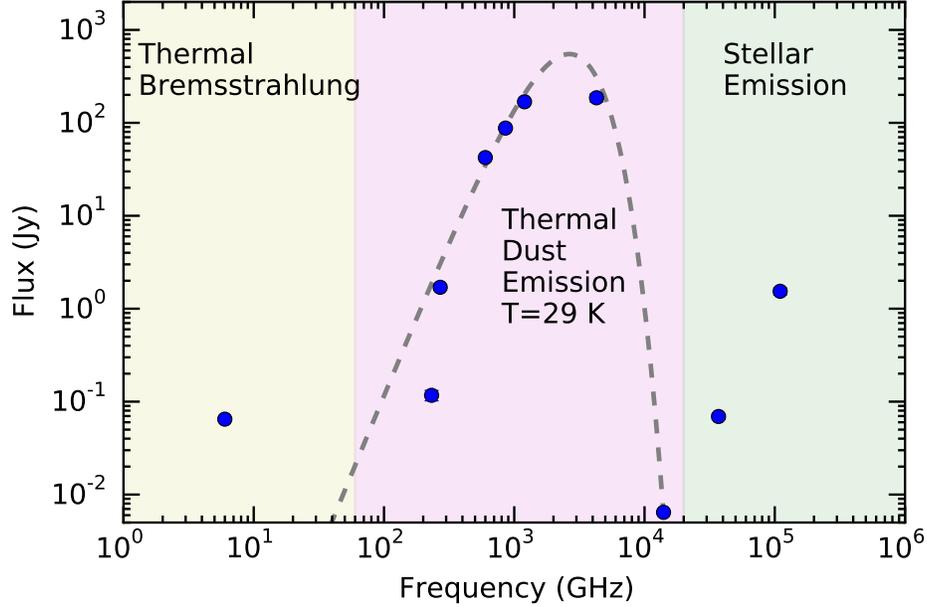
Figure 8.3: Broad-band spectrum of the continuum emission from IRAS 19132+1035. The blue points indicate the integrated flux densities from Table 8.2, and the grey dotted line indicates a modified blackbody fit to the 22–1110 μm data points (see text in §8.4.1 for details). Different emission processes (highlighted colour bands labeled on plot) dominate the IRAS 19132+1035 continuum emission in different frequency ranges.

Table 8.3: Best-fit parameters for dust emission in IRAS 19132+1035

Parameter	Best-fit value	
T_{dust}	$29.01^{+0.14}_{-0.13}$	K
Σ_{mol}	$450.0^{+11.1}_{-11.0}$	$M_\odot\,\mathrm{pc}^{-2}$
β	$1.44^{+0.03}_{-0.03}$	
M^a_{mol}	1200^{+690}_{-450}	$M_\odot$

[a] The mass of the molecular medium derived from the dust emission is not a fitted parameter, but found using the expression $M_{\mathrm{mol}} = \Sigma_{\mathrm{mol}}\Omega D^2$. To properly account for uncertainties in distance (D) and surface density (Σ_{mol}) we performed Monte Carlo simulations, sampling from the posterior distribution of Σ_{mol} output from the fitting procedure, and the known geometric parallax distance distribution (Reid et al., 2014a).
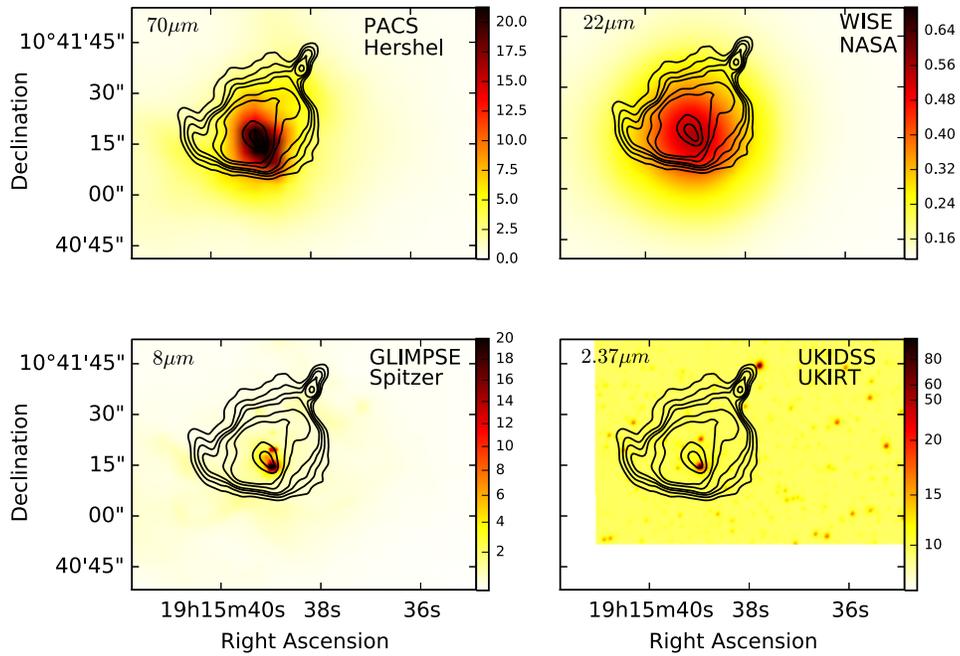
Figure 8.4: Multi-wavelength continuum observations of the IRAS 19132+1035 region. Each panel is labeled with the wavelength (*top left*), and the instrument/telescope/survey (*top right*) for that specific image. The contours in all panels are the VLA radio frequency contours, as seen in Figure 8.2; 0.2, 0.3, 0.4, 0.5, 0.75, 1, 2, and 3 mJy bm^{-1}. The colour bars indicate the flux density in units of mJy bm^{-1}, except for the *top left panel* which has units of Jy bm^{-1} . These multi-wavelength images display the extent of the contributions from other continuum emission sources in the region, namely dust (*top row*) and stellar emission (*bottom row*).

8.4.2 CO line emission from IRAS 19132+1035

Integrated intensity maps of the ^{12}CO, ^{13}CO, and C^{18}O emission across the IRAS 19132+1035 region are shown in the bottom panels of Figure 8.2. In these maps, we detect bright emission from the different isotopologues of CO, coincident with the radio continuum feature. However, we see very little emission to the south of the radio continuum feature (other than in ^{12}CO).

As the CO emission tracks where most of the molecular gas is located, we expect signatures of a jet-ISM interaction to appear best within the CO emission morphology. In particular, in the framework of the jet-ISM interaction model presented in Kaiser et al. (2004), the radio continuum feature is housed inside a jet-blown bubble in the molecular cloud, and the entire IRAS source is thought to represent shock-heated ISM material located near the jet impact zone. The key morphological features we then anticipate to observe are a cavity structure surrounding the linear non-thermal emission feature (possibly extending towards the peak of the radio continuum), a ring-like bow shock feature hugging the sharp southern edge of the entire radio continuum, and shocked molecular gas to the south of the radio continuum feature (see Figure 8.1 *right*). However, we see none of these expected features within the CO emission. While this does not rule out a jet-ISM interaction in this region, it strongly suggests that the entire IRAS 19132+1035 region (or at least the flat-spectrum radio continuum feature) is not predominantly shaped by such an interaction.

To investigate the possibility of a jet-ISM interaction on smaller scales (i.e. smaller than the extent of the radio continuum feature), we examined the CO emission properties, namely spectra and line ratios, across different regions of interest in the imaged field; the base of the non-thermal jet feature (A), the radio peak of the non-thermal jet-feature (B), the peak of the radio continuum (C), and an off position well away from the radio continuum feature (D; shown in Figure 8.5 *left*). To characterize the spectral line properties, we fit each

detected line with one or more Gaussian components, where we have estimated the uncertainties on the spectral data points for each line by taking the median absolute deviation of spectral data points well away from the line emission (see Table 8.4).

The line profiles and intensities of the CO emission clearly vary across the IRAS 19132+1035 region (see Figure 8.5 *right*). Regions A and B display CO lines with double peaked, more asymmetric profiles, when compared to regions C and D. The peak intensities also differ between regions, where the brightest emission from all the isotopologues occurs in region C, coincident with the peak of the radio continuum emission.

In a previous molecular line study of this region conducted with the IRAM 30m telescope (which had lower sensitivity, as well as lower spectral and angular resolution, when compared to our ALMA observations), Chaty et al. (2001) detected the ^{12}CO ($J = 2 - 1$) and ^{13}CO ($J = 2 - 1$) transitions at multiple positions along a slice through the radio jet feature. Our new spectral measurements of the CO emission in the IRAS 19132+1035 region are consistent with those reported in this previous study, in terms of the central velocities and peak intensities of the ^{12}CO and ^{13}CO lines (~ 67 km s^{-1} and ~ 20, 11 K, respectively), as well as the asymmetric line profiles observed near the jet feature.

The CO line ratios also vary substantially across the IRAS 19132+1035 region (see Figure 8.6[4]). In particular, region A displays an atypical ratio of ^{12}CO/^{13}CO~ 1. This line ratio indicates the presence of optically thick (likely very dense) gas, preferentially located in the region coincident with the base of the non-thermal jet feature.

---

[4]To create this ratio map, we use the ^{13}CO as a template to find the velocity channel with the maximum intensity in each pixel, then compute the line ratio for each pixel using the intensity in the matching velocity channel of the ^{12}CO spectrum. This procedure ensures that we are not comparing emission at different velocities.

Table 8.4: CO line emission properties from Gaussian fits to IRAS 19132+1035 sub-mm emission

Reg.	Line	# of Comp.[a]	T_p[b] (K)	FWHM $(km\,s^{-1})$	V_c[c] $(km\,s^{-1})$
A	^{12}CO	2	$10.60^{+0.05}_{-0.05}$	$2.76^{+0.03}_{-0.03}$	$65.73^{+0.02}_{-0.01}$
			$16.23^{+0.06}_{-0.06}$	$2.68^{+0.01}_{-0.01}$	$68.54^{+0.01}_{-0.01}$
	^{13}CO	2	$10.31^{+0.10}_{-0.10}$	$1.85^{+0.02}_{-0.02}$	$66.32^{+0.01}_{-0.01}$
			$7.45^{+0.07}_{-0.07}$	$2.10^{+0.03}_{-0.03}$	$68.27^{+0.02}_{-0.02}$
	$C^{18}O$	2	$2.05^{+0.05}_{-0.05}$	$0.90^{+0.03}_{-0.03}$	$66.04^{+0.01}_{-0.01}$
			$3.75^{+0.02}_{-0.02}$	$2.10^{+0.03}_{-0.03}$	$67.59^{+0.01}_{-0.01}$
B	^{12}CO	2	$10.16^{+0.02}_{-0.02}$	$2.73^{+0.01}_{-0.01}$	$65.54^{+0.01}_{-0.01}$
			$19.75^{+0.03}_{-0.02}$	$2.43^{+0.01}_{-0.01}$	$68.43^{+0.003}_{-0.003}$
	^{13}CO	2	$9.56^{+0.06}_{-0.07}$	$2.77^{+0.03}_{-0.03}$	$66.91^{+0.02}_{-0.02}$
			$3.49^{+0.2}_{-0.2}$	$1.63^{+0.04}_{-0.05}$	$68.61^{+0.02}_{-0.02}$
	$C^{18}O$	2	$1.13^{+0.16}_{-0.11}$	$1.32^{+0.10}_{-0.10}$	$66.22^{+0.07}_{-0.04}$
			$3.21^{+0.05}_{-0.07}$	$1.98^{+0.05}_{-0.06}$	$67.61^{+0.05}_{-0.03}$
C	^{12}CO	1	$22.10^{+0.02}_{-0.03}$	$3.70^{+0.004}_{-0.004}$	$67.37^{+0.002}_{-0.002}$
	^{13}CO	1	$15.25^{+0.01}_{-0.01}$	$2.83^{+0.002}_{-0.002}$	$66.91^{+0.001}_{-0.001}$
	$C^{18}O$	1	$5.25^{+0.01}_{-0.01}$	$1.88^{+0.003}_{-0.003}$	$67.07^{+0.001}_{-0.001}$
D	^{12}CO	1	$11.05^{+0.009}_{-0.007}$	$2.89^{+0.002}_{-0.003}$	$67.40^{+0.001}_{-0.001}$
	^{13}CO	1	$3.02^{+0.007}_{-0.006}$	$2.03^{+0.005}_{-0.004}$	$67.56^{+0.002}_{-0.002}$
	$C^{18}O$	1	$0.25^{+0.009}_{-0.009}$	$2.04^{+0.08}_{-0.07}$	$67.72^{+0.04}_{-0.04}$

[a]Number of Gaussian components needed to fit the line.
[b]Peak intensity of Gaussian components.
[c]Central velocity of Gaussian components.
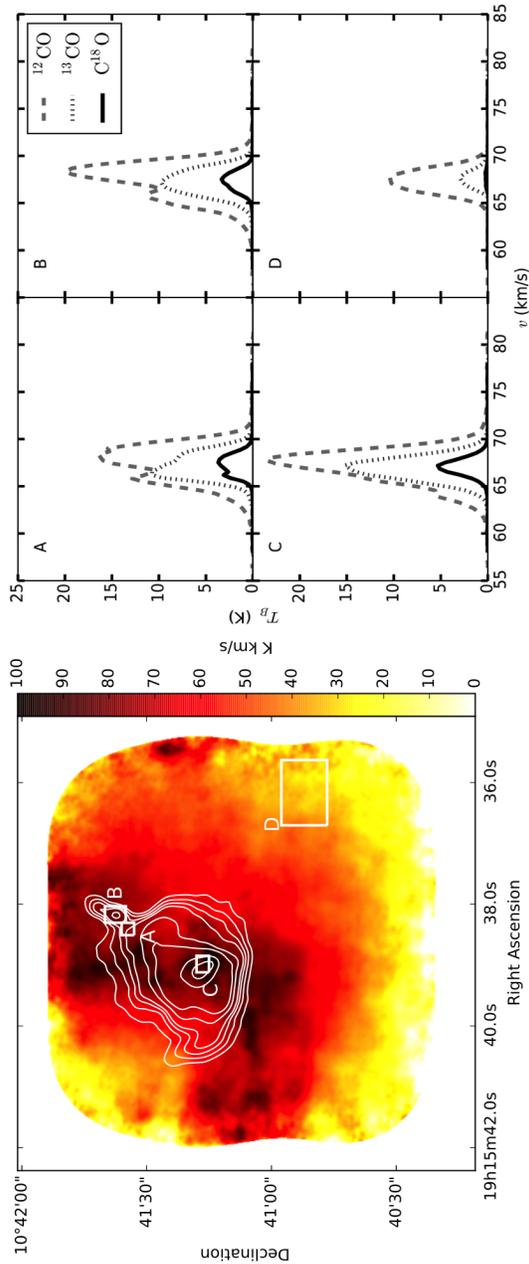
Figure 8.5: CO emission in different zones of the IRAS 19132+1035 region. The *left panel* displays the ^{12}CO integrated intensity map with four marked regions. The contours are the VLA radio frequency contours; levels of 0.2, 0.3, 0.4, 0.5, 0.75, 1, 2, and 3 mJy bm^{-1} (see Figure 8.2). The *right panel* displays the spectra of the different isotopologues of CO taken in the labelled regions; ^{12}CO (dashed grey line), ^{13}CO (dotted light grey line), and C^{18}O (solid black line). The CO line profiles and peak intensities clearly vary between different zones in the IRAS 19132+1035 region.
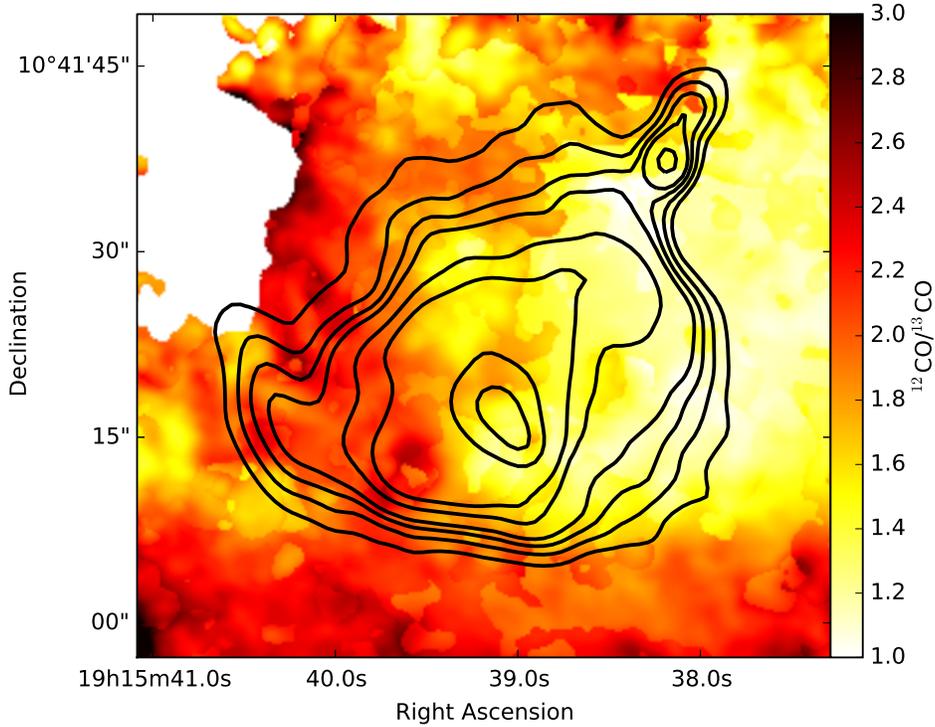
Figure 8.6: ^{12}CO/^{13}CO isotopologue ratio map of the IRAS 19132+1035 region. The colour bar indicates the line ratio values. The contours represent the VLA radio frequency contours; levels of 0.2, 0.3, 0.4, 0.5, 0.75, 1, 2, and 3 mJy bm^{-1} (see Figure 8.2). Regions where the ^{13}CO emission is < 5 K are masked. The region located at the base of the radio jet feature displays an atypical line ratio, ^{12}CO/^{13}CO~ 1, signifying very optically thick (dense) gas in this zone.

To examine the kinematics of the molecular gas near our regions of interest, we created Position-Velocity (PV) diagrams of ^{12}CO, ^{13}CO, and C^{18}O, from a slice through the linear non-thermal jet feature (see Figure 8.7 *right*). Within these diagrams, we observe a distinct hole in the ^{13}CO and C^{18}O molecular emission, spatially coincident with the location of the non-thermal jet feature. Additionally, we observe an elongated lobe, extended towards lower velocities, located at the inner edge of the jet feature. These PV features are unique to the jet feature region (i.e. they do not appear in the shifted PV slices; see Figure 8.7 *left*), and indicate not only that the gas is being spatially displaced away from the linear jet feature region, but also that this displaced gas is being pushed
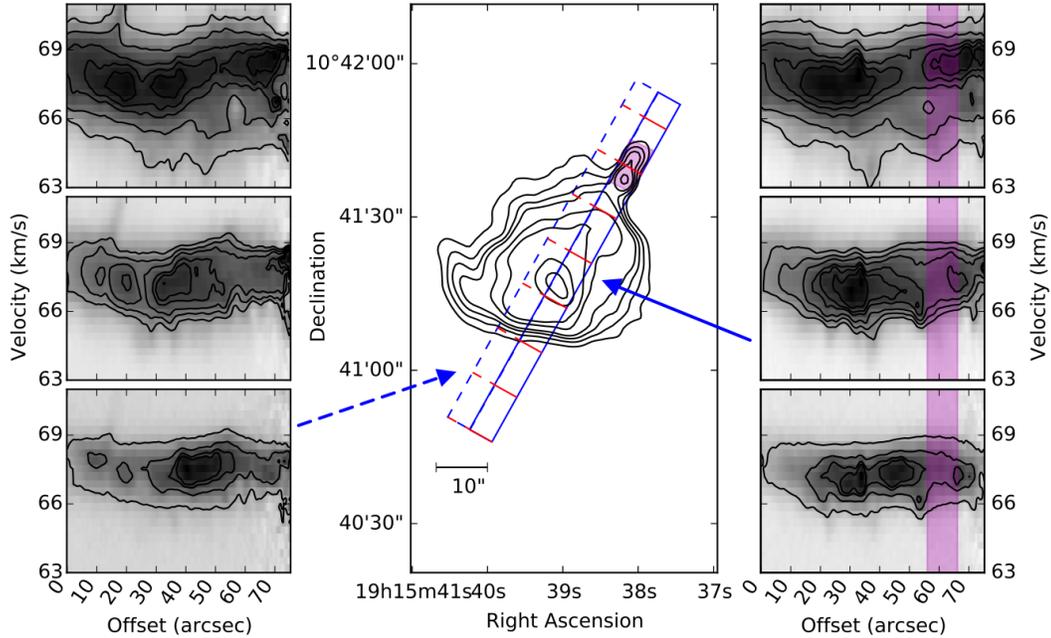
Figure 8.7: Kinematic analysis of the CO emission in the IRAS 19132+1035 region, over a slice through the radio jet feature (solid blue rectangle) and a slice offset from the radio jet feature (dotted blue rectangle). The *left* and *right* panels display the PV diagrams of ^{12}CO (*top*), ^{13}CO (*middle*), and C^{18}O (*bottom*) from the respective slices. Contours are 5.0, 10.0, 15.0, 17.5, and 20.0 K for ^{12}CO, 5.0, 6.5, 8.0, 10.0, 11.0, and 12.5 K for ^{13}CO, and 1.0, 2.5, 3.5, and 4.0 K for C^{18}O in both the *left and right panels*. The *middle panel* displays the location of the slices through the CO cubes, where the contours represent the VLA radio frequency contours; levels of 0.2, 0.3, 0.4, 0.5, 0.75, 1, 2, and 3 mJy bm^{-1} (see Figure 8.2). The purple shading in the *right and middle panels* indicate the spatial location of the radio jet feature. The red ticks in the middle panel correspond to the offset along the slices, in increments of 10 arcsec (from the lower left; 0, 10, 20, 30, 40, 50, 60, 70 arcsec). Kinematic features unique to the radio jet feature region (i.e. a distinct hole in the ^{13}CO and C^{18}O emission, and an elongated lobe extended towards lower velocities), suggest that the gas in this region is being punched from behind (the direction of the BHXB jet), resulting in the excavation of a jet-blown cavity.

Table 8.5: Shock tracing line emission properties from Gaussian fits to IRAS 19132+1035 sub-mm emission

Line	# of Comp.[a]	T_{p}[b] (K)	FWHM (km s^{-1})	V_{c}[c] (km s^{-1})
CH$_3$OH	1	$0.08^{+0.005}_{-0.005}$	$2.63^{+0.19}_{-0.17}$	$67.00^{+0.07}_{-0.05}$
SiO North	1	$0.11^{+0.02}_{-0.02}$	$1.01^{+0.24}_{-0.18}$	$66.66^{+0.10}_{-0.09}$
SiO South	1	$0.04^{+0.003}_{-0.003}$	$10.01^{+0.88}_{-0.86}$	$65.56^{+0.19}_{-0.21}$
CS North[d]	1	$0.05^{+0.03}_{-0.01}$	$2.70^{+0.67}_{-0.94}$	$66.73^{+0.47}_{-0.57}$
CS South	1	$0.12^{+0.10}_{-0.02}$	$2.12^{+0.83}_{-0.83}$	$67.03^{+0.38}_{-0.59}$

[a]Number of Gaussian components needed to fit the line.
[b]Peak intensity of Gaussian components.
[c]Central velocity of Gaussian components.
[d]Note that an additional constant baseline flux component was required when fitting this line; its amplitude was $0.022^{+0.002}_{-0.002}$ K.

to lower velocities. Both of these kinematic properties are consistent with the gas in the jet feature region being punched from behind (i.e. in line with the direction of the BHXB jet), resulting in the excavation of a potential jet-blown cavity. We note that these enhancements/depletions in the CO emission are not seen as clearly in the ^{12}CO compared to the ^{13}CO and C^{18}O emission. This is likely a result of opacity effects; the ^{12}CO emission is optically thick, and this will in turn make it difficult to detect such enhancements/depletions in the ^{12}CO emission.

8.4.3 Shock-tracing line emission from IRAS 19132+1035

Integrated intensity maps and spectra for the CH$_3$OH, CS, and SiO transitions detected in the IRAS 19132+1035 region are shown in Figure 8.9, with the spectral line characteristics from Gaussian fits displayed in Table 8.5. We did not detect the N$_2$D$^+$ molecule in the region, where we place an estimated 3σ upper limit on the integrated intensity across the IRAS 19132+1035 region of 0.69 K km s^{-1}.

The majority of the emission, showing the brightest integrated intensities,

from the CH_3OH, CS, and SiO molecules are confined to a region located to the north of the radio continuum peak, coincident with sub-mm continuum emission. Additionally, the CS line is detected in another region near the radio continuum peak, and the SiO line is detected in a compact region near the base of the jet feature. These shock tracing emission lines have much lower peak intensities than the CO lines; the CH_3OH line has a peak intensity of ~ 80 mK, CS has a peak intensity between ~ 50–120 mK, and SiO has a peak intensity of ~ 40–110 mK.

While the CH_3OH and CS lines appear to have similar line widths to that of the CO in region C (~ 2–$3\,\mathrm{km\,s^{-1}}$), the SiO detections show both significantly wider (southern detection) and narrower (northern detection[5]; also see Figure 8.8) line widths when compared to CO ($\sim 10\,\mathrm{km\,s^{-1}}$ and $\sim 1\,\mathrm{km\,s^{-1}}$).

In their previous molecular line study of IRAS 19132+1035, Chaty et al. (2001) reported the detection of the shock tracing molecules, CS ($J = 2 - 1$) and SiO ($J = 2 - 1$ & $J = 3 - 2$), at locations near the radio continuum peak and the non-thermal jet feature, respectively. The location, central velocity ($\sim 67\,\mathrm{km\,s^{-1}}$) and line width ($\sim 2 - 3\,\mathrm{km\,s^{-1}}$) of our southernmost detection of CS ($J = 5 - 4$), is consistent with the previous detection of the $J = 2 - 1$ transition of this molecule. Similarly, the spectral line properties of our northernmost detection of SiO ($J = 5 - 4$) also appears to be consistent with the previous detection of the $J = 2 - 1$ and $J = 3 - 2$ transitions by Chaty et al. (2001), especially in terms of the observed narrow line widths of only a few $\mathrm{km\,s^{-1}}$.

Given its proximity to the non-thermal jet feature (i.e. the suspected jet impact site), and the compact nature of the emission region, our northernmost SiO detection may originate in a shock produced as the BHXB jet collides with the ISM. However, the narrow line width implies the shock velocity must be

---

[5]Despite the narrow line width and low integrated intensity for the northern SiO detection (when compared to the southern SiO detection), we are confident this detection is real, as the central velocity matches that of the other shock tracing line detections, and the peak intensity of the line is $> 5\sigma$ above the estimated noise level (~ 0.02 K) in the spectrum.
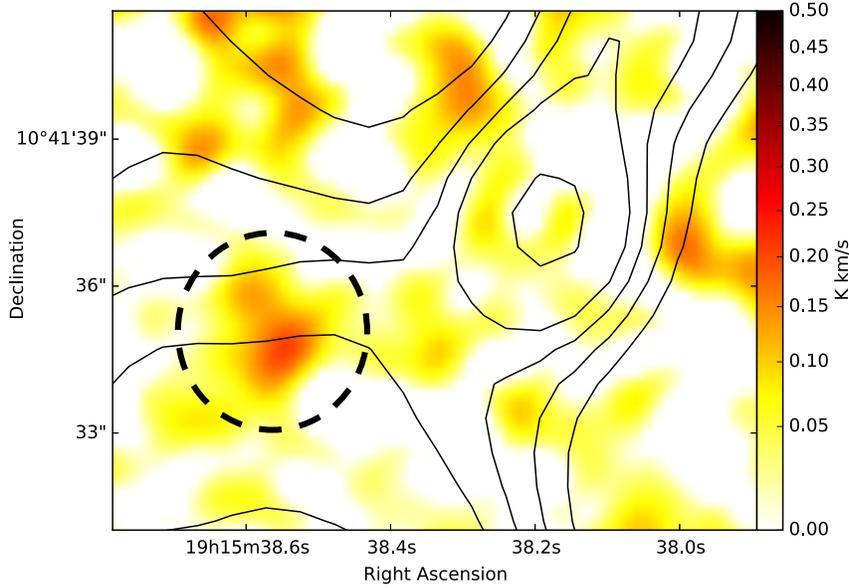
Figure 8.8: Integrated intensity map of SiO ($\nu = 0$, $J = 5 - 4$) emission in IRAS 19132+1035, zoomed in to show the northernmost detection (indicated by the black circle). The integrated intensity map covering the entire IRAS 19132+1035 region can be seen in the rightmost panel of Figure 8.9. We are confident that this detection is real and not simply a noise feature; the emission spans multiple channels, the peak intensity of the line is $> 5\sigma$ above the estimated noise level (~ 0.02 K), and the central velocity matches that of our other shock tracing line detections.

quite low[6]. The remainder of the shock tracing emission we detect is only found in regions located well away from the non-thermal jet feature. Therefore, these detections are unlikely to be associated with a potential jet-ISM interaction site in IRAS 19132+1035 and must originate from another source of feedback in the region, likely from high mass star formation (see §8.5.2). This conclusion is also supported by the vastly differing line widths between the SiO detections in these two shocked emission regions. The molecular gas to the south-east of the jet feature likely has a much faster shock compared to the molecular gas near the base of the jet feature (see Figure 8.9 and Table 8.5), suggesting that these shock features are powered by feedback from different objects.

---

[6]See §8.5.5 for a discussion on this low shock velocity.
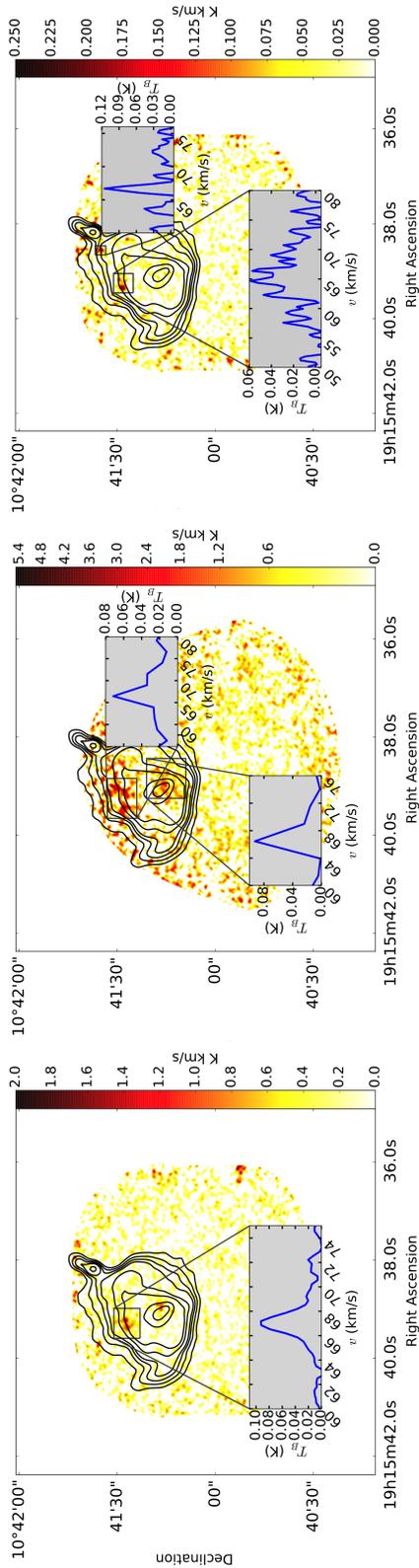
Figure 8.9: Emission from the shock-tracing molecules detected in the IRAS 19132+1035 region. The panels from *left to right* display the CH_3OH ($J = 4_{2,2} - 3_{1,2}$), CS ($\nu = 0$, $J = 5 - 4$), and SiO ($\nu = 0$, $J = 5 - 4$), integrated intensity maps. The contours in all the panels are the VLA radio frequency contours; levels of 0.2, 0.3, 0.4, 0.5, 0.75, 1, 2, and 3 mJy bm^{-1} (see Figure 8.2). The colour bars indicate the integrated intensity in units of K km s^{-1}. Inset panels show spectra of each line, in regions where we detect significant emission (marked by the black boxes). Note that the CS line has a noticeably lower spectral resolution, as this line was detected within the continuum spectral window. Due to the compact nature of the northernmost SiO detection, we also provide an alternate version of the SiO integrated intensity map zoomed in on this feature in Figure 8.8. We observe shock-tracing emission with varying line widths and intensities across IRAS 19132+1035, suggesting multiple feedback sources are powering the region.

Table 8.6: H_2CO line emission properties from Gaussian fits to IRAS 19132+1035 sub-mm emission

H_2CO Transition	# of Comp.[a]	T_p[b] (K)	FWHM (km s^{-1})	V_c[c] (km s^{-1})
$J = 3_{0,3} - 2_{0,2}$ North	1	$0.64^{+0.003}_{-0.003}$	$2.22^{+0.01}_{-0.01}$	$67.15^{+0.006}_{-0.005}$
$J = 3_{0,3} - 2_{0,2}$ South	1	$0.49^{+0.003}_{-0.004}$	$2.00^{+0.02}_{-0.02}$	$66.89^{+0.007}_{-0.006}$
$J = 3_{2,1} - 2_{2,0}$ North	1	$0.10^{+0.004}_{-0.004}$	$2.36^{+0.14}_{-0.14}$	$67.07^{+0.05}_{-0.05}$
$J = 3_{2,1} - 2_{2,0}$ South	1	$0.11^{+0.003}_{-0.002}$	$1.86^{+0.06}_{-0.06}$	$66.98^{+0.02}_{-0.02}$
$J = 3_{2,2} - 2_{2,1}$ North	1	$0.10^{+0.005}_{-0.005}$	$2.37^{+0.15}_{-0.14}$	$67.20^{+0.05}_{-0.04}$
$J = 3_{2,2} - 2_{2,1}$ South	1	$0.09^{+0.003}_{-0.002}$	$2.18^{+0.06}_{-0.07}$	$66.96^{+0.03}_{-0.02}$

[a]Number of Gaussian components needed to fit the line.
[b]Peak intensity of Gaussian components.
[c]Central velocity of Gaussian components.

8.4.4 H_2CO line emission from IRAS 19132+1035

Integrated intensity maps and spectra for the three H_2CO lines detected in the IRAS 19132+1035 region are shown in Figure 8.11, with the spectral line characteristics from Gaussian fits displayed in Table 8.6.

The majority of the emission from H_2CO is confined to regions coincident with the sub-mm continuum emission (i.e. centred on the radio continuum peak, and a region to the north of the radio peak). The brightest H_2CO line displays a peak intensity of ~ 0.6 K, while the weaker lines display peak intensities of ~ 0.1 K. The line widths of all three transitions are similar to those of the CH_3OH and CS molecules present in the same region ($\sim 2\,\mathrm{km\,s^{-1}}$).

To derive an estimate of the physical properties of the molecular gas (i.e. temperature and density) in the IRAS 19132+1035 region, we model the H_2CO lines with RADEX radiative transfer models, using the PYSPECKIT python package[7]. This package implements RADEX model grids over a range of densities, column densities, and temperatures[8] to fit a five parameter model to the

---

[7]https://github.com/pyspeckit/pyspeckit
[8]We implement pre-computed RADEX model grids over temperature, density, and column density; $5 < T < 205$ K, $10^2 < n < 10^7 \mathrm{cm^{-3}}$, and $10^{10} < N < 10^{17}\,\mathrm{cm^{-2}}$.

H$_2$CO spectrum: line intensity, line width, temperature, density, and column density. For this modelling, we simultaneously fit the H$_2$CO($J = 3_{0,3} - 2_{0,2}$), H$_2$CO ($J = 3_{2,2} - 2_{2,1}$), and H$_2$CO ($J = 3_{2,1} - 2_{2,0}$) lines in regions where we detect significant H$_2$CO emission. We define a significant detection of H$_2$CO as regions where emission in the T_{max} map of the brightest transition ($J = 3_{0,3} - 2_{0,2}$) reaches a $\geq 3\sigma$ level. This translates to regions where the H$_2$CO ($J = 3_{0,3} - 2_{0,2}$) emission is > 0.25 K.

When performing the RADEX modelling, with all of the parameters left free, we are unable to accurately map the temperature in the region, as variations in density appear to be driving artificial variations in the fitted temperature. This result is likely due to the degeneracies between the temperature and density parameters in the model. Therefore, we choose to fix the density at the central value of $n = 10^4 \, \mathrm{cm}^{-3}$, and refit the spectrum. A temperature map of the region output from this process is shown in Figure 8.10. Based on this map, the hottest molecular gas in the region appears to be clustered around the radio continuum peak. Additionally, there is a distinct lack of H$_2$CO emission within, and at the base of, the non-thermal jet feature (see Figure 8.11). This indicates the absence of hot molecular gas within and at the base of the jet feature, when compared to the surrounding zones.
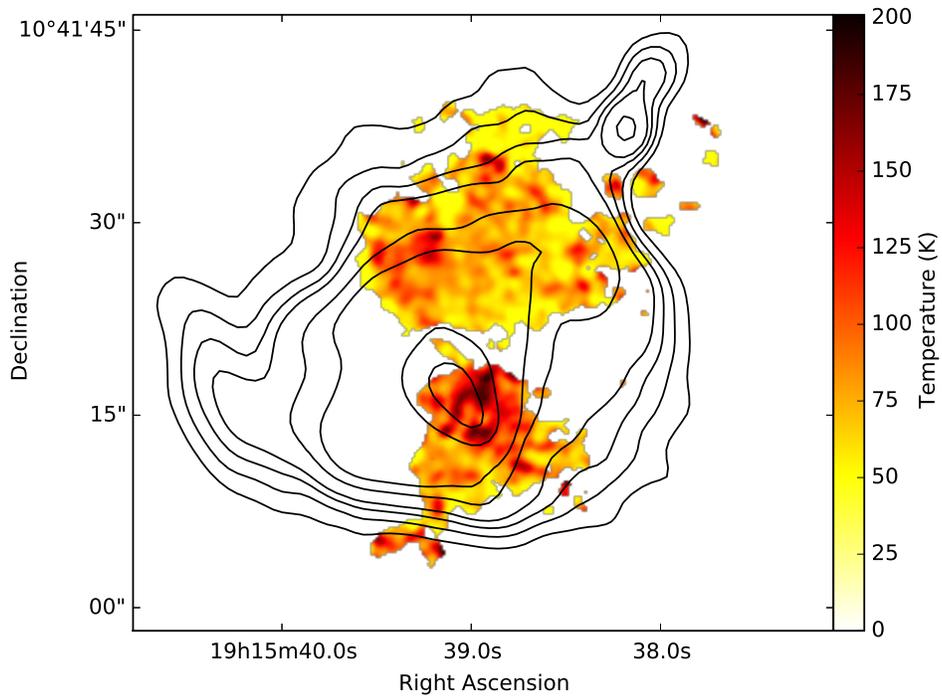
Figure 8.10: Temperature map of the molecular gas in the IRAS 19132+1035 region, obtained from fitting the H_2CO lines with RADEX models. In this fit, we fix the density in the region to $n = 10^4$ cm^{-3}. The temperature map shown here is masked to regions where we detected H_2CO emission (see §8.4.4 for details). The contours are the VLA radio frequency contours; levels of 0.2, 0.3, 0.4, 0.5, 0.75, 1, 2, and 3 mJy bm^{-1} (see Figure 8.2). The colour bar indicates the temperature in units of K. The largest temperatures in the region appear to coincide with the peak of the radio continuum.
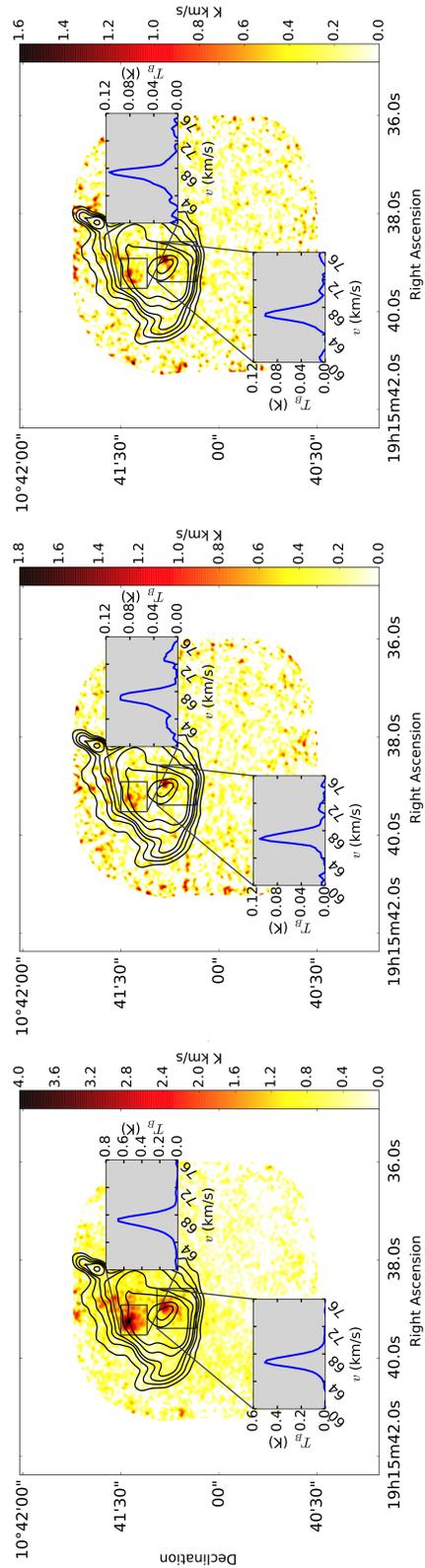
Figure 8.11: H₂CO emission from the IRAS 19132+1035 region. The panels from *left to right* display the H₂CO ($J = 3_{0,3} - 2_{0,2}$), H₂CO ($J = 3_{2,1} - 2_{2,0}$), and H₂CO ($J = 3_{2,2} - 2_{2,1}$), integrated intensity maps. The contours in all the panels are the VLA radio frequency contours; levels of 0.2, 0.3, 0.4, 0.5, 0.75, 1, 2, and 3 mJy bm⁻¹ (see Figure 8.2). The colour bars indicate the integrated intensity in units of K km s⁻¹. Inset panels show spectra of each line in the brightest emission zones (marked by the black boxes). A lack of H₂CO emission within, and at the base of, the non-thermal jet feature indicates the absence of hot molecular gas, when compared to the surrounding zones.

303
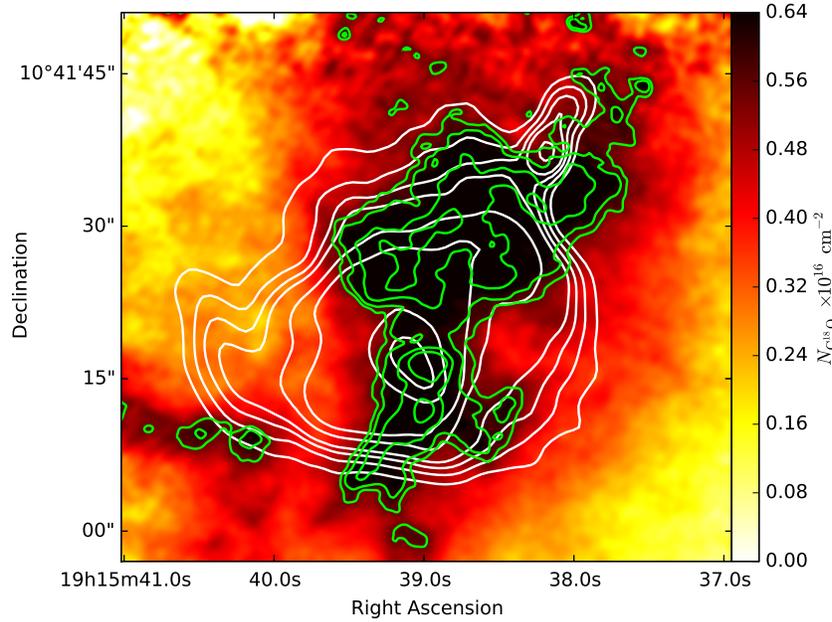
Figure 8.12: C^{18}O column density map of the IRAS 19132+1035 region. The colour bar represents the C^{18}O column density in units of 10^{16} cm^{-2}. The green contours indicate regions with the highest column densities, at levels of 5.5, 6.0, 7.0, and 8.0 $\times 10^{15}$ cm^{-2}. The white contours represent the VLA radio continuum contours; levels of 0.2, 0.3, 0.4, 0.5, 0.75, 1, 2, and 3 mJy bm^{-1} (see Figure 8.2). These data should represent the column densities of H$_2$ after scaling the map values by a factor of 1.5×10^6. Molecular gas with the highest column densities appears to hug the jet feature, consistent with the presence of a jet-blown cavity in this region.

8.4.5 Column densities

To accurately map the column density of the molecular gas in the IRAS 19132+1035 region, we use the C^{18}O line emission. A detailed derivation of this column density is provided in Appendix 8.7.2. Figure 8.12 shows the C^{18}O column density map of the IRAS 19132+1035 region. This column density should give a good indication of where the majority of the gas mass is located in the region. Similar to what is observed in the CO integrated intensity maps (Figure 8.2 *bottom row*), most of the molecular gas coincides with the radio continuum feature. Additionally, the gas with highest column densities (indicated by the green contours) appears to surround and hug the linear jet feature, consistent with the gas building up along the edges of a potential jet-blown cavity in that

region.

We opt to calculate the H_2 surface density from the molecular emission, since the dust maps lack sufficient resolution to map the small-scale structure of the region. Assuming a fractional abundance of $^{12}CO/H_2 = 2 \times 10^{-4}$ and $^{16}O/^{18}O = 300$ for $R_{gal} = 6$ kpc (Wilson & Rood, 1994), yields a ratio of $H_2/C^{18}O = 1.5 \times 10^6$. The implied H_2 column densities of the molecular gas can be obtained by scaling the values in Figure 8.12 by this factor.

8.5   Discussion

8.5.1   Evidence for a jet-ISM interaction

In this work, we have presented extensive new data tracing the molecular line emission and mapping the ISM conditions across the IRAS 19132+1035 region. These data provide multiple lines of new evidence supporting an association between the IRAS 19132+1035 region and the GRS 1915+105 jet. In particular, our key new evidence for a jet-ISM interaction in the IRAS 19132+1035 zone are as follows:

1. CO kinematics indicate the gas in the region covered by the radio jet feature is being hit from behind (in line with the direction of the GRS 1915+105 jet), resulting in the creation of a jet-blown cavity in the molecular gas at this location (see §8.4.2 and Figure 8.7).

2. CO line ratios indicate the presence of over-dense gas at the apex of the suspected jet impact zone (i.e. the base of the radio jet feature), consistent with gas being excavated to form a cavity in the radio jet feature region (see §8.4.2 and Figure 8.6).

3. Regions with the highest CO column densities, tracing where most of the gas mass is located, surround and hug the radio jet feature. This

morphology likely traces out the extent of the jet-blown cavity in this region (see §8.4.5 and Figure 8.12).

4. CO lines display asymmetric, double peaked line profiles, in regions located at the base of, and within the radio jet feature. This indicates the presence of multiple gas components, at different velocities, consistent with a collision between the jet and molecular gas in these regions (see §8.4.2, Figure 8.5, and Table 8.4).

5. The lack of H_2CO emission indicates the absence of hot molecular gas in the suspected cavity region (where the molecular gas may have been excavated by the jet in this region; see §8.4.4, Figures 8.11 & 8.10, and Table 8.6).

6. Shock-tracing emission (SiO) is detected in a compact region near the jet impact zone, potentially indicating a weak shock in the molecular gas at this site (see §8.4.3, Figure 8.9, and Table 8.5).

While all of this new evidence supports a jet-ISM interaction in the IRAS 19132+1035 region, we find that this interaction occurs on much smaller scales than postulated by previous works, and does not dominantly power or shape the whole IRAS 19132+1035 region. Rather, our data suggests that in the IRAS 19132+1035 region, we are observing a weaker long-range jet-ISM interaction with a molecular cloud that also hosts a high-mass star forming region. Figure 8.13 displays an update on the Kaiser et al. (2004) schematic model (shown in Figure 8.1 *right*) of the IRAS 19132+1035 region, based on our new data, where we label key morphological and emission features.
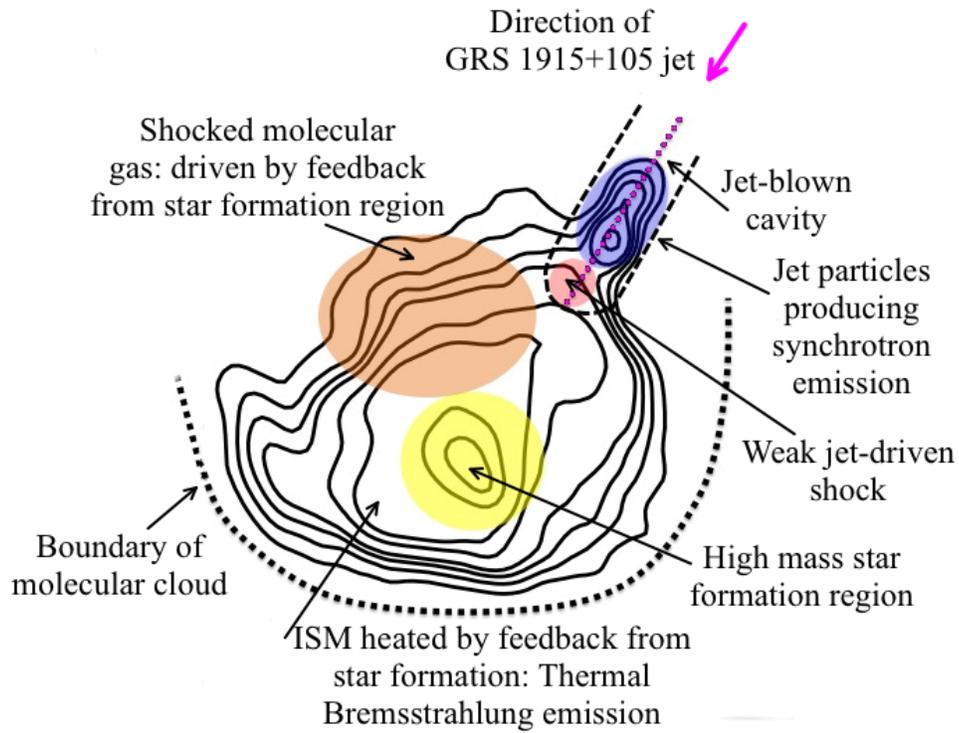
Figure 8.13: Schematic of the IRAS 19132+1035 region, mapping out the key morphological and emission features detected in our ALMA data. All regions of interest are colour coded and labelled, and the magenta dotted line indicates the center of the jet-blown cavity. The contours represent the VLA radio continuum contours; levels of 0.2, 0.3, 0.4, 0.5, 0.75, 1, 2, and 3 mJy bm^{-1} (see Figure 8.2). Our high resolution ALMA data has allowed us to distinguish between two different feedback mechanisms powering the IRAS 19132+1035 region; the BHXB jet and a high mass star formation region.

8.5.2 Star formation feedback in the IRAS 19132+1035 region

To estimate the influence that star formation may have had on shaping and powering the IRAS 19132+1035 region, we consider the thermal component of the radio continuum to estimate the properties of a young cluster that would be required to explain the thermal continuum. We calculate the emission measure (EM) of the region to be 1.3×10^5 pc cm^{-6} (Wilson et al., 2013), based on the peak brightness temperature of the radio emission at $\nu = 5$ GHz ($T_{\mathrm{B}} = 8.3$ K; from Table 8.2). The projected area of the radio continuum emission region is $\Omega = 1200$ arcsec^2. If we assume a spherical geometry with $R = (\Omega D^2/\pi)^{1/2}$ at a distance of $D = 8.6$ kpc, the radius of the region is $R = 0.81$ pc, and the implied density for a uniform gas is $n_e = 290$ cm^{-3}. Assuming a steady state, a pure-hydrogen nebula, and Case B recombination (using $\alpha_B = 4 \times 10^{-13}$ cm^3 s^{-1}; $T_e = 1.2 \times 10^4$ K; Kaiser et al. 2004), we require an ionizing photon budget of $Q \sim (\frac{4\pi}{3} R^3 \alpha_B n_e^2) \sim 2 \times 10^{48}$ s^{-1}, which corresponds roughly to the output of a single O8.5V star with mass $M \sim 19\ M_\odot$ (Martins et al., 2005).

Given the coarseness of the estimate, this conclusion is consistent with the analysis of Kraemer et al. (2003), who analysed the mid-infrared and 3.6 cm radio continuum fluxes, and determined that the driving source for this object is a B0V star (G45.19 in their study). Assuming a Kroupa (2001) IMF, this implies the region hosts a small cluster with a total mass of $M_\star \sim 200\ M_\odot$, with some uncertainty owing to the stochastic sampling of the IMF. The mass of the molecular gas, as seen in the entire ALMA imaging field is $\sim 500\ M_\odot$, which implies a typical star formation efficiency of $\epsilon_{\mathrm{SF}} = M_\star/(M_{\mathrm{gas}} + M_\star) = 0.3$ (cf., Lee et al., 2016).

Using the same radius for the infrared emission and the dust properties derived in Table 8.3, we calculate the infrared luminosity of the associated

cluster to be $L \sim 2.8 \times 10^4$ $L_\odot$. If the cluster luminosity is dominated by the O star ($L \sim 7 \times 10^4$ $L_\odot$ Martins et al., 2005), this implies $< 40\%$ of the luminous output is re-radiated in the infrared. This finding is consistent with the "bubble" morphology seen in the infrared imaging (Figure 8.14). The size of the larger blowout is ~ 2 pc, all consistent with a young cluster driving a blister H$_{\mathrm{II}}$ region (Gendelev & Krumholz, 2012) expanding at the sound speed in $T \sim 10^4$ K gas, giving an age of $t \sim 0.2$ Myr. If we take $E_{\mathrm{SF}} = L_{\mathrm{IR}}t$ as the amount of energy deposited as feedback by star formation in the region, we find $E_{\mathrm{SF}} = 7 \times 10^{50}$ erg. The remainder of the energy is assumed to leave the region as optical/UV light.

In summary, IRAS 19132+1035 is small molecular cloud ($M \sim 500$ $M_\odot$) that hosts a young, medium mass stellar cluster with $M \sim 200$ $M_\odot$ and age $t \sim 0.2$ Myr. A single O9 star is sufficient to explain (1) the total infrared luminosity in this region, (2) the thermal radio continuum, and (3) the blowout morphology seen in the mid- and far-infrared imaging. Such a young region would also be sufficient to explain the weak SiO emission and the gas heating seen in the H$_2$CO emission. Given the apparent youth of the region, the non-thermal emission in the radio continuum is difficult to explain through supernovae and thus represents good evidence for the presence of the jet interaction in the field of view.

8.5.3 Jet induced star formation

Given that we have shown compelling evidence that the GRS 1915+105 jet is colliding with a molecular cloud in IRAS 10132+1035, which houses a high mass star forming region, we must consider the possibility that the jet has triggered the star formation process in this region. Previous studies of the IRAS 19132+1035 region have suggested that, given the compact nature of the molecular gas in the region, the jet may not only have triggered star formation in the region (via compression of the molecular gas), but may also have in-
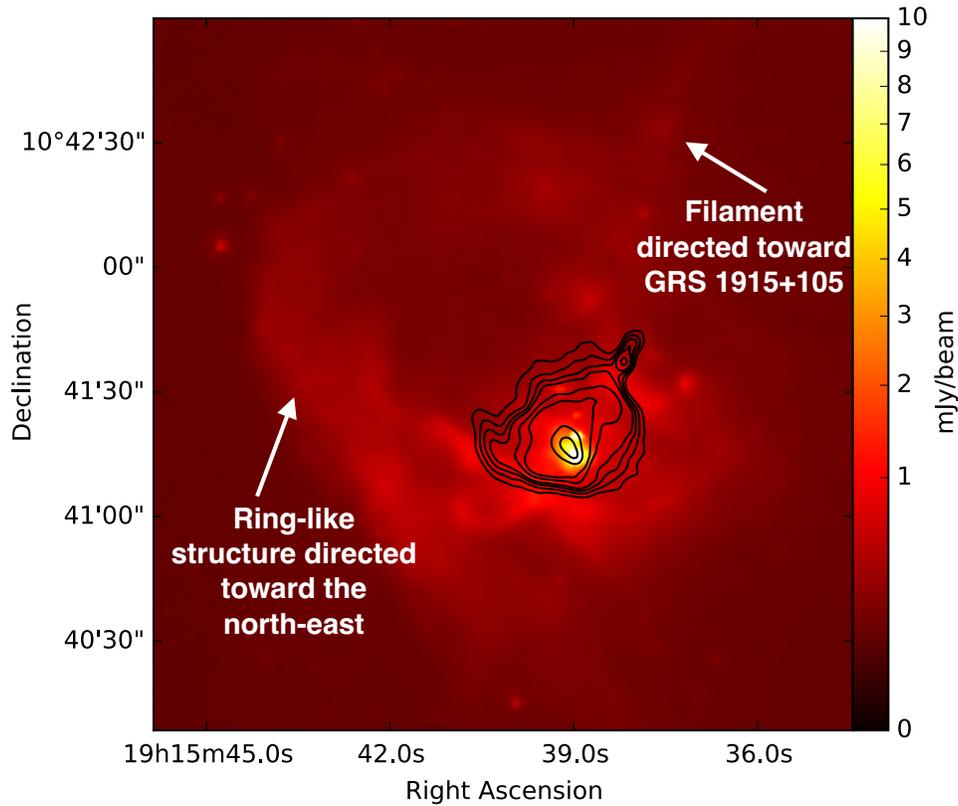
Figure 8.14: . Zoomed out version of the $8\mu m$ Spitzer GLIMPSE continuum image displayed in the *bottom left* panel of Figure 8.4, where we have labeled the fainter, diffuse emission features observed around IRAS 19132+1035. The contours represent the VLA radio continuum contours; levels of 0.2, 0.3, 0.4, 0.5, 0.75, 1, 2, and 3 mJy bm^{-1} (see Figure 8.2). The colour bar displays the $8\mu m$ flux density in units of mJy bm^{-1}. The morphology of the diffuse dust emission in this infrared map is consistent with a young cluster in the region driving a blister HII region expanding at the sound speed.

duced the formation of the original molecular cloud by gradually collecting the interstellar gas in its path (Chaty et al., 2001; Mirabel et al., 2015). In order for either of these processes to occur, the GRS 1915+105 jet must have been active for much longer than we have been able to observe it (i.e. prior to 1992). For example, the approximate timescale for a molecular cloud to collapse and begin to form stars is on the order of a few Myr (Cazaux & Tielens, 2002).

While the age of GRS 1915+105 (and in turn the timescale of past jet activity) is not well constrained, there are many observable clues that suggest GRS 1915+105 may in fact be a very old stellar system. Given measured proper motions of the jet ejecta launched from GRS 1915+105 ($\mu_{\mathrm{app}} = 17.6\,\mathrm{mas\,day}^{-1}$, $\mu_{\mathrm{rec}} = 9.0\,\mathrm{mas\,day}^{-1}$; Mirabel & Rodríguez 1994), and the known inclination angle ($i = 60 \pm 5°$; Reid et al. 2014a), we estimate the true velocity of the jet ejecta to be

$$\beta\cos(i) = \frac{\mu_{\mathrm{app}} - \mu_{\mathrm{rec}}}{\mu_{\mathrm{app}} + \mu_{\mathrm{rec}}} = 0.94c. \qquad (8.2)$$

When combined with the 42.5 pc separation between GRS 1915+105 and IRAS 19132+1035 (i.e. 17 arcmin at 8.6 kpc), this implies a travel time of the jet between the two of > 150 years (allowing for the potential of a decelerating jet), which supports the hypothesis that the source must have been active prior to 1992. Additionally, the donor star in GRS 1915+105 is known to be a red giant undergoing Roche lobe overflow, meaning the source has likely been actively accreting (and producing a jet) on a timescale at least as long as the time for the donor star to cross the Hertzsprung gap and remain in the giant branch ($\sim 10^2 - 10^3$ years; Mirabel et al. 2015). Further, GRS 1915+105 is one of a handful of systems with measured 3-dimensional velocities (Miller-Jones, 2014). The low measured peculiar velocity of GRS 1915+105 ($22 \pm 24\,\mathrm{km\,s}^{-1}$)[9] indicates that this system likely did not receive a large natal kick at birth (i.e. no supernova explosion), but rather may have obtained its current velocity by

---

[9]As this measurement is consistent with zero velocity (within the errors), it cannot be used to derive an age estimate.

galactic diffusion (random gravitational perturbations due to collisions with the spiral arms and giant molecular clouds; Reid et al. 2014a). In this case, GRS 1915+105 could have orbited the Galaxy several times, and be as old as a few Gyr (Dhawan et al., 2007; Mirabel, 2017).

Even though the predicted age of GRS 1915+105 may be consistent with the timescales for triggered star formation to occur, the thermal dust morphology provides hints that this may not be the case for IRAS 19132+1035. In particular, a ring-like structure directed towards the north-east can be seen in the $8\mu m$ Spitzer GLIMPSE continuum image of the region surrounding IRAS 19132+1035 (Figure 8.14). The presence of this structure suggests that the star formation in the IRAS 19132+1035 zone could have been triggered by another bout of star formation to the north-east, rather than the jet from GRS 1915+105, which is observed to come from the north-west direction. However, we note that Mirabel et al. (2015) identify a faint filamentary structure in a $160\mu m$ image of the same field (also visible in our $8\mu m$ image), pointing in the direction of GRS 1915+105; these authors suggest this structure could indicate the BHXB jet played at least a minor role in shaping the molecular cloud and governing the star formation activity in this region.

8.5.4 Constraints on jet properties

A common technique in AGN jet studies involves using the interaction sites between the jets and the surrounding medium (i.e. the large-scale jet-blown radio lobes) as accurate calorimeters, to estimate the jets' *power × lifetime* products (e.g. Burbidge 1959; Castor et al. 1975; Kaiser & Alexander 1997; McNamara & Nulsen 2007). This technique can also be applied to jet-ISM interaction sites near Galactic BHXBs in the cases where a jet-blown bubble or cavity is detected (e.g. Cyg X-1; Gallo et al. 2005b; Russell et al. 2007; Sell et al. 2015).

We follow the self-similar fluid model of Kaiser & Alexander (1997), which

balances the ram pressure of the shocked ISM with the interior pressure exerted by the jet-blown cavity (see Figure 8.13 for a schematic showing the cavity in IRAS 19132+1035, where non-thermal synchrotron emission in the cavity is coloured blue). Assuming the jet direction remains constant (i.e. the jet is not precessing), the jet is colliding with a medium of density ρ_0, the power being transported by the jets (Q_{jet}; averaged over the lifetime of the jets), solely dependent on the properties of the ISM at the interaction site, is represented as,

$$Q_{\mathrm{jet}} = \left(\frac{5}{3}\right)^3 \frac{\rho_0}{C_1^5} L_j^2 v^3 \tag{8.3}$$

where L_j represents the length of the jet as a function of time (t), C_1 is a constant dependent on the adiabatic indices of the material in the jet, cavity, and external medium (Γ_j, Γ_x, Γ_c) and the jet opening angle (ϕ), and v represents the velocity of the shocked gas at the interaction site (colored red in Figure 8.13). The full derivation of this jet power expression is provided in Appendix 8.7.3.

Given the angular distance of IRAS 19132+1035 from GRS 1915+105 (17 arcmin; see Figure 8.1 *left*), the length of the jet, L_j, can be expressed as (Kaiser et al., 2004),

$$L_j = 1.52 \times 10^{19} \frac{D}{\sin i} \quad \mathrm{cm}, \tag{8.4}$$

where D represents the distance to the source in kpc, and i represents the inclination angle of the jet to our line of sight.

As the source geometry is unknown, to estimate the average density of the medium the jet is colliding with in IRAS 19132+1035, we follow Kaiser et al. (2004), and model the region as a sphere of diameter 36.5 arcsec (centered at coordinates 19:15:39.087, +10:41:22.652, to cover the extent of the radio continuum feature; see Figures 8.1 and 8.13), at the distance to the source.

The volume (in units of cm^{-3}) of this spherical region is represented as

$$V_{\text{sphere}} = 8.53 \times 10^{52} D^3 f, \tag{8.5}$$

where f represents a volume filling factor ($f << 1$ would indicate a hollow shell). Using our H$_2$ column density map (see §8.4.5 and Appendix 8.7.2 for details), we estimate the gas mass[10] in this spherical region to be 226 $M_\odot$. These measurements yield an estimate of the average density in the region of

$$\rho_0 = 2.65 \times 10^{-18} D^{-3} f^{-1} \quad \text{g cm}^{-3}. \tag{8.6}$$

Through combining these expressions, we can place constraints on the average power carried by the BHXB jet over its lifetime. We performed Monte Carlo simulations, sampling from the known distributions of distance ($D = 8.6^{+2.0}_{-1.6}$ kpc), inclination ($i = 60 \pm 5°$), opening angle (we use a uniform distribution between 0 and 4°, as Miller-Jones et al. 2006 report opening angle constraints of $\phi < 4°$), and shocked gas velocity ($v = 1.01^{+0.24}_{-0.18}$ km s^{-1}; equivalent to the FWHM of the northernmost SiO detection, coloured red in Figure 8.13), and setting $f = 0.1$ (a reasonable assumption given that the jet is displacing molecular gas), and $\Gamma_j = \Gamma_x = \Gamma_c = 5/3$. This procedure yields an estimate of the energy carried in the GRS 1915+105 jet of $(6.7^{+6.4}_{-6.6}) \times 10^{47}$ erg, over a lifetime of $29.5^{+8.6}_{-8.7}$ Myr, resulting in a total time-averaged jet power of $(8.4^{+7.7}_{-8.1}) \times 10^{32}$ erg s^{-1}.

Our GRS 1915+105 jet power estimate lies below the distribution of estimated jet powers in the BHXB population ($10^{36} - 10^{39}$ erg s^{-1}; Curran et al. 2014), and is orders of magnitude lower than estimated from the intensity/duration

---

[10]The mass reported here is estimated from the molecular gas contained by the radio continuum feature, while the mass reported in §8.5.2 is estimated from the molecular gas contained in the whole ALMA field of view. We use the former for these calculations, as this estimate is more representative of the gas mass interacting with, and being displaced by, the BHXB jet.

of the radio flares that accompany transient jet ejections launched by GRS 1915+105 (e.g.,10^{39} erg s^{-1}; Fender et al. 1999a). This discrepancy in estimated jet power could be a result of simplifying assumptions used in both methods leading to over/under estimations of the jet power in either case. For example, in our calorimetric method we have assumed a constant jet power over the source's lifetime. However, as GRS 1915+105 was only discovered when it entered outburst in 1992, the source must have spent at least some of its pre-1992 lifetime in a significantly less active quiescent state (presumably launching less powerful jets; Plotkin et al. 2015). Further, in addition to transient ejection events (Mirabel & Rodríguez, 1994), GRS 1915+105 has also been observed to undergo extended periods in which a compact jet is present instead (Dhawan et al., 2000). As these different types of jets are thought to produce different radiative energies, travel at different bulk speeds (resulting in varying kinetic energies), and be active over different timescales (Fender et al., 2004a; Fender, 2006; Russell et al., 2013a), it is reasonable to expect that the power output from the jets does not remain constant in this source.

We have also assumed a constant external density. Given the ~ 40 pc distance between GRS 1915+105 and IRAS 19132+1035, this is unlikely to be the case. While there is no strong evidence that the transient ejections launched from GRS 1915+105 are decelerating on large (arcsec) scales (presumably due to a collision with a denser medium), deceleration on smaller scales (< 70 mas; Miller-Jones et al. 2007a) cannot be ruled out. This in turn could indicate the presence of a denser medium closer to the source, violating this second assumption. The unknown geometry of IRAS 19132+1035 is also a source of uncertainty in our calculations. Equally, estimates of jet power using the radio flaring counterparts to transient ejections are known to fold in many assumptions about unknown jet properties (i.e. composition, efficiency, equipartition between jet particles and the magnetic field), which could contribute to over/under estimations of the jet power in this case. Further, given that the

transient jet events are rare, and relatively short lived when compared to the compact jets in this source, their high jet power is not likely representative of the average jet power over the source's lifetime.

On the other hand, given the uncertainty regarding outburst duration and jet duty cycle in GRS 1915+105, our lower time-averaged jet power measurement may instead reflect a jet that carries a much higher energy than we have estimated, but has only been turned on for a relatively small fraction of its total lifetime (rather than a jet with a constant, lower power output). For instance, the discrepancy between our jet power and other estimates suggests that the jet has only been on (i.e. GRS 1915+105 has roughly been in outburst) for a fraction of 10^{-3}–10^{-6} of its total lifetime.

Further, it has been postulated that the GRS 1915+105 jet may be precessing (Rodriguez & Mirabel, 1999; Rushton et al., 2010), which could result in the energy carried by the jet being smeared around a conical path, with only a fraction of the arc traced out by the precessing jet depositing energy into the molecular cloud. Assuming the precessing jet traces out a cone, with opening angle of ~ 10 degrees (Rodriguez & Mirabel, 1999) and edge length of the distance between the sources (42.5 pc), then the power in the jet would be larger by a factor of $\frac{2\pi R_{\text{cone}}}{\text{arclength}} \sim 150$ (for $R_{\text{cone}} = 7$ pc and arclength $= 0.3$ pc), resulting in $Q_{\text{jet,precess}} \sim 1 \times 10^{35}\,\text{erg s}^{-1}$.

Moreover, until this point, we have only considered the case where the GRS 1915+105 jet is always pointed in the direction of IRAS 19132+1035. In fact, it is unlikely that the BHXB source and the IRAS 19132+1035 source would be lined up for the ~ 30 Myr jet lifetime we have estimated above. If the relative velocities between the molecular cloud in IRAS 19132+1035 and the BHXB are different, the jet could be slicing through the molecular cloud for a limited period of time, only depositing energy into the molecular cloud during traversal. We briefly consider this case by exploring a simple model, where we assume an elastic collision between the jet and molecular cloud. In this case,

the power in the jet could be estimated by the kinetic energy of the displaced mass, divided by the interaction time, according to

$$Q_{\text{jet,slice}} = \frac{\frac{1}{2}\delta M \delta v^2}{\left(\frac{R_{\text{cloud}}}{\Delta V}\right)}, \tag{8.7}$$

where δM represents displaced mass, δv represents the velocity of the displaced gas, and ΔV represents the magnitude of the difference between the velocity vectors of the BHXB and molecular cloud. Substituting in values calculated above, $\delta M = 226\,M_\odot$, $\delta v = 1\,\text{km s}^{-1}$, $R_{\text{cloud}} = 2$ pc, and $\Delta V = 22\,\text{km s}^{-1}$ (equivalent to the BHXB's peculiar velocity[11], where we assume the molecular cloud undergoes pure Galactic rotation), yields $Q_{\text{jet,slice}} \sim 4 \times 10^{32}\,\text{erg s}^{-1}$. This jet power estimate is on par with that estimated from the calorimetric method above.

Overall, from the above calculations, it is clear that the jet is depositing relatively very little energy into the molecular cloud ($\sim 10^{47}$ erg), especially when compared to the feedback from the star formation process ($\sim 10^{50}$ erg), and thus does not dominantly power the IRAS 19132+1035 region.

Lastly, given the extent of the jet-blown cavity detected in the molecular gas (8 arcsec at 8.6 kpc, equivalent to 0.3 pc) in IRAS 19132+1035, we can also place an estimate on the GRS 1915+105 jet opening angle where,

$$\phi = \arctan(0.3\,\text{pc}/42.5\,\text{pc}) = 0.4°. \tag{8.8}$$

This opening angle estimate is consitent with the upper limit of $< 4°$, reported in Miller-Jones et al. (2006).

---

[11]We note that given the large uncertainties on the peculiar velocity measurement, it is also consistent with zero (22+/-24 km/s).

8.5.5 Comparison to other known jet-ISM interaction zones

Given our uncertainty in how BHXB jet-ISM interactions are likely to manifest in the surrounding ISM, it is of interest to compare the features of other interaction sites with our observations of IRAS 19132+1035. Prior to this work, two confirmed jet-ISM interaction sites near BHXBs in our Galaxy, which show both a jet-blown bubble/cavity and evidence for shock excited gas, had been identified; SS 433 and Cyg X-1. Additionally, there are four other BHXBs, in which a jet-ISM interaction has been invoked to explain atypical radio and X-ray emission properties, such as downstream radio/X-ray hot-spots and decelerating jet components; XTE J1550-564, H1743-322, XTE J1752-223, XTE J1908+094.

SS 433 is known to launch precessing jets (Margon, 1984; Hjellming & Johnson, 1981; Fabrika, 2004), and is located inside the large-scale W50 radio nebula (192×96 pc at 5.5 kpc distance). This nebula displays a unique "sea-shell" morphology, consisting of a central spherical component, and two oppositely directed, elongated "ears", believed to have been inflated by the jets (Dubner et al., 1998). The eastern ear shows a helical pattern within the radio continuum morphology, thought to mirror the large scale precession of the jets. The western ear (which is believed to be located in a higher density medium) is smaller in scale, brighter at radio frequencies, and displays multiple hot-spots (Fuchs, 2002) that coincide with X-ray (Safi-Harb & Ogelman, 1997), infrared (Band, 1987; O'Neill et al., 2000), and sub-mm molecular emission (CO, HCO^+; Huang et al. 1983; Durouchoux et al. 2000; Chaty et al. 2001). These hot-spots are thought to mark sites where the precessing jet collides with the ambient medium, and the dust and gas are being heated by a shock driven jet-ISM interaction (Fuchs, 2002). Dubner et al. (1998) estimated the jets of SS 433 inject an energy of $\sim 10^{51}$ erg, over a lifetime of $\sim 10^4$ years, into the surrounding

nebula, resulting in an estimated total jet power of $\sim 10^{39}\,\mathrm{erg\,s^{-1}}$.

Cyg X-1 displays persistent, radio emitting jets (Stirling et al., 2001) that are thought to be propagating through the tail end of a dense H$\textsc{ii}$ region (Russell et al., 2007; Sell et al., 2015). Deep radio-frequency observations of the field surrounding Cyg X-1 revealed a shell-like structure ~ 5 pc in diameter, aligned with the jet axis of Cyg X-1 (Gallo et al., 2005b). This shell structure was also observed in optical line emission (Hα, Hβ, [O$\textsc{iii}$], [N$\textsc{ii}$], [S$\textsc{ii}$]; Russell et al. 2007; Sell et al. 2015), although no diffuse X-ray emission was detected in the region (Sell et al., 2015). To date, no molecular emission has been detected in or around the shell structure. Gallo et al. (2005b) interpreted this shell as a jet-blown bubble, containing thermal plasma, which formed as the result of a strong radiative shock created when the jet impacted the ISM. However, alternative explanations for the shell have been put forward, including a supernova remnant, and a shock wave driven by the strong stellar wind from the high mass companion star in Cyg X-1 (Sell et al., 2015). Gallo et al. (2005b) inferred that the jets of Cyg X-1 would need to carry a time-averaged power of $\sim 9 \times 10^{35} - 10^{37}\,\mathrm{erg\,s^{-1}}$, over a lifetime of $\sim 0.02 - 0.32$ Myr, to create and maintain the jet-blown bubble structure in the surrounding medium.

XTE J1550-564, H1743-322, XTE J1752-223, and XTE J1908+094 are transient BHXBs, which occasionally enter into bright outburst periods, typically lasting on the order of months. During these outbursts, all of these systems have been observed to launch transient jet ejecta. Following these ejection events, compact radio and X-ray hot-spots, aligned with the jet axis, and located at distances ranging from hundreds of mas up to arcseconds from the central source (sub-parsec physical distance scales), have been observed in the fields surrounding these systems (Corbel et al., 2005, 2002; Kaaret et al., 2003; Yang et al., 2010; Miller-Jones et al., 2011; Yang et al., 2011; Ratti et al., 2012; Rushton et al., 2017). Lateral expansion was detected in the radio hot spots of XTE J1752-223 and XTE J1908+094 (Yang et al., 2010; Rushton et al., 2017).

These features have been interpreted as working surfaces, where the jet ejecta collide with the surrounding ISM, creating a moving shock front. Such features are similar to those observed in the neutron star system, Sco X-1 (Fomalont et al., 2001b,a). Further, deceleration detected in the bulk motion of jet ejecta components launched from XTE J1550-564, H1743-322, and XTE J1752-223, on timescales of tens to hundreds of days, provides additional evidence in favor of the jet colliding with a dense medium surrounding these BHXBs (Corbel et al., 2005, 2002; Yang et al., 2010; Miller-Jones et al., 2011). In XTE J1550-564 and H1743-322, the two hot spot components (located on both sides of the BHXB) were initially detected at the same angular distance from the central source. This may indicate that the jets are propagating through an evacuated cavity (carved out during a previous outburst by jets or accretion disc winds), and become observable only when they collide with a denser phase of the ISM at the edge of the cavity (Corbel et al., 2005; Hao & Zhang, 2009). On the other hand, in XTE J1752-223 and XTE J1908+094, asymmetries between the two detected hot spots (i.e. differing brightness, expansion rate, and proper motions) have been attributed to varying ISM densities.

In the majority of the interaction cases, there is evidence that the BHXB jet carves out some form of cavity/bubble in the intervening medium as it propagates away from the central BHXB. An interaction only becomes observable when the jet collides with a much denser portion of the surrounding medium (e.g. HII region, radio nebula, or molecular cloud). However, the morphological and emission features at the jet impact sites, as well as the distances traversed by the jet (sub-parsec to tens of parsecs) before an interaction occurs, vary greatly between the different cases. The wide jet-blown bubble of Cyg X-1 terminates in a high velocity ($\sim 200\,\mathrm{km\,s^{-1}}$), radiative bow shock located on parsec scales from the central source, SS 433 displays compact hot spots (located tens of parsecs from the central source) where the precessing jet collides with the nebular structure, the cavity we detected in IRAS 19132+1035 is nar-

row and terminates in a weak shock ($\sim 1\,\mathrm{km\,s^{-1}}$)[12] at a ~ 40 pc separation from the central source, and the transient systems all display compact hot spots (located < 1 pc from the central source) which appear only following jet ejection episodes. Additionally, the only sites that emit non-thermal synchrotron emission (characteristic of BHXB jets) are IRAS 19132+1035 and the transient systems, while the only cases where high-energy X-ray emission is detected are in the impact zones of SS 433 and the transient systems.

The observational differences between these interaction sites could be a result of the differing jet properties among the sources. For instance, the high-velocity bow shock near Cyg X-1 may be characteristic of the interaction of a steady, compact jet with the ISM, while the hot spot morphology may be more characteristic of jet ejections launched in SS 433 and the transient systems. The significantly higher power carried by the SS 433 jets (and presumably the short-lived ejections from the transient systems), in comparison to the GRS 1915+105 jets, may explain why only these jet impact sites emit in the high-energy X-ray bands. As well, the large-scale precession of the SS 433 jets results in the energy carried by the jet being deposited across multiple impact sites, rather than constantly bombarding a single site (as in IRAS 19132+1035). All of the transient sources, which undergo occasional, short-lived outbursts (XTE J1550-564, H1743-322, XTE J1752-223, and XTE J1908+094), display compact interaction sites much closer to the central BHXB than the persistently (or long-duration) out-bursting Cyg X-1, SS 433 and GRS 1915+105 systems (sub-parsec scales vs. tens of parsecs). Therefore, the timescale over which the jet is active and the duty cycle of the jets, may also govern the size scale and structure of interaction zones. For instance, we may expect parsec scale

---

[12]We note that a low shock velocity in this case may not be unexpected. Bromberg et al. 2011 derive an analytical expression for the propagation speed of a jet-driven bow-shock (Table 1 and Equation B3 in Bromberg et al. 2011). Substituting in our values for density, jet power, opening angle, and source age from §8.5.4, results in a propagation speed of $\sim 0.5\,\mathrm{km\,s^{-1}}$ (similar to our measured value). Therefore, it seems that finding a low shock velocity is plausible in this case.

cavities/bubbles to only form near persistently accreting systems.

Although, the differing ISM environments that the jets are propagating through (e.g. molecular gas in IRAS 19132+1035 vs atomic gas in Cyg X-1, different density gradients in the radio nebula surrounding SS 433 when compared to the HII region that the Cyg X-1 jet is propagating through) may also play a key role in the way that a jet-ISM interaction manifests itself in the surrounding medium. Further, contributions from other feedback mechanisms in these regions may explain the differences between interaction sites. For instance, given the possibility that the stellar wind may also be powering the Cyg X-1 bubble, the jet-driven shock velocity may have been overestimated, possibly explaining the stark contrast between the estimated shock velocity in the Cyg X-1 and IRAS 19132+1035 cases. A comparison between the observational characteristics of these interaction sites and numerical simulations of jet-ISM interactions in XBs (e.g., Perucho & Bosch-Ramon 2008; Bordas et al. 2009; Bosch-Ramon et al. 2011) could help disentangle the complex processes that are driving such interactions. Performing numerical simulations of the jet-ISM interaction in IRAS 19132+1035 is beyond the scope of this work, but will be explored in future work.

So far we have only discussed interactions from black hole systems in our own Galaxy. However, several cases of ionized nebula surrounding ultra-luminous X-ray (ULX) sources (i.e., ULX bubbles[13]), have been detected in other nearby galaxies (e.g. Roberts et al. 2003; Feng & Kaaret 2008; Soria et al. 2010). These large-scale (> 100 pc) structures are thought to either be shock-ionized (e.g. NGC 7793 S26; Pakull et al. 2010), purely photo-ionized (e.g. NGC 5408 X-1; Grise et al. 2012), or a combination of the two, where shock-ionized and photo-

---

[13] Although we note that a number of these bubble structures have been detected around sources that show X-ray luminosity lower than typical ULXs (i.e., $L_{\mathrm{X}} < 1 \times 10^{39} \, \mathrm{erg \, s^{-1}}$). In these cases, it is likely that either the central X-rays are being obscured, or there has been a change in X-ray luminosity over time. An example of such a source is NGC 7793-S26 (Soria et al., 2010).

ionized gas co-exists in the bubble structures. In this last case, photo-ionization occurs from ionizing photons generated by the forward shock (e.g., M83 MQ1 Soria et al. 2014). The shock-ionized cases can be inflated by different types of outflows; a collimated jet (e.g. Holmberg II X-1; Cseh et al. 2014, NGC 7793 S26; Pakull et al. 2010, IC342 X-1; Cseh et al. 2012) or winds (e.g. NGC 1313 X-2; Grise et al. 2008). While the ULX bubbles are much larger in scale than most of the Galactic interaction zones, these ULX interactions display striking similarities to many Galactic cases, such as radio and X-ray hotspots characteristic of jet impact sites (similar to SS 433 and the transient systems; e.g., NGC 7793 S26), optically thin radio synchrotron emission (similar to IRAS 19132+1035; e.g., Holmberg II X-1), and optical line emission characteristic of shock excited gas (similar to Cyg X-1; e.g., M83 MQ1). Further, similar to the black hole systems in our own Galaxy, it appears as though the way in which an ULX interaction manifests is also highly dependent on the properties of the central source and the local environmental conditions.

8.5.6 Jet molecular cloud interaction probabilities

In this work we have shown that the jet launched from GRS 1915+105 is colliding with a molecular cloud in IRAS 19132+1035. As such, we wish to estimate the likelihood of detecting more jet molecular cloud collisions in our Galaxy. This interaction probability can be found by estimating the chance that a given BHXB jet is found within the volume where molecular clouds are formed in our Galaxy.

We begin by modelling a population of molecular clouds using the principal observation that molecular clouds have constant, average column density regardless of mass or radius; $\Sigma_0 \sim 10^2$ $M_\odot$ pc^{-2} (e.g. Solomon et al. 1987; Heyer et al. 2009). The mass distribution of this population will be expressed as a power law distribution with a truncation at the upper mass end $M_u = 10^6$ $M_\odot$ (Colombo et al., in preparation). Assuming that clouds be-

low a mass of $M_l = 10^2\ M_\odot$ are diffuse and will not show significant jet-ISM interactions, the mass distribution can be represented as,

$$\frac{dN}{dM} = \frac{K}{M_u}\left(\frac{M}{M_u}\right)^\alpha.$$

$$(8.9)$$

Here $\alpha = -1.8$, and K is a normalization constant, such that the integrated mass of molecular clouds yields the total molecular mass in the Galaxy, $M_{H_2} = 10^9\ M_\odot$ (Wolfire et al., 2003). Integrating from M_l to M_u yields $K = 200$.

To transform this mass distribution to a radius distribution, we use the definition $M = \Sigma_0 \pi R^2$. Here Σ_0 is constant (as defined above) and R represents cloud radius, therefore we can write $dM = 2\pi\Sigma_0 R dR$. Substituting this result into Equation 8.9 yields,

$$\frac{dN}{dR} = \frac{2K}{R_u}\left(\frac{R}{R_u}\right)^\beta.$$

$$(8.10)$$

where the index $\beta = 2\alpha + 1 = -2.6$, Σ_0 is as above, $R_l = 0.5$ pc, and the radius of the cloud at the upper mass cutoff $R_u = 50$ pc.

We define the volume of the Galaxy in which there can be a jet-cloud interaction, as the volume inside a cloud or within a jet length, R_J, of a cloud, such that,

$$V_{\text{int}} = \int_{R_l}^{R_u} \frac{4\pi}{3}(R + R_J)^3 \frac{dN}{dR} dR.$$

$$(8.11)$$

Although, we note that this is an overestimate, since jets at a distances larger than the cloud radius can be oriented such that they will not hit the cloud. For compactness in the computation, we set $u \equiv R/R_u$ and $r = R_l/R_u$, yielding,

$$V_{\text{int}} = \frac{8\pi K}{3} \left[R_u^3 \left(\frac{u^{4+\beta}}{4+\beta} \bigg|_r^1 \right) + R_u^2 R_J \left(\frac{u^{3+\beta}}{3+\beta} \bigg|_r^1 \right) \right.$$
$$\left. + R_u^1 R_J^2 \left(\frac{u^{2+\beta}}{2+\beta} \bigg|_r^1 \right) + R_J^3 \left(\frac{u^{1+\beta}}{1+\beta} \bigg|_r^1 \right) \right] \tag{8.12}$$

We will take $R_J = 10$ pc. The first term corresponds to the volume within the clouds, for which an interaction is likely. Thus, we obtain a volume of molecular clouds in the Galaxy of 4×10^8 pc^3. The remaining three terms each contribute $\sim 2 \times 10^8$ pc^3, suggesting that, for this jet length, jet-ISM interactions for BHXBs outside clouds, are about as likely as interactions from within the clouds. The total volume in the interaction region is $V_{\text{int}} = 10^9$ pc^3.

Secondly, we calculate the volume over which molecular clouds are found in the Galaxy (V_{mol}). Using the model of Wolfire et al. (2003) as a basis, we approximate the molecular medium of the Galaxy as a hollow cylinder with inner radius of $\mathcal{R}_{\text{inner}} = 3$ kpc and $\mathcal{R}_{\text{outer}} = 10$ kpc and a (full) thickness of $h = 100$ pc. For this model, we find $V_{\text{mol}} = 3 \times 10^{10}$ pc^3.

Therefore, over the volume where molecular clouds are found, the filling fraction of the interaction volume is equivalent to, $V_{\text{int}}/V_{\text{mol}} = 3\%$. The interaction probability per X-ray binary where molecular clouds are found is then given by this filling fraction. Since most low-mass X-ray binaries, which accrete from older stars, are not co-located where molecular clouds are typically found, the above interaction probability likely applies only to low-mass X-ray binaries close to the Galactic plane ($|b| \lesssim 0.5°$; GRS 1915+105 is at $b = -0.2191°$). As high mass X-ray binaries by (typical) definition are accreting from an O or B star, they may be preferentially located near molecular clouds and have a higher interaction probability than 3%.

8.5.7 Distance considerations

Our detection of an interaction between the GRS 1915+105 jet and the IRAS 19132+1035 region can allow us to place further constraints on the distance to both objects. The distance to GRS 1915+105 has been estimated from model-independent geometric parallax measurements to be $8.6^{+2.0}_{-1.6}$ kpc, while the kinematic distance to IRAS 19132+1035 is estimated to be 6.0 ± 1.4 kpc. However, for a jet-ISM interaction to be occurring, both GRS 1915+105 and IRAS 19132+1035 must be located at the same distance (within ~ 40 pc). While it is difficult to pinpoint the true common distance, given that the current distance constraints are consistent within their one sigma errors, a common distance that lies between the two estimates could satisfy such a condition. Note that throughout this paper we have chosen to use the GRS 1915+105 parallax distance in all our calculations as it is model-independent (see Reid et al. 2014b for a comparison of kinematic and parallax distances). However, if the true distance is indeed closer, this affects our constraints on jet energetics and geometry, as well as the estimated peculiar velocity for GRS 1915+105. For example, assuming a common distance of 7 kpc, we estimate a slightly more energetic jet ($\sim 7.3 \times 10^{47}$ erg), with a shorter lifetime ($\sim$24 Myr), and larger opening angle ($\sim 0.5°$), as well as an increased peculiar velocity for GRS 1915+105 ($\sim 46\,\mathrm{km\,s^{-1}}$).

8.5.8 IRAS 19124+1106: the second candidate interaction zone near GRS 1915+105

In addition to IRAS 19132+1035, Rodríguez & Mirabel 1998 also identified another candidate interaction zone to the north of GRS 1915+105; IRAS 19124+1106 (see Figure 8.1). This second candidate zone is located at a remarkably similar distance from the central BHXB as IRAS 19132+1035, and is also aligned with the position angle of the jet from GRS 1915+105.

IRAS 19124+1106 displays a flat radio spectrum, consistent with thermal Bremsstralung emission, and a cometary radio continuum morphology, commonly observed from H$_{\text{II}}$ regions. No non-thermal radio emission features are observed in IRAS 19124+1106. Strong molecular emission from the ^{12}CO (J=2-1), ^{13}CO (J=2-1), H^{13}CO$^+$ (J=1-0), and CS (J=2-1) transitions were observed in this region, while no SiO transitions were detected (Chaty et al., 2001). Given the similarities between the emission properties of IRAS 19124+1106 and the star forming zone in IRAS 19132+1035, it seems plausible that IRAS 19124+1106 also contains a star forming molecular cloud. However, the lack of non-thermal radio emission features, as well as the low likelihood that both the approaching and receding components of the GRS 1915+105 jet happen to line up with a star forming molecular cloud, suggests a low probability that IRAS 19124+1106 is also the site of an interaction. As we have shown that sensitive, high resolution observations were needed to observe the jet interaction in IRAS 19132+1035, the same treatment is likely required to draw any further conclusions about the true nature of the IRAS 19124+1106 region.

8.5.9 Distinguishing between BHXB jet driven feedback and high mass star formation

In this work, we have shown that there are two main sources of feedback powering the IRAS 19132+1035 region; the BHXB jet and high-mass star formation. This suggests that the star formation process may act as a contaminant when probing other BHXB jet-ISM interaction sites in our Galaxy. In particular, as star formation is also known to drive fast outflows, which are likely to generate shocks upon impact with the surrounding gas, it may be difficult to distinguish between BHXB jet-driven feedback and high-mass star formation in terms of the signatures they leave behind in the molecular gas. When comparing molecular emission originating from the BHXB jet-driven feedback zone

to that originating from the star formation feedback zone in IRAS 19132+1035, we find that while the SiO shock-tracing emission typically showed similar peak intensities, the emission in the BHXB jet driven feedback zone displayed much narrower line widths, over a more compact emission region. While this could suggest that these properties reflect differences between jet-driven and star formation-driven feedback zones, we require a larger sample of observations of multiple systems to fully understand the differences (if any) that exist between the molecular line properties of these different feedback zones.

8.6 Summary

In this paper, we present the results of our ALMA observations of IRAS 19132+1035. This region was first identified by Rodríguez & Mirabel (1998) as a potential interaction zone between the jet launched from the BHXB GRS 1915+105 and the surrounding ISM, based on its location and unique radio continuum morphology. However, despite several follow-up observing campaigns, no definitive evidence had been found to confirm this hypothesis, with compelling arguments on either side.

As molecular lines are excellent diagnostics of shock energetics and ISM excitation, we used these ALMA observations to map the molecular line emission in the IRAS 19132+1035 region, aiming to resolve this long-standing question. We detect emission from the ^{12}CO [J=2-1], ^{13}CO [$\nu = 0$, J=2-1], C^{18}O [J=2-1], H$_2$CO [$J = 3_{0,3} - 2_{0,2}$], H$_2$CO [$J = 3_{2,2} - 2_{2,1}$], H$_2$CO [$J = 3_{2,1} - 2_{2,0}$], SiO [$\nu = 0$, J=5-4], CH$_3$OH [$J = 4_{2,2} - 3_{1,2}$], and CS [$\nu = 0$, J=5-4] molecular lines.

Given this molecular emission, we identify several new lines of compelling evidence supporting a connection between the IRAS 19132+1035 region and the GRS 1915+105 jet. In particular, the morphological, spectral, and kinematic properties of the detected molecular emission indicate the presence of a jet-blown cavity and weak jet-driven shock at the impact site. However, contrary

to the scenario put forward by previous work, we find that feedback from the BHXB jet does not dominantly power or shape the IRAS 19132+1035 region. Rather, a high mass star formation region, housed inside a molecular cloud, is heating the dust and gas in the region, and the jet appears to be simply colliding with this molecular cloud. All the thermal radio and infrared emission from the IRAS 19132+1035 region can be explained by a young, medium mass ($\sim 200 M_\odot$) stellar cluster with an age of 0.2 Myr, where it is unlikely that the BHXB jet significantly contributed to shaping the molecular cloud and/or triggering the star formation process in the IRAS 19132+1035 region.

Through considering the properties of the detected cavity and displaced molecular gas in the region, we estimate properties of the GRS 1915+105 jets. Following the self-similar fluid model of Kaiser & Alexander (1997), we used the detected cavity as a calorimeter to calculate the energy carried in the GRS 1915+105 jet of $(6.7^{+6.4}_{-6.6}) \times 10^{47}$ erg, over a lifetime of $29.5^{+8.6}_{-8.7}$ Myr, resulting in a total time-averaged jet power of $(8.4^{+7.7}_{-8.1}) \times 10^{32}$ erg s^{-1} (although this may be up to a factor of 150 higher if the GRS 1915+105 jet is undergoing small-scale precession). These estimates reiterate that the BHXB jet is depositing relatively very little energy into the molecular cloud, when compared to feedback from the star formation process ($\sim 10^{50}$ erg).

Upon comparing the characteristics of the IRAS 19132+1035 interaction zone with other jet-ISM interaction sites in our Galaxy and other nearby galaxies, we find that the morphological and emission features at the jet impact sites can vary substantially between the interaction zones driven by jets launched from different systems. We find that the way in which a BHXB jet-ISM interaction manifests itself appears to be highly dependent on the jet properties (e.g. jet power, duty cycle) and local environment conditions (e.g. composition, density, other sources of feedback), similar to what has been observed at jet interaction sites surrounding other astrophysical systems (e.g., AGN, ULXs).

Overall, our analysis demonstrates that molecular lines are excellent diag-

nostics of the physical conditions in jet-ISM interaction zones near BHXBs. With the molecular tracers toolbox we have developed here (along with our imaging and analysis techniques), we have opened up a new way to conclusively identify more of these highly sought after interaction sites, and use their ISM conditions to probe jet properties across the BHXB population.

8.7 Appendix

8.7.1 ALMA Mosaic Field and Noise Map

We set up our ALMA observations to observe a large rectangular mosaic field, of dimensions 75 arcsec $\times$ 60 arcsec, centred on the coordinates of the peak of the radio continuum, as reported in Chaty et al. (2001) (J2000 RA 19:15:39.1300, Dec 10:41:17.100). This field was chosen to cover the radio continuum feature, as well as regions to the south of the radio continuum. We did this, as based on previous work, we expected a complex molecular interaction around the suspected bow shock feature, located at the southern most edge of the radio continuum (see Figure 8.1). A primary beam noise map of the mosaic field is displayed in Figure 8.15, and pointing maps are displayed in Figure 8.16.
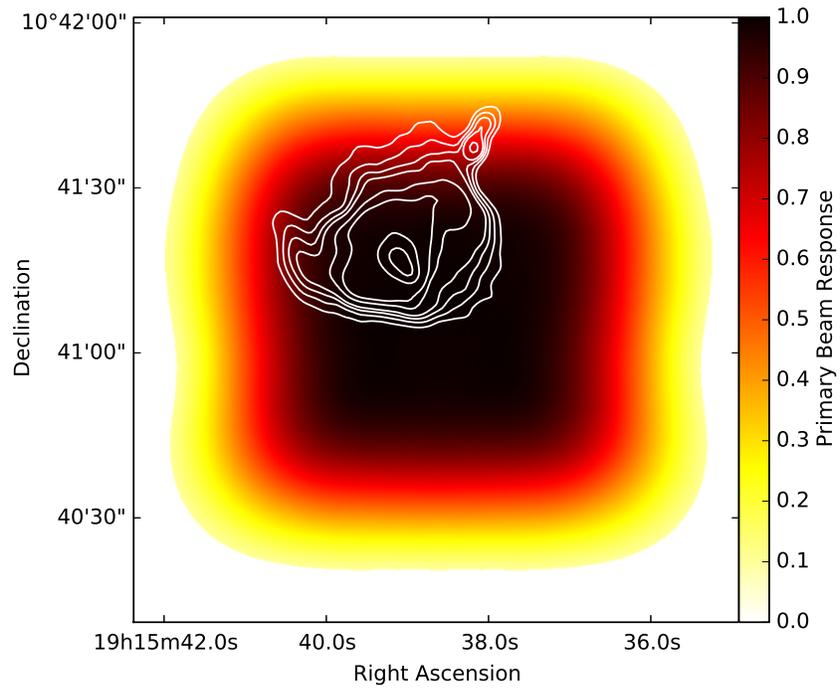
Figure 8.15: ALMA primary beam noise map. The contours are the VLA radio frequency contours, as seen in Figure 8.2; 0.2, 0.3, 0.4, 0.5, 0.75, 1, 2, and $3\,\mathrm{mJy\,bm^{-1}}$. The colour bar indicates the primary beam response.
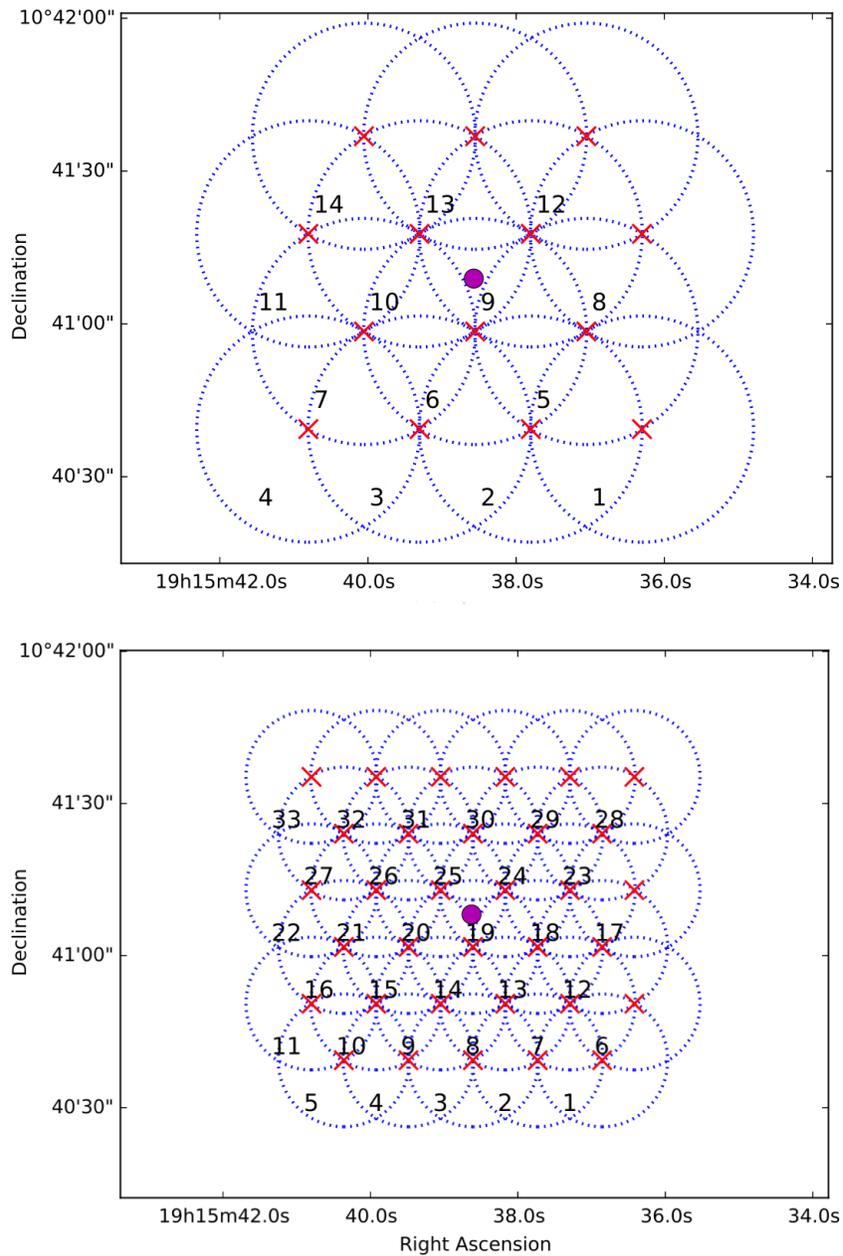
Figure 8.16: ALMA ACA 7 m array (*top panel*) and 12 m array (*bottom panel*) mosaic maps. Each individual pointing (labelled with a number) is represented by a blue circle, with the centre coordinates marked by a red X. The magenta point marks the coordinates of the peak of the radio continuum in IRAS 19132+1035 reported in Chaty et al. (2001).

8.7.2 Column density calculation

We follow the procedure of Wilson et al. (2013), assuming that the C^{18}O emission is optically thin, in LTE, and has an excitation temperature, T_{ex}, equivalent to that of the optically thick ^{12}CO emission (Pineda et al., 2008).

The intensity of line emission can be represented as

$$I_{\mathrm{line}} = (S - I_0)(1 - \exp[-\tau]) \tag{8.13}$$

where S represents the source function, τ represents the optical depth, and I_0 represents the intensity of the initial background radiation field.

Assuming that both the S and I_0 can be represented by black-bodies at T_{ex} and $T_{\mathrm{bg}} = 2.73$ K, respectively, the radiation temperature is represented as

$$
\begin{aligned}
T_R &= I_{\mathrm{line}} \frac{c^2}{2\nu^2 k} \\
&= (S - I_0)(1 - e^{-\tau}) \frac{c^2}{2\nu^2 k} \\
&= \frac{h\nu}{k}(1 - e^{-\tau}) \left(\frac{1}{\exp[h\nu/kT_{\mathrm{ex}}] - 1} - \frac{1}{\exp[h\nu/kT_{\mathrm{bg}}] - 1} \right)
\end{aligned}
\tag{8.14}
$$

Defining $T_{\mathrm{max},12}$ as the main beam brightness temperature at the peak of the ^{12}CO line, and assuming that ^{12}CO is optically thick ($\tau \to \infty$), Equation 8.14 can be re-arranged to yield

$$T_{\mathrm{ex}} = \frac{C_{12}}{\ln\left(1 + \frac{C_{12}}{T_{\mathrm{max},12} + C_{12}C_{\mathrm{bg}}}\right)} \tag{8.15}$$

where $C_{12} = \frac{h\nu_{12}}{k}$, and $C_{\mathrm{bg}} = \frac{1}{\exp[C_{12}/T_{\mathrm{bg}}] - 1}$.

Defining $C_{18} = \frac{h\nu_{18}}{k}$, and assuming the excitation temperature of C^{18}O is equal to that of the ^{12}CO, the optical depth at a given line-of-sight velocity V can be found by re-arranging Equation 8.14,

$$\tau(V) = -\ln\left(1 - \frac{kT(V)}{h\nu_{18}}\left[\frac{1}{\exp[C_{18}/T_{\mathrm{ex}}] - 1} - \frac{1}{\exp[C_{18}/T_{\mathrm{bg}}] - 1}\right]^{-1}\right). \tag{8.16}$$

Given the optical depth, we can then find the optical column density in the Jth state from the definitions of the optical depth (see Wilson et al., 2013):

$$N(J) = \frac{8\pi\nu_0^2}{c^2}\frac{g_l}{g_u}\frac{1}{A_{ul}}\left[1 - \exp\left(-\frac{h\nu_0}{kT_{\text{ex}}}\right)\right]^{-1}\int \tau d\nu, \qquad (8.17)$$

$$= \frac{8\pi\nu_0^3}{c^3}\frac{g_l}{g_u}\frac{1}{A_{ul}}\left[1 - \exp\left(-\frac{h\nu_0}{kT_{\text{ex}}}\right)\right]^{-1}\int \tau dV, \qquad (8.18)$$

where the integral is carried out over the line width. We infer the optical depth from Equation 8.16. For $C^{18}O(2 \to 1)$, $A_{ul} = 1.165 \times 10^{-11}\mu^2\nu^3\frac{(J+1)}{2J+3}$ for the $J + 1 \to J$ transition, and $\mu^2 = (0.122D)^2$ for CO.

The total column density is found from summing over all the energy levels of the molecule. Assuming LTE, for a CO molecule ($J + 1 \to J$ rotational transition), with a population characterized by a single temperature, T_{ex}, the total column density is represented as

$$N_{\text{total}} = N(J)\frac{Z}{g_J}\exp\left[\frac{hB_eJ(J + 1)}{kT_{\text{ex}}}\right], \qquad (8.19)$$

where $g_J = 2J + 1$ for CO, $k/hB_e = 1/2.65$ K^{-1}, and the partition function is given by,

$$Z = \sum_{J=0}^{\infty}(2J + 1)\exp\left[\frac{-hB_eJ(J + 1)}{kT_{\text{ex}}}\right]. \qquad (8.20)$$

8.7.3 Calorimetry Method

Following Kaiser & Alexander (1997), assuming the jet direction remains constant (i.e. the jet is not precessing), the jet is colliding with a medium of density ρ_0, and that the power is being transported by the jets at a constant rate (Q_{jet}; averaged over the lifetime of the jets), the length of the jet as a function of time (t) is given by

$$L_j = C_1\left(\frac{t}{\tau}\right)^{\frac{3}{5-\beta}}, \qquad (8.21)$$

where the characteristic timescale $\tau = (\rho_0/Q_{\text{jet}})^{1/3}$, and the constants

$$C_1 = \left(\frac{C_2}{C_3\phi^2} \frac{(\Gamma_x + 1)(\Gamma_c - 1)(5 - \beta)^3}{18\left[9\{\Gamma_c + (\Gamma_c - 1)\frac{C_2}{4\phi^2}\} - 4 - \beta\right]} \right)^{\frac{1}{(5-\beta)}}, \qquad (8.22)$$

$$C_2 = \left(\frac{(\Gamma_c - 1)(\Gamma_j - 1)}{4\Gamma_c} + 1 \right)^{\frac{\Gamma_c}{(\Gamma_c - 1)}} \frac{(\Gamma_j + 1)}{(\Gamma_j - 1)}, \qquad (8.23)$$

$$C_3 = \frac{\pi}{4R_{\text{ax}}^2}. \qquad (8.24)$$

Here ϕ represents the jet opening angle (in radians), $R_{\text{ax}} = \sqrt{\frac{1}{4}\frac{C_2}{\phi^2}}$ represents the axial ratio of the jet-blown cavity, and Γ_j, Γ_x, and Γ_c represent the adiabatic indices of the material in the jet, jet-blown cavity, and external medium with which the jet is colliding, respectively.

The power that the jet would need to carry (averaged over its lifetime, t), to create and maintain the jet-blown cavity structure in the surrounding ISM, can be found from re-arranging Equation 8.21,

$$Q_{\text{jet}} = \rho_0 \left(\frac{L_j}{C_1} \right)^5 t^{-3}. \qquad (8.25)$$

where we have set $\beta = 0$ for a constant density medium.

To estimate the jet lifetime, we first take the derivative of Equation 8.21 (again setting $\beta = 0$),

$$\frac{dL_j}{dt} = \frac{3}{5}C_1 \left(\frac{Q_{\text{jet}}}{\rho_0} \right)^{\frac{1}{5}} t^{-\frac{2}{5}}, \qquad (8.26)$$

then combine Equations 8.21 and 8.26, to yield,

$$t = \frac{3}{5}\left(\frac{L_j}{v} \right), \qquad (8.27)$$

where $v = dL_j/dt$ represents the velocity of the shocked gas at the interaction site.

Substituting Equation 8.27 into Equation 8.25 yields an expression for the power carried by the jet, solely dependent on the properties of the ISM at the interaction site,

$$Q_{\text{jet}} = \left(\frac{5}{3}\right)^3 \frac{\rho_0}{C_1^5} L_j^2 v^3 \qquad (8.28)$$

Chapter 9

Conclusion

9.1 Summary of Results

Throughout this thesis I have studied the different forms of relativistic jets launched from XB systems. The main goals of this body of work were to develop new ways to observe and analyze jet emission. My ultimate goal is to advance our understanding of the underlying physics that governs jet behaviour in XB systems.

In Chapters 2 and 3, I construct and fit the radio/X-ray correlation ($L_R \propto L_X^{\beta}$, where β represents the disc-jet coupling index), linking the accretion flow to the relativistic jet, for different classes of NSXB systems. Comparing this correlation between different types of XB systems is key in understanding the properties that affect the jet production process in accreting objects. However, while BHXB systems have been well sampled in this plane, prior to my work very few neutron stars had a measured radio/X-ray correlation and the interplay between the different classes of NS systems (i.e., non-pulsating versus pulsating neutron stars) had not been well characterized. In these chapters, I demonstrate that unlike black hole systems, all neutron stars systems do not follow a single common correlation in this plane. In particular, neutron star systems can display a range of radio luminosities at a similar X-ray luminosity,

resulting in varying disc-jet coupling indices, as well as varying normalizations. I analyze a host of possible mechanisms that could be driving such discrepancies, by exploring the relationships between radio luminosity and distance, mass, spectral state, spin, magnetic field, orbital period, accretion regime, and evolutionary state in these systems. Ultimately, I find that no one factor can fully account for the discrepancies we observe, and thus a combination of the above factors may be required to produce a given radio luminosity in neutron star systems. Overall, these results highlight the need for more radio and X-ray measurements (especially in the low X-ray luminosity regime; $L_X < 10^{36} \, \mathrm{erg\,s^{-1}}$) of all classes of NSXBs to place improved constraints on the mechanisms that govern radio luminosity, jet production, and jet evolution in NSXBs. Further, despite the lack of a clear correlation for neutron star systems, the sources sampled in this work are clear examples that the radio/X-ray plane can still be a reliable diagnostic to identify the nature of the accretor in these binary systems.

In Chapter 4, I present a detailed study of rapid (probing second to hour timescales) compact jet variability at radio frequencies in BHXBs. In this study, my team and I obtained simultaneous multi-band radio and X-ray observations of the BHXB Cyg X-1. Through extracting high time resolution light curves of the source, I detect structured variability (in the form of small amplitude flaring events) consistent with emission originating in a compact jet. To better characterize this compact jet variability and probe how this variability propagates down the jet flow, I performed a timing analyses on our data. These include Fourier domain analyses (PSDs and cross-spectral analyses between radio bands), and cross-correlation analyses. I find that the radio jet emission shows no significant power at Fourier frequencies above ~ 0.03 Hz (faster than ~ 30 sec timescales) and that the higher frequency radio bands are strongly correlated over a range of time scales, showing a roughly constant time lag of a few tens of seconds at low Fourier frequencies. However, in the lower fre-

quency radio bands I find a significant loss of coherence over the same range of timescales. I discuss different mechanisms that could be causing this effect (e.g., noise contribution, other sources of emission, non-linear processes [such as shocks] acting on our radio signals). Further, I detect a clear correlation between the X-ray and radio emission, measuring time lags between the X-ray and radio bands on the order of tens of minutes. I use these X-ray/radio lags to present a direct measurement of the compact jet speed in a BHXB, finding that the Cyg X-1 jet is more relativistic than usually assumed for compact jets, $\beta = 0.92^{+0.03}_{-0.06}$, ($\Gamma = 2.59^{+0.79}_{-0.61}$). Lastly, I constrain how the jet size scale changes with frequency, finding a shallower relation ($\propto \nu^{-0.4}$) than predicted by simple jet models ($\propto \nu^{-1}$), and I estimate the jet opening angle to be $\phi \sim 0.4 - 1.8$ degrees. Overall, my team and I have developed observational techniques designed to overcome the challenges of rapid radio timing analyses, and laid the groundwork needed to connect radio jet variability properties to internal jet physics.

In Chapters 5, 6, and 7, I analyze the spectral, temporal, and morphological properties of jet emission observed from the BHXB V404 Cygni during its 2015 outburst. Chapters 5 and 7 focus on probing the jet emission during a period of extreme flaring activity coinciding with the launching of multiple discrete jet ejection events, while Chapter 6 focuses on tracking the changes in the jet emission as the system transitioned away from the flaring state and began to decay back into quiescence.

In Chapter 5, I present the results of our simultaneous radio through sub-mm observations of the V404 Cyg during the most active phase of its 2015 outburst. Our comprehensive data set extends across 8 different frequency bands (5, 7, 21, 26, 220, 230, 350, and 666 GHz), including the first detection of a BHXB jet at 666 GHz. Using custom procedures my team and I developed, I created high time resolution light curves of V404 Cyg, detecting extraordinary multi-frequency variability in the form of multiple large amplitude flaring

events reaching Jy-level fluxes (characteristic of discrete jet ejections). To understand the source of the emission in our light curves I constructed a detailed jet model for V404 Cyg, capable of reproducing emission from multiple, discrete, bi-polar plasma ejection events, which travel at bulk relativistic speeds (along a jet axis inclined to the line of sight) and evolve according to the van der Laan synchrotron bubble model (van der Laan, 1966). Through implementing a Bayesian technique to simultaneously fit all of our multi-frequency light curves with my jet model, I find that a total of 8 bi-polar ejection events can reproduce the emission that we observe. I use the best fit model to probe the intrinsic properties of the jet ejecta, including jet speed, structure, energetics, and geometry. In addition, I discuss the interplay between the jet ejecta and the other form of outflow detected in V404 Cyg, the accretion disc wind. Based on these properties, it appears as though the V404 Cyg ejection events we observe are smaller-scale analogues of major ejection events, typically seen during the hard to soft accretion state transition in BHXBs. Further, given the similarity between the rapid ejection events in V404 Cyg and those seen in another BHXB, GRS 1915+105, I postulate that the ejection events in both systems may have a common origin, in the repeated ejection and refilling of some reservoir in the inner accretion flow. This suggests that, in agreement with the findings of Kimura et al. (2016) & Muñoz-Darias et al. (2016), the presence of a large accretion disc in both systems may be a key ingredient in producing the rare, rapid ejection events we observe. Overall, my team and I have demonstrated that simultaneous multi-band photometry of outbursting BHXBs can provide a powerful probe of jet properties and that the mm/sub-mm bands provide a critical new perspective on BHXB jets (especially in the time-domain) that cannot be achieved with radio frequency observations alone.

In Chapter 6, I present the results of our multi-frequency monitoring observations of the entire 2015 outburst of V404 Cyg. With this well-sampled data set, I created detailed diagnostics of the jet emission in V404 Cyg, tracking the

spectral and variability properties throughout different stages of the outburst. Using these diagnostics I find that the jet emission was originally dominated by emission from discrete jet ejecta during the brightest stages of the outburst. This ejecta appeared to become fainter, slower, less frequent, and less energetic, before the emission abruptly (over 1–2 days) transitions to being dominated by a compact jet. While the broad-band spectrum of this compact jet shows very little evolution throughout the outburst decay (despite the intensity of the jet emission fading by an order of magnitude), the emission still remains intermittently variable at mm/sub-mm frequencies. Through phenomenological modelling of the broad-band emission from this compact jet, I postulate that the compact jet could be significantly contributing to the X-ray emission observed during the outburst decay. Additionally, upon comparing the radio jet emission throughout the 2015 and previous 1989 outbursts of V404 Cyg, I find that the radio emission in the 2015 outburst decayed significantly (~ 30 times) faster than in the 1989 outburst. I suggest that, given the robust disc-jet coupling relationship found between these two outbursts, this difference could indicate that the average mass accretion rate dropped (possibly due to the strong accretion disc wind) much quicker following the peak of the 2015 outburst, when compared to the 1989 outburst. Lastly, our sub-mm observations during the fainter mini-outburst following the main outburst suggest that jet ejecta are not exclusive to the highest luminosity states in V404 Cyg. Overall, this work has demonstrated the importance of simultaneous, multi-frequency, time-resolved observations, to fully understand the rapidly evolving jet sources in BHXBs.

In Chapter 7, I present Very Long Baseline Array (VLBA) radio frequency observations of V404 Cyg during its 2015 outburst. With these data, my team and I create a series of high angular resolution images of the jets in this source. Through analysis of these images, we detect and track the motion of multiple discrete jet ejection events launched from the system. These ejection events

evolve in both morphology and brightness, and we observe the orientation of the jet axis vary on timescales as short as minutes. We associate the changes in the orientation of the jet axis with jet precession and demonstrate that this precession could originate from Lense-Thirring precession of a vertically-extended accretion disc, arising from a super-Eddington accretion rate in V404 Cyg. Using our VLBA measurements, we place constraints on the precession period (< 2.6 hours), precession cone opening angle (~ 15 degrees), and the stability of the precession process. Further, we consider the occurrence of jet precession in other sources, as well as the implications jet precession has on the jet launching mechanism and the impact of these jets on the surrounding environment. Ultimately, our findings show that Eddington-rate accretion from a reservoir whose angular momentum is misaligned with the black hole spin can drive a rapidly precessing accretion disc and jet system. In turn the dynamics of a precessing inner accretion disc play a key role in either directly launching or redirecting jets within the inner few hundred gravitational radii of the black hole.

In Chapter 8, I present a new technique where astrochemistry is used to identify and probe the regions where BHXB jets are colliding with the surrounding ISM. In this study, I present ALMA observations of IRAS 19132+1035. This region was first identified by Rodríguez & Mirabel (1998) as a potential interaction zone between the jet launched from the BHXB GRS 1915+105 and the surrounding ISM, based on its location and unique radio continuum morphology. However, despite several follow-up observing campaigns, no definitive evidence had been found to confirm this hypothesis, with compelling arguments on either side. As molecular lines are excellent diagnostics of shock energetics and ISM excitation, I used these ALMA observations to map the molecular line emission in the IRAS 19132+1035 region, aiming to resolve this long-standing question. Given this molecular emission, I identify several new lines of compelling evidence supporting a connection between the IRAS

19132+1035 region and the GRS 1915+105 jet. In particular, the morphological, spectral, and kinematic properties of the detected molecular emission indicate the presence of a jet-blown cavity and weak jet-driven shock at the impact site. Through considering the properties of the detected cavity and displaced molecular gas in the region, I estimate the energy carried in the GRS 1915+105 jet of $(6.7^{+6.4}_{-6.6}) \times 10^{47}$ erg, over a lifetime of $29.5^{+8.6}_{-8.7}$ Myr, resulting in a total time-averaged jet power of $(8.4^{+7.7}_{-8.1}) \times 10^{32}$ erg s^{-1} (although this may be up to a factor of 150 times higher if the GRS 1915+105 jet is undergoing small-scale precession). Upon comparing the characteristics of the IRAS 19132+1035 interaction zone with other jet-ISM interaction sites in our Galaxy and other nearby galaxies, I find that the morphological and emission features at the jet impact sites can vary substantially between the interaction zones driven by jets launched from different systems. Further, the way in which a BHXB jet-ISM interaction manifests itself appears to be highly dependent on the jet properties (e.g., jet power, duty cycle) and local environment conditions (e.g., composition, density, other sources of feedback), similar to what has been observed at jet interaction sites surrounding other astrophysical systems (e.g., AGN, ULXs). Overall, this analysis demonstrates that molecular lines are excellent diagnostics of the physical conditions in jet-ISM interaction zones near BHXBs. With the molecular tracers toolbox my team and I have developed here (along with our imaging and analysis techniques), we have opened up a new way to conclusively identify more of these highly sought after interaction sites and use their ISM conditions to probe jet properties across the BHXB population.

9.2 Future Work

In this thesis, I have presented the development and implementation of new tools and techniques to study jet emission, as well as opened up a new window

for studying jets through the mm/sub-mm bands. I plan to expand this work by applying the insights gained from this thesis across the XB population.

Time Domain: My work has demonstrated that time domain techniques are incredibly powerful tools for unlocking complicated jet physics. To build on my previous studies, I plan to utilize my custom software to extract high time-resolution measurements from more systems, using both archival and new data sets.

Through utilizing archival radio frequency data of out-bursting BHXBs from the VLA as a baseline, I aim to compile a suite of variability metrics to best identify and characterize jet variability, as well as track changes in these variability properties over the course of the outburst. By searching for empirical correlations, relating these jet variability properties to X-ray spectral and timing properties (e.g., photon index, appearance/disappearance of QPOs), which track the physical conditions in the accretion flow, I can work to determine which processes in the accretion flow drive jet variability.

Chapter 4 of this thesis specifically has shown that long, continuous observations of BHXB jets across multiple frequencies are needed to connect variability properties with internal jet physics. Taking advantage of today's more sensitive instruments, and coordination capabilities, I will work to obtain new multi-band (radio, sub-mm, and X-ray) data of jets in more out-bursting BHXBs. I currently lead time domain mm/sub-mm programs, as part of a global collaboration with accepted observations across radio (VLA, VLBA), sub-mm (NOEMA, ALMA, SMA, and JCMT), and X-ray (Swift, AstroSat) facilities, to obtain these new data sets. With these new data I will compare BHXB jet variability across a wide range of observing frequencies, searching for variability correlations and time lags across radio, sub-mm & X-ray frequencies, while simultaneously tracking changes in jet morphology, creating a detailed probe of jet behaviour.

In the long term, I also plan to expand my timing studies to jets launched

from other compact objects (e.g., neutron stars), as well as compile the software tools I utilize for low frequency timing analysis for use with studies of other transient astrophysical phenomena (e.g., gamma ray bursts, tidal disruption events, AGN, flare stars). Overall, I aim to contribute to the growth of time-domain astronomy, by expanding our capabilities in the radio/sub-mm bands.

Jet-ISM Interaction Zones: My work has demonstrated that through mapping molecular line emission near BHXBs, we can develop several lines of evidence to conclusively identify jet-ISM interaction regions and accurately probe the ISM conditions at these sites. In particular, I have found that the successful recipe for probing jet-ISM interactions with molecular tracers involves first detecting excited molecular emission in the candidate interaction zones, and then using followup high resolution observations to confirm the BHXB jet is powering these regions.

To identify new targets beyond the three confirmed jet-ISM interaction zones identified near BHXBs, I have compiled a list of candidate interaction zones (see Table 9.1), on the basis that their emission properties are consistent with those expected from a jet interaction. Additionally, I include high mass X-ray binaries (HMXBs) with radio detections (a proxy for the presence of a jet) in this candidate list. These systems, containing a high mass companion star, tend to be clustered where the molecular gas mass is located in our Galaxy (within 100 pc of the Galactic plane and near high mass star forming regions). Thus HMXBs represent sources with a higher probability of a jet molecular cloud collision.

My team and I have already used ALMA to observe a suite of molecular lines in the fields surrounding the remaining two candidate interaction zones with existing molecular line detections, BHXBs 1E 1740–2942 and GRS 1758–258. With these data, I plan to use the analysis tools developed in Chapter 8 of this thesis to answer the following questions: Is there sufficient evidence to classify these zones as confirmed jet-ISM interaction regions? Are other forms

345

of feedback contributing to the energy budget in the region? What do the ISM conditions in these regions reveal about jet properties (e.g., jet power and geometry)? Do jet properties correlate with molecular gas properties? How do the properties of the molecular line emission compare to those observed near GRS 1915+105? Is there a common molecular signature across all systems?

Further, I lead projects that have been awarded observing time on the JCMT and the IRAM 30m telescopes to perform a survey in search of excited molecular line emission in multiple candidate interaction zones. The survey targets all the candidate zones, visible with these instruments, without previous molecular line detections, as well as the interaction zones near Cyg X-1 and SS 433 (highlighted yellow/pink in Table 9.1). With this survey I aim to accomplish two main goals: (i) catalog candidate interaction regions containing excited molecular gas (positive detections will be targets of a future followup high resolution ALMA/NOEMA campaign) and (ii) quantify BHXB feedback in our Galaxy by developing a statistical modelling approach to estimate the level of energy input into the ISM from these BHXB jets.

The results of both these time domain and jet-ISM interaction studies will derive new constraints on highly sought after jet properties for multiple BHXBs, providing crucial ingredients needed in understanding the mechanisms that drive astrophysical jets.

Table 9.1: Candidate Jet-ISM Interaction Zones Near Galactic BHXBs

BHXB Source[a]	Evidence for Interaction	Molecular Detection[b]	References	Status
Cyg X-1	bow shock, jet blown bubble structure	No	Gallo et al. 2005	Confirmed
GRS 1915+105	radio lobes	Yes	Rodriguez & Mirabel 1998	Confirmed
SS 433	radio lobes, X-ray hot spots	Yes	Dubner et al. 1998	Confirmed
1E 1740-2942	radio lobes	Yes	Mirabel et al. 1992	Unconfirmed
4U 1755-33	X-ray hot spots	No	Kaaret et al. 2006	Unconfirmed
CI Cam	HMXB with radio detection	No	Smith et al. 1998	Unconfirmed
Cyg X-3	HMXB with radio detection	No	Marti et al. 2001	Unconfirmed
GRO J1655-40	radio lobes, shell-like structure in Hα	No	Hjellming & Rupen 1995	Unconfirmed
GRS 1739-278	HMXB with radio detection	No	Durouchoux et al., 1996	Unconfirmed
GRS 1758-258	radio lobes	Yes	Marti et al. 2002	Unconfirmed
GX 339-4	resolved large-scale radio jet	No	Gallo et al. 2004	Unconfirmed
H1743-322	X-ray hot spots	No	Corbel et al. 2005	Unconfirmed
MWC 656	HMXB with radio detection	No	Dzib et al. 2015	Unconfirmed
V4641 Sgr	HMXB with radio detection	No	Hjellming et al. 2000	Unconfirmed
XTE J1550-564	X-ray hot spots, deceleration	No	Corbel et al. 2002	Unconfirmed
XTE J1650-500	optically thin radio emission	No	Corbel et al. 2004	Unconfirmed
XTE J1748-288	optically thin radio emission	No	Brocksopp et al 2007	Unconfirmed
XTE 1752-223	X-ray hot spots, deceleration	No	Ratti et al. 2012; Yang et al. 2010	Unconfirmed
XTE J1908+094	asymmetric, expanding radio hot-spots	No	Rushton et al. 2017	Unconfirmed
LSI+61303	HMXB with radio detection	No	Paredes et al., 2000	Unconfirmed
GRS 1009-45	Hα shell	No	Russell et al. 2006	Unconfirmed
LSI+61303	HMXB with radio detection	No	Paredes et al., 2000	Unconfirmed
LMC X-1	Hα shell	No	Russell et al., 2006	Unconfirmed

[a] Entries highlighted in blue represent target sources covered by my teams's ALMA campaigns, while entries highlighted in yellow and pink are those sources covered by my team's upcoming JCMT/IRAM 30m surveys or archival JCMT observations.
[b] Flag to indicate whether molecular gas has been previously detected in the field surrounding each BHXB source.

Bibliography

Alexander, T. 1997, Astronomical Time Series, Eds. D. Maoz, A. Sternberg, and E.M. Leibowitz, 163

Alexander, T. 2013, ArXiv e-prints, arXiv:1302.1508

Altamirano, D., H.A., K., Patruno, A., et al. 2015, The Astronomer's Telegram, 7240, 1

Altamirano, D., Keek, L., Cumming, A., et al. 2012, MNRAS, 426, 927

Archibald, A. M., Stairs, I. H., Ransom, S. M., et al. 2009, Science, 324, 1411

Arkharov, A., et al. 2015, The Astronomer's Telegram, 7760, 1

Arnaud, K. 1996, in Astronomical Data Analysis Software and Systems V of Astronomical Society of the Pacific Conference Series, Vol. 101, 17

Baars, J., Altenhoff, W., Hein, H., & Steppe, H. 1986, Nature, 324, 39

Bahramian, A., Heinke, C., Degenaar, N., et al. 2015a, MNRAS, 452, 3475

Bahramian, A., Heinke, C., Sivakoff, G., & Gladstone, J. C. 2013, ApJ, 766, 10

Bahramian, A., Heinke, C., Sivakoff, G., et al. 2014, ApJ, 780, 127

Bahramian, A., Altamirano, D., Heinke, C., et al. 2015b, The Astronomer's Telegram, 7242, 1

Bahramian, A., Heinke, C. O., Tudor, V., et al. 2017, MNRAS, 467, 2199

Bahramian, A., Miller-Jones, J., Strader, J., et al. 2018, Radio/X-ray correlation database for X-ray binaries, Astrophysics Source Code Library, doi:10.5281/zenodo.1252036. `https://doi.org/10.5281/zenodo.1252036`

Balbus, S., & Hawley, J. 1991, ApJ, 376, 214

Ballard, K., & Heavens, A. 1992, MNRAS, 259, 89

Band, D. 1987, ASP, 99, 1269

Barthelmy, S., D'Ai', A., D'Avanzo, P., et al. 2015, GCN Circular, 17929, 1

Bassa, C. G., Patruno, A., Hessels, J. W. T., et al. 2014, MNRAS, 441, 1825

Beardmore, A. P., Page, K. L., & Kuulkers, E. 2015, The Astronomer's Telegram, 8455, 1

Beardmore, A. P., Willingale, R., Kuulkers, E., et al. 2016, MNRAS, 462, 1847

Beckwith, S., Sargent, A., Chini, R., & Guesten, R. 1990, ApJ, 99, 924

Bell, A. 1978, MNRAS, 182, 147

Belloni, T. 2010, in The Jet Paradigm - From Microquasars to Quasars, ed. Belloni, T.M., Lecture Notes in Physics 794, Springer

Belloni, T., & Hasinger, G. 1990, A&A, 227, L33

Belloni, T., Mendez, M., King, A. R., van der Klis, M., & van Paradijs, J. 1997, ApJ, 479, 145

Benjamin, R., Churchwell, E., Babler, B., et al. 2003, PASP, 115, 953

Bernardini, F., Russell, D. M., & Lewis, F. 2016a, The Astronomer's Telegram, 8515, 1

Bernardini, F., Russell, D. M., Shaw, A. W., et al. 2016b, ApJL, 818, L5

Bjornsson, C., & Aslaksen, T. 2000, ApJ, 533, 787

Blackburn, J. 1995, in Astronomical Data Analysis Software and Systems IV of Astronomical Society of the Pacific Conference Series, ed. H. J. J. E. Shaw R. A., Payne H. E., Vol. 77, 367

Blandford, R., & Payne, D. 1982, MNRAS, 199, 883

Blandford, R., & Znajek, R. 1977, MNRAS, 179, 433

Blandford, R. D., & Eichler, D. 1987, Phys. Rep., 154

Blandford, R. D., & Königl, A. 1979, ApJ, 232, 34

Blundell, K., & Bowler, M. 2005, ApJ, 622, L129

Bogdanov, S., Deller, A. T., Miller-Jones, J. C. A., et al. 2018, ApJ, 856, 54

Bordas, P., Bosch-Ramon, V., Paredes, J. M., & Perucho, M. 2009, A&A, 497, 325

Bordas, P., Kuulkers, E., Alfonso-Garzon, J., et al. 2010, The Astronomer's Telegram, 2919, 1

Bosch-Ramon, V., Perucho, M., & Bordas, P. 2011, A&A, 528, A89

Bozzo, E., Grinberg, V., Wilms, J., et al. 2017a, The Astronomer's Telegram, 10880, 1

—. 2017b, The Astronomer's Telegram, 10881, 1

Bradt, H. 2008, Astrophysical Processes- The Physics of Astronomical Phenomena, Cambridge University Press

Brandt, N., & Podsiadlowski, P. 1995, MNRAS, 274, 461

Brocksopp, C., Corbel, S., Tzioumis, A., et al. 2013, MNRAS, 432, 931

Brocksopp, C., Fender, R. P., Larionov, V., et al. 1999, MNRAS, 309, 1063

Brocksopp, C., Fender, R. P., & Pooley, G. G. 2002, MNRAS, 336, 699

Brocksopp, C., Miller-Jones, J. C. A., Fender, R. P., & Stappers, B. W. 2007, MNRAS, 378, 1111

Brocksopp, C., Fender, R. P., McCollough, M., et al. 2002, MNRAS, 331, 765

Broderick, J., Stewart, A., Fender, R., Miller-Jones, J., & Mooley, K. nad Pietka, M. 2015, The Astronomer's Telegram, 7720, 1

Bromberg, O., Nakar, E., Piran, T., & Sari, R. 2011, ApJ, 740, 100

Burbidge, G. 1959, ApJ, 129, 849

Burrows, D. N., Hill, J. E., Nousek, J. A., et al. 2005, Space Science Reviews, 120, 165

Capellupo, D. M., Haggard, D., Choux, N., et al. 2017, ApJ, 845, 35

Cardelli, J., Clayton, G., & Mathis, J. 1989, ApJ, 345, 245

Carrasco, L., Recillas, E., Porras, A., et al. 2015, The Astronomer's Telegram, 7751, 1

Cartwright, T. F., Engel, M. C., Heinke, C. O., et al. 2013, ApJ, 768, 183

Casares, J., & Charles, P. A. 1994, MNRAS, 271, L5

Casares, J., Charles, P. A., & Naylor, T. 1992, Nature, 355, 614

Casares, J., Charles, P. A., Naylor, T., & Pavlenko, E. P. 1993, MNRAS, 265, 834

351

Casella, P., Altamirano, D., Patruno, A., Wijnands, R., & van der Klis, M. 2008, ApJ, 674, L41

Casella, P., & Pe'er, A. 2009, ApJ, 703, L63

Casella, P., Maccarone, T., O'Brien, K., et al. 2010, MNRAS, 404, L21

Casili, M., Adamson, A., Alves de Oliveira, C., Almaini, O., et al. 2007, A&A, 496, 777

Castor, J., McCray, R., & Weaver, R. 1975, ApJ, 200, L107

Castro-Tirado, A., Branndt, S., & Lund, S. 1992, IAU Circular, 5590, 1

Cavecchi, Y., Patruno, A., Haskell, B., et al. 2011, ApJ, 740, L8

Cazaux, S., & Tielens, A. 2002, ApJ, 575, L29

Chakrabarty, D., Jonker, P., & Markwardt, C. 2017, The Astronomer's Telegram, 10898, 1

Chandra, P., & Kanekar, N. 2017, ApJ, 846, 111

Chapin, E., Berry, D., Gibb, A., et al. 2013, MNRAS, 430, 2545

Chaty, S., Dubus, G., & Raichoor, A. 2011, A&A, 529, A3

Chaty, S., Rodríguez, L. F., Mirabel, I. F., et al. 2001, A&A, 366, 1035

Churchwell, E., Babler, B., Meade, M., et al. 2009, PASP, 121, 213

Clark, B. 1980, A&A, 89, 377

Collins, R., Kaiser, C., & Cox, S. 2003, MNRAS, 338, 331

Cooke, R., Kuncic, Z., Sharp, R., & Bland-Hawthorn, J. 2007, ApJ, 667, L163

Coppejans, D., Körding, E., Miller-Jones, J., et al. 2015, MNRAS, 451, 3801

Corbel, S., Coriat, M., Brocksopp, C., et al. 2013, MNRAS, 428, 2500

Corbel, S., & Fender, R. 2002, ApJ, 573, L35

Corbel, S., Fender, R. P., Tomsick, J., Tzioumis, A. K., & Tingay, S. 2004, ApJ, 617, 1272

Corbel, S., Fender, R. P., Tzioumis, A. K., et al. 2000, A&A, 359, 251

—. 2002, Science, 298, 196

Corbel, S., Kaaret, P., Fender, R. P., et al. 2005, ApJ, 632, 504

Corbel, S., Körding, E., & Kaaret, P. 2008, MNRAS, 389, 1697

Corbel, S., Nowak, M., Fender, R., Tzioumis, T., & Markoff, S. 2003, A&A, 400, 1007

Corbel, S., Kaaret, P., Jain, R. K., et al. 2001, ApJ, 554, 43

Coriat, M., Tzioumis, T., Corbel, S., et al. 2011a, The Astronomer's Telegram, 3119

Coriat, M., Corbel, S., Prat, L., et al. 2011b, MNRAS, 414, 677

Croton, D. J., Springel, V., White, S. D. M., et al. 2006, MNRAS, 365, 11

Cseh, D., Corbel, S., Kaaret, P., et al. 2012, ApJ, 749, 11

Cseh, D., Kaaret, P., Corbel, S., et al. 2014, MNRAS, 439, L1

Curran, P., Coriat, M., Miller-Jones, J., et al. 2014, MNRAS, 437, 3265

Davies, M. L., Franzen, T. M. O., Davies, R. D., et al. 2009, MNRAS, 400, 984

Degenaar, N., & Wijnands, R. 2012, MNRAS, 422, 581

Deller, A. T., Moldon, J., Miller-Jones, J. C. A., et al. 2015, ApJ, 809, 13

Dempsey, J., Friberg, P., Jeness, T., et al. 2012, MNRAS, 430, 2534

Dhawan, V., Mirabel, I., Ribo, M., & Rodrigues, I. 2007, ApJ, 668, 430

Dhawan, V., Mirabel, I. F., & Rodríguez, L. F. 2000, ApJ, 543, 373

Díaz Trigo, M., Migliari, S., Miller-Jones, J. C. A., et al. 2017, A&A, 600, A8

Díaz Trigo, M., Miller-Jones, J., Migliari, S., Broderick, J., & Tzioumis, T. 2013, Nature, 504, 260

Díaz Trigo, M., Altamirano, D., Dincer, T., et al. 2018, A&A Accepted, arXiv:1804.08322

Dincer, T., Bailyn, C. D., Miller-Jones, J. C. A., Buxton, M., & MacDonald, R. K. D. 2018, ApJ, 852, 4

Done, C., Gierllinski, M., & Kubota, A. 2007, ARA&A, 15, 1

Drappeau, S., Malzac, J., Belmont, R., Gandhi, P., & Corbel, S. 2015, MNRAS, 447, 3832

Drappeau, S., Malzac, J., Coriat, M., et al. 2017, MNRAS, 466, 4272

Drury, L., & Volk, J. 1981, ApJ, 248, 344

Dubner, G. M., Holdaway, M., Goss, W. M., & Mirabel, I. F. 1998, ApJ, 116, 1842

Durouchoux, P., Sood, R., Oka, T., et al. 2000, AdSpR, 25, 703

Edelson, R. A., & Krolik, J. H. 1988, ApJ, 333, 646

Eichler, D. 1993, ApJ, 419, 111

Fabian, A. 2012, ARA&A, 50, 455

Fabrika, S. 2004, Astrophysics and Space Physics Reviews, 12, 1

Falcke, H., & Biermann, P. 1995, A&A, 293, 665

Falcke, H., Körding, E., & Markoff, S. 2004, A&A, 414, 895

Fan, X., Strauss, M. A., Schneider, D. P., et al. 2003, AJ, 125, 1649

Fender, R. 2001, MNRAS, 322, 31

—. 2003, MNRAS, 340, 1353

—. 2006, Compact Stellar X-ray Sources, Vol. No. 39 (Cambridge Astrophysics Series, ed. Lewin W.H.G., van der Klis M.), 381–419

—. 2010, in The Jet Paradigm - From Microquasars to Quasars, ed. Belloni, T.M., Lecture Notes in Physics 794, Springer

Fender, R., Bell Burnell, S., Garrington, S., Spencer, R., & Pooley, G. 1995, MNRAS, 274, 633

Fender, R., & Belloni, T. 2004, ARA&A, 42, 317

Fender, R., Belloni, T., & Gallo, E. 2004a, MNRAS, 355, 1105

Fender, R., Garrington, S., McKay, D., et al. 1999a, MNRAS, 304, 865

Fender, R., Hjellming, R., Tilanus, R., et al. 2001, MNRAS, 322, L23

Fender, R., Homan, J., & Belloni, T. 2009, MNRAS, 396, 1370

Fender, R., & Kuulkers, E. 2001, MNRAS, 324, 923

Fender, R., & Pooley, G. 2000, MNRAS, 318, L1

Fender, R., Pooley, G., Durouchoux, P., Tilanus, R., & Brocksopp, C. 2000, MNRAS, 312, 853

Fender, R., Wu, K., Johnson, H., et al. 2004b, Nature, 427, 222

Fender, R., Corbel, S., Tzioumis, T., et al. 1999b, ApJ, 519, L165

Fender, R. P., & Hendry, M. A. 2000, MNRAS, 317, 1

Fender, R. P., Maccarone, T. J., & van Kesteren, Z. 2005, MNRAS, 360, 1085

Fender, R. P., & Pooley, G. G. 1998, MNRAS, 300, 573

Feng, H., & Kaaret, P. 2008, ApJ, 675, 1067

Ferraro, F., Pallanca, C., Lanzoni, B., et al. 2015, ApJ, 807, L1

Ferrigno, C., Bozzo, E., Boissay, R., Kuulkers, E., & Kretschmar, P. 2015a,
    The Astronomer's Telegram, 7731, 1

Ferrigno, C., Fotopoulou, S., Domingo, A., et al. 2015b, The Astronomer's
    Telegram, 7662, 1

Foight, D. R., Güver, T., Özel, F., & Slane, P. O. 2016, ApJ, 826, 66

Fomalont, E., Geldzahler, B. J., & Bradshaw, C. 2001a, ApJ, 558, 283

—. 2001b, ApJ, 553, L27

Foreman-Mackey, D., Hogg, D. W., Lang, D., & Goodman, J. 2013, PASP,
    125, 306

Fragile, P. C., Blaes, O. M., Anninos, P., & Salmonson, J. D. 2007, ApJ, 668,
    417

Frank, J., King, A., & Raine, D. 2002, Accretion Power in Astrophysics (Cam-
    bridge University Press)

Fruscione, A., McDowell, J. C., Allen, G. E., et al. 2006, in SPIE Proceed-
    ings, Vol. 6270, Society of Photo-Optical Instrumentation Engineers (SPIE)
    Conference Series, 62701V

Fuchs, Y. 2002, ArXiv e-prints, arXiv:0207429

Gaia Collaboration, Brown, A. G. A., Vallenari, A., et al. 2018, A&A Accepted, arXiv:1804.09365

Gaia Collaboration, Prusti, T., de Bruijne, J. H. J., et al. 2016, A&A, 595, A1

Gallo, E., Corbel, S., Fender, R., Maccarone, T., & Tzioumis, A. K. 2004, MNRAS, 347, L52

Gallo, E., Degenaar, N., & van den Eijnden, J. 2018, MNRAS, 478, L132

Gallo, E., Fender, R., & Hynes, R. 2005a, MNRAS, 356, 1017

Gallo, E., Fender, R., Kaiser, C., et al. 2005b, Nature, 7052, 819

Gallo, E., Fender, R., & Pooley, G. G. 2003, MNRAS, 344, 60

Gallo, E., Fender, R. P., Miller-Jones, J. C. A., et al. 2006, MNRAS, 370, 1351

Gallo, E., Migliari, S., Markoff, S., et al. 2007, ApJ, 670, 600

Gallo, E., Miller, B., & Fender, R. 2012, MNRAS, 423, 590

Gallo, E., Plotkin, R. M., & Jonker, P. G. 2014, MNRAS, 438, L41

Gallo, E., Miller-Jones, J. C. A., Russell, D., et al. 2014, MNRAS, 445, 290

Galloway, D., Muno, M. P. amd Hartman, J., Psaltis, D., & Chakrabarty, D. 2008, ApJSS, 179, 360

Gandhi, P., Littlefair, S., Hardy, L., et al. 2015, The Astronomer's Telegram, 7686, 1

Gandhi, P., Rao, A., Johnson, M. A. C., Paice, J. A., & Maccarone, T. J. 2018, ArXiv e-prints, arXiv:1804.11349

Gandhi, P., Makishima, K., Durant, M., et al. 2008, MNRAS, 390, L29

Gandhi, P., Bachetti, M., Dhillon, V. S., et al. 2017, Nature Astronomy, 1, 859

Gaskell, C. M., & Peterson, B. M. 1987, ApJs, 65, 1

Gazeas, K., Vasilopoulos, G., Petropoulou, M., & Sapoutntzis, K. 2015, The
    Astronomer's Telegram, 7650, 1

Gendelev, L., & Krumholz, M. R. 2012, ApJ, 745, 158

Gies, D. R., & Bolton, C. T. 1986, ApJ, 304, 371

Ginsburg, A., Glenn, J., Rosolowsky, E., et al. 2013, ApJS, 208, 15

Ginsburg, A., Henkel, C., Ao, Y., et al. 2015, A&A, 573, 106

Gleissner, T., Wilms, J., Pooley, G. G., et al. 2004, A&A, 425, 1061

Goodman, J., & Weare, J. 2010, Comm. App. Math. Comp. Sci., 5, 65

Greisen, E. W. 2003, in Astrophysics and Space Science Library, Vol. 285,
    Information Handling in Astronomy - Historical Vistas, ed. A. Heck, 109

Griffin, M., Abergel, A., Abreu, A., Ade, P., et al. 2010, A&A, 518, 7

Grinberg, V., Pooley, G., Cadolle-Bell, M., et al. 2015, The Astronomer's Tele-
    gram, 7316, 1

Grinberg, V., Boeck, M., Pottschmidt, K., et al. 2011, The Astronomer's Tele-
    gram, 3616, 1

Grinberg, V., Hell, N., Pottschmidt, K., et al. 2013, A&A, 554, 88

Grinberg, V., Wilms, J., Pottschmidt, K., et al. 2014, The Astronomer's Tele-
    gram, 6344, 1

Grindlay, J. E., & Seaquist, E. R. 1986, ApJ, 310, 172

Grise, F., Kaaret, P., Corbel, S., et al. 2012, ApJ, 745, 12

Grise, F., Pakull, M. W., Soria, R., et al. 2008, A&A, 486, 151

Guo, F., Li, H., Daughton, W., & Liu, Y. 2014, Physical Review Letters, 113, 15

Gusinskaia, N. V., Deller, A. T., Hessels, J. W. T., et al. 2017, MNRAS, 470, 1871

Han, X., & Hjellming, R. M. 1992, ApJ, 400, 304

Hannikainen, D. C., Hunstead, R. W., Campbell-Wilson, D., et al. 2000, ApJ, 540, 521

Hao, J. F., & Zhang, S. N. 2009, ApJ, 702, 1648

Harrison, F. A., Craig, W. W., Christensen, F. E., et al. 2013, ApJ, 770, 103

Hastings, W. 1970, Biometrika, 57, 97

Heinke, C., Edmonds, P., Grindlay, J. E., et al. 2003, ApJ, 590, 809

Heinke, C., Wijnands, R., Cohn, H. N., et al. 2006, ApJ, 651, 1098

Heinke, C. O., Jonker, P. G., Wijnands, R., Deloye, C. J., & Taam, R. E. 2009, ApJ Letters, 691, 1035

Heinz, S. 2002, A&A, 388, L40

—. 2006, ApJ, 636, 316

Heinz, S., Corrales, L., Smith, R., et al. 2016, ApJ, 825, 15

Heinz, S., & Grimm, H. 2005, ApJ, 633, 384

Heinz, S., Grimm, H., Sunyaev, R. A., & Fender, R. P. 2008, ApJ, 686, 1145

Heinz, S., & Sunyaev, R. 2003, MNRAS, 343, L59

Heyer, M., Krawczyk, C., Duval, J., & Jackson, J. 2009, ApJ, 699, 1092

Hill, A. B., Szostek, A., Corbel, S., et al. 2011, MNRAS, 415, 235

Hjellming, R., & Johnson, K. 1988, ApJ, 328, 600

Hjellming, R., & Rupen, M. 1995, Nature, 375, 464

Hjellming, R., Rupen, M. P., Mioduszewski, A., & Narayan, R. 2000a, The Astronomer's Telegram, 54, 1

Hjellming, R. M., Calovini, T. A., Han, X., & Cordova, F. A. 1988, ApJ, 335, L75

Hjellming, R. M., & Han, X. 1989, IAU Circular, 4796, 2

Hjellming, R. M., & Han, X. 1995, X-ray Binaries, 308

Hjellming, R. M., & Johnson, K. 1981, ApJ, 246, L141

Hjellming, R. M., Rupen, M. P., Mioduszewski, A. J., et al. 1999, ApJ, 514, 383

Hjellming, R. M., Rupen, M. P., Hunstead, R. W., et al. 2000b, ApJ, 544, 977

Hogbom, J. 1974, ApJS, 15, 417

Hogg, D., Bovy, J., & Lang, D. 2010, ArXiv e-prints, arXiv:1008.4686v1

Holland, W., et al. 2013, MNRAS, 430, 2513

Holt, S., Kaluzienski, L., Boldt, E., & Serlemitsos, P. 1979, ApJ, 233, 344

Homan, J., van der Klis, M., Fridriksson, J., et al. 2010, ApJ, 719, 201

Huang, Y., Dame, T., & Thaddeus, P. 1983, ApJ, 272, 609

Huppenkothen, D., Bachetti, M., Stevens, A. L., Migliari, S., & Balm, P. 2016, Stingray: Spectral-timing software, Astrophysics Source Code Library, ascl:1608.001

Huppenkothen, D., Younes, G., Ingram, A., et al. 2017, ApJ, 834, 90

Hyde, E. A., Russell, D., Ritter, A., et al. 2017, PASP, 129, 094201

Hynes, R., Bradley, C., Rupen, M. P., et al. 2009, MNRAS, 399, 2239

Hynes, R., Haswell, C., Chaty, S., Shrader, C., & Cui, W. 2002a, MNRAS, 331, 169

Hynes, R., Zurita, C., & Haswell, C. 2002b, ApJ, 330, 1009

Hynes, R. I. 2005, ApJ, 623, 1026

Iacolina, M. N., Burgay, M., Burderi, L., Possenti, A., & di Salvo, T. 2010, A&A, 519, A13

Icke, V., Mellema, G., Balick, B., Eulkerink, F., & Frank, A. 1992, Nature, 355, 524

Ingram, A., van der Klis, M., Middleton, M., et al. 2016, MNRAS, 461, 1967

Inoue, H., Koyama, K., Makino, F., et al. 1984, PASJ, 36, 855

Jamil, O., Fender, R., & Kaiser, C. 2010, MNRAS, 401, 394

Jiang, Y., Stone, J. M., & Davis, S. W. 2014, ApJ, 796, 106

Jonker, P. G., Miller-Jones, J. C. A., Homan, J., et al. 2012, MNRAS, 423, 3308

Jonker, P. G., Steeghs, D., Chakrabarty, D., & Juett, A. M. 2007, ApJ Letters, 665, L147

Kaaret, P., Corbel, S., Tomsick, J., et al. 2006, ApJ, 641, 410

Kaaret, P., Corbel, S., Tomsick, J. A., et al. 2003, ApJ, 582, 945

Kaiser, C. 2006, MNRAS, 367, 1083

Kaiser, C., & Alexander, P. 1997, MNRAS, 286, 215

Kaiser, C. R., Gunn, K. F., Brocksopp, C., & Sokoloski, J. L. 2004, ApJ, 612, 332

Kajava, J. J. E., Motta, S. E., Sánchez-Fernández, C., & Kuulkers, E. 2018, A&A Accepted, arXiv:1803.02161

Kalamkar, M., Casella, P., Uttley, P., et al. 2016, MNRAS, 460, 3284

Kalemci, E., Begelman, M., Maccarone, T. J., et al. 2016, MNRAS, 463, 615

Kalemci, E., Dincer, T., Tomsick, J., et al. 2013, ApJ, 779, 14

Kassim, N. E., Giacintucci, S., Lane-Peters, W. M., et al. 2015, The Astronomer's Telegram, 7728, 1

Khargharia, J., Froning, C., & Robinson, E. L. 2010, ApJ, 716, 1105

Kimura, M., Isogai, K., Kato, T., et al. 2016, Nature, 529, 54

Kitamoto, S., Tsunemi, H., Miyamoto, S., Yamashita, K., & Mizobuchi, S. 1989, Nature, 342, 518

Koljonen, K., Russell, D., Fernandez Ontiveros, J., et al. 2015, ApJ, 814, 139

Komossa, S. 2015, Journal of High Energy Astrophysics, 7, 148

Körding, E., Fender, R., & Migliari, S. 2006, MNRAS, 369, 1451

Körding, E., Rupen, M., Knigge, C., et al. 2008, Science, 320, 1318

Kotani, T., Kawai, N., Aoki, T., et al. 1994, PASJ, 46, L147

Kraemer, K. E., Jackson, J. M., Kassis, M., et al. 2003, ApJ, 588, 918

Krimm, H. A., Holland, S. T., Corbet, R. H. D., et al. 2013, ApJSS, 209, 14

Kroupa, P. 2001, MNRAS, 322, 231

Kuulkers, E. 2015, The Astronomer's Telegram, 7758, 1

Kuulkers, E., den Hartog, P. R., in 't Zand, J. J. M., et al. 2003, A&A, 399, 663

Kuulkers, E., Fender, R. P., Spencer, R., Davis, R., & Morison, I. 1999, MNRAS, 306, 919

Kuulkers, E., Motta, S., Kajava, J., et al. 2015, The Astronomer's Telegram, 7647, 1

Lanzoni, B., Ferraro, F., Dalessandro, E., et al. 2010, ApJ, 717, 653

Lawrence, A., Warren, S., Almaini, O., Edge, A., et al. 2007, MNRAS, 379, 1599

Lee, E. J., Miville-Deschênes, M.-A., & Murray, N. W. 2016, ApJ, 833, 229

Lehto, H. J., Machin, G., McHardy, I. M., & Callanan, P. 1990, Nature, 347, 49

Lense, J., & Thirring, H. 1918, Physikalische Zeitschrift, 19, 156

Linares, M., Altamirano, D., Chakrabarty, D., Cumming, A., & Keek, L. 2012, ApJ, 748, 13

Linares, M., Chakrabarty, D., Marshall, H., et al. 2015, The Astronomer's Telegram, 7247, 1

Lindfors, E., Turler, M., Hannikainen, D. C., et al. 2007, A&A, 473, 923

Ling, J., Mahoney, W., Wheaton, W., Jacobson, A., & Kaluzienski, L. 1983, ApJ, 275, 307

Lipunov, V., Gorbovskoy, E., Tiurina, N., et al. 2015, The Astronomer's Telegram, 8453, 1

Liska, M., Hesp, C., Tchekhovskoy, A., et al. 2018, MNRAS, 474, L81

Longair, M. 2011, High Energy Astrophysics (New York: Cambridge University Press)

Ludlam, R., Miller, J. M., Miller-Jones, J., & Reynolds, M. 2017, The Astronomer's Telegram, 10690

Maccarone, T. J. 2002, MNRAS, 336, 1371

—. 2003, A&A, 409, 697

Machin, G., Lehto, H. J., McHardy, I. M., Callanan, P. J., & Charles, P. A. 1990, MNRAS, 246, 237

Magorrian, J., Tremaine, S., Richstone, Douglas; Bender, R., et al. 1998, ApJ, 115, 2285

Maitra, D., Scarpaci, J. F., Grinberg, V., et al. 2017, ApJ, 851, 148

Makino, F. 1989, IAU Circular, 4782, 1

Makishima, K., Ohashi, T., Inoue, H., et al. 1981, ApJ, 247, L23

Malyshev, D., Savchenko, V., Ferrigno, C., Bozzo, E., & Kuulkers, E. 2015, The Astronomer's Telegram, 8458, 1

Malzac, J. 2014, MNRAS, 443, 229

Malzac, J., Belloni, T., Spruit, H., & Kanbach, G. 2003, A&A, 407, 335

Margon, B. 1984, ARA&A, 22, 507

Margon, B., Ford, H. C., Grandi, S. A., & Stone, R. P. S. 1979, ApJ Letters, 233, L63

Markoff, S., Falcke, H., & Fender, R. 2001, A&A, 372, L25

Markoff, S., Nowak, M., Corbel, S., Fender, R., & Falcke, H. 2003, A&A, 397

364

Markoff, S., Nowak, M., & Wilms, J. 2005, ApJ, 635, 1203

Marscher, A. P., & Gear, W. 1985, ApJ, 298, 114

Marsh, T. R., Gänsicke, B. T., Hümmerich, S., et al. 2016, Nature, 537, 374

Marshall, H. L., Rutledge, R., Fox, D. W., et al. 2001, AJ, 122, 21

Martí, J., Mirabel, I. F., Rodríguez, L. F., & Smith, I. A. 2002, A&A, 386, 571

Marti-Vidal, I., Vlemmings, W., Muller, S., & Casey, S. 2014, A&A, 563, 9

Martin, R. G., Tout, C. A., & Pringle, J. E. 2008, MNRAS, 387, 188

Martin-Carrillo, A., Murphy, D., Hanlon, L., et al. 2015, The Astronomer's Telegram, 7729, 1

Martins, F., Schaerer, D., & Hillier, D. J. 2005, A&A, 436, 1049

Massi, M., & Kaufman Bernadó, M. 2008, A&A, 477, 1

McClintock, J. E., & Remillard, R. A. 2006, Black hole binaries (Cambridge Astrophysics Series, ed. Lewin, W. H. G. and van der Klis, M.), 157–213

McMullin, J. P., Waters, B., Schiebel, D., Young, W., & Golap, K. 2007, Astronomical Data Analysis Software and Systems XVI, ed. R.A. Shaw, F. Hill and D.J. Bell, Astronomical Society of the Pacific Conference Series, Volume 376, 127

McNamara, B., & Nulsen, P. 2007, ARA&A, 45, 117

McNamara, B. R., Nulsen, P. E. J., Wise, M. W., et al. 2005, Nature, 433, 45

Meier, D., Koide, S., & Uchida, Y. 2001, Science, 291, 84

Melrose, D., & Pope, M. 1993, Publ. Astron. Soc. Australia, 10, 222

Merloni, A., Heinz, S., & Di Matteo, T. 2003, MNRAS, 345, 1057

Metropolis, N., Rosenbluth, A., Rosenbluth, M., Teller, A., & Teller, E. 1953, Journal of Chemical Physics, 21, 1087

Middleton, M. J., Fragile, P. C., Bachetti, M., et al. 2018, MNRAS, 475, 154

Migliari, S., & Fender, R. 2006, MNRAS, 366, 79

Migliari, S., Fender, R., Rupen, M., et al. 2004, MNRAS, 351, 186

Migliari, S., Fender, R. P., Rupen, M., et al. 2003, MNRAS, 342, L67

Migliari, S., Ghisellini, G., Miller-Jones, J., & Russell, D. 2012, in International Journal of Modern Physics Conference Series, Vol. 8, International Journal of Modern Physics Conference Series, 108–113

Migliari, S., Miller-Jones, J. C. A., & Russell, D. M. 2011, MNRAS, 415, 2407

Migliari, S., Tomsick, J. A., Miller-Jones, J. C. A., et al. 2010, ApJ, 710, 117

Migliori, G., Corbel, S., Tomsick, J. A., et al. 2017, MNRAS, 472, 141

Miller-Jones, J. 2014, PASA, 31, 14

Miller-Jones, J., Jonker, P. G., Ratti, E. M., et al. 2011, MNRAS, 415, 306

Miller-Jones, J. C. A., Blundell, K. M., Rupen, M. P., et al. 2004, ApJ, 600, 368

Miller-Jones, J. C. A., Fender, R., & Nakar, E. 2006, MNRAS, 367, 1432

Miller-Jones, J. C. A., Heinke, C. O., Sivakoff, G. R., et al. 2010, The Astronomer's Telegram, 2377

Miller-Jones, J. C. A., Jonker, P., Maccarone, T., Nelemans, G., & Calvelo, D. E. 2011, ApJ, 739, L18

Miller-Jones, J. C. A., Jonker, P. G., Dhawan, V., et al. 2009, ApJ, 706, L230

366

Miller-Jones, J. C. A., Jonker, P. G., Nelemans, G., et al. 2009, MNRAS, 394, 1440

Miller-Jones, J. C. A., Rupen, M. P., Fender, R. P., et al. 2007a, MNRAS, 375, 1087

Miller-Jones, J. C. A., Rupen, M. P., Turler, M., et al. 2009, MNRAS, 394, 309

Miller-Jones, J. C. A., Kaiser, C., Maccarone, T. J., et al. 2007b, Conf. Proc. "A Population Explosion: The Nature and Evolution of X-ray Binaries in Diverse Environments", Editors: R.M. Bandyopadhyay, S. Wachter, D. Gelino, & C. R. Gelino

Miller-Jones, J. C. A., Sivakoff, G., Altamirano, D., et al. 2010, MNRAS, 716, L109

Miller-Jones, J. C. A., Sivakoff, G. R., Altamirano, D., et al. 2012, MNRAS, 421, 468

Mirabel, F. 2017, New Astronomy Reviews, 78, 1

Mirabel, I., Chaty, S., Rodriguez, L., & Sauvage, M. 2015, Proc. IAU Symp., 313, 370

Mirabel, I., Rodriguez, L., Cordier, B., Paul, J., & LeBrun, F. 1992, Nature, 358, 215

Mirabel, I. F., Dhawan, V., Chaty, S., et al. 1998, A&A, 330, L9

Mirabel, I. F., Dijkstra, M., Laurent, P., Loeb, A., & Pritchard, J. R. 2011, A&A, 528, 6

Mirabel, I. F., & Rodríguez, L. F. 1994, Nature, 371, 46

—. 1999, ARA&A, 37, 409

Mirabel, I. F., Rodriguez, L. F., Marti, J., et al. 1993, IAU Circular, 5773, 1

Miyamoto, S., Kitamoto, S., Iga, S., Negoro, H., & Terada, K. 1992, ApJ, 391, L21

Molinari, S., Swinyard, B., Bally, J., et al. 2010, PASP, 122, 314

Mooley, K., Fender, R., Anderson, G., et al. 2015, The Astronomer's Telegram, 7658, 1

Motta, S., Beardmore, A., Oates, S., et al. 2015a, The Astronomer's Telegram, 7665, 1

—. 2015b, The Astronomer's Telegram, 7666, 1

Motta, S., Sanchez-Fernanedz, C., Kajava, J., et al. 2016, The Astronomer's Telegram, 8510, 1

Motta, S. E., Franchini, A., Lodato, G., & Mastroserio, G. 2018, MNRAS, 473, 431

Motta, S. E., Kajava, J. J. E., Sánchez-Fernández, C., Giustini, M., & Kuulkers, E. 2017a, MNRAS, 468, 981

Motta, S. E., Kajava, J. J. E., Sánchez-Fernández, C., et al. 2017b, MNRAS, 471, 1797

Muñoz-Darias, T., Casares, J., Mata Sánchez, D., et al. 2016, Nature, 534, 75

—. 2017, MNRAS, 465, L124

Mukherjee, D., Bult, P., van der Klis, M., & Bhattacharya, D. 2015, MNRAS, 452, 3994

Muno, M., & Mauerhan, J. 2006, ApJ, 648, L135

Naik, S., Agrawal, P., Rao, A., et al. 2001, ApJ, 546, 1075

Nandi, A., Chakrabarti, S., Vadawale, S. V., & Rao, A. R. 2001, A&A, 380, 245

Narayan, R., & Yi, I. 1995, ApJ, 452, 710

Negoro, H., Itoh, D., Ueno, S., et al. 2015, The Astronomer's Telegram, 7579, 1

Neilsen, J., Coriat, M., Fender, R., et al. 2014, ApJ, 784, L5

Nipoti, C., Blundell, K., & Binney, J. 2005, MNRAS, 361, 633

Nowak, M. A., Vaughan, B. A., Wilms, J., Dove, J. B., & Begelman, M. C. 1999, ApJ, 510, 874

Oates, S. R., et al. 2015, The Astronomer's Telegram, 7734, 1

O'Neill, P., Sood, R., Durouchoux, P., & Safi-Harb, S. 2000, IAU Symposium, Vol. 195, 419

Oosterbroek, T., van der Klis, M., van Paradijs, J., et al. 1997, A&A, 321, 776

Orosz, J., McClintock, J., Aufdenberg, J., et al. 2011, ApJ, 742, 84

Pakull, M., Soria, R., & Motch, C. 2010, Nature, 466, 209

Pandey, M., Rao, A., Pooley, G., et al. 2006, A&A, 447, 525

Papitto, A., Ferrigno, C., Bozzo, E., et al. 2013, Nature, 501, 517

Paredes, J., Marti, J., Peracaula, M., Pooley, G., & Mirabel, I. 2000, A&A, 357, 507

Parfrey, K., Spitkovsky, A., & Beloborodov, A. M. 2017, MNRAS, 469, 3656

Patruno, A., Haskell, B., & Andersson, N. 2017, ApJ, 850, 106

Patruno, A., & Watts, A. L. 2012, ArXiv e-prints, arXiv:1206.2727

Patruno, A., Wette, K., & Messenger, C. 2018, ApJ, 859, 112

Patruno, A., Archibald, A. M., Hessels, J. W. T., et al. 2014, ApJ Letters, 781, L3

Pe'er, A., & Casella, P. 2009, ApJ, 699, 1919

Pe'er, A., & Markoff, S. 2012, ApJ, 753, 177

Perley, R. A., & Butler, B. J. 2017, ApJ Supplements, 230, 7

Perrott, Y. C., Scaife, A. M. M., Green, D. A., et al. 2013, MNRAS, 429, 3330

Perucho, M., & Bosch-Ramon, V. 2008, A&A, 482, 917

Pineda, J., Caselli, P., & Goodman, A. 2008, ApJ, 679, 481

Plotkin, R., Gallo, E., & Jonker, P. 2013, ApJ, 773, 59

Plotkin, R., Gallo, E., Markoff, S., et al. 2015, MNRAS, 446, 4098

Plotkin, R., Markoff, S., Kelly, B., Körding, E., & Anderson, S. 2012, MNRAS, 419, 267

Plotkin, R. M., Gallo, E., Jonker, P., et al. 2016, MNRAS, 456, 2707

Plotkin, R. M., Bright, J., Miller-Jones, J. C. A., et al. 2017, ApJ, 848, 92

Plotkin, R. M., Miller-Jones, J. C. A., Gallo, E., et al. 2017, ApJ, 834, 19

Poglitsch, A., Waelkens, C., Geis, N., Feuchtgruber, H., et al. 2010, A&A, 518, 12

Polko, P., Meier, D., & Markoff, S. 2010, ApJ, 723, 1343

—. 2013, MNRAS, 428, 587

—. 2014, MNRAS, 438, 559

Pooley, G., & Fender, R. 1997, MNRAS, 292, 925

Pooley, G. G., Fender, R. P., & Brocksopp, C. 1999, MNRAS, 302, L1

Pottschmidt, K., Wilms, J., Nowak, M. A., et al. 2003, A&A, 407, 1039

Poutanen, J., Lipunova, G., Fabrika, S., Butkevich, A. G., & Abolmasov, P. 2007, MNRAS, 377, 1187

Primiani, R., Young, K., Young, A., et al. 2016, Journal of Astronomical Instrumentation, 5, 19

Punsly, B., & Coroniti, F. V. 1990, ApJ, 350, 518

Radhika, D., Nandi, A., Agrawal, V. K., & Mandal, S. 2016, MNRAS, 462, 1834

Ratti, E. M., Jonker, P. G., Miller-Jones, J., et al. 2012, MNRAS, 423, 2656

Reid, M., McClintock, J., Narayan, R., et al. 2011, ApJ, 742, 83

Reid, M., McClintock, J., Steiner, J., et al. 2014a, ApJ, 796, 2

Reid, M., Menten, K. M., Brunthaler, A., et al. 2014b, ApJ, 783, 130

Remillard, R., & McClintock, J. 2006, ARA&A, 44, 49

Ribó, M., Munar-Adrover, P., Paredes, J. M., et al. 2017, ApJ Letters, 835, L33

Richter, G. 1989, IBVS, 3362, 1

Roberts, T., Goad, M., Ward, M., & Warwick, R. 2003, MNRAS, 342, 709

Rodriguez, J., Cadolle Bel, M., Alfonso-Garzón, J., et al. 2015, A&A, 581, L9

Rodríguez, L. F., & Mirabel, I. 1998, A&A, 340, L47

Rodriguez, L. F., & Mirabel, I. F. 1999, ApJ, 511, 398

Romanova, M. M., Ustyugova, G. V., Koldoba, A. V., & Lovelace, R. V. E. 2009, MNRAS, 399, 1802

Rupen, M. P., Dhawan, V., & Mioduszewski, A. J. 2002, IAU Circular, 7893

Rushton, A., Spencer, R., Pooley, G., & Trushkin, S. 2010, MNRAS, 401, 2611

Rushton, A. P., Shaw, A., Fender, R. P., et al. 2016, MNRAS, 463, 628

Rushton, A. P., Miller-Jones, J. C. A., Curran, P. A., et al. 2017, MNRAS, 468, 2788

Russell, D., Fender, R., Gallo, E., Miller-Jones, J., & Kaiser, C. 2006, Proceedings of the VI Microquasar Workshop: Microquasars and Beyond, Editor: T. Belloni

Russell, D., Fender, R., Hynes, R., et al. 2006, MNRAS, 371, 1334

Russell, D., Gallo, E., & Fender, R. 2013a, MNRAS, 431, 405

Russell, D., Maitra, D., Dunn, R., & Markoff, S. 2010, MNRAS, 405, 1759

Russell, D., Markoff, S., Casella, P., et al. 2013b, MNRAS, 429, 815

Russell, D. M., Fender, R. P., Gallo, E., & Kaiser, C. R. 2007, MNRAS, 376, 1341

Russell, D. M., Miller-Jones, J. C. A., Maccarone, T. J., et al. 2011, ApJ, 739, L19

Russell, D. M., Russell, T. D., Miller-Jones, J. C. A., et al. 2013c, ApJ, 768, L35

Russell, T., Soria, R., Miller-Jones, J., et al. 2014, MNRAS, 439, 1390

Russell, T. D., Miller-Jones, J. C. A., Curran, P. A., et al. 2015, MNRAS, 450, 1745

Russell, T. D., Miller-Jones, J. C. A., Curran, P. A., et al. 2015, MNRAS, 450, 1745

Russell, T. D., Miller-Jones, J. C. A., Sivakoff, G. R., et al. 2016, MNRAS, 460, 3720

Rutledge, R., Moore, C., Fox, D., Lewin, W., & van Paradijs, J. 1998, The Astronomer's Telegram, 8

Safi-Harb, S., & Ogelman, H. 1997, ApJ, 483, 868

Sánchez-Fernández, C., Kajava, J. J. E., Motta, S. E., & Kuulkers, E. 2017, A&A, 602, A40

Sanna, A., Bahramian, A., Bozzo, E., et al. 2018, A&A, 610, L2

Sari, R., Piran, T., & Narayan, R. 1998, ApJ Letters, 497, L17

Sault, R. J., Teuben, P. J., & Wright, M. C. H. 1995, in Astronomical Society of the Pacific Conference Series, Vol. 77, Astronomical Data Analysis Software and Systems IV, ed. R. A. Shaw, H. E. Payne, & J. J. E. Hayes, 433

Scarpaci, J., Maitra, D., Hynes, R., & Markoff, S. 2015, The Astronomer's Telegram, 7737, 1

Sell, P. H., Heinz, S., Richards, E., et al. 2015, MNRAS, 446, 3579

Serino, M., Mihara, T., Matsuoka, M., et al. 2012, PASJ, 64, 5

Shahbaz, T., Ringwald, F. A., Bunn, J. C., et al. 1994, MNRAS, 271, L10

Shahbaz, T., Russell, D., Covino, S., et al. 2016, MNRAS, 463, 1822

Sharma, S. 2017, ARA&A, 55, 213

Shaw, A. 2015, The Astronomer's Telegram, 7738, 1

Shepherd, M. C. 1997, in Astronomical Society of the Pacific Conference Series, Vol. 125, Astronomical Data Analysis Software and Systems VI, ed. G. Hunt & H. Payne, 77

Silk, J., & Rees, M. 1998, A&A, 331, L1

Sironi, L., Giannios, D., & Petropoulou, M. 2016, MNRAS, 462, 48

Sironi, L., & Spitkovsky, A. 2014, ApJ, 783, L21

Sivakoff, G., Bahramian, A., Altamirano, D., et al. 2015a, The Astronomer's Telegram, 7959, 1

Sivakoff, G. R., Bahramian, A., Altamirano, D., Miller-Jones, J. C. A., & Russell, D. 2015b, The Astronomer's Telegram, 7763, 1

Sivakoff, G. R., Bahramian, A., Heinke, C., et al. 2015c, The Astronomer's Telegram, 7788, 1

Sivakoff, G. R., Heinke, C. O., Miller-Jones, J. C. A., et al. 2011, The Astronomer's Telegram, 3393

Solomon, P., Rivolo, A., Barrett, J., & Yahil, A. 1987, ApJ, 319, 730

Soria, R., Long, K. S., Blair, W. P., et al. 2014, Science, 343, 1330

Soria, R., Pakull, M., Broderick, J., Corbel, S., & Motch, C. 2010, MNRAS, 409, 541

Spencer, R., Rushton, A. P., Balucinska-Church, M., et al. 2013, MNRAS, 435, L48

Stanimirovic, S., Altschuler, D., Goldsmith, P., & Salter, C. 2002, Single-Dish Radio Astronomy: Techniques and Applications, Astronomical Society of the Pacific Conference Series, Volume 278

Stevens, J., Hannikainen, D. C., Wu, K., Hunstead, R., & McKay, D. 2003, MNRAS, 342, 623

Stirling, A., Spencer, R., de la Force, C., et al. 2001, MNRAS, 327, 1273

Strohmayer, T. E., & Markwardt, C. B. 2010, The Astronomer's Telegram, 2569, 1

Tanaka, Y., & Lewin, W. 1995, in X-Ray Binaries, Vol. Lewin, W.H.G. and van Paradijs, J. and van den Heuvel, E.P.J. (Cambridge University Press), 126–174

Tananbaum, H., Gursky, H., Kellogg, E., & Giacconi, R. 1972, ApJ, 177, L5

Taylor, G., Carilli, C., & Perley, R. 1998, Synthesis Imaging in Radio Astronomy II, Astronomical Society of the Pacific Conference Series, Volume 180

Terada, K., Miyamoto, S., Kitamoto, S., & Egoshi, W. 1994, PASJ, 46, 677

Tetarenko, A., Sivakoff, G., Gurwell, M., et al. 2015a, The Astronomer's Telegram, 7661, 1

Tetarenko, A., Sivakoff, G., Young, K., Wouterloot, J., & Miller-Jones, J. 2015b, The Astronomer's Telegram, 7708, 1

Tetarenko, A., Sivakoff, G. R., Bremer, M., et al. 2015c, The Astronomer's Telegram, 7740, 1

Tetarenko, A., Sivakoff, G. R., Miller-Jones, J., & Coulson, I. 2016a, The Astronomer's Telegram, 8499, 1

Tetarenko, A. J., Sivakoff, G. R., Miller-Jones, J. C. A., et al. 2015d, ApJ, 805, 30

Tetarenko, A. J., Bahramian, A., Sivakoff, G. R., et al. 2016b, MNRAS, 460, 345

Tetarenko, A. J., Bahramian, A., Sivakoff, G. R., et al. 2017a, The Astronomer's Telegram, 10894

—. 2017b, The Astronomer's Telegram, 10843

Tetarenko, A. J., Sivakoff, G. R., Heinke, C. O., et al. 2017c, The Astronomer's Telegram, 10422

Tetarenko, A. J., Sivakoff, G., Miller-Jones, J., et al. 2017, MNRAS, 469, 3141

Tetarenko, B., Sivakoff, G., Heinke, C., & Gladstone, J. C. 2016c, ApJS, 222, 15

Tingay, S. J., Jauncey, D. L., Preston, R. A., et al. 1995, Nature, 374, 141

Tremou, E., Sivakoff, G., Bahramian, A., et al. 2015, The Astronomer's Telegram, 7262, 1

Trushkin, S. A., Nizhelskij, N. A., & Tsybulev, P. 2015, The Astronomer's Telegram, 8454, 1

Tsubono, K., Aoki, T., Asuma, K., et al. 2015, The Astronomer's Telegram, 7733, 1

Tudor, V., Bahramian, A., Sivakoff, G., et al. 2016, The Astronomer's Telegram, 8914

Tudor, V., Miller-Jones, J. C. A., Patruno, A., et al. 2017, MNRAS, 470, 324

Tudose, V., Fender, R., Tzioumis, A. K., Spencer, R., & van der Klis, M. 2008, MNRAS, 390, 447

Tudose, V., Fender, R. P., Linares, M., Maitra, D., & van der Klis, M. 2009, MNRAS, 400, 2111

Turler, M., Courvoisier, T. J.-L., Chaty, S., & Fuchs, Y. 2004, A&A, 415, L35

Turler, M., Courvoisier, T. J.-L., & Paltani, S. 2000, A&A, 361, 850

Uemura, M., Kato, T., Ishioka, R., et al. 2004, PASJ, 56, 61

Uttley, P., & Casella, P. 2014, Space Science Reviews, 183, 453

Vadawale, S. V., Rao, A. R., Naik, S., et al. 2003, ApJ, 597, 1023

Vadawale, S. V., Rao, A. R., Nandi, A., & Chakrabarti, S. 2001, A&A, 370, L17

Valenti, E., Ferraro, F., & Origlia, L. 2007, AJ, 133, 1287

van den Eijnden, J., Degenaar, N., Russell, T. D., et al. 2018a, MNRAS, 474, L91

—. 2018b, MNRAS, 473, L141

van der Horst, A., Curran, P., Miller-Jones, J., et al. 2013, MNRAS, 436, 2625

van der Klis, M. 2006, in Compact Stellar X-Ray Sources, ed. W. Lewin & M. van der Klis (Cambridge University Press), 39–112

van der Laan, H. 1966, Nature, 5054, 1131

van Haaften, L. M., Voss, R., & Nelemans, G. 2012, A&A, 543, A121

Vaughan, B. A., & Nowak, M. A. 1997, ApJ Letters, 474, L43

Vaughan, S., Edelson, R., Warwick, R. S., & Uttley, P. 2003, MNRAS, 345, 1271

Vernaleo, J. C., & Reynolds, C. S. 2006, ApJ, 645, 83

Verner, D. A., Ferland, G. J., Korista, K. T., & Yakovlev, D. G. 1996, ApJ, 465, 487

Vincentelli, F. M., Casella, P., Maccarone, T. J., et al. 2018, MNRAS, 477, 4524

Wagner, R. M., Starrfield, S. G., Cassatella, A., et al. 1989, IAU Circular, 4783, 1

Walton, D. J., Mooley, K., King, A. L., et al. 2017, ApJ, 839, 110

Wang, Y., & Méndez, M. 2016, MNRAS, 456, 1579

Watts, A., Krishnan, B., Bildsten, L., & Schutz, F. 2008, MNRAS, 389, 839

Wiersema, K., Russell, D. M., Degenaar, N., et al. 2009, MNRAS, 397, L6

Wijnands, R., Degenaar, N., & Page, D. 2017, Journal of Astrophysics and Astronomy, 38, 49

Wijnands, R., Heinke, C., Pooley, D., et al. 2005, ApJ, 618, 883

Wijnands, R., Homan, J., Heinke, C. O., Miller, J. M., & Lewin, W. H. G. 2005, ApJ, 619, 492

Williams, D., & Viti, S. 2013, Observational Molecular Astronomy: Exploring the Universe Using Molecular Line Emissions (Cambridge University Press)

Wilms, J., Allen, A., & McCray, R. 2000, ApJ, 542, 914

Wilms, J., Nowak, M. A., Pottschmidt, K., Pooley, G. G., & Fritz, S. 2006, A&A, 447, 245

Wilms, J., Pottschmidt, K., Pooley, G. G., et al. 2007, ApJ Letters, 663, L97

Wilson, T., Rohlfs, K., & Huttemeister, S. 2013, Tools of Radio Astronomy (Springer)

Wilson, T. L., & Rood, R. 1994, ARA&A, 32, 191

Wolfire, M., McKee, C., Hollenbach, D., & Tielens, A. 2003, ApJ, 587, 278

Wright, E., Eisenhardt, P., Mainzer, A., Ressler, M., et al. 2010, ApJ, 140, 1868

Wu, X., Wang, F., Fan, X., et al. 2015, Nature, 518, 512

Yan, Z., & Yu, W. 2017, MNRAS, 470, 4298

Yang, H. K., & Reynolds, C. S. 2016, ApJ, 829, 90

Yang, J., Brocksopp, C., Corbel, S., et al. 2010, MNRAS, 409, L64

Yang, J., Paragi, Z., Corbel, S., et al. 2011, MNRAS, 418, L25

Yusef-Zadeh, F., Wardle, M., Heinke, C., et al. 2008, ApJ, 682, 361

Zdziarski, A., Poutanen, J., Paciesas, W., & Wen, L. 2002, ApJ, 578, 357

Zurita, C., Casares, J., & Shahbaz, T. 2003, ApJ, 582, 369

Zwart, J. T. L., Barker, R. W., Biddulph, P., et al. 2008, MNRAS, 391, 1545

Zwarthoed, G. A. A., Stewart, R., Penninx, W., et al. 1993, A&A, 267, 101

Zycki, P., Done, C., & Smith, D. 1999, MNRAS, 309, 561

Zycki, P. T., Done, C., & Smith, D. A. 1999, MNRAS, 305, 231